ISBN 978-82-326-1468-4 (printed ver.)
ISBN 978-82-326-1469-1 (electronic ver.)
ISSN 1503-8181

NTNU
Norwegian University of
Science and Technology

Kai Erik Ekstrøm

Doctoral thesis

Doctoral theses at NTNU, 2016:65

NTNU
Norwegian University of
Science and Technology
Thesis for the Degree of
Philosophiae Doctor
Faculty of Natural Sciences and Technology
Department of Materials Science and
Engineering

NTNU

Doctoral theses at NTNU, 2016:65

Kai Erik Ekstrøm

Structure Control of Multicrystalline Silicon

NTNU
Norwegian University of
Science and Technology

Kai Erik Ekstrøm

Structure Control of Multicrystalline Silicon

Thesis for the Degree of Philosophiae Doctor

Trondheim, March 2016

Norwegian University of Science and Technology
Faculty of Natural Sciences and Technology
Department of Materials Science and Engineering

NTNU
Norwegian University of
Science and Technology

NTNU
Norwegian University of Science and Technology

Thesis for the Degree of Philosophiae Doctor

Faculty of Natural Sciences and Technology
Department of Materials Science and Engineering

ISBN 978-82-326-1468-4 (printed ver.)
ISBN 978-82-326-1469-1 (electronic ver.)
ISSN 1503-8181

IMT-report 2016:224

Doctoral theses at NTNU, 2016:65

Printed by NTNU Grafisk senter

This thesis has been submitted to

Department of Materials Science and Engineering
Norwegian University of Science and Technology

in partial fulfilment of the requirements for

the academic degree

Philosophiae Doctor

December 2015

PREFACE

The work of this thesis was carried out from August 2012 until December 2015. My main supervisor has been Assoc. Prof. Marisa Di Sabatino Lundberg together with Prof. Lars Arnberg and Dr. Gaute Stokkan as co-supervisors. The work has mainly been funded by the Norwegian Research Centre for Solar Cell Technology (contract number 193829), a Centre for Environment-Friendly Energy Research that is co-sponsored by the Norwegian Research Council, and research and industry partners in Norway. Additional funding was provided through the "Impurity Control in High Performance Multicrystalline Silicon" project, financed by The Research Council of Norway (RCN), and research and industry partners in Norway.

The author has performed all experimental work, with the following exceptions:

- Wafering of the ingots was performed by Dipl. Eng. Bern Weber at the Fraunhofer Institute for Solar Energy Systems, Freiburg, Germany.

- The X-Ray Laue Scanner measurements were performed by Dr. Toni Lehmann at the Fraunhofer Technology Centre for Semiconductor Materials (THM), Freiberg, Germany.

- Minority carrier lifetime measurements were performed by Dr. Rune Søndenå at Institute for Energy Technology, Kjeller, Norway.

- Most of the experimental characterization in Paper P4 was coordinated and done by Sergio Castellanos at Massachusetts Institute of Technology (MIT), Cambridge, USA.

Most of the experimental work done by the author has been done at the Department of Materials Science and Engineering at the Norwegian University of Science and Technology. The characterization of the iron content in seeded multicrystalline silicon was done at Fraunhofer Institute for Solar Energy Systems (ISE) in Freiburg, Germany.

Parts of the work have been published or submitted for publication, as given in the list below.

PAPER P1

K. E. Ekstrøm, H. Dalaker, A. Autruffe, R. Søndenå, G. Stokkan, L. Arnberg, M. Di Sabatino, «Characterization of mono-like silicon grown by a seed-assisted Bridgman method», Proceedings of The 7th International Workshop on Crystalline Silicon Solar Cells, 77-81 (2013).

PAPER P2

K. E. Ekstrøm, G. Stokkan, R. Søndenå, H. Dalaker, T. Lehmann, L. Arnberg, M. Di Sabatino, «Structure and dislocation development in mono-like silicon», Physica Status Solidi A: Applications and Materials Science, 212(10), 2278-2288 (2015).

PAPER P3

K. E. Ekstrøm, A. Autruffe, R. Søndenå, H. Dalaker, G. Stokkan, L. Arnberg, M. Di Sabatino, «The microstructure of multicrystalline silicon seeded by polysilicon chips and fluidized bed reactor granules", Journal of Crystal Growth, To be Submitted (2015).

PAPER P4

S. Castellanos, K. E. Ekstrøm, A. Autruffe, M. A. Jensen, A. E. Morishige, J. Hofstetter, P. Yen, B. Lai, G. Stokkan, C. del Cañizo, T. Buonassisi,
"Comparison of gettering responses and lifetime-limiting defects in high-performance and traditional multicrystalline silicon", IEEE Journal of Photovoltaics, Submitted (2015) .

PAPER P5

K. E. Ekstrøm, E. Undheim, G. Stokkan, L. Arnberg, M. Di Sabatino,"Beta-Si_3N_4 particles as nucleation sites in multicrystalline silicon", Acta Materialia, Submitted (2015).

Trondheim, December 14th 2015,

Kai Erik Ekstrøm

ACKNOWLEDGEMENTS

First and foremost I wish to express my gratitude towards my main supervisor Assoc. Prof. Marisa Di Sabatino Lundberg, and co-supervisors Prof. Lars Arnberg and Dr. Gaute Stokkan for excellent support and guidance throughout these years. Your doors have always been open and I have always greatly enjoyed our discussions. With your combined knowledge you make a strong and great team. Thank you Marisa and Lars, for always being encouraging, enthusiastic and open minded about my work. Thank you Gaute, for all our mind-bending discussions. I also want to take the opportunity to wish Lars all the best with his retirement. Your contribution to the scientific community is indescribable, and I see you as a true inspiration.

During these years I have also had the privilege to work with great colleagues. I want to give a special thanks to Adjunct Assoc. Prof. Eivind Øvrelid, for making me want to do a PhD in the first place. Much of this work had probably not been realized, and my PhD would have looked very different, if it had not been for Dr. Halvor Dalaker, who approached me with the desire to do the included solidification experiments. The additional support from Dr. Martin Syvertsen and Dr. Martin Bellmann has also been invaluable for these experiments.

Antoine, thank you very much for all our years as office mates and friends. Our discussions, both scientific and non-scientific, have been inspiring and invaluable to me. Thank you Guilherme, for being a great friend and helping me out whatever the problem, it has been greatly valued. I also want to express my gratitude towards Espen Undheim, Torunn Ervik and Emil Dyrvik for our cooperation.
A special gratitude also goes to the staff at our department, and at SINTEF Materials and Chemistry. Especially Dr. Yingda Yu, Prof. Jarle Hjelen and Senior Engineer Wilhelm Dall for being helpful at the microscopy lab, Dr. Julian Tolchard for helping me with X-ray measurements, and Engineers Torild Krogstad, Harald Holm and Trygve Schanche for always being available and helping out with various lab difficulties. My thanks also goes to Engineers Birgitte Karlsen, for training me on different characterization tools and always spreading joy and happiness, and Ove Darell for all the help with ingot cutting.

My exchange stay became a challenge due to a long period of sick leave. However, I finally got the possibility to go to Freiburg in Germany for a small period during winter 2014. I want to thank the group at Fraunhofer ISE for hosting me, especially Prof. Martin Schubert, Dr. Jonas Schön and Dr. Florian Schindler for taking good care of me. I really enjoyed the stay.

We have also had a close collaboration with the Institute for Energy Technology here in Norway. My thanks goes out to all the people working in the solar division, especially Dr. Rune Søndenå and Adjunct Prof. Erik Marstein. Thank you Rune for our collaboration and always welcoming me to IFE. Thank you Erik for your support, and never-ending positivity and enthusiasm towards the Norwegian solar community.

Finally, I also want to show my deepest gratitude towards my dearest friends and family. Thank you Mom for your never-ending support and being only a phone call away. Thank you Knut for telling 16-years-old-me that solar technology is the future and something worth looking into. Thank you Kamilla and Stine, for being the most awesome sisters a brother can ever have. And finally, to the love of my life, Heidi. Thank you for your endless love and support, and for taking my mind of work when I needed it the most.

ABSTRACT

This work targets multiple approaches for controlling the initial growth conditions of directional solidification, and their effect on the final material microstructure and performance. Challenges related to both seeded and non-seeded growth conditions are addressed.

Seeding with pre-defined silicon crystals are a relatively simple way of limiting random nucleation, and tuning the final microstructure of the ingot. The microstructure of the ingot will, to a large extent, reflect the microstructure of the seed particles, meaning that monocrystalline seeds lead to a near-monocrystalline, or mono-like, microstructure, while fine-grained multicrystalline seeds lead to the more refined high performance multicrystalline microstructure. This work reveals that the main challenges with the mono-like method are i) the parasitic grain structure developing from the periphery of the ingot and ii) dislocation sources appearing between multiple seed crystals. While dislocations generated at stress-points can be minimized by proper seed preparation, and by introducing small gaps between individual seeds, the dislocation structures generated due to seed misorientation can become very detrimental for the final material performance. The magnitude and complexity of the misorientation appears to be determinative in the advance of these dislocation structures, and a better understanding of the mechanisms governing the dislocation behaviour at the seed junctions is needed. While the mono-like method targets to eliminate both grain boundaries and dislocations, the high performance method utilize certain properties of random angle grain boundaries to terminate the propagation of dislocation clusters. Seeding of this type of material is therefore usually done with very fine-grained seeds that contains a very high fraction of random angle grain boundaries. This part of the work focuses on investigating the microstructural differences between ingots seeded with polysilicon chips and fluidized bed reactor granules. The work suggests that larger and more uniformly shaped seeds may be more suitable for seeding purposes, as they contain less morphological extremities for stress and dislocation generation, and are less prone to microstructural coarsening. Nevertheless, due to the high density of grain boundaries, further performance improvements to this type of material can mainly be realized through advances in impurity control and/or post-processing.

Non-seeded growth methods are mainly governed by the nucleation conditions during the earliest stages of solidification, i.e. the nucleation stage. In this work, samples cut from the bottom of ingots are investigated in terms of locating possible nucleation sites, and mechanisms active during this stage. By correlating experimental observations with the free growth model, we posit that nucleation takes place preferably on β-Si_3N_4 particles, due to their high compatibility with silicon and their large size. The clear signs of dendritic growth indicate that dendrites play an important role also during directional solidification of multicrystalline silicon, and should be avoided if a finer grain structure is desired. Based on this study, it is also suggested that proper engineering of Si_3N_4 particles, together with certain cooling parameters, may prove useful for achieving different microstructures.

TABLE OF CONTENTS

SYMBOLS AND ABBREVIATIONS

Symbols	Description	Unit
a	Lattice spacing	Å
A	Cross-sectional area	cm^2
$\vec{b}$	Burgers vector of a dislocation	
$\boldsymbol{C_C}$	Matrix representing the coordinate system / orientation of a grain	
$\boldsymbol{C_S}$	Matrix representing the coordinate system / orientation of a sample	
$C(\Delta n)$	Shockley-Read-Hall pre-factors	
$\boldsymbol{G}$	Orientation matrix, relating the grain orientation to the sample orientation	
$\boldsymbol{G_D}$	Disorientation matrix, relating the orientation matrix of two individual grains	
F	Applied force	N
$f(\theta)$	Factor adjusting for the wettability	
$[Fe_i]$	Concentration of interstitial iron	cm^{-3}
$FoR_{Fe(i)}$	Fraction of total recombination caused by interstitial iron	
ΔG	Total Gibbs free energy of change	J/mol
ΔG_i	Gibbs free energy of change for formation of a new solid interface	J/mol
ΔG_v	Gibbs free energy of change for formation of a new solid volume	J/mol
ΔG_{r^*}	Critical Gibbs free energy of change for formation of a stable nucleus	J/mol
Δg_V	Gibbs free energy of change per unit volume	$J/(cm^3mol)$
ΔH_v	Enthalpy of change for solidification	J/mol
κ	Sphere curvature	cm^{-1}
$K_{\alpha 1}$	K-alpha emission lines for EDS	keV
$\vec{l}$	Line vector of a dislocation	
Δn	Injection level	cm^{-3} (sun)
ρ_{sol}	Solid phase density	g/cm^3
ρ_{sol}	Liquid phase density	g/cm^3
$\vec{r}$	Rotation vector	
r	Radius of nucleus	µm
r^*	Critical radius of nucleus	µm
R_{nuc}	Radius of substrate particle	µm
t	Time	min
T_{dwell}	Furnace dwell temperature	K
ΔT	Nucleation undercooling	K

ΔT_{fg}	Critical undercooling for onset of free growth	K
T_m	Melting point temperature	K
p	Position of molybdenum cup	mm
τ_{shear}	Resolved shear stress	Pa
τ	Minority carrier lifetime	µs
$\tau_{Fe(i)}$	Minority carrier lifetime in Fe_i-state	µs
τ_{FeB}	Minority carrier lifetime in FeB state	µs
$\tau_{SRHFe(i)}$	Minority carrier lifetime associated with Shockley-Read Hall recombination	µs
v	Pulling speed	mm/min
V	Growth velocity	mm/min
V_C	Critical growth velocity	mm/min
$\gamma_{liq-sol}$	Interfacial energy between a liquid and solid nucleus	J/m^2
$\gamma_{liq-subst}$	Interfacial energy between a liquid and solid substrate	J/m^2
$\gamma_{sol-subst}$	Interfacial energy between a solid nucleus and solid substrate	J/m^2
λ	Angle between the applied force and the slip direction	°
ϕ	Angle between the applied force and the slip-plane normal	°
Ω	Angle between the longitudinal {110}-plane and the desired top plane of monocrystalline seed plates	°
$\theta_{\vec{r}}$	Misorientation angle between two grains	°
θ_d	Decomposed disorientation angles	°
θ	Wetting angle	°
$(\varphi_1, \Phi, \varphi_2)$	Set of Euler rotations	°

Abbreviation	Description
Al_2O_3	Aluminium oxide
CSL	Coincident Site Lattice
CZ	Czochralski
EDS	Energy Dispersive X-ray Spectroscopy
EBSD	Electron Backscatter Diffraction
FBR	Fluidized Bed Reactor
FeB	Iron-Boron complex
Fe_i	Interstitial iron
FE-SEM	Field Emission Scanning Electron Microscope
G5/7	Generation 5/7 ingot size
HF	Hydrofluoric acid
HPMC Si	High-performance multicrystalline silicon
LAGB	Large-angle grain boundary
mc-Si	Multicrystalline silicon
Mono-Si	Monocrystalline silicon
Mono-like Si	Near-monocrystalline silicon

PECVD	Plasma-enhanced chemical vapour deposition
PL	Photoluminescence
Poly-Si	Polysilicon
QSSPC	Quasi Steady State Photoconductivity
QSSPL	Quasi Steady State Photoluminescence
ROI	Region of interest
SAGB	Small-angle grain boundary
SEM	Scanning Electron Microscopy
Si	Silicon
SiC	Silicon carbide
SiO_2	Silicon dioxide
Si_3N_4	Silicon nitride
SiO_xN_y	Silicon oxynitride
TEM	Transmission Electron Microscopy
μ-PCD	Microwave Photoconductance Decay
VGF	Vertical Gradient Freeze

1. INTRODUCTION

The global energy consumption has been increasing by approximately 1.5% annually in recent years [1], mainly driven by an increasing demand for higher living standards in developing countries, and with no signs of it slowing down. Resource extraction and energy production based on fossil fuels will therefore put considerable strain on our planet for many years to come. However, according to the Renewable Energy Policy Network for the 21st Century (REN21) [1], 2014 has been the first year in four decades where the global carbon emissions associated with energy consumption have remained stable during economic growth. This stabilization can be attributed to increased environmental awareness and increased interest in utilizing renewable energy sources. Several countries, as well as the European Union, have announced new policies and large investments targeted towards renewables that, hopefully, will set the stage for new economic opportunities and can provided clean energy to the millions of people still living without any energy services.

Today, approximately 22.8% of the global energy production originates from renewable energy sources, but with solar energy contributing only 0.9% [1]. However, more than 60% of all PV capacity in operation worldwide at the end of 2014 has been added over the past three years, and the total share of renewables is expected to continue to rise sharply [2]. Thus, the scientific and industrial community need to push for further efficiency improvements and cost reductions.

Approximately 92% of the global annual solar electricity is today produced by crystalline silicon materials. While the percentage of total energy produced by monocrystalline silicon (mono-Si) has remained stable around 36% since 2010, the production by multicrystalline silicon (mc-Si) has seen a steady increase from 47% to 56% over the same time period [3]. Laboratory cell efficiencies give an indication of the development of the different technologies, and by the start of 2015 the highest confirmed terrestrial cell efficiencies at standard conditions (i. e. AM1.5 spectrum at 25°C) were 25.6% and 20.8% for monocrystalline and multicrystalline cells, respectively. Today's commercial cell efficiencies are, on the other hand, closer to 18% and 15%, respectively.

The actual solidification of the crystalline silicon material covers a considerable fraction of the total cost of a finished module [3]. After the entry of low-cost cells from China, the difference in retail cost between monocrystalline and multicrystalline cells has been diminishing. As of August 2015, the retail price for a silicon wafer is approximately 18% higher for a monocrystalline cell [4]. However, despite the diminishing price difference, there is still a considerable momentum in favour of multicrystalline cells that is mainly driven by a higher production throughput and the solidification process being less energy intensive. The appearance of new and promising modifications to the otherwise mature directional solidification method has also spawned additional interest for multicrystalline technologies, both scientifically and industrially.

1.1. MOTIVATION

Multicrystalline silicon produced by directional solidification usually contains large amounts of crystal defects, such as dislocations and grain boundaries that, upon interaction with impurities, can be very harmful for the final device performance. Dislocations are generally considered to be, by far, the most detrimental defect in multicrystalline silicon, and it has been estimated that the final cell efficiency can be increased 3-4% by complete elimination of dislocations in the material [5]. However, the importance of grain boundaries should not be underestimated. Even though grain boundaries are generally known to be less detrimental, they may still act as sources for additional dislocation generation and thereby indirectly affect device performance. The negative impact of crystal defects on the material quality and final device performance has, especially in recent years, spawned a demand for better control of the final material microstructure. Post-treatment methods are not very efficient in highly dislocated materials and the focus has therefore shifted towards controlling the microstructure directly during the solidification step instead.

The main motivation for this thesis has been to gain further insight into how to control the microstructure of directionally solidified silicon, and how to produce a material with characteristics superior to those of conventional multicrystalline silicon. The foundations for the ingot microstructure are established during the earliest stage of solidification, and multiple approaches have therefore been used to investigate and control the initial nucleation and growth conditions.

Methods based on growth from seed crystals are of particular interest in literature, especially with the advance of the so-called mono-like and high performance multicrystalline silicon. The initial stage of solidification, i.e. the nucleation step, is currently associated with considerable contingency, and considered to be relatively uncontrollable. The introduction of seed crystals has been found to be a simple but effective way to limit random nucleation events occurring on the crucible, as growth of the added seed crystals is favoured over nucleation of new crystals. However, seeding methods are not without challenges, and the first part of this work aims at identifying limitations in both methods.

In addition to new microstructural challenges, these methods also bring additional costs and completely new challenges if they are to be used industrially, e.g. costs related to production and design of seed material and modifications of existing furnace infrastructure. Due to the size of industrially grown ingots, precise control over thermal conditions in the furnace is also required in order to acquire ingots with uniform, and reproducible, microstructure and quality. Methods based on seeding may therefore not be viable in the long term, and in the second part of this work we consider if more potent methods can be developed by focusing on the actual nucleation process instead.

1.2. OUTLINE

The thesis is divided into six main chapters along with a final collection of scientific manuscripts produced during the course of these three years.

The present chapter, Chapter 1, aims at adapting the work to a broader context according to the current state of the photovoltaic community. The motivation for this thesis is shortly presented together with a summary of the scientific papers.

Chapter 2 will present the theoretical knowledge necessary to understand the concepts and approaches presented in this work; including crystallography, structural defects, nucleation and growth. The final part of this chapter will then give a general overview of emerging growth methods and the methods used in this work.

Chapter 3 describes the different experimental procedures that have been used during the course of this work; including seed-preparation, solidification methods and characterization techniques.

Finally, chapter 4 puts the results together in a broader and conclusive assessment that will be used as a basis for discussing potential future work in Chapter 5.

1.3. SUMMARY OF SCIENTIFIC MANUSCRIPTS

The major part of this work is divided into five separate scientific papers. The first four papers cover the work done on seed-assisted growth, namely the so-called mono-like (P1 and P2) and high performance multicrystalline (P3 and P4) silicon methods. The final work on nucleation is presented in paper P5.

PAPER P1

K. E. Ekstrøm, H. Dalaker, A. Autruffe, R. Søndenå, G. Stokkan, L. Arnberg, M. Di Sabatino, «Characterization of mono-like silicon grown by a seed-assisted Bridgman method», Proceedings of The 7th International Workshop on Crystalline Silicon Solar Cells, 77-81 (2013).

This papers covers the introductory work done on small-scale and pilot-scale solidification experiments. The main part of this work consisted of growing small-scale ingots from single monocrystalline seeds, cut with different crystallographic orientation from a Czochralski ingot, in order to study the effect of seed orientation on the ingot grain structure. The crystallographic orientation of the different seeds, parallel to the growth direction, was varied between <100>, <110>, <211> and <111>. A monocrystalline core crystal grew directly from the seed crystal, with the same crystallographic orientation as the seed. However, parasitic grains were found to nucleate on the crucible wall during the growth process, forming a multicrystalline roof over the central core crystal that limited its progress. The extent of the core crystal depends on the orientation of its low-energy crystallographic {111}-planes, and it was suggested that the fraction of monocrystalline material could be increased by using seed with favourably oriented {111}-planes.

The pulling speed clearly affected the parasitic structure, with a slow pulling-speed favouring a twinned grain structure and a fast pulling-speed favouring a more random grain structure, which was suggested to be related to a much more convex growth interface in the fast pulling case. <110>-oriented seeds appeared to have the most favourably oriented {111}-planes and was therefore selected as growth direction for the pilot-scale ingot presented in P2. Even though this paper covers some introductory results from the pilot-scale ingot, the main part of this work will be explained in paper P2.

PAPER P2

K. E. Ekstrøm, G. Stokkan, R. Søndenå, H. Dalaker, T. Lehmann, L. Arnberg, M. Di Sabatino, «Structure and dislocation development in mono-like silicon», Physica Status Solidi A: Applications and Materials Science, 212(10), 2278-2288 (2015).

As a continuation of the work presented in paper P1 and the previous work by Ervik et al on industrially solidified mono-like silicon [6], this paper mainly focuses on challenges related to using multiple seed crystals in growth of larger mono-like ingots. Morphological imperfections and imperfect placement of individual seeds are usually related to considerable dislocation generation, which has to be addressed in order to make the method more viable in the future. The ingot was grown from a seeding-structure consisting of six <110>-oriented seed arranged with pre-defined crystallographic junctions, where the seeds were placed either in physical contact or with mm-sized gaps in-between.

It became evident that even sub-1° misorientations in the placement of neighbouring seed crystals lead to formation of small-angle grain boundaries that, in most cases, were accompanied by broad dislocation clusters. The extent of the dislocation clusters was found to correlate well with the complexity of the misorientation at the respective junctions, i.e. the number of tilt axes and their respective tilt values. Based on this observation it was suggested that a larger misorientation can be tolerated if it is limited to a single and/or a specific tilt axis, which is probably related to the specific types of dislocations generated at each boundary, and their movement in the silicon lattice.

Even though seed misorientation was found to be most detrimental for material performance, additional dislocations were also found to originate from the bulk volume of the seeds, on the surfaces of the seeds and in the peripheral areas of the ingot. Dislocations originating from the bulk seed volume were, however, found to not necessary move far into the main ingot volume. Surficial sources can generally be related to morphological imperfections, such as scratches, or indentation of other seeds or solid particles. The majority of these sources could be removed by introducing small gaps in-between neighbouring seeds. On the other hand, the gap should still remain below 1mm to prevent dislocation generation inside the gaps. Peripheral dislocations are usually a result of thermal expansion of the ingot towards the crucible wall, which will continue to be a persistent problem for ingots that grows in direct contact with a crucible. However, the propagation of dislocations from the periphery towards the interior of the ingot was hindered by the parasitic structure surrounding the monocrystalline core, suggesting that a surrounding multicrystalline structure in fact can be beneficial for reducing the dislocation concentration in the main part of the ingot.

PAPER P3

K. E. Ekstrøm, A. Autruffe, R. Søndenå, H. Dalaker, G. Stokkan, L. Arnberg, M. Di Sabatino, «The microstructure of multicrystalline silicon seeded by polysilicon chips and fluidized bed reactor granules", Journal of Crystal Growth, Submitted (2015).

This paper focuses on the microstructure achieved by seeding with multicrystalline seed material, so-called High-performance multicrystalline silicon (HPMC Si). Contrary to conventionally grown mc-Si, where the initial grain structure of the ingot is determined by the nucleation conditions, the initial grain structure of seeded HPMC Si ingots are pre-defined by the grain structure of the seed particles. A pilot-scale ingot was grown from both polycrystalline silicon chips (poly-Si) and granular fluidized bed reactor silicon (FBR) in separate compartments, for studying the effect of seed material on the final ingot microstructure. In addition to being produced in fundamentally different ways, these particles also have different particle morphologies, where poly-Si chips are sharp and irregular and FBR granules are even and spherical.

Both compartment of the seeded ingot displayed a considerable reduction in the average grain size when compared to a conventional multicrystalline (mc-Si) ingot grown under similar conditions. The compartments also displayed a considerable increase in the density of random angle grain boundaries relative to the mc-Si ingot. Both of these properties can be related to the grain structure of the seed particles. Closer investigations of the seed particles reveal that there is a considerable coarsening of the seed grain structure during ingot solidification, especially in the case of the granular FBR seeds. However, due to the irregular shapes of poly-Si chips, melt may penetrate into the seed structure and initiate growth below the main seed interface. The average grain size therefore ended up being similar for both seed interfaces, and remained fairly similar throughout the whole ingot height.

More importantly, the seeded ingot was found to generate less dislocations that the conventional mc-Si ingot, which can be related to the high density of random grain boundaries. Random grain boundaries are known to terminate dislocation clusters and do therefore not allow clusters to become as big, and dominate to the same degree, as in conventional mc-Si. Poly-Si chips were found to contain more random grain boundaries than FBR granules. But, as twins appear to form relatively quickly within the gaps between poly-Si chips, the net density of random grain boundaries became relatively similar to that of the FBR compartment. The top parts of the poly-Si compartment contained approximately 35% more area covered in dislocation clusters than the top parts of the FBR compartment. This may be explained by an increased influence of $\sum 27$ grain boundaries in the chip-seeded compartment, which are well known to generate dislocations. There are also indications on that poly-Si seeded ingots may be more prone to dislocation generation during the earliest stage of solidification, due to the irregular shape of the poly-Si chips allowing for indentation and melt penetration into the seeding structure.

Supplementary photoluminescence measurements revealed high concentrations of interstitial iron in the material (Appx. B), and, based on this, we assume that there are considerable amounts of precipitated iron in the material, especially at dislocations and grain boundaries. Due to a low response to phosphorus gettering, it is assumed that considerable amounts of precipitated iron also remains in the material after the gettering process, thereby being the main contributor to the remaining low lifetime regions found at the grain boundaries after phosphorus gettering. Smaller grains responded less to phosphorus gettering than larger grains, due to increased influence of the grain boundary on the bulk volume of the grains, which resulted in larger grains having a higher lifetime increase with phosphorus gettering than smaller grains.

PAPER P4

S. Castellanos, K. E. Ekstrøm, A. Autruffe, M. A. Jensen, A. E. Morishige, J. Hofstetter, P. Yen, B. Lai, G. Stokkan, C. del Cañizo, T. Buonassisi, "Comparison of gettering responses and lifetime-limiting defects in high-performance and traditional multicrystalline silicon", IEEE Journal of Photovoltaics, Submitted (2015) .

The second part of the work on multicrystalline seeding aims to further elaborate the difference in gettering response between seeded and conventionally grown multicrystalline silicon. It supplies additional experimental results that relate to this thesis, particularly from the work on defect eccentricity characterization and metal-decoration analysis by micro X-Ray Fluorescence (μ-XRF).

Eccentricity characterization is a method previously developed by the MIT group for associating the recombination activity of specific dislocation clusters with their complexity, i.e. the eccentricity variation of the dislocations located in the cluster. This approach has previously been shown to be valid for clusters in conventional multicrystalline silicon and is in this work also validated for very fine-grained materials, despite the lower dislocation density. The μ-XRF results are also consistent with these and previous observations, where metal-rich (e.g. iron) precipitates appear to form favourably at the few disordered dislocation structures existing in the material.

The remaining part of the work complements paper P3 by observing that smaller, non-dislocated, grains suffer from increased influence from grain boundaries, with a tight correlation between grain size and maximum intragranular lifetime entitled by the bulk point-defect concentration.

PAPER P5

K. E. Ekstrøm, E. Undheim, G. Stokkan, L. Arnberg, M. Di Sabatino,"Beta-Si_3N_4 particles as nucleation sites in multicrystalline silicon", Acta Materialia, Submitted (2015).

This work focuses on revealing information about the nucleation mechanisms acting during the earliest stage of solidification, by studying bottom cuts from multicrystalline ingots, and is a continuation of the previous work by Brynjulfsen [7]. The experimental study is mainly based on observations done by Scanning Electron Microscopy (SEM) on Sopori etched samples and Energy Dispersive Spectroscopy (EDS) for qualitative composition analysis. These observations are further discussed in terms of the athermal nucleation model and the free growth model, previously used for grain refinement in aluminium, in order to explain microstructural differences commonly observed in non-seeded multicrystalline silicon.

The work is based on the assumption that the α-Si_3N_4 coating is an essential part of the nucleation process. Experimental observations indicate that α-Si_3N_4 coating particles readily transform into a nearly continuous layer of large and clearly faceted β-Si_3N_4 particles on the bottom interface between the solidified ingot and the crucible. By using the free growth model it is further suggested that initial nucleation mainly takes place on the large β-Si_3N_4 particles, at undercoolings below what has usually been reported in literature. It is, however, important to note that we do not rule out nucleation on α-Si_3N_4 particles.

The β-Si_3N_4 layer appears to be in contact with the solidified silicon only at localized points, and not continuously, and it is therefore suggested that nucleation can only take place at these positions. This is further supported by an apparent accumulation of grains and parallel twins at several of these locations. The parallel twins indicate that dendrites may have an important effect also on the grain structure of conventionally grown multicrystalline silicon, and thereby limit the potential for grain refinement for the most common growth conditions. However, by engineering the size of the Si_3N_4 particles and carefully controlling the temperature profile during the nucleation step, one may be able to tailor the grain structure of the ingot.

2. MULTICRYSTALLINE SILICON

2.1. SILICON BASICS

Approximately 26wt% of the Earth's crust consists of Silicon (Si), where it occurs mainly in the form of quartz (SiO_2) and other silicate minerals. The extraction of elemental silicon is mainly performed by various metallurgical processes, achieving purities of approximately 99.0wt% Si [8]. As elemental silicon has proven to be a very robust and accessible semiconductor material for the microelectronics industry, and more recently for the photovoltaics industry, there is today a comprehensive technological base for this element. Both industries do, however, require a substantially higher purities than in metallurgical grade silicon (i.e. 9N and 6N respectively), achievable through purification techniques. Purification has traditionally been done by chemical methods, such as the well-known Siemens process or the Fluidized Bed Reactor process, but there have also been recent advances in metallurgical methods [8].

2.1.1. CRYSTAL STRUCTURE AND PHYSICAL PROPERTIES

Silicon crystallizes with a diamond cubic crystal structure (Figure 2.1 (a)) that can be visualized as a stacking of densely packed {111}-planes in an ABCABC… sequence (Figure 2.1 (b)). The lattice spacing at room temperature (25°C) has been measured to be *a* = 5.43Å.

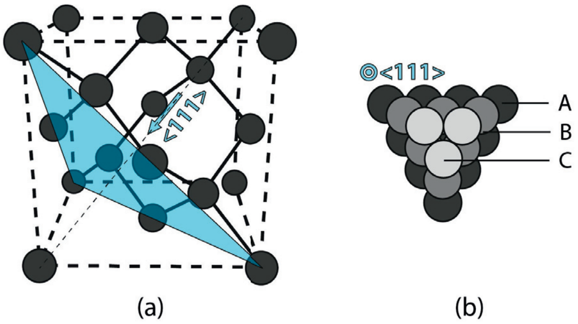

Figure 2.1. (a) The diamond cubic crystal structure of elemental silicon. (b) The structure can be described as a stacking of densely packed {111}-planes in an ABCABC… sequence.

The material has a relatively high melting point of 1687K and will expand upon solidification, with the densities of the solid phase (close to 298K) and liquid phase (close to 1687K) being $\rho_{sol} = 2.33\frac{g}{cm^3}$ and $\rho_{liq} = 2.57\frac{g}{cm^3}$, respectively.

Bulk silicon can be composed of either a single crystal (monocrystalline) or a large number of crystallites (multicrystalline) separated from each other by grain boundaries.

2.2. STRUCTURAL DEFECTS

Grain boundaries are only one of many types of structural defects that can exist in crystalline silicon. Structural defects can be categorized into either point defects, line defects, planar defects and volume defects, and they can all have a considerable impact on the final solar cell performance. This work mainly concerns dislocations (i.e. line defect) and grain boundaries (i.e. planar defect), and the current chapter is therefore limited to these.

2.2.1. DISLOCATIONS

Dislocations are defined as line defects within a crystal structure that results from plastic deformation, i.e. slip of neighbouring atomic planes. Such a slip process can take place in a perfect crystal if the shear stress acting on a slip-plane reaches a critical value [9], e.g. by neighbouring regions expanding or contracting differently due to thermal gradients. Dislocations nucleate in order to release parts of this stress. Once dislocations are present, slip may occur at much lower stresses by movement of the dislocations. Dislocations can also nucleate at so-called stress-concentrators, where the crystal becomes locally stressed by secondary features as impingement points, precipitates, surface irregularities and grain boundaries. Pre-existing dislocations in seed-crystals may also propagate into the growing crystal.

Average dislocation densities of $10^4 – 10^6$ cm^{-2} are typically found in multicrystalline silicon, but local clusters with densities up to 10^8 cm^{-2} are also not uncommon [10]. Dislocations can be observed visually by etching silicon samples in a suitable etchant and single dislocations will become visible as etch-pits (Figure 2.2 (a)). The shape of the etch pits may be used to visualize the direction of the dislocation line, projected onto the sample surface. Highly dislocated areas can be seen as black areas in micrographs taken by conventional light microscopy, as shown in Figure 2.2 (b). So-called dislocation rosettes are also commonly observed, where dislocation align in star-shaped arms (Figure 2.2 (c)), and are typical for localized stress points formed e.g. by impingement.

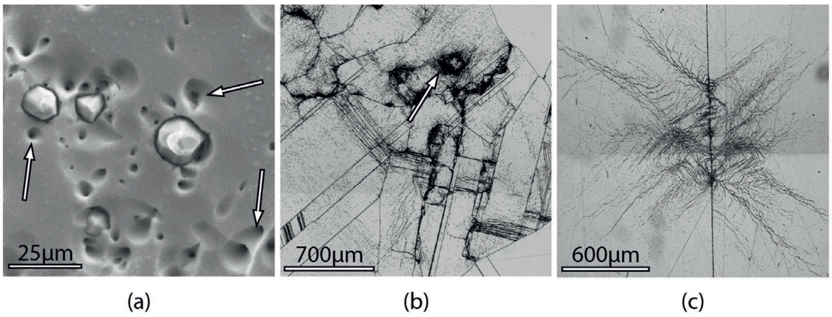

Figure 2.2. (a) Dislocation etch-pits surrounding β-Si_3N_4 particles that are embedded into solidified silicon. (b) Highly concentrated dislocation clusters found by light microscopy. (c) Dislocation rosettes with their well-known star-shaped structures.

Impingement: Impingement can take place either in the form of solid indentation or in the form of melt impingement. Solid indentation describes a situation where two solid surface meet during growth, creating contact stresses large enough to release dislocations (e.g. between multiple seed-particles placed in physical contact with each other [6]). Furthermore, as silicon expands during solidification, the crucible will create considerable stresses when the crystal comes into contact with the crucible. Melt impingement, on the other hand, occurs when melt becomes trapped in narrow spaces and cavities, and, upon solidification, expands towards the surrounding solid, in generation of stresses.

Precipitates: Precipitates have different crystallographic properties than silicon that, when embedded into a silicon crystal, may facilitate nucleation of dislocations. (i) The thermal expansion of the precipitates may differ from that of silicon, which will introduce stresses around the precipitates upon cooling of the crystal. Such stresses may lead to distortions in the silicon lattice and generation of dislocations (Figure 2.2 (a)). Similar generation has previously been observed for multi-metallic precipitates, typically involving nickel, copper and iron, and for silicides [11], silicon oxides and carbides [12, 13]. However, previous work also suggests that these dislocation structures do not develop very far into the surrounding silicon if the difference in thermal expansion coefficient is small [14]. (ii) Dislocations may also generate to compensate for crystallographic misfit between a precipitate and the silicon crystal. Note that, while misfit is defined between two different phases, misorientation, as described later, is defined between two crystals of the same material. The misfit varies with different crystallographic orientations, and therefore depends on the orientation of the precipitate and the silicon.

Surface irregularities: Seed crystals may contain surface irregularities such as cracks and scratches that have been generated during handling and/or sawing. Such features usually contain large amounts of dislocations that may redistribute during heating [15].

Grain boundaries: Grain boundaries have on numerous occasions shown to be a major source of dislocations in multicrystalline silicon [14, 16-19]. When a multicrystalline material is strained, grain boundaries strive to preserve the compatibility of neighbouring grains at the grain boundaries. As a consequence, dislocation generation can occur at grain boundaries at relatively low stresses. Clusters are also frequently found to originate at junctions between multiple grain boundaries [17, 20], and at grain boundary kinks [21]. Ryningen et al observed that the majority of dislocations existing in multicrystalline, in fact, originate at grain boundaries [19]. Recent work by Takahashi [22] suggests that dislocations generated at a grain boundary between two crystals will propagate into the crystal showing the highest shear stress, i.e. the least favourable oriented slip-planes. Dislocations generated at grain boundaries show clear relations to the character of the grain boundary, and will be described in more detail in Ch. 2.2.2.

Dislocations are known to have a considerable impact on the electrical properties of the material [9] and final device performance, as they readily interact with impurities that greatly enhance the recombination activity of the surrounding area [23]. In recent years, grain boundary engineering has been suggested as a promising method for reducing the amount of dislocations in solidified silicon, especially with the development of the new mono-like and high-performance multicrystalline silicon growth methods. These methods will be presented in more detail in Ch. 2.5.

Geometric considerations: Dislocations are commonly characterized by a line vector $\vec{l}$ and a displacement vector $\vec{b}$, commonly called the Burgers vector. The line vector is a description of the actual dislocation line while the Burgers vector can be explained in terms of a Burgers circuit (Figure 2.3). A Burgers circuit is an atom-to-atom path that forms a closed loop in a dislocated crystal. The crystal in Figure 2.3 (a) contains an extra half-plane, forming a so-called edge dislocation with a line vector $\vec{l}$. After transferring the same atomic *MNOPQ* loop stepwise to a non-dislocated crystal (Figure 2.3 (b)), an additional displacement vector *QM*, or $\vec{b}$, has to be added in order to close the loop. As seen from this figure, it becomes evident that the Burgers vector for an edge dislocation will be perpendicular to the line vector. A second distinct type of dislocation can be visualized by displacing one part of the crystal relative to a second part, as illustrated in Figure 2.3 (c) – (d). By drawing a similar *MNOPQ* Burgers circuit, it becomes evident that the Burgers vector in this case is parallel to the line vector instead, which is commonly known as a screw dislocation. These (i.e. edge and screw) are known as perfect dislocations, and describe the two outer extremes of the dislocation line. In its most general case the dislocation line lies at an arbitrary angle to its Burgers vector, and the dislocation can be said to have a mixed edge and screw character. The shortest lattice vector, and the most likely Burgers vector, for silicon, and for the diamond structure in general, is of the $\vec{b} = \frac{1}{2}\langle 110\rangle$ type.

An important feature of a dislocation is that it can never end inside a crystal. It must always end at the surface of a crystal and/or at a grain boundary. They must therefore either form closed dislocation loops (e.g. as Frank-Read sources [9]) or branch into other dislocations. In the latter case the Burgers vector has to be conserved, meaning that the net Burgers vector of the new dislocations must equal the Burgers vector of the initial dislocation.

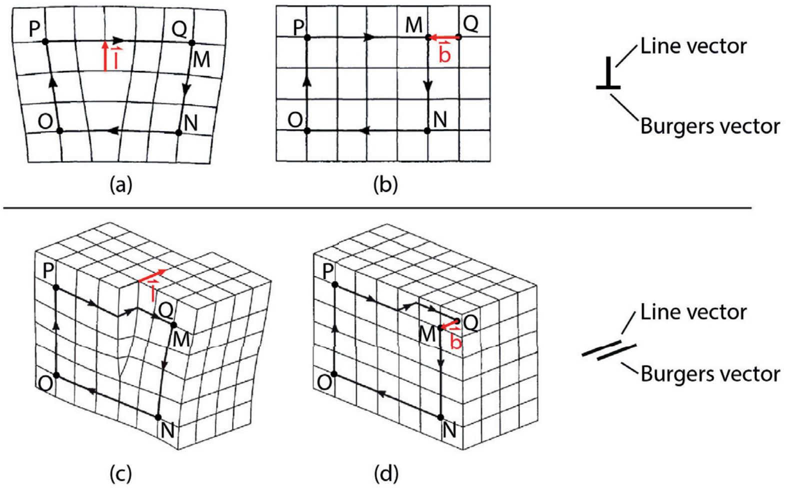

Figure 2.3. (a) An edge dislocation with line vector $\vec{l}$ can be generated by inserting an additional half-plane into an otherwise perfect crystal. (b) The Burgers vector $\vec{b}$ equals the closing-failure *QM,* perpendicular to the line vector. (c) A similar loop can be made for a screw dislocation. (d) The Burgers vector will in this case be parallel to the line vector.

<u>*Dislocation movement*</u>*:* There are two basic types of dislocation movements, namely glide and climb. Glide occurs when a dislocation move in the crystallographic plane that contains both its line vector and Burgers vector. Climb, on the other hand, occurs when a dislocation moves out of its glide plane, and thus normal to the Burgers vector. Glide of many dislocations results in slip, which is the most common manifestation of plastic deformation in crystalline solids, whereas one atomic plane glides over a second similar plane (Figure 2.4 (a)). The

characteristic shear stress required for slip τ_{shear}, resolved on the slip plane in the slip direction, is given as:

$$\tau_{shear} = \frac{F}{A}\cos\phi\cos\lambda \qquad \text{(Equation 2.1)}$$

Where F is the applied force, A is the cross-sectional area, ϕ is the angle between F and the slip plane normal, and λ is the angle between F and the slip direction. Slip in silicon occurs between the closely packed $\{111\}$-planes. However, covalent crystals, such as silicon, generally have a high resistance to dislocation motions, due to a relatively high Peierls barrier [24], and slip therefore only occurs at high temperatures. On the other hand, due to deep troughs in the Peierls barrier in <110>-directions, slip is generally known to occur in the <110> directions that lie in the four $\{111\}$-planes (Figure 2.4 (b)). As there are four unique $\{111\}$-planes and three <110>-directions in each plane, there are a total of 12 possible slip systems [9]. Based on these assumptions, Hornstra [25] theoretically determined all possible types of dislocation available to the diamond lattice. However, the most favourable types, based on the number of broken bonds per lattice distance a, are listed in Table 2.1 [20] and can be visualized in Figure 2.4 (b).

Table 2.1. The most favourable dislocation types for the silicon, based on the number of broken bonds per lattice distance a [20].

Line vector, $\vec{l}$	Burgers vector, $\vec{b}$	Type	Angle between $\vec{l}$ and $\vec{b}$ [°]	Number of broken bonds per a $[cm^{-1}]$
$\langle 110\rangle$	$\langle 110\rangle$	Screw	0	0
$\langle 1\bar{1}0\rangle$	$\langle 01\bar{1}\rangle$	60°	60	1.41
$\langle 11\bar{2}\rangle$	$\langle 01\bar{1}\rangle$	30°	30	0.82
$\langle 11\bar{2}\rangle$	$\langle 1\bar{1}0\rangle$	Edge	90	1.63

For energetic reasons it may be more favourable for a perfect dislocation to dissociate into Shockley partials [9, 20], where a $\frac{1}{2}\langle 110\rangle$ type Burgers vector splits into two partials, each with a Burgers vector of the $\frac{1}{6}\langle 112\rangle$ type, bounded by stacking faults. Both screw and 60° dislocations tend to dissociate into such partials, and partial dislocations has therefore been subject to great interest due to their possible influence on dislocation motion [20].

Screw dislocations can switch between slip planes if the target plane can contain the Burgers vector of the dislocation, a process commonly called cross-slip. An example of this can be seen in Figure 2.4 (b), where the screw dislocation given by $\vec{l} = \vec{b} = \langle\bar{1}01\rangle$ can switch between the (111) and $(1\bar{1}1)$ planes. Cross slip has previously been observed in silicon at a temperature of 957K [26]. Edge dislocations can also leave their initial slip planes, but only through climb. The most common climb process involves diffusion of vacancies, either towards or away from the dislocation. Only small portions of the dislocation will climb, creating steps, or so-called jogs [9], on the dislocation line that move it from one slip plane to another. Similar steps can also be formed within the same slip plane, by glide, but are in this case called kinks. The Burgers vector are retained for both step types, meaning that the

Burgers vector for the step is equal to that of the rest of the dislocation line. Kinks will therefore not impede the glide of the dislocation. Similarly, jogs on edge dislocations do not affect glide, but jogs on screw dislocations will.

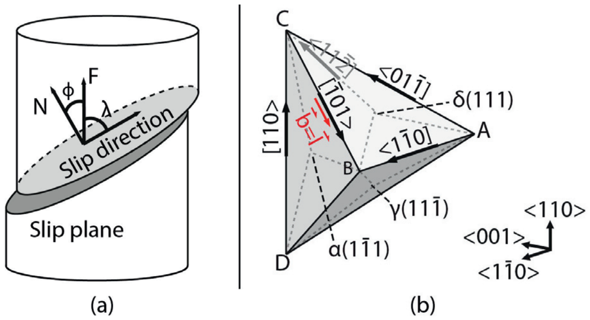

Figure 2.4. (a) Glide of many dislocations result in plastic deformation of the crystal in the form of slip. (b) The four {111}-planes of the diamond structure can be organized as a tetrahedron, commonly known as a Thompsons tetrahedron. Each of the four planes contain three <110>-directions and three <112>-directions, indicated by black and grey arrows, respectively.

Dislocation multiplication: Already existing dislocations may act as nucleation sites for new dislocations, a process commonly called dislocation multiplication. The Alexander-Haasen model, published in 1968, remains today as one of the most notable models for multiplication of dislocations in the diamond structure [27]. The model has proven to give satisfactory agreements with experimental data for single crystals, but there are some aspects of the model that limits its use in multicrystalline silicon [28]. The model treats deformation as a single slip of only one type of dislocations, meaning that all dislocations, independent of type, is grouped together in a common density variable N. But as there is no evidence for a single-slip scenario, as dislocations in diamond crystals are expected to be of multiple types and slip systems, the model becomes insufficient for multicrystalline silicon. An alternative model, which is based on the principles of the Alexander-Haasen model, expanded to include notions of multiple slip systems, different types of dislocations and modified multiplication laws has been discussed by Prasad and Pendurti [28].

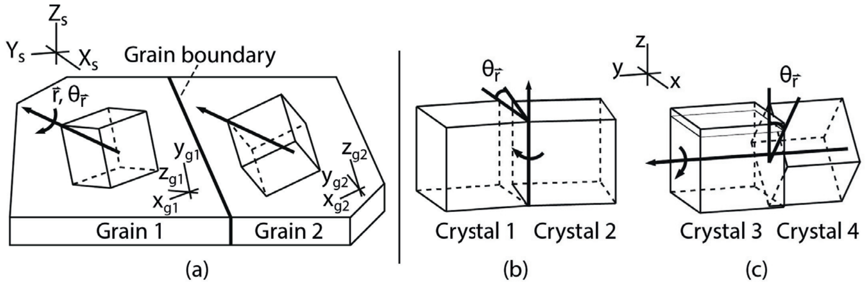

Figure 2.5. (a) A grain boundary is formed between two crystals, or grains, that are misoriented with respect to each other, by an misorientation angle $\theta_{\vec{r}}$, around a given rotation vector $\vec{r}$. The two simplest rotations are the so-called (b) simple tilt and (c) simple twist boundaries.

The Frank-Read mechanism is the most fundamental multiplication mechanism. A dislocation line can be pinned at a single or both edges by other crystallographic imperfections or steps. If exposed to stresses, the dislocation line will start to bend in the glide plane and develop repetitive dislocation loops, and thereby multiply. Single ended Frank-Read sources are probably dominant, as they require only a single pinning point.

Multiplication may also occur by two additional multiplication mechanisms, namely by the so-called multiple cross slip and multiplication by climb mechanisms.

The multiple cross slip mechanism concerns screw dislocations. When a screw dislocation encounters an obstacle in its primary glide plane, the dislocation will cross-slip onto a second glide plane. Upon passing the obstacle, the cross-slipped segment will tend to cross-slip back it its original glide plane, hence double cross slip. The double cross slipped segment will be relative immobile and can therefore act as a Frank-Read source.

A similar regenerative multiplication mechanism, commonly known as a Bardeen-Herring source [20], can occur by climb of edge- or screw-dislocations. If the dislocation line becomes pinned in both edges, a presence of excess vacancies will cause the dislocation line to bow out by climb, similar to that of a Frank-Read source. This can create jogs which again may act as new multiplication sources.

2.2.2. GRAIN BOUNDARIES

A grain boundary is an interface between two crystals, or grains, having different crystallographic orientation. The two crystals are rotated with respect to each other by a misorientation angle $\theta_{\vec{r}}$ around an arbitrary rotation axis $\vec{r}$, as illustrated in Figure 2.5 (a). The relationship between them are generally complex, but with two exceptions, namely the simple tilt and simple twist grain boundaries that are illustrated in Figure 2.5 (b) and (c), respectively.

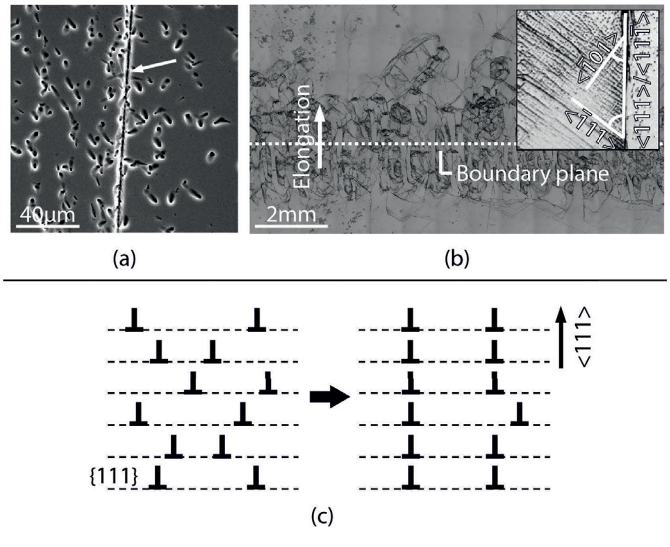

Figure 2.6. (a) A simple small-angle grain boundary with dislocations aligning in a single linear array. (b) A more complex small-angle grain boundary, where dislocations have aligned parallel to {110} plane traces on parallel rows of {111}-planes. (c) Small-grain boundaries are formed by recovery, where dislocations glide on {111}-planes until reaching the most energetically favourable position. Dislocations are often be hindered from reaching this position, leading to a slightly distorted array.

In a simple tilt boundary, crystal 2 is simply tilted an angle $\theta_{\tilde{r}}$, with respect to crystal 1, around a rotation axis that lies in the grain boundary plane between the two crystals. A similar action can also describe the simple twist boundary, but in this case the rotation axis is oriented perpendicular to the grain boundary plane.

A general grain boundary can be defined as either a small-angle (SAGB) or large-angle (LAGB) grain boundary by the magnitude of the misorientation angle, i.e. $\theta_{\tilde{r}} \leq 15°$ and $\theta_{\tilde{r}} > 15°$, respectively.

Small-angle grain boundaries (SAGB): Grain boundaries with small differences in crystallographic orientation can be described as periodically spaced arrays of aligned dislocations, or polygon walls [9]. Figure 2.6 (a) and (b) shows micrographs of SAGBs where dislocations have aligned in such arrays. While the SAGB in (a) consist of a single dislocation line, the boundary in (b) is more complex and consist of several parallel arrays. The zoomed in micrograph in (b) shows how dislocations have aligned parallel to {110} plane traces on parallel rows of {111}-planes, in accordance with Transmission Electron Microscopy (TEM) observations by Kivambe et al [29].

The formation of such grain boundaries takes place by the so-called recovery process, in which dislocations rearrange to lower the energy of the crystal. The later stage of the recovery process, where the actual grain boundaries are formed, is called *polygonization*. This process requires a sufficient thermal activation in order to allow diffusion of defects, and will therefore only take place at elevated temperatures. As mentioned previously, dislocations glide on {111}-planes (e.g. as illustrated in Figure 2.6 (c)), and align when they find an energetically favourable position. However, single dislocations are often be hindered from reaching their most favourable position, leading to slightly distorted arrays.

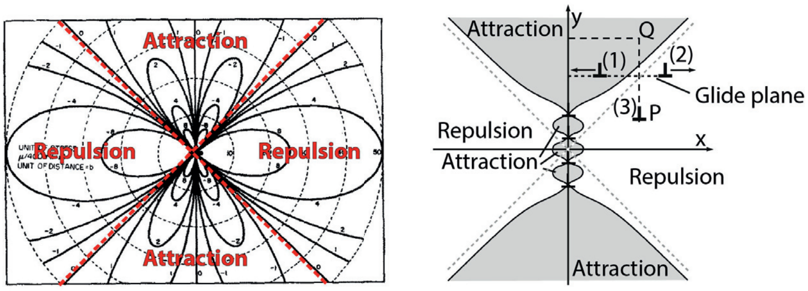

(a) (b)

Figure 2.7. (a) The total stress distribution around a single dislocation can be divided into attractive and repulsive regions. (b) An edge dislocation interacting with the common stress field generated by four similar edge dislocations.

Dislocations may have both long- and short-range stress fields, and the distribution of stresses in an array of dislocations depends on the arrangement, crystallographic orientation and Burgers vector of the individual dislocations [9]. The stress field for a single edge dislocation is shown in Figure 2.7 (a), with the red lines separating regions where incoming dislocations will encounter attractive and repulsive forces. Dislocations in an array will form a common periodic stress field, as depicted for an array of four similar edge dislocations in Figure 2.7 (b). The grey areas in the figure illustrate regions of attractive forces and white regions of repulsive forces. When a dislocation enters the vicinity of the array it will be influenced by these forces, which in this figure is illustrated by a single edge dislocation being influenced by a wall of similar edge dislocations. (1) If a gliding dislocation enters the attractive region, it will align with the existing array. (2) If not, it will be repelled from the array. (3) However, dislocations initially residing in the repulsive region may also climb into the attractive region ($P \rightarrow Q$), and can from there glide into the boundary.

Dislocations can readily be introduced by plastic bending of silicon samples at elevated temperatures, and early studies performed by Green et al [30] and Vogel [31] reported that dislocations in such samples tend to be of the <112>edge type that align parallel to traces of $\{111\}$-planes after bending. Vogel also studied the polygonization process by exposing the samples to a temperature of 1223K for four days. This resulted in the dislocations aligning in low energy polygonised arrays, i.e. small-angle grain boundaries, perpendicular to the $\{111\}$-planes. The latter investigation by Vogel also observed that intersection of multiple slip systems lead to so-called Lomer-Cottrell locks [9] that prevented polygonization in some areas of the samples. Later investigations by Ervik et al [32] were also consistent with these results. Dislocations were found to align in arrays parallel with $\{111\}$ traces before annealing and in arrays perpendicular to the $\{111\}$ traces after annealing. These samples were also compared to as-grown multicrystalline silicon that showed polygonised structures, perpendicular to $\{111\}$-planes, similar to that of the previously annealed samples.

Booker and Stickler [33], and Hill and Rowcliff [34] successfully observed the <112>30° dislocation type in germanium and silicon and, more recently, Kivambe et al [29] confirmed their tendency to align parallel to $\{110\}$ plane traces on parallel rows of $\{111\}$-planes (i.e. as previously seen in Figure 2.6 (b)), by TEM analysis. This is also consistent with an earlier study by Stickler and Booker [35], on surface abraded samples, where one observed that dislocations tended to change from a $\langle 110\rangle$ line vector to a $\langle 112\rangle$ line vector by annealing at 900°C. It was suggested that $\langle 110\rangle$ dislocations form much more easily, but that $\langle 112\rangle$ are more energetically stable, and such a transformation is therefore suggested to be possible with the existence of a free surface, such as the solidification front [29]. By growing silicon single crystals with different crystallographic orientations, Dashevsky et al [36] concluded that small-angle grain boundaries mainly consisted of $\langle 112\rangle$edge and $\langle 110\rangle$edge dislocations. However, the latter type were only found in $\{110\}$-oriented crystals, and was suggested to form as a result of so-called Lomer locks between 60° dislocations of the $\langle 110\rangle 60°$ type [9]. Both $\langle 110\rangle 60°$ and $\langle 110\rangle$screw dislocation types are also frequently found in silicon [37].

Small-angle grain boundaries are often associated with considerable dislocation generation and multiplication, which has shown to be a serious problem for growth of mono-like silicon (Ch. 2.5.2), especially for complex misorientations (P2).

Large-angle grain boundaries (LAGB): When the misorientation between two grains exceeds 15° the dislocation spacing becomes so small that the dislocations cores starts overlapping. LAGBs are related to poor fit between the two crystals and a relatively open boundary structure, and are therefore associated with higher grain boundary energies than SAGBs. The energy and properties of LAGBs are almost independent of $\theta_{\vec{r}}$, but there are some special boundaries occurring at specific misorientations that have considerable lower energies. Such grain boundaries are usually called Coincident Site Lattice boundaries, or CSL boundaries, and are usually given as a certain ∑-value that describe the degree of crystallographic fit, or symmetry, between the two grains. A lower number implies a higher fit and less atomic distortion. The variation in boundary energy for a symmetrical $\langle 110 \rangle$ tilt boundary in silicon is shown in Figure 2.8 (a). The lowest energy is found for the coherent $\Sigma 3$ boundary, which, therefore, is considered to be the most stable LAGB, and the most commonly encountered type in multicrystalline silicon. It is also usually called a twin boundary, as the boundary can be described as a mirror plane (Figure 2.8 (b)). It is not unusual to find quantities of twin boundaries that accounts for 50-70% of the total grain boundary density in conventional multicrystalline silicon [38]. Due to their high symmetry, twins are usually associated with low dislocation densities and insignificant interaction with impurities, and are therefore considered to be a benign defect with low impact on the electrical performance of the material [39]. While coherent twin boundaries form on $\{111\}$ boundary planes, the more rarely encountered incoherent twins describe twin boundaries that form on other crystallographic planes, which hold much higher grain boundary energies than its coherent counterpart [40].

Twin boundaries can be formed either by grain boundaries reorganizing, in order to reduce their internal energy [17], or by nucleation of twinned crystals, i.e. twinning (Ch. 2.4.2) [41]. Successive twinning ($\Sigma 3^n$, $n = 1, 2, 3$) leads to formation of higher-order twins (i.e. $\Sigma 9$ and $\Sigma 27$) that are also frequently observed in conventional multicrystalline silicon [38]. In order to reduce their energy, higher-order CSL boundaries have been observed to dissociate into lower-order CSL boundaries, a process that is often associated with dislocation generation [17]. A similar reorganization has also been observed for near-CSL boundaries, were dislocations tend to generate at certain grain boundary steps [42, 43].

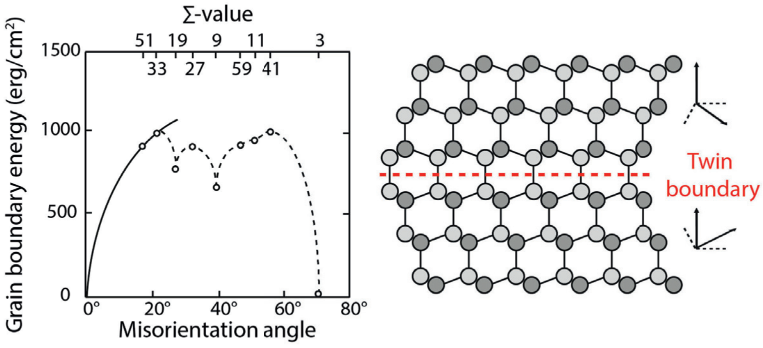

(a) (b)

Figure 2.8. (a) The grain boundary energy of LAGBs are almost independent of the misorientation angle. However, the high degree of symmetry for CSL boundaries leads to dips in the grain boundary energy at respective misorientations [44]. (b) Twin boundaries ($\Sigma 3$) can be described as a mirror plane, where the crystal is mirrored, typically on a $\{111\}$-plane (i.e. coherent boundary).

2.2.3. IMPURITIES AND PHOSPHORUS GETTERING

Crystallographic defects become recombination active when they are decorated by impurities, hence they become detrimental to the electrical performance of the material. The most common impurity sources are the feedstock, crucible, coating and furnace parts. Transition metals, and their precipitates, are known to have especially high recombination activities [45], and the presence of such impurities may seriously limit the final device performance [46, 47].

The concentration of metallic impurities can be reduced by the well-known phosphorus gettering process [48]. However, studies show that crystallographic defects, such as grain boundaries and dislocations, tend to concentrate impurities and promote precipitation of non-getterable precipitates in the vicinity of these defects, which will limit the potential for gettering in these areas [48, 49].

Chen et al measured the recombination activity of SAGBs and LAGBs by using an Electron-beam induced current (EBIC) tool [50, 51]. It was found that SAGBs generally had a higher recombination activity than LAGBs after contamination, due to the trapping properties of the dislocations. A later publication by Castellanos et al [52] found that the recombination activity in fact depends on the degree of disorder in a grain boundary, where highly disordered boundaries had higher recombination activities. The second study by Chen et al [50] showed how high-Σ boundaries had considerable stronger recombination activity than low-Σ boundaries, whereas the coherent $\Sigma 3$ boundary found to hold the weakest activity (i.e. $\sum 3$ (coherent) < $\sum 3$ (incoherent) < $\sum 9 < \sum 27$). This was also suggested to be related to the increased impurity decoration for high-Σ boundaries. Both dislocation clusters and grain boundaries are usually found in large amounts in conventional multicrystalline silicon, and extraction of impurities in the form of post-processing do therefore not reach full potential. Alternative methods to reach better electrical properties, by controlling the formation of defects directly through the solidification process instead, have therefore been the main motivation for structure control.

2.3. NUCLEATION

This chapter will introduce the classical nucleation theory and spherical-cap model, and continue by expanding the concept of nucleation with the alternative athermal nucleation theory and the free growth model. The chapter will then conclude by relating these concepts to the case of silicon.

2.3.1. CLASSICAL NUCLEATION THEORY

Nucleation is the first stage of forming a new macroscopic crystal, and basically consists of rearranging atoms from the liquid into a more ordered solid phase [53]. Solid clusters of atoms (e.g. as illustrated in Figure 2.9 (a)), usually called nuclei, can (1) form directly in the liquid phase by homogeneous nucleation, or (2) on an already existing solid phase, in contact with the liquid, by heterogeneous nucleation. Nucleation is initiated by cooling the melt below the melting point T_m. A typical cooling curve is illustrated in Figure 2.9 (b) and, as seen from this figure, nucleation does not start instantaneously, but at a given temperature below the melting point. This temperature difference is more commonly called the nucleation undercooling ΔT, and is related to the stability of the nucleus. Minute solid clusters, or nuclei, form already above the melting point, due to random fluctuations in the liquid phase, but they are not stable and will quickly melt back again.

A newly formed nucleus will only become stable when it reaches a certain critical size, where it can successfully surpass the energy barrier associated with the phase transformation from liquid to solid. The overall nucleation rate I is influenced both by the rate of cluster formation and the rate of atom transport to the nucleus. At low undercoolings the energy barrier for nucleus formation is very high, and the nucleation rate is correspondingly low. However, as the undercooling increases, the nucleation rate also increases sharply towards a maximum value, before reducing again. At this point nucleation will be limited by atomic diffusion from the liquid to the nucleation site, leading to an equally sharp decrease in the nucleation rate. The final step of nucleation is the so-called recalescence. A phase transformation from liquid to solid is usually associated with a release of latent heat (i.e. the transformation is exothermic). When this release is large enough to balance the forced cooling, the melt will experience a temperature increase, called recalescence. This increase in temperature will lead to a complete halt in formation of any new nuclei, and the nucleation step can be considered to be finished.

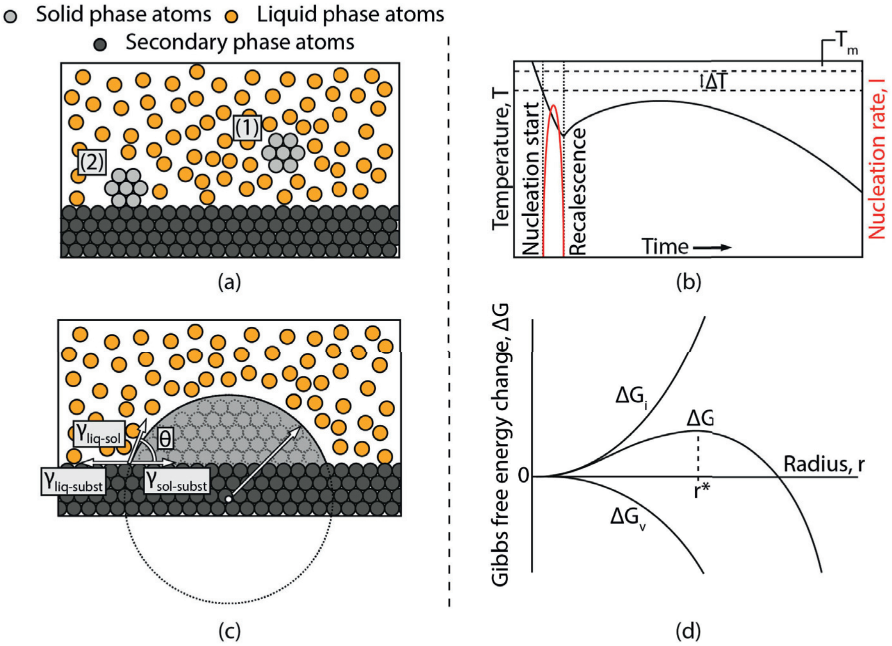

Figure 2.9. (a) Solid nuclei form either (1) homogeneously or (2) heterogeneously. (b) A typical cooling curve, where nucleation initiates at a certain undercooling ΔT below the melting point T_m. The initial increase in nucleation rate I is followed by a sharp reduction due to kinetic limitations, and halts at the point of recalescence. (c) Classical nucleation theory treats the nucleus as a spherical particle, balanced by the interfacial energies between the interfaces of the system. (d) The energy barrier ΔG_{r^*} for a nucleus to become stable can be given as a sum of the change in Gibbs free energy resulting from generation of a new solid volume (ΔG_v) and the associated solid-liquid interface (ΔG_i).

The phase transformation from liquid to solid requires formation of a solid volume and a solid surface. By assuming that the nucleus attain a spherical shape (Figure 2.9 (c)), the energy associated with such a transformation (ΔG) can be described by the following formula:

$$\begin{aligned}\Delta G &= (\Delta G_v + \Delta G_i) \cdot f(\theta) \\ &= (-\frac{4}{3}\pi r^3 \Delta g_V + 4\pi r^2 \gamma_{sl}) \cdot f(\theta)\end{aligned} \qquad \text{(Equation 2.2)}$$

where ΔG_v is the volume free energy difference, ΔG_i is the surface free energy difference, $f(\theta)$ is a factor adjusting for the wettability between the nucleus and the underlying substrate, r is the radius of the nucleus, Δg_V is the free energy difference between the liquid and solid per unit volume, and γ_{sl} is the interfacial energy between the nucleus and the surrounding melt. This equation is illustrated in Figure 2.9 (d) and, as evident from this illustration, there will be a certain energy barrier for the nucleus to overcome in order to become stable. The smallest size which allows equilibrium between a spherical crystal and the melt, i.e. the critical radius r^*, can be written as:

$$r^* = \frac{2\gamma_{sl}T_m}{\Delta T \Delta H_v} \qquad \text{(Equation 2.3)}$$

where ΔH_v is the enthalpy of change for solidification. The probability of successfully arranging the amount of atoms necessary for forming larger nuclei is very small, and the phase transformation can therefore not occur at any arbitrarily small undercooling. The formula for calculating the energy barrier ΔG_{r^*} is found by inserting Equation 2.3 into Equation 2.2:

$$\Delta G_{r^*} = \left(\frac{16\pi}{3}\right)\left(\frac{{\gamma_{sl}}^3}{{\Delta g_V}^3}\right) \cdot f(\theta) \qquad \text{(Equation 2.4)}$$

As soon as the energy barrier is overcome, the crystal can continue to grow into a macroscopic crystal. In the case of heterogeneous nucleation, the energy barrier is affected by the interactions between the nucleus and the underlying substrate, represented by the wettability factor $f(\theta)$. The wettability factor is calculated as a function of the wetting angle θ between the solid nucleus and the underlying substrates by the following formula:

$$f(\theta) = \left(\frac{1}{4}\right)(2 + \cos\theta)(1 - \cos\theta)^2 \qquad \text{(Equation 2.5)}$$

The wetting angle is illustrated in Figure 2.9 (c), and represents the energetically most favourable shape of the nucleus, determined by the different surface tensions between the solid nucleus, the melt and the underlying substrate. The balance in interfacial energy can be written as following:

$$\gamma_{liq-sub} = \gamma_{sol-sub} + \gamma_{liq-sol}\cos\theta \qquad \text{(Equation 2.6)}$$

Where $\gamma_{liq-sub}$, $\gamma_{sol-sub}$ and $\gamma_{liq-sol}$ are the interfacial energies of the melt-substrate, substrate-nucleus and melt-nucleus interfaces, respectively. While homogeneous nucleation corresponds to $f(\theta) = 1$ ($\theta = 180°$), or no wetting at all, heterogeneous nucleation describes any value below unity, i.e. $0 \leq f(\theta) < 1$, where $f(\theta) = 0$ ($\theta = 0°$) corresponds to complete wetting and no nucleation barrier at all. Substrate particles can, in other words, have a considerable effect on the energy barrier and the nucleation conditions. In reality, solidification usually initiates heterogeneously, either on the crucible and/or on solid particles. Homogeneous nucleation can in most cases only be initiated in levitating droplets containing very low contamination levels, where there is no contact with a crucible and secondary precipitates [54].

In order to ensure a high catalytic potency the substrate particles should have a crystallographic lattice similar to that of the nucleating material, i.e. a low lattice mismatch [55], and large enough crystallographic facets to support nuclei with critical dimensions, i.e. corresponding to the critical radius [56].

Even though the spherical cap model successfully explains the origins of the nucleation barrier it still has a very simplified view on nucleation that frequently fails to quantitatively explain experimental results [56]. The main weaknesses are:

1. The equilibrium shape of the solid nucleus cannot easily be observed, as it grows in a melt, and one can therefore not measure the wetting properties directly.

2. The expressions above have originally been calculated from vapour condensation experiments, and taken to be universally applicable for all nucleation-based first-order phase transitions.

3. The model cannot be applied to substrates with high catalytic potency, i.e. when $f(\theta)$ and the corresponding nucleation barrier ΔG_{r^*} approach zero. The nucleus will in this case only be a few atoms thick, even down to less than a single monolayer when $\theta \leq 10°$, and the spherical cap model still considers the nucleus as a macroscopic droplet.

In order to address the second argument, an alternative model based on atomic adsorption has been proposed by Cantor, stating that $f(\theta)$ is not an adequate measure for the catalytic efficiency [57, 58].

An important addition to the spherical cap model is the so-called free growth model, presented by Greer et al in 2000 for grain refinement in aluminium melts, which can be applied independently of if the nucleus forms as a low-contact angle spherical cap or by adsorption [56, 59].

2.3.2. ATHERMAL NUCLEATION AND THE FREE GROWTH MODEL

In contrast to thermal nucleation, which involves thermal activation over an energy barrier ΔG_{r^*}, athermal nucleation treats sub-critical nuclei as dormant until the critical undercooling for free growth is reached by cooling. While thermal nucleation is a purely stochastic process, with nuclei forming by random fluctuations in the melt, athermal nucleation is a more deterministic process, where the number of nucleation events depends on the undercooling, but not on time nor mechanism.

The equation for critical undercooling for onset of free growth ΔT_{fg} is very similar to that previously reported for the critical radius r^* in Equation 2.3. However, assuming a spherical substrate particle, the critical radius r^* has, in this case, been replaced by the radius R_{nuc} of the substrate particle:

$$\Delta T_{fg} = \frac{2\gamma_{sl} T_m}{\Delta H_v R_{nuc}} \qquad \text{(Equation 2.7)}$$

The nucleation process initiates, at very small undercoolings, by formation of a thin layer of solid material, either by adsorption, wetting or heterogeneous nucleation. The layer will spread to cover the whole substrate particle and is limited by the radius R_{nuc} of the particle facet, as illustrated in Figure 2.10 (a). The only way for the nucleus to grow will be by increasing the height h of the spherical cap. Note that the cap is no longer defined by the balance of the surface tensions, as previously in Figure 2.9 (c). The initial radius r of the cap is much larger than R_{nuc}. However, as h increases, the radius of the cap will decrease. The cap may continue to grow until it reaches the critical radius r^* defined by the minute undercooling, given by Equation 2.3, but no further. The nucleus is dormant.

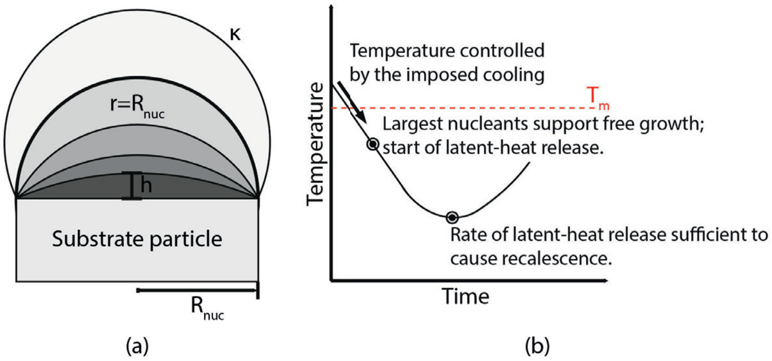

Figure 2.10. (a) According to the free growth model [59], the nucleus is limited by the size of the particle facet R_{het}. The radius of the nucleus, r, decreases as the height h of the cap increases. Free growth may only be achieved when the critical radius r^* becomes equal to the radius of the substrate particle, R_{nuc}. (b) The model states that nucleation initiates at the largest substrate particles first, and progressively on smaller particles as the undercooling increases.

The undercooling increases gradually over the whole time span of the nucleation step, as illustrated in Figure 2.9 (b), and the minute critical radius r^* will decrease accordingly. The critical radius will, at some point, become equal to the radius of the substrate particle, and the nucleus can then obtain a radius that is equal to that of the substrate particle, i.e. $r = r^* = R_{nuc}$. At this point, further growth will imply a favourable decrease in the sphere curvature $\kappa = \frac{1}{r}$, and the nucleus has surpassed the barrier to free growth and is no longer dormant. The nucleus can now grow into a macroscopic crystal.

An important consequence of Equation 2.7 is, as illustrated in Figure 2.10 (b), that free growth initiates on the largest substrate particles, i.e. at the smallest critical undercoolings, first. Progressively smaller nucleation substrates become active in successfully initiating free growth as the undercooling of the system increases. The model is adapted to an earlier model by Maxwell and Hellawell [60], stating that nucleation only proceeds until the onset of recalescence, where the increase in temperature leads to loss of undercooling and final cease of nucleation. The model has shown to correlate well to experimental observations in aluminium alloys inoculated with Al-Ti-B refiner [59]. The author clearly states that the model is not successful in predicting the grain size of columnar growth, such as in directional solidification. This is, however, probably related to fundamental differences in the equiaxed and columnar growth mechanisms, and not to the nucleation mechanism. We therefore believe that the nucleation conditions during directional solidification still can be explained by this model.

2.3.3. NUCLEATION IN SILICON

Silicon is not particularly well explored in terms of nucleation. It is well known that silicon favours heterogeneous nucleation on solid substrates that are in contact with the melt, but the interaction with the substrates and their effect on the nucleation conditions is not well understood. There has until today, to my knowledge, only been published a single robust method for controlling the nucleation conditions during crystal growth, namely the dendritic solidification method developed by Fujiwara et al in 2006 [61]. This method will be further elaborated in Ch. 2.5.1.

Potential substrate particles and their properties:
Coating and other impurity particles are commonly in contact with the silicon melt during the solidification process. The crucibles are spray-coated with a thin layer of Si_3N_4-based coating to prevent sticking of the ingot to the crucible. The coating contains a mixture of both α- and β-Si_3N_4, usually with an excess of the α-polymorph. Other impurity particles follow the feedstock material and may precipitate during the solidification process. Carbon and oxygen may also enter the melt from carbon-based furnace parts and the surrounding atmosphere, respectively.

During directional solidification, grains are generally found to nucleate on the crucible bottom and grow as elongated grains parallel to the temperature gradient towards the top of the ingot (Ch. 2.4.2), suggesting that the crucible plays an important role in the nucleation process.

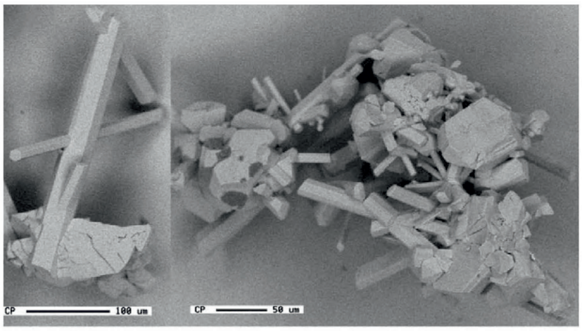

Figure 2.11. Rod-like β-Si_3N_4 particles and more cubic β-SiC particles are commonly found in multicrystalline silicon ingots. This image is reproduced from the work by Søiland et al [62].

In addition to hexagonal α-Si_3N_4 coating particles, the most commonly observed particles in freshly grown multicrystalline silicon are β-Si_3N_4 and β-SiC particles [62-64]. While β-Si_3N_4 particles are generally found to have hexagonal rod-like shapes, β-SiC particle are found to have a more cubic shape. Both are imaged in Figure 2.11, reproduced from the work by Søiland et al [62]. SiC also comes in two polymorphs, namely α- and β-SiC. The difference in Gibbs energy of formation for the two polymorphs is small [64] and the preference for the β-polymorph can therefore not rely solely on thermodynamic considerations. There are, however, indications on that nitrogen, which is readily available in silicon melts because of the Si_3N_4-coating, may increase the preference for the cubic β-polymorph [65].

Precipitation occurs when the melt becomes supersaturated with a certain element [53]. As silicon melts are kept at temperatures above the melting temperature, usually for several hours, in order to fully melt the feedstock and stabilize the melt, there is plenty of time for in-diffusion of contaminants. Due to direct contact between the coating and the silicon melt we expect there to be a rapid and continuous in-diffusion of nitrogen from the α-Si_3N_4 coated crucible wall and into the melt, which upon cooling will reprecipitate as β-Si_3N_4 [62].

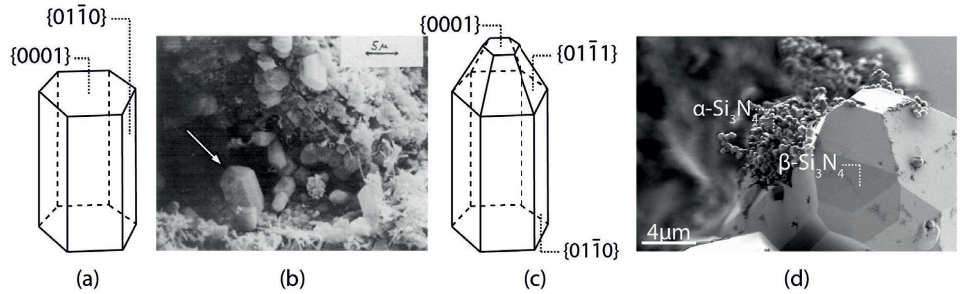

Figure 2.12. (a) The ideal hexagonal shape is bounded by $\{0001\}$-oriented top planes and $\{01\bar{1}0\}$-oriented side planes. (b) However, experimentally observed Si_3N_4 particles rarely show flat edges. This image is reproduced from the work of Jennings et al [66]. (c) This can be explained by the growth habits of these crystals, where slowly growing $\{01\bar{1}1\}$ or other high-index facets appear in later stages of particle growth. (d) Even so, there is still a considerable size difference between α- and β-Si_3N_4 particles. This micrograph is from the current work.

Only top wafers were studied in the work by Søiland et al [62], but in order for particles to act as substrates for nucleation in directional solidification they have to be located at the bottom of the crucible, where the initial nucleation events take place. Mjøs et al [67] located multiple Si_3N_4 precipitates in bottom wafers cut from a directional solidified silicon ingot, by chemical-mechanical polishing, but was not successful in locating SiC precipitates due to their small size. Reimann et al [68] found that, even though precautions were taken in order to limit SiC- and Si_3N_4-precipitation in bulk melt, they were not able to prevent precipitation close to the coated crucible bottom, suggesting that the melt is saturated with nitrogen and carbon already from the start.

Table 2.2. Crystallographic properties, showing crystal structure, lattice mismatch to silicon and commonly found particle size for β-SiC, α- and β-Si_3N_4.

Substrate	Crystal structure	Lattice mismatch [%]	Particle size [μm]
β-SiC	Cubic	20 [69, 70]	>10 [62]
α-Si_3N_4	Hexagonal	3 [71, 72]	0 - 1 [72]
β-Si_3N_4	Hexagonal	1.1 [73, 74]	> 10 [62]

In the case of silicon, we have now established that β-SiC and the two α- and β-Si_3N_4 polymorphs are in abundance at the crucible bottom, and therefore most likely to be the most relevant nucleation substrates. The crystallographic properties of the substrates are summarized in Table 2.2. As previously mentioned in Ch. 2.3.1, in order to secure a high catalytic efficiency, the interfacial free energy between solid silicon and substrate should be kept to a minimum. This is possible only with low crystallographic mismatch between the corresponding phases [56]. The crystallographic mismatch to β-SiC has previously been found to be 20%, and is therefore not consistent with high nucleation potency. Nucleation on β-SiC has been observed by Pupazan et al [75] but, as this was done in an uncoated graphite crucible, this is probably related to the lack of a more efficient substrate.

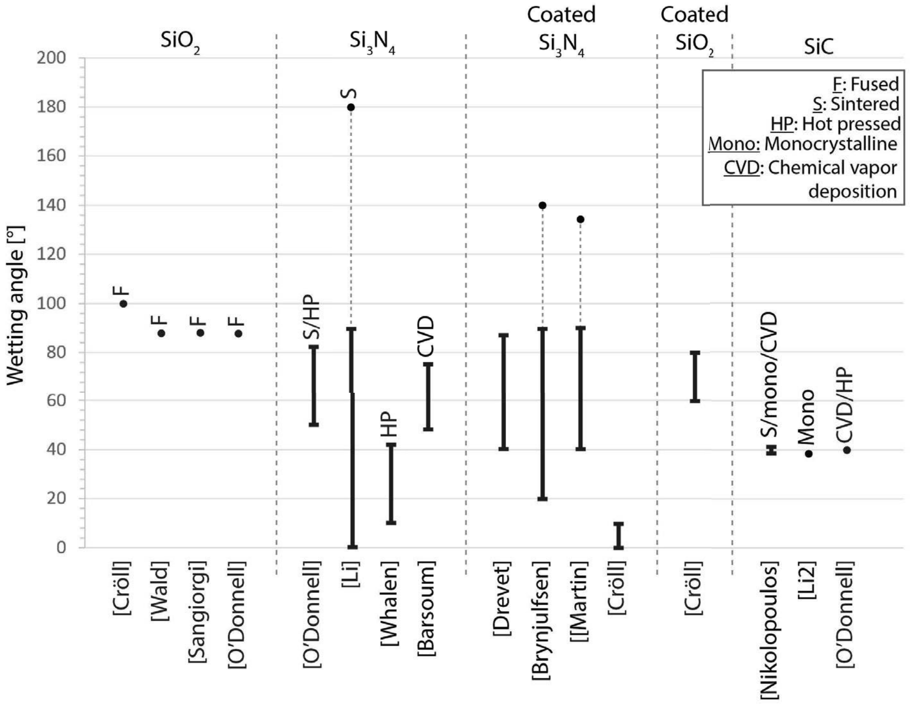

Figure 2.13. Wetting angles for liquid silicon on substrates/particles commonly observed in silicon melts. The production of the different particles varies and, in the cases where specified, the production is marked by a simple letter or keyword. The data has been collected from Cröll [76], Wald [77], Sangiorgi [78], O'Donnell [79], Li [80, 81], Whalen [82], Barsoum [83], Drevet [84], Brynjulfsen [85], Martin [86], and Nikolopoulos [87]. Measured intervals are marked as lines, while single measurements are marked as dots.

The lattice mismatch to β-Si_3N_4 is only 1.1%, thus being a much more potent nucleation substrate. No experimental measurements have been found for α-phase particles but, due to the structural similarities to the β-phase, we believe the mismatch to be closely related. Theoretical calculations by Brynjulfsen [72] found a mismatch of approximately 3%, by using crystallographic data from Kuwabara et al [71], but this has yet to be confirmed by TEM. Brynjulfsen also found no evident effect of increased carbon concentrations on ingot microstructure [88], suggesting that SiC formation has minimal effect on the nucleation conditions in presence of more favourable Si_3N_4 substrates.

According to the free growth model previously presented in Ch. 2.3.2, the particle size of potential substrate particles also plays an important role in terms of nucleation probability. Previous studies have shown that β-Si_3N_4 may grow to considerable sizes with diameters of several tens of micrometres [62] and, due to the high aspect ratio of the β-Si_3N_4 rods, the largest facet can even become several hundreds of micrometres in the longitudinal direction (Figure 2.11). Alpha-Si_3N_4 coating particles, on the other hand, are typically found with sizes below 1μm.

The ideal morphology of hexagonal crystals is illustrated in Figure 2.12 (a), i.e. a hexagonal shape bonded by $\{0001\}$ and $\{01\bar{1}0\}$ family planes. Depending on which plane the nucleus is formed, the size of the nucleus will either be limited by the diameter of the rod or by the smallest dimension of the side facet, respectively. However, the top and bottom faces of the rods are rarely found to be planar, but usually display a more pyramidal shape (Figure 2.12 (b)) [66]. This may be related to the growth habits of hexagonal crystals, where crystals in the end are bound by the slowest growing facets [53]. Li et al [89] investigated the growth habits of oxide crystals and found a tendency for the crystals to become bounded by angular $\{01\bar{1}1\}$ family planes, as illustrated in Figure 2.12 (c), and derived the following relation between the growth velocities V of the different planes:

$$V_{\langle 0001\rangle} > V_{\langle 01\bar{1}0\rangle} > V_{\langle 01\bar{1}1\rangle} \qquad \text{(Equation 2.8)}$$

This implies that the $\{0001\}$ planes progressively disappear during particle growth and, after disappearing, they become unavailable for silicon to nucleate on. Alternatively, other similar high-index planes may also replace the flat $\{0001\}$ edge plane. However, independent of which types of facets are available, the facet size of β-Si_3N_4 particles are still several order of magnitude larger than that of their α-phase counterpart, as illustrated in Figure 2.12 (d).

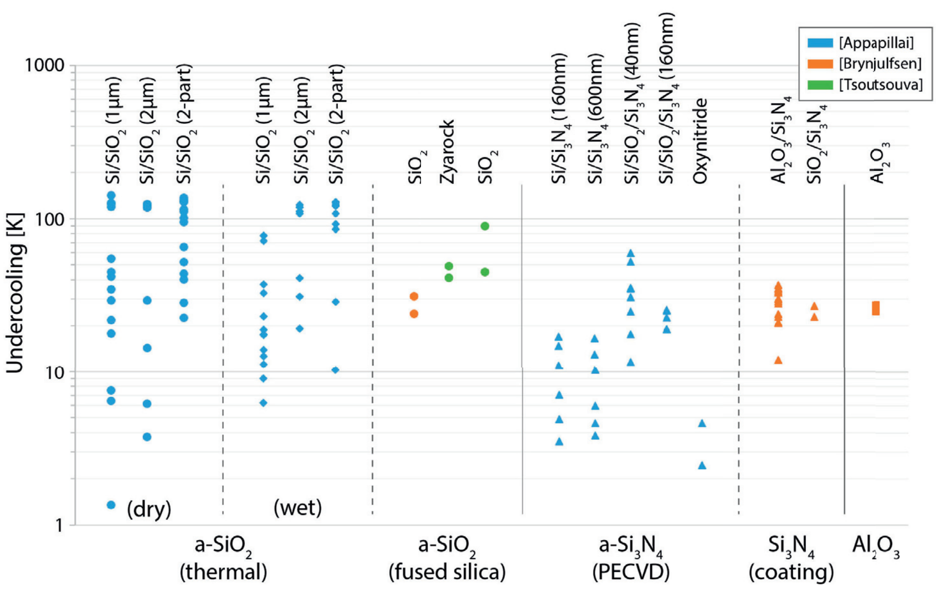

Figure 2.14. An overview of nucleation undercoolings measured by Appapillai et al [90] (blue dots), Brynjulfsen et al [7] (orange dots) and Tsoutsouva et al [91] (green dots) for thermally grown SiO_2, fused silica, PECVD deposited Si_3N_4, industrial Si_3N_4 coating and Al_2O_3 crucible material.

Wetting measurements:

As suggested by the classical spherical cap model, measuring the wettability between the solid silicon nucleus and the substrate material may be a possible way of probing the catalytic properties of a substrate material. The wetting angle between the nucleus and a potent substrate particle should be as small as possible, indicating a low barrier for nucleation. However, as mentioned in Ch. 2.3.1, the fact that the nuclei are formed within the melt complicates such measurements. There are, on the other hand, considerable amounts of data regarding the wetting properties of liquid silicon on different substrates, and Brynjulfsen [72] suggested that the interfacial energy balance for the liquid-substrate system could be used to estimate the energy balance for the solid-substrate system. However, she realized that such an operation was not straight-forward, especially due to the large variations in reported values (Figure 2.13). It appears to be generally accepted that one of the main reason for the spreading values is related to interactions with oxygen, forming an oxynitride (SiO_xN_y) layer on top of the Si_3N_4, that alters the wetting properties of the substrate [80]. The largest wetting angles was, in the work by Li [80], obtained at very high partial pressures of oxygen, and assumed to be related to the formation of a SiO_2 layer instead of the oxynitride. The wetting angle is also frequently found to change over time [85, 86]. Brynjulfsen was therefore not successful in correlating the estimated wetting angles with measured undercooling values, and concluded with that the wetting angle could not be used as a sole indication on the nucleation conditions. As also suggested by Tsoutsouva et al [91], measurements of liquid wetting angles are therefore only useful for studying adhesion and infiltration phenomena [84] and not nucleation.

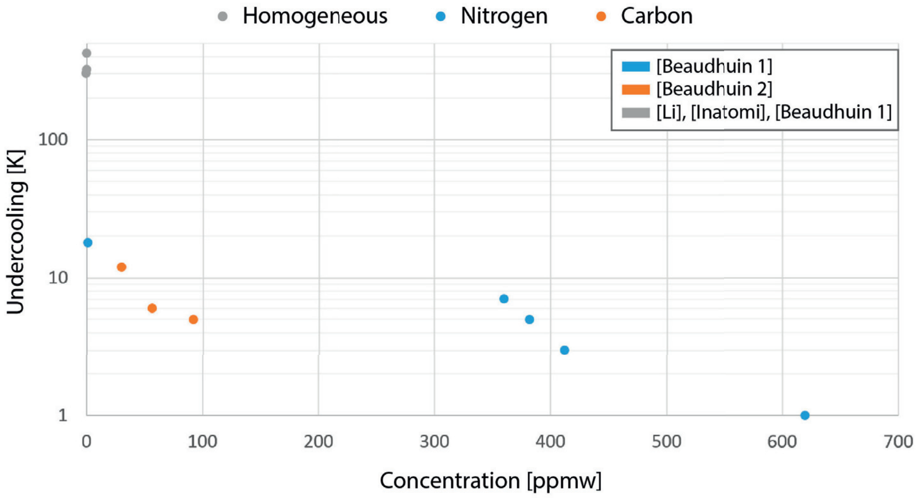

Figure 2.15. Nucleation undercooling measured in levitating silicon droplets. Homogeneous nucleation of silicon usually take place at undercoolings above $\Delta T = 300K$, measured by Li [92], Inatomi [54] and Beaudhuin [93]. The undercooling could be considerably lowered by adding gaseous nitrogen [93] and carbon [94] to the droplets, which was attributed to the precipitation of Si_3N_4 and SiC particles respectively.

Undercooling measurements:
Numerous studies have also focused on measuring the nucleation undercooling directly (Figure 2.14). The grouping of the different samples sets is, in this figure, based on the inner-most layer, which is in direct contact with the silicon melt, and includes dry- and wet-oxidized

silicon (a-SiO_2), fused silica (a-SiO_2), deposited amorphous Si_3N_4 (a-Si_3N_4), Si_3N_4 coating and Al_2O_3 crucible material. While SiO_2 substrates reach maximum undercoolings above 100K, Si_3N_4 substrates appear to favour undercoolings below 40K, suggesting that Si_3N_4 substrates are more potent. The similar values found for the amorphous a-Si_3N_4 phase and the crystalline Si_3N_4 coating material may be related to a transformation of the amorphous phase to a crystalline β-Si_3N_4 phase, as previously observed by Alphei et al [95]. The increase in maximum nucleation undercooling for the Si/SiO_2/Si_3N_4 40nm sample was explained by Appapillai in terms of thermal stresses between the layers, but may also just be a result of increased influence from the underlying SiO_2 layer due to the Si_3N_4 layer being very thin. However, as clearly seen from this figure, the measurements span over several orders of magnitude (2 – 150K), also within individual sample sets, making it difficult to find any clear trends in terms of nucleation potency. Appapillai [90] suggested that this variation might be related to nucleation on other impurity particles and not necessary on the substrate under investigation, and assumed that the undercooling for the actual substrate corresponded to the maximum undercooling measured within each individual sample set.

We do, however, not believe that these large values reflect real melt conditions. They are also not consistent with the free growth model, where initial nucleation takes place at low undercoolings. Contrary to these values are also the measurements done on levitating silicon droplets by Beaudhuin, Li and Inatomi (Figure 2.15). Levitation experiments are more commonly used to measure undercoolings during homogeneous nucleation, but by adding carbon and nitrogen to the droplet Beaudhuin successfully observed formation of SiC and Si_3N_4 substrate particles inside the droplets. These particles acted as substrates for silicon nucleation and lowered the nucleation undercooling down to as little as 1K for the highest nitrogen concentration. By assuming that the melt is saturated on nitrogen close to the crucible wall, we suggest this value is a better representation of real melt conditions, and will be the base for discussion in paper P5.

2.4. CONVENTIONAL GROWTH

This chapter will cover an introduction to the basic growth mechanisms occurring during directional solidification of multicrystalline silicon.

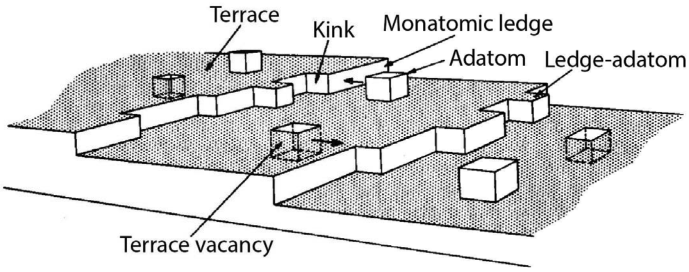

Figure 2.16. An illustration of the so-called Kossel crystal, reprinted from [96]. An incoming liquid phase atom, or adatom, may adsorb on multiple positions of a growing crystal interface, whereas the energetic favourability is determined by the number of neighbouring atoms.

2.4.1. CRYSTAL GROWTH BASICS

As soon as stable nuclei has formed, they continue to grow into macroscopic crystals by addition of atoms from the liquid phase. Growth of a crystal can be visualized by the so-called Kossel crystal, illustrated in Figure 2.16 [96]. In this illustration, atoms are represented as cubes that can have six nearest neighbours, one at each of the six faces. An incoming atom (adatom) may position itself in multiple positions at the growth interface, or terrace, characterized by the number of nearest neighbours. The most energetically preferred position will be inside a terrace vacancy, where the adatom gets 5 neighbours, and the preference reduces progressively for the kink, ledge and single adatom positions.

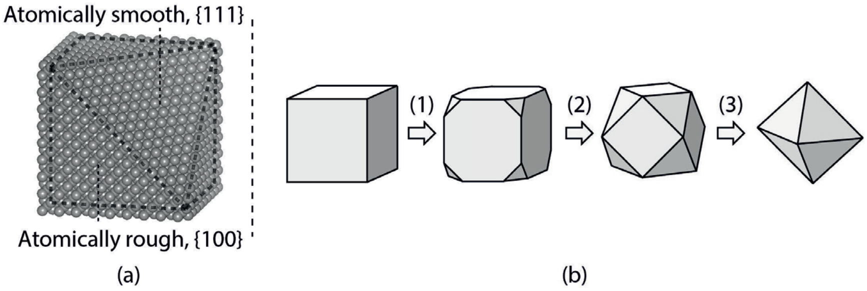

Figure 2.17. (a) The most densely close packed {111}-planes of the diamond cubic crystal structure are atomically smooth. All other planes, like the {100}-planes are rougher. (b) Rougher planes have higher growth velocities than smoother planes, and e.g. a cubic crystal, bounded by {100}-faces will therefore transform its shape into an octahedron, bounded by the slowest growing {111}-planes.

Growth occurs by continuous atomic adsorption at such positions, whereas the actual probability of the atom remaining adsorbed, and becoming fully incorporated into the crystal, depends on the number of neighbours. Crystals may have different growth habits, where the shape of the crystal is largely determined by the crystallographic properties of its crystal structure. As previously mentioned in Ch. 2.1.1, the diamond cubic crystal structure consists of densely packed {111}-planes, and considered to be atomically smooth (Figure 2.17 (a)).

It is increasingly difficult for incoming atoms to remain adsorbed on densely packed planes, and the growth velocity of the plane is therefore low. All other planes, like the {100} plane, are rougher [97], and expose more steps for incoming atoms to adsorb onto. Rougher planes therefore tend to have higher growth velocities than atomically smoother planes. This is manifested as a marked anisotropy in the growth rate of the crystal, where the slowest growing planes become progressively dominant, and a final crystal shape that becomes bounded by these planes (Figure 2.17 (b)). Similar growth habits can also be observed during directional solidification, as presented in the next sub-chapter.

2.4.2. DIRECTIONAL SOLIDIFICATION OF SILICON

Directional solidification is a method commonly used for solidification of multicrystalline silicon. It is a relatively simple method, where a crucible is filled with feedstock material that is molten and re-solidified. The simplest method is the so-called Bridgman method (Figure 2.18 (a)), where the temperature gradient is fixed by the heaters and the melt will progressively solidify as it is pulled past the melting point temperature T_m. Due to the directionality in the pulling, grains will nucleate on the bottom face of the crucible and grow into elongated grains that are parallel to the pulling direction.

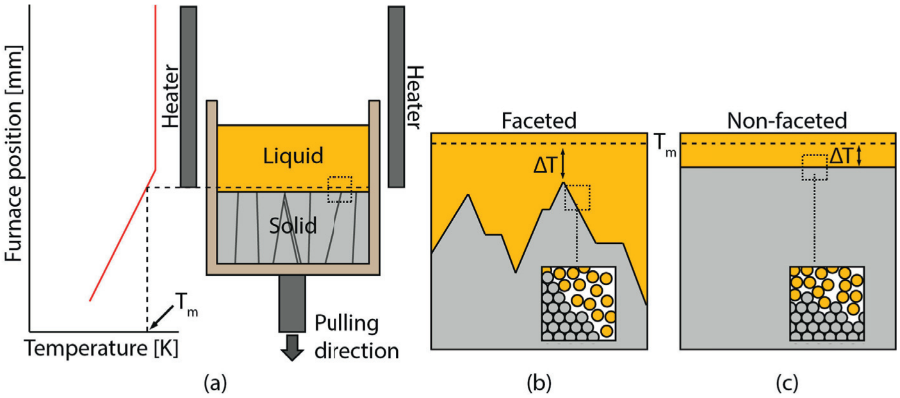

Figure 2.18. (a) An illustration of a Bridgman, where the temperature gradient is fixed, and the growth interface moves towards the top of the crucible by pulling the crucible in the opposite direction. (b) An atomically smooth growth interface appear rough at a microscopic scale. (c) An atomically rough growth interface appear smooth at a microscopic scale.

The interface between the solid- and liquid phases, i.e. the growth interface, will be either atomically smooth or rough, i.e. faceted (Figure 2.18 (b)) or non-faceted planar (Figure 2.18 (c)), depending on the growth habits of the material. Growth require a certain undercooling ΔT to proceed, and an atomically rough interface, containing many favourable adsorption points, tend to grow at much lower undercoolings than an atomically smooth interface. Silicon is known to solidify preferentially with a {111}-faceted growth interface, due to the low surface energy of this plane [98]. Zig-zag facets have previously been observed, by in-situ experiments [99, 100], to form on {100}-, {112}-, {110}- and {111}-oriented interfaces. It was suggested that the facets initiate as atomic scale perturbations, on an otherwise planar growth interface (Figure 2.19 (a)). Above a certain critical growth rate V_c, the perturbations are amplified into macroscopic facets by a negative temperature gradient appearing in front of the growth interface (Figure 2.19 (b)).

Twins are important defects in multicrystalline silicon, not due to their direct impact on the electrical activity, which is low (Ch. 2.2.2), but due to their high abundance. Successive twinning may also create ∑9, ∑27 and random angle boundaries which are much more recombination active (Ch. 2.2.2). Stokkan et al [38] reported on a fraction of approximately 70% of the total grain boundary density in multicrystalline silicon being twin grain boundaries (∑3). In addition to being formed with dendrites [97], twin formation is also closely related to a faceted growth interface (Figure 2.20), where a twinned nucleus can nucleate on the {111}-facets of the interface [97].

Duffar and Nadri [101] developed a theory for twin formation during directional solidification, and found that not only a faceted interface is necessary, but also the presence of a grain boundary with a specific angle to the melt. Later experimental investigations by Stokkan et al [41] supported this theory, by finding that twins often originate at special features on grain boundaries between multiple grains.

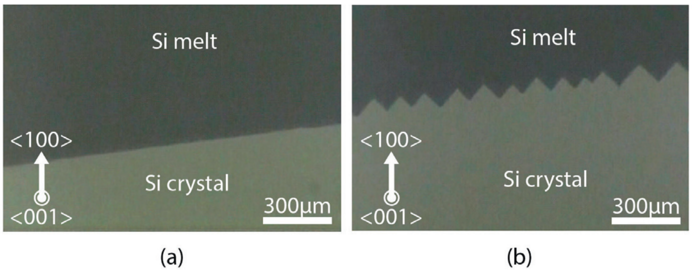

Figure 2.19. The growth interface between a growing <100>-oriented silicon crystal and its melt, reproduced from [97]. The interface is transformed from (a) planar to (b) zigzag-faceted during growth at a growth rate of 9.6mm/min.

An alternative method for growing directionally solidified multicrystalline silicon ingots is by the so-called vertical gradient freeze (VGF) method. In this case the crucible is stationary and solidification occurs by extracting heat from the bottom of the crucible by a heat leak feature [102] instead.

Industrial ingots are usually made in the range of 400 – 600kg (G5 ingots) [6], but with new technologies allowing for ingots up to 1000 – 1200kg (G7 ingots) [103]. The quality of the solidified material is largely dependent on the growth parameters, and an accurate control of the crystallization is necessary to obtain optimum performance. An especially important parameter is the macroscopic shape of the growth interface, as this bends relatively to the total heat flow. In order to minimize thermal stresses the growth interface should be planar, but in order to minimize unwanted parasitic nucleation on the crucible walls a slightly convex growth interface is optimal.

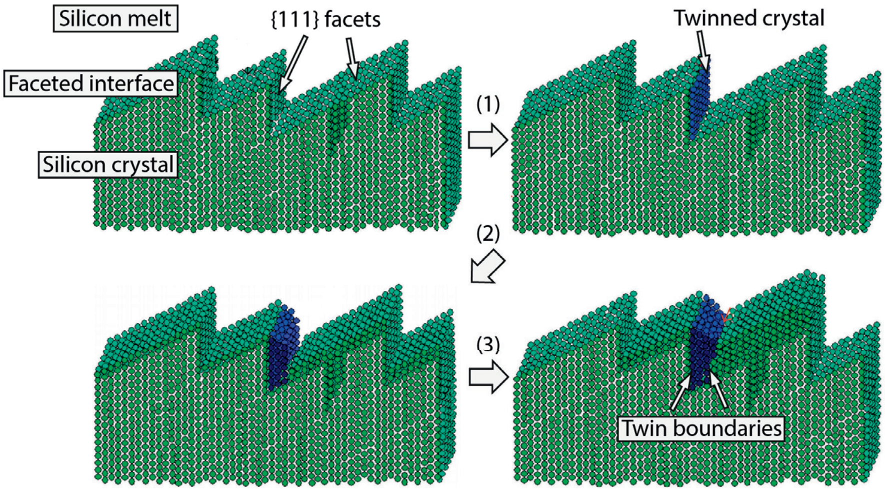

Figure 2.20. An illustration of the formation of a twinned crystal on a {111}-faceted growth interface. Reprinted from the work by Fujiwara [97].

2.5. STRUCTURE CONTROL AND EMERGING GROWTH METHODS

Crystallographic defects, such as dislocations and grain boundaries, are today considered to be the biggest limitation to higher efficiencies in multicrystalline silicon [104], as they tend to trap transition metal impurities and increase the recombination activity of the material. Dislocation densities as low as 10^4cm^{-2} have shown to affect the local recombination activity, and typical regions containing densities in the range of 10^4 - 10^6 cm^{-2} can reduce the final performance of the cell considerably [48, 105]. Much effort has been put into increasing the electrical performance of the material by removing these impurities, e.g. by phosphorus gettering. However, the efficiency of these methods has proven to be relatively limited in highly defected areas. Hartman et al [106] suggested that up to 95% of the initial density of dislocations in newly solidified silicon could be removed by annealing silicon samples at 1366°C, which, if proven to be reproducible, would be a remarkable discovery. A similar observation was also done by annealing mc-Si samples at 1093K [107], resulting in a 60% reduction of the initial dislocation concentration. This was stated to be a combined effect of dislocations diffusing to free surfaces and pairwise annihilation. However, a comprehensive follow-up study published by Reimann et al [108] experienced no reduction in the dislocation density at all, and the studies by Hartman et al [106] and Choi et al [107] are therefore currently being questioned. Dislocations have previously shown to move for several hundreds of micrometres at elevated temperatures, but only in single crystals, and in order for a dislocation to annihilate it needs to counter a second dislocation with an exact opposite Burgers vector [9]. The probability for this to happen at a scale which allows for a reduction of 60 – 95% therefore seems unlikely. Pinning of dislocations by other dislocations, impurities and other crystallographic defects reduces the mobility of dislocations [9] and the probability of annihilation even further. Alternative methods for controlling and/or reducing the defect concentration are therefore needed.

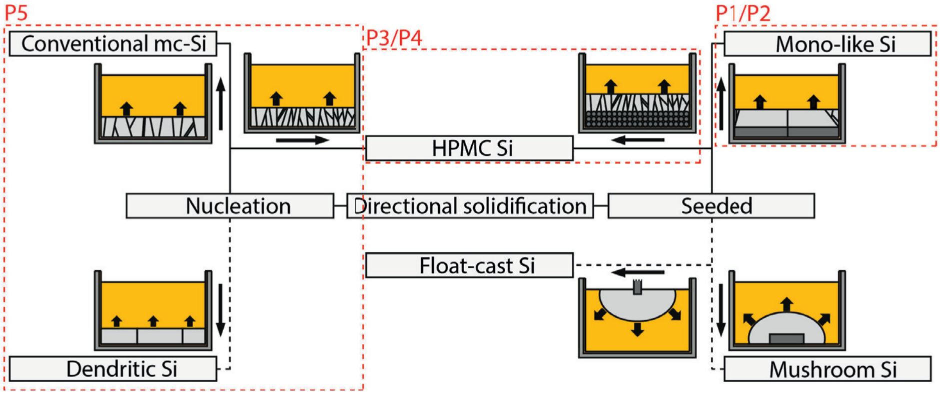

Figure 2.21. Structure control can either be based on modifying the nucleation conditions, such as in the dendritic growth method, or by using seeds placed either in the bottom of the crucible (e.g. by the mono-like, HPMC or mushroom methods) or on top of the melt (e.g. by the float-cast method).

Structure control, in its broadest sense covers all methods that can be used to modify the final microstructure of solidified silicon. The foundations for the microstructure are laid already at the earliest stages of the solidification process, either during or shortly after the nucleation stage. It is therefore necessary to shift the focus towards improving the fundament on which the structure develops rather than attempting to improve the structure after solidification. There are mainly two ways to control the grain structure of mc-Si; either by modifying the nucleation conditions or by eliminating the nucleation step altogether. Different methods for controlling the microstructure are summarized in Figure 2.21 and will be further elaborated in the following sub-chapters.

2.5.1. GROWTH BY MODIFICATION OF THE NUCLEATION PROCESS

There is a great deal of contingency associated to the nucleation process and controlling it is not necessarily straight forward. The amount of research on understanding the actual nucleation mechanisms acting during silicon solidification is surprisingly sparse, compared to other materials, as e.g. aluminium [56]. Apart from the doctoral work by Brynjulfsen [72], only one single robust method has been published for modifying the nucleation conditions for improved ingot quality, namely the so-called dendritic casting method. The remaining literature is mainly targeted towards measuring the melt wetting behaviour and nucleation undercooling of different crucible materials, as previously summarized in Ch. 2.3.3.

The dendritic casting method, first published by Fujiwara et al in 2006 [61], has been subject to extensive research. By applying a high undercooling to the crucible bottom during the initial stages of solidification, they could induce rapidly growing <110>- and <112>-dendrites along the bottom of the crucible. These grains effectively limited the amount of nucleation events taking place in the bottom of the crucible, and lead to a coarsening of the grain-structure. Dendrite crystals contain parallel twins, with {111} grain boundary planes, along their primary arm, and the ingots are therefore often found, in addition to the already reduced amount of grain boundaries, to be dominated mainly by electrically inactive $\sum 3$ grain boundaries [109]. Highly twinned areas are often, but not always, associated with low dislocation densities [39, 109] and it is therefore believed that the twinning process may be beneficial for the dislocation concentration in the material [41]. Some dendritic ingots have, on the other hand, been found to contain higher amounts of dislocations, and it has been suggested that this in some way may be related to dendrites growing away from the crucible bottom [39] and not parallel to it. Dendrites which grow away from the crucible bottom will at some point encounter a volume of insufficient undercooling and are therefore forced to change direction. A study by Usami et al [110] found a reasonable correlation between the dislocation density generated at grain boundaries between dendrites and the contact angle between the respective dendrites (i. e. the magnitude of the accompanying shear stress).

Even though the idea behind dendritic growth has successfully been applied to small-scale experiments, it has unfortunately not been easy to apply these principles industrially [111], as the size of industrial crucibles make it difficult to maintain uniform thermal conditions throughout the whole crucible bottom. Improvements have recently been made by implementing cooling-spots close to the centre of the crucible together with a convex growth front [109, 111]. This resulted in nucleation of rapidly growing dendrites in the centre of the crucible that came to dominate the grain structure. However, due to uneven heat extraction and nucleation conditions, the method still suffers from poor reproducibility [112], and, combined with considerable dislocation generation, the method, in its current state, is not applicable to large-scale industrial growth.

Due to higher undercoolings in areas close to the crucible bottom, traces of dendritic growth are also frequently found near the bottom of grown conventional mc-Si ingots [39, 113], and it is believed that dendrites may in fact also have an important role in initial growth of conventional mc-Si. This will, however, be further explored in paper P5.

2.5.2. GROWTH BY SEEDING METHODS

The most adapted approach for performing structure control is to eliminate the nucleation step altogether, by placing silicon seed crystals into the melt. All seeding methods are fundamentally similar where, instead of spontaneous nucleation, liquid atoms will attach to more favourable positions on the seed crystals instead. The atoms attach in the same arrangement as the default seed atoms, and the microstructure of the ingot will, to a certain degree, be determined by the microstructure of the seeds.

Several new solidification methods that attempt to deal with the defect structures present in conventional mc-Si silicon are currently under development. Most of them are illustrated in Figure 2.21, including the mono-like (Mono-like Si) and high-performance multicrystalline (HPMC Si) growth methods, and the more recent mushroom-shaped (Mushroom Si) and noncontact crucible (Float-cast Si) growth methods [114, 115]. The two latter are novel methods that only have been investigated in small-scale furnaces, for research purposes, and the industrial applicability is questionable, as both methods require considerable modifications of existing infrastructure.

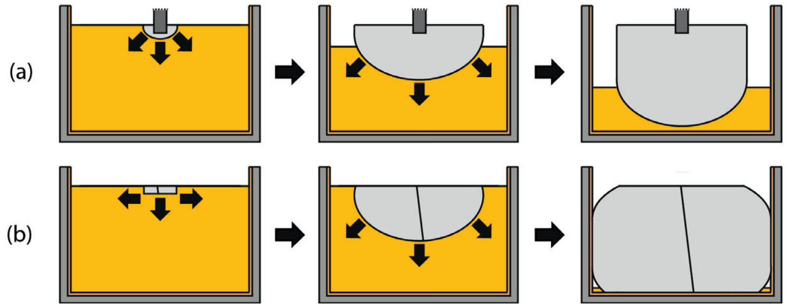

Figure 2.22. (a) The noncontact crucible method consists of placing a monocrystalline seed at the top the melt interface and grow the ingot downwards. (b) An alternative version applies a high undercooling at the top of the melt to nucleate a rapidly growing dendrite.

Growth by the float-cast method:

The float-cast method, more commonly called the noncontact crucible method, dips a seed in molten silicon, similarly to the Czochralski (CZ) process. By establishing a low-temperature zone ahead of the seed one can grow ingots without direct contact with the crucible (Figure 2.22 (a)) [116]. Ingots grown by this method will therefore have advantages over conventionally grown mc-Si in terms of less random nucleation and peripheral stresses. While CZ ingots are grown with a concave growth front [117], float-cast ingots are grown with a convex growth front instead, which repels melt impurities much more efficiently.

An alternative float-cast method is also under development, which utilises nucleation of rapidly growing dendrites instead of seeding [118] (Figure 2.22 (b)). However, due to contact with the crucible towards the end of the solidification process, the issues related to parasitic nucleation and peripheral stress generation remains. A partial solution to this problem has been to design crucibles that remove residual melt residing in the crucible at the final stage of solidification [119]. However, the authors clearly state that significant improvements are needed if the method is to be adaptable for crucible sizes larger than 100mm. Also, in both these methods Si_3N_4 coating may dissolve into the melt and lead to precipitation of β-Si_3N_4 particles, leading to nucleation of additional grains [120]. As the ingot is not in contact with the crucible, there is generally no need for a release agent such as a Si_3N_4. However, by removing the coating layer, the melt becomes exposed to increased contamination from the crucible, e.g. by oxygen, which also may be detrimental for the final device performance [121].

Growth by the mono-like method:

The mono-like growth method requires less adjustment to existing infrastructure than the methods mentioned above. The method was introduced by Stoddard [122] in 2006, as a method for growing silicon ingots with near monocrystalline structure and low density of crystallographic defects. The method consists of placing one or more monocrystalline seeds in the bottom of the crucible, and initiate solidification by growth of the seed crystals instead of by nucleation of new crystals (Figure 2.23). The melting step therefore has to be optimized to prevent complete melting of the seeds. The method has already proven to be adaptable to industrial sized infrastructure [123], but not without challenges. The main challenges are related to nucleation and growth of parasitic grains from the periphery of the ingot, and dislocation generation due to the necessary use of multiple seeds for larger crucibles.

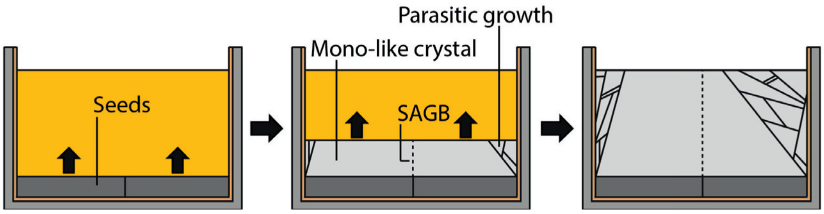

Figure 2.23. The mono-like methods consists of covering the crucible bottom in monocrystalline seeds, promoting growth of the seed crystals instead of nucleation. However, spontaneous nucleation of parasitic grains may still take place on the crucible walls, limiting the monocrystalline fraction. Grain boundaries, may also appear if the seeds are not placed identically in the crucible.

Parasitic grains will nucleate on the crucible wall at some point during solidification, and continue to grow inwards, forming a roof over the central monocrystal. This parasitic volume reduces the final device efficiency, and is therefore unwanted for high-quality mono-like devices [124]. The parasitic grains are generally found to be limited by the {111}-planes of the central monocrystal, and the extent of the parasitic grain structure can therefore be partially controlled by optimizing the crystallographic orientation of the seeds [125]. There are, however, some unpredictability associated with which of the four {111}-planes that are active, and a more reproducible way of reducing the ingrowth should be found. Jouini et al

[126] have proposed that, by making the growth interface slightly convex, one should be able to prevent most of the parasitic ingrowth.

There are multiple sources of dislocations when growing mono-like silicon, and most of them can be traced back to the interfaces of the monocrystalline seeds. Pre-existing structural defects on the faces of the seeds, surface roughness and generation of localized stress points due to indentation are some of the dislocation sources that have been identified [15] and, as shown by Jiptner et al [127], some of them can penetrate deep into the monocrystal, and have a serious detrimental effect on the final device efficiency. High concentrations are also generally found in the periphery of ingots, due to stresses being generated between the crucible and ingot [128], as silicon expands upon solidification. Also, when multiple seeds are used, imperfect placement of neighbouring seed will lead to formation of small-angle grain boundaries that are accompanied by dislocation generation [129, 130]. Dislocation clusters resulting from seed misorientation can become very large and have a profound effect on the final device performance, and there is a large need for understanding and limiting such generation. Trempa et al [43] investigated the potential of replacing the small-angle grain boundaries by pre-defined CSL boundaries. They showed how nearly perfect high-symmetry CSL boundaries ($\sum 3$ and $\sum 9$) resulted in a significant defect-area, while the more random low-symmetry CSL boundaries ($\sum 33$ and $\sum 41$) led to very little dislocation formation. This has later also been confirmed by Takahashi et al [131]. Such pre-defined grain boundaries, commonly called functional grain boundaries, have also recently been shown to limit ingrowth of parasitic grains [132].

Growth by the mushroom method:

The mushroom method is a possible modification to the mono-like method. However, not much is known about the final crystallographic structure of ingots grown by this method, due to the limited amount of experimental results published by the group developing the method. The main idea is to solidify a near-monocrystalline ingot from a single seed placed in the middle of the crucible bottom to limit growth of parasitic grains from the crucible wall [133]. One would also not have to deal with multiple seeds.

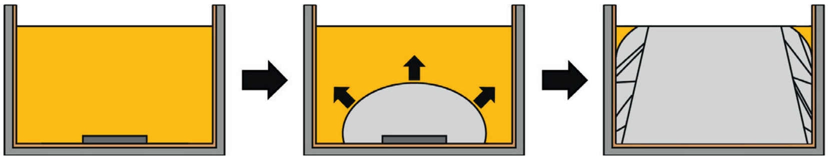

Figure 2.24. The mushroom method consists of placing a single monocrystalline seed crystal centrally in the bottom of the crucible. By applying a very specific thermal gradient, the authors have been successful in attaining a so-called mushroom shaped growth interface.

The method requires isotherms shaped like a mushroom, as illustrated Figure 2.24, and therefore needs redesign of existing furnace infrastructure. Even though this shape should suppress ingrowth of parasitic grains, issues related to parasitic nucleation remain unsolved [134]. The average dislocation density is reported to be approximately 10^4 cm^{-2}, but no good overview of the dislocation distribution is given. It is also expected that also the method will suffer from dislocation generation when the ingot comes into contact with the crucible walls.

The applicability to larger crucibles is also questionable, as it may be difficult to maintain the necessary temperature field to achieve a mushroom-shaped growth front.

Growth by the seeded HPMC method:

All methods described above have two common goals, namely to reduce the amount of both grain boundaries and dislocations. However, it has recently become evident that grain boundaries can have a positive effect on the average concentration of dislocations and the size of dislocation clusters in multicrystalline material.

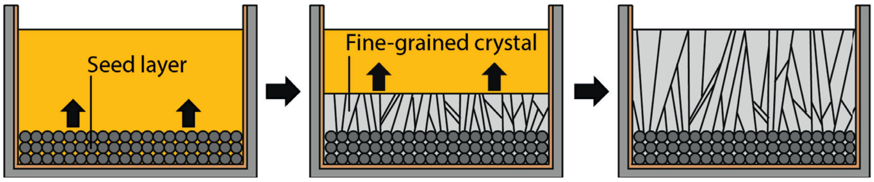

Figure 2.25. Growth of HPMC silicon is usually done with a multicrystalline seed layer on the bottom of the crucible, here illustrated by a granules. A fine grained crystal will then grow from the top layer.

In contrast to the previously described methods, the HPMC term does not describe a certain production process, but rather certain characteristics held by the final ingot. This includes a small average grain size, low dislocation density and a high density of random angle grain boundaries. A smaller grain size is not necessarily directly beneficial for the minority carrier lifetime, as this implies an increased amount of grain boundaries, but, as shown by Stokkan et al [16], dislocation clusters tend to terminate at random angle grain boundaries. The small grain size and high density of random angle grain boundaries therefore prevent dislocation clusters from dominating the structure to the same degree as in conventional mc-Si. There are several potential approaches for producing such a material, but the most frequently reported is based on a seeding layer, similar to that of mono-like silicon, only with a very fine-grained multicrystalline microstructure instead [112, 135-138]. As previously described for the mono-like silicon, only parts of the seeding layer are molten and solidification initiates by growth of the top layer of seed particles (Figure 2.25).

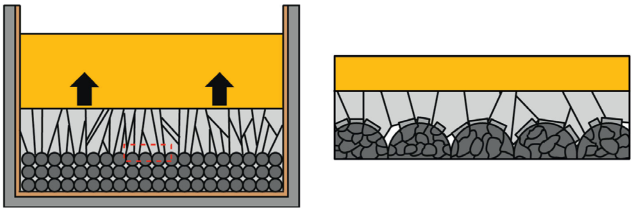

Figure 2.26. The initial grain structure of the ingot will be determined by the grain structure of the seed particles that are facing the melt.

As the top layer consists of a large number of grains (Figure 2.26), the final ingot will attain a much more refined microstructure than conventional mc-Si. This method has been successfully applied to industrial G5 crucibles (840mm x 840mm x 260mm), resulting in final cell properties superior those of both dendritic and conventional mc-Si cells [112].

3. SOLIDIFICATION AND CHARACTERIZATION TECHNIQUES

This chapter covers the different experimental techniques used in this work, including solidification and sample preparations, the solidification experiments themselves and different characterization techniques. The use of the different techniques is summarized in Table 3.1.

Table 3.1. The use of the different experimental techniques in the different parts of the work. The vertical column is divided into the three main parts of the work and the horizontal row indicates the chapters of the given experimental techniques.

Work	3.1	3.2	3.4	3.5	3.6	3.7	3.8	3.9	3.10
Mono-like Si (P1 & P2)	x	x	x	x	x	x	x	x	x
HPMC Si (P3 & P4)	-	-	x	x	x	x	x	-	x
Beta-Si_3N_4 *(P5)*	-	-	-	x	x	x	-	-	-

3.1. PREPARATION OF SEEDS FOR MONO-LIKE SILICON

Monocrystalline seeds used in the solidification of mono-like silicon were cut from a <001>-oriented monocrystalline CZ ingot with a diameter of Ø = 150mm. The seeds were cut with different crystallographic orientations, i.e. with {001}, {110}, {111} and {211} top-planes perpendicular to the growth direction, and a special tilt table was constructed for this purpose (Figure 3.1 (a)). The table consists of an ingot mount for mounting half-split ingots, screw holes for mounting the table to the saw stage, and a graduated arc for accurate orientation of the ingot.

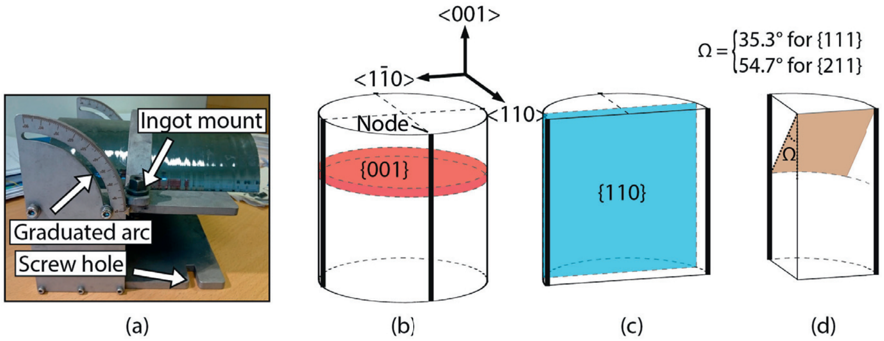

Figure 3.1. (a) The tilting table consisted of features for mounting the ingot to the table (ingot mount) and the table to the saw (screw holes), and a graduated arc for tilting. The (b) {001} and (c) {110} planes can be cut perpendicular and parallel to the longitudinal axis of the CZ ingot, respectively. (d) The {111} and {211} planes can be cut by tilting the ingot 54.7° and 35.3°, respectively.

<001>-oriented Czochralski ingots have four clear edge markings, or so-called nodes, that can be used to visualize the silicon unit cell (Figure 3.1 (b)) and the different crystal planes. Seeds with {001} top-plane can readily be cut perpendicular to the longitudinal direction of the

ingot. The {110}-plane can be accessed by splitting the ingot in the longitudinal direction between two opposite nodes (Figure 3.1 (c)), and the two final {111}- and {211}-planes can be accessed by tilting a half-split ingot 90°- Ω = 54.7° and 35.3°, respectively (Figure 3.1 (d)).

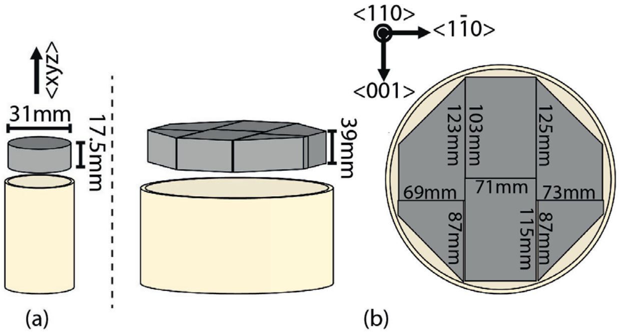

Figure 3.2. (a) Small-scale experiments required single cylindrical seeds with diameters of Ø = 31mm and heights of h = 17.5mm. (b) Due to the large diameter of the crucible (Ø = 250mm) the pilot-scale experiment required six seeds which was cut as square blocks with the dimensions illustrated. The edges of the corner seeds were cut off and adapted to the crucible.

The solidification experiments required different seed geometries depending on the dimensions of the crucibles. Small-scale experiments (Paper P1) were performed in cylindrical crucibles with an inner diameter of Ø = 32mm. The seeds were drilled out by a hollow drill, attaining diameters of Ø = 31mm and a height of h = 17.5mm (Figure 3.2 (a)). In this case, only the direction of the top plane <xyz> was controlled. The more advanced pilot-scale experiment (Paper P2) required multiple seeds due to the size of the crucible (diameter of Ø = 250mm), and these seeds were cut with pre-defined orientations on all faces. The seeds were cut as 39mm thick blocks from {110}-oriented slabs (Figure 3.1 (c)) and placed together in a common seed structure, as illustrated in Figure 3.2 (b). The top plane was cut with a {110}-orientation, while the two sides where cut with {001}- and $\{1\bar{1}0\}$-orientations. The exact seed dimensions are printed in the same figure, with the right-most illustration drawn as a top-view above the seed-structure.

Table 3.2: Procedures for grinding and polishing the surfaces of small-scale and pilot-scale seeds.

Small-scale seeds			Pilot-scale seeds		
Equipment	Size	Time	Equipment	Size	Time
SiC	800 grit	10s	Diamond wheel	D107	120 – 180min
SiC	1200 grit	1min	Diamond wheel	D28	120 – 180min
Diamond suspension	3μm	1min	CP4 etch		4min
Diamond suspension	1μm	1min			

In order to limit the amount of surface damage on the seeds, they went through the grinding and polishing procedure summarized in Table 3.2. Due to their small size, the small-scale seeds could easily be ground and polished manually. The grinding was performed with 800 and 1200 grit SiC paper, while polishing was performed with 3μm and 1μm diamond suspensions. The pilot-scale seeds, on the other hand, were too large to be prepared by this method, and grinding was therefore done with larger automatic grinding equipment (Artech

ASTERA II-2S). Both coarse (D107; FEPA standard) and fine (D28; FEPA standard) grinding wheels were used. Polishing was done chemically, in a CP4 etch ($3HF:5HNO_3:3CH_3COOH$) for 4min.

3.2. CRUCIBLE COATING

Before solidification the crucibles were coated with α-Si_3N_4 coating, made by the following procedure:

1. 50g of α-Si_3N_4 coating powder was put inside a flask containing milling balls.
2. 75ml of distilled water was mixed with 2.5g of Optapix binding agent in a separate beaker. After mixing, it was added to the milling flask.
3. 1g of Darvan dispersing agent was added to the flask and mixed thoroughly.
4. The flask was then put on a ball mill at medium milling speed for at least 18 h.

Two layers of coating was spray-coated onto the inside of the crucible and heat treated at 1100° for 4h.

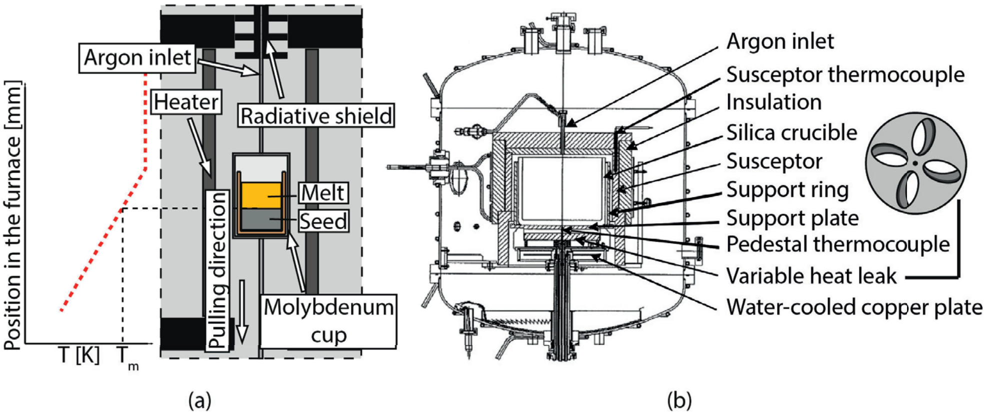

Figure 3.3: (a) The small-scale Bridgman furnace consists of heater elements, a radiative shield and an argon inlet. The crucible is inserted into a molybdenum cup that is pulled out of the hot zone at a given rate. (b) The Vertical Gradient Freeze (VGF) pilot-scale furnace uses a heat leak valve to induce the cooling flux instead.

3.3. SMALL-SCALE SOLIDIFICATION OF MONO-LIKE SILICON

The small-scale ingots were grown in a Bridgman-type furnace illustrated in Figure 3.3 (a), producing ingots with diameters of $Ø = 31$mm and heights up to $h = 60$mm. Coated Al_2O_3 crucibles were filled with seed and feedstock material before being placed inside a molybdenum cup and into the furnace. The cup was used to limit contamination of the melt from the surrounding atmosphere and furnace parts. The cup was carefully positioned at a position p inside the furnace. The exact position depends on both the temperature set point T_{sp} and the pulling speed v, and is given for both solidification regimes in Table 3.3. The crucible was kept at this position for a time t, allowing the feedstock to melt completely and the seed to melt only partially. After the dwell the crucible was pulled downwards in order to move the solidification front upwards and solidify the ingot.

The crucibles were pulled approximately 70mm downwards, resulting in a pulling time of approximately 350min and 35 min for pulling speeds of 0.2mm/min and 2.0mm/min, respectively.

Table 3.3. Growth parameters used for growth of small-scale mono-like ingots at pulling rates v of 0.2 mm/min and 2.0mm/min in the small-scale Bridgman furnace. The position of the molybdenum cup p is held at a temperature of T_{dwell}, for a holding time of t minutes before pulling is initiated.

Temp., T_{dwell} [K]	Cup position, p [mm]	Dwell time, t [min]	Pulling speed, v [mm/min]
1793	360	27	0.2
1793	354	27	2.0

3.4. PILOT-SCALE SOLIDIFICATION OF MONO-LIKE AND HPMC SILICON

The pilot-scale experiments were performed in a Crystalox DS250 directional solidification furnace that is able to produce 12kg ingots with diameters of *Ø*=250mm and heights of *h*=105mm. This is a VGF type furnace that uses a variable heat leak valve in the bottom of the furnace to induce a cooling flux and temperature gradient (Figure 3.3 (b)). The SiO_2-crucibles were coated in α-Si_3N_4 before filling them with the respective seeds and feedstock. The filling of the mono-like silicon experiment is illustrated in Figure 3.4 (a) and consists of a bottom layer of monocrystalline seeds, as previously illustrated in Figure 3.2 (b), which accounted for approximately 3.5kg of the total 12kg, and an 8.5kg top-layer of polysilicon feedstock. The filling of the HPMC silicon experiment is illustrated in Figure 3.4 (b), were the bottom seed-layer is divided into two separate compartments. The two compartments were separated by multicrystalline silicon wafers and separately filled with polysilicon and granular fluidized bed reactor (FBR) material as seeds.

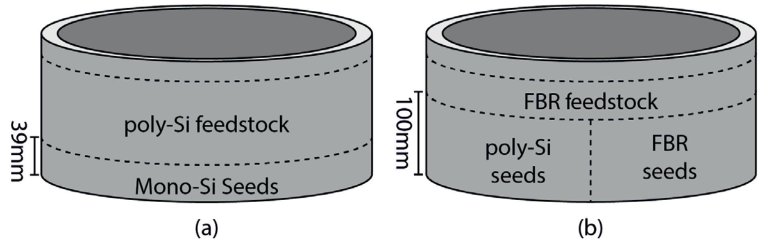

Figure 3.4. The crucibles used for pilot-scale experiments were filled with the respective seeding material and topped off with remaining feedstock in order to achieve a desired 12kg ingot size. (a) The mono-like case consisted of the previously illustrated seeding structure (Figure 3.2 (b)) placed in the bottom of the crucible and polysilicon feedstock on top. The (b) HPMC case consisted of two seeding compartments, filled with polysilicon seed and fluidized bed reactor granules respectively.

The seed volume had a total height of approximately 100mm and accounted for approximately 8.4kg of the total 12kg, and the remaining volume was filled with a 3.6kg top-layer of FBR feedstock.

The solidification parameters for both experiments were optimized in order to prevent complete melting of the respective seed structures (Table 3.4). The furnace was heated to and held at 1803K in order to start the melting process. After the dwell a two-step cooling procedure was initiated, with a relatively fast initial cooling rate the first 60 – 70min followed by a slower cooling rate for the main duration of the solidification process.

Table 3.4. The parameters used for the pilot-scale mono-like and HPMC ingots, including holding temperature and time, and a two-step cooling procedure.

			Cooling step 1		Cooling step 2	
Ingot	Temp., T_{dwell} [K]	Holding time [min]	Rate [K/min]	Time [min]	Rate [K/min]	Time [min]
Mono-like	1803	215	0.95	60	0.31	430
HPMC	1803	170	0.75	70	0.1	400

3.5. CHARACTERIZATION PREPARATION

Defect etching and electron backscatter diffraction (EBSD) require samples with near mirror-like polished surfaces, and samples for investigation had to go through a thorough grinding and polishing procedure. Grinding and polishing were done by SiC paper and diamond suspensions, respectively. The exact time for each step varies considerably with equipment and sample size, but the procedure can be described approximately as in Table 3.5. Note that only one sample was prepared at a time, as preparing multiple wafers at the same time increases the chance of destroying one or more samples during the process.

Table 3.5. The procedure used to prepare samples for defect etching and EBSD. The procedure was performed step-wise from top to bottom. Note that the step-time is only approximate as visual confirmation after each step is also needed.

Step	Equipment	Size	Time
Grinding	SiC paper	320 or 500 grit	10s
	SiC paper	800grit	1 - 2min
	SiC paper	1200grit	1 – 2min
Polishing	Diamond suspension	9µm or 6µm	3 - 4min
	Diamond suspension	3µm	3 – 4min
	Diamond suspension	1µm	4 – 5min

The preparation started with the coarsest 320 grit SiC paper and continued step-wise to a finer grit size. After the 1200 grit paper the samples were transferred onto diamond cloths where they were sequentially polished with 9µm, 3µm and 1µm diamond suspensions. The step-time is only approximate, as the samples had to be visually inspected in-between etch step before moving on to the next step.

3.6. DEFECT ETCHING

Structural defects become visible as etch pits when the samples are exposed to suitable etchants. The etchant will in principle etch the whole sample but, due to atomic distortion and strain fields appearing in the vicinity of defects, the etch rate will be much higher in defected areas than in areas without defects.

There are a large number of different defect etches for silicon, but with the most notable being the hydrofluoric (HF)-based Wright [139], Secco [140] and Sopori [141] etches. While the Wright etch is anisotropic, where the etching rate depends on the crystallographic orientation of the grain, both the Secco and Sopori etches are isotropic, having a etch rate which is independent on the orientation of crystal. This work uses a Sopori etch that consists of a 2:15:36 volume mixture of nitric acid, acetic acid and hydrofluoric acid, respectively, that is known to result in etch pits with geometries influenced by the spatial direction of the defects (as illustrated in Figure 3.5 (a) and (b)). The etch time was optimized to 25s.

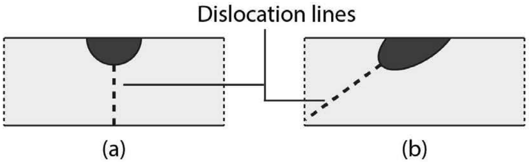

Figure 3.5. The shape of the etch pit groove will depend on the direction of the dislocation line, with a vertical dislocation giving a spherical groove and a tilted dislocation giving an oblong groove.

3.7. SCANNING ELECTRON MICROSCOPY

Scanning Electron Microscopy (SEM) has been frequently used to characterize regions of interest (ROIs) on samples throughout the work. However, due to different sample requirements the SEM parameters had to be adjusted accordingly. The samples investigated in this work can be divided into two groups, depending on material type, i.e. solid silicon or Si_3N_4-coating. Both groups were investigated using the same Zeiss Ultra, 55 Limited Edition FE-SEM microscope, but with different acceleration voltages and working distances. The parameters are summarized in Table 3.6.

Table 3.6. The parameters used for SEM-characterization of solid silicon samples and Si_3N_4-coating.

Parameter	Si characterization	Si_3N_4 characterization
Acceleration voltage	20kV	0.5 – 2.0kV
Aperture size	30µm	30µm
Microscope	Zeiss Ultra, 55 Limited Edition FE-SEM	
Working distance	> 5mm	< 5mm
EDS	-	Quantax EDS

Characterization of solid silicon samples is fairly straight-forward, as the conductivity of the material allows high acceleration voltages (20kV), resulting in good quality micrographs attainable also at high working distances. Silicon nitride (α- and β-Si_3N_4) coating particles, on the other hand were nearly impossible to study at high acceleration voltages due to electrical charging of the particles. In order to minimize the electrical charging to acceptable levels the acceleration voltage had to be reduced below 1kV. At such low voltages the electrons are not able to travel very far, and the working distance had to be correspondingly reduced to 1-3mm.

Energy Dispersive X-Ray spectroscopy (EDS) was also used for qualitative analysis of the composition of Si_3N_4 particles. The elements selected for EDS analysis in this work were carbon (C), nitrogen (N), oxygen (O) and silicon (Si), with respective K-alpha emission lines given Table 3.7. For this reason the acceleration voltage had to be set to minimum 2 kV. This led to an increase in electrical charging, which made the scans unsuitable for high-resolution imaging, but the quality was more than acceptable for analytical purposes.

Table 3.7. Qualitative EDS-investigation of Si_3N_4 coating particles required an acceleration voltage surpassing the K-alpha emission lines of carbon (C), nitrogen (N), oxygen (O) and silicon (Si).

Element	$K_{\alpha 1}$ [keV]	Element	$K_{\alpha 1}$ [keV]
C	0.282	O	0.526
N	0.392	Si	1.74

3.8. ELECTRON BACKSCATTER DIFFRACTION

Microstructural characterization of samples is mainly based on results achieved by Electron Backscatter Diffraction (EBSD). This technique, combined with the EDAX Orientation Microscopy (OIM) Data Analysis tool, enables relatively fast and accurate determination of crystallographic information from a solid material [142]. Typical uses include crystal- and grain orientations, grain relationships and grain boundary character, and statistical data can be extracted with the included analytical modules. The technique uses so-called backscattered electrons, where electrons sent from the SEM electron gun are reflected on the atomic planes of the sample under investigation [143]. Some of these electrons are directed towards the EBSD detector (Figure 3.6 (a)) and form a characteristic Kikuchi pattern that represents the reflecting atomic planes of the sample. In order to maximize the amount of electrons on the phosphorus screen the sample is typically tilted 70° to the horizontal plane. The recorded data are then used to create an orientation map (Figure 3.6 (b)) of a selected area on the sample. The sample coordinates following a scan are usually named the normal direction (ND), the transverse direction (TD) and the reference direction (RD).

The scanning was done with a JEOL JSM840 Scanning Electron Microscope (SEM), equipped with an EBSD detector from Nordif. This tool also supports so-called combo-scanning, which involves a movable stage that can be controlled by the scanning software. With this option enabled, the stage can move the sample in a pre-defined raster and stitch together multiple EBSD maps, allowing for scans of areas up to 40mm x 50mm. Ideal settings for EBSD scans consist of a 70° tilt-angle combined with a working distance of 20mm. However, in order to scan larger areas the settings had to be adjusted to a less than ideal 62° tilt-angle and 32mm working distance. This will reduce the sharpness of the Kikuchi lines, but for silicon samples, the patterns are still more than good enough for the computer to assess. The SEM was set to 20kV, and the step size was in most cases set to approximately 60μm to get a good resolution of the scan.

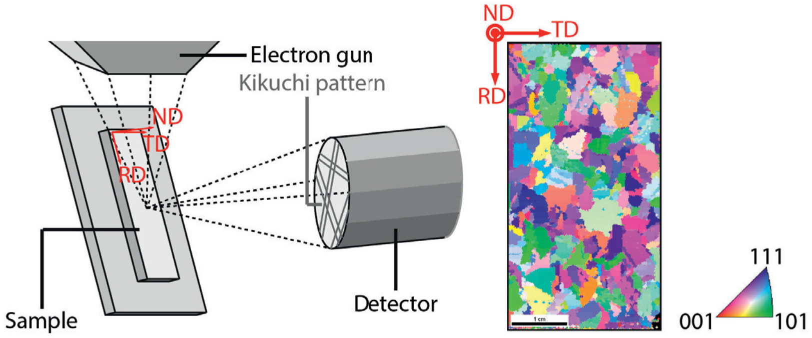

(a) (b)

Figure 3.6. (a) The sample is ideally tilted towards the EBSD detector at an angle of 70° to the horizontal plane. (b) The final scan reveals the grain structure of the sample with different colours representing different crystallographic orientations that are defined by the inverse pole figure.

3.9. X-RAY LAUE SCANNER

Traditional EBSD is not suitable for detecting grain misorientations below 0.5° [144], and even sub-1° misorientations are difficult to detect. Bragg diffraction of X-rays is known to have high sensitivity to crystal orientation, and so-called rocking curve measurements have previously shown to be able to detect misorientations below 0.01° [145]. An X-ray Laue Scanner is considered to hold approximately the same resolution. The scanner consists of a tungsten X-ray tube with a collimator, a motorized sample stage and an X-ray detector (Figure 3.7 (a)), and depending on the chosen collimator the smallest spatial resolution available is 0.3mm. The technique is therefore not suitable for measuring small grains, but for the large grains of the mono-like ingot this method works well.

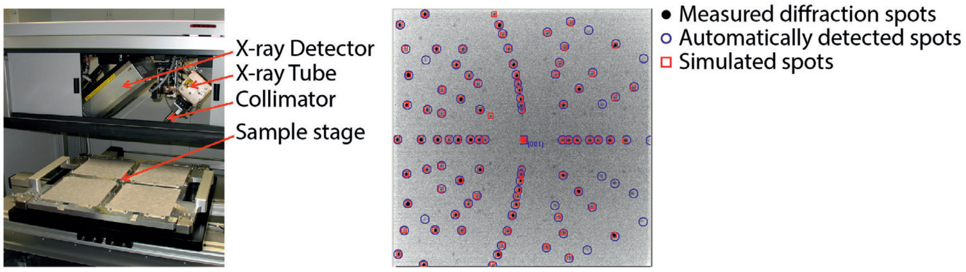

(a) (b)

Figure 3.7. (a) The setup consists of an X-ray tube sending a beam of white X-rays through a collimator onto the sample. Reflected X-rays are recorded by an X-ray detector. (b) The detector records a backscattered diffraction pattern, a so-called Laue pattern, and compares it to a simulated one. Both images are reproduced from [146].

The technique has been described in detail in [146] and will only be briefly summarized. A grain detector scans the sample for grains, and the X-ray spot will automatically move between the different grains. Depending on the orientation of the measured spot, the white X-ray beam creates a backscatter diffraction pattern of all possible lattice plane families. The measured Laue Pattern (Figure 3.7 (b)) is compared to a second Laue pattern achieved by simulation, and the correct orientation can be obtained if 97% of the spots of the measured pattern coincide with the spots from the simulated pattern. Aided by the recorded Laue pattern, an orientation matrix was calculated for each of the six grains in the mono-like ingot. These matrices was then be used to calculate the misorientation values reported in Paper P2 by using the procedure given in Appx. A.

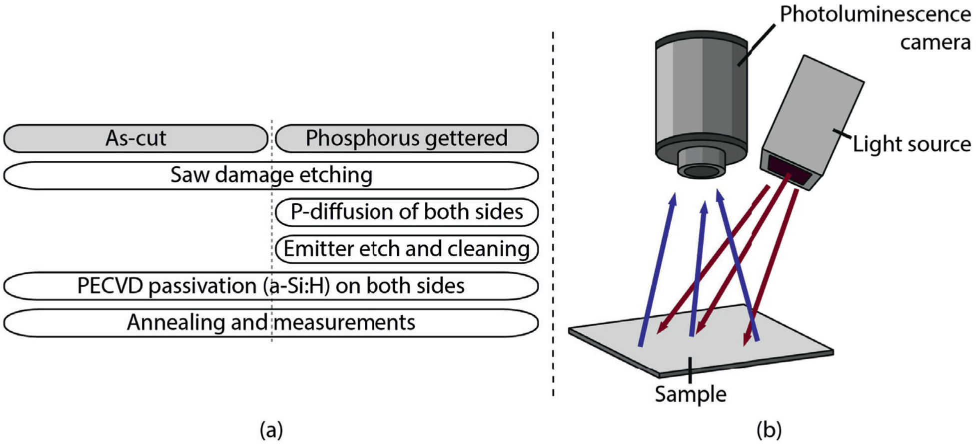

Figure 3.8. The work sheet used for preparation and phosphorus gettering of samples to be investigated for minority carrier lifetimes. Reproduced from e.g. [147]. (b) The lifetime measurements were done by photoluminescence, in which a light source irradiates the sample and a camera detects luminescence emission from the sample.

3.10. PHOTOLUMINESCENCE IMAGING

Photoluminescence imaging has been used for measuring the minority carrier lifetime of wafers cut from the mono-like ingot (P2) and the HPMC ingot (P3), and for measuring the concentration of interstitial iron in wafers cut from the HPMC ingot (Appx. B).

Minority carrier lifetime:

The minority carrier lifetime τ is a measure on how long a carrier is likely to be in its free state before recombining, and is typically measured on neighbouring as-cut and phosphorus gettered wafers. As phosphorus gettering reduce the amount of metallic impurities in the samples, it is not unusual to observe a considerable increase in minority carrier lifetime after this process. Typical preparations of neighbouring wafer-pairs are shown in Figure 3.8 (a) [147]. Both samples went through an initial saw damage etch, in order to chemically polish the surface of the samples, before one of the samples was exposed to phosphorus gettering, consisting of a phosphorus diffusion step and an emitter etching step. The final step before lifetime measurements consisted of passivating the surfaces of the wafers by deposition of amorphous silicon and annealing them for 1min at 450°.

The actual minority carrier lifetime measurements were done by a BT Imaging LIS-R1 photoluminescence (PL) imaging system, and the measured photoluminescence intensities were calibrated by Quasi Steady State Photoconductivity (QSSPC), as described in e.g. [148]. Compared to other techniques, such as the microwave photoconductance decay (μ-PCD) technique, PL offers superior speed and spatial resolution. The method is also contactless and non-destructive. Optical excitation by a light source stimulates luminescence emission from the sample, which is captured by an infrared photoluminescence camera (Figure 3.8 (b)). The conversion of PL intensities into lifetime values is done by coupling the intensities with QSSPC measurements [149].

Mapping of interstitial iron:

Interstitial iron can also be mapped by using photoluminescence imaging. The method has been developed at ISE Fraunhofer in Germany, and consists of an "in-house" built multitool for photoluminescence imaging and a Quasi Steady State Photoluminescence (QSSPL) for exact calibration of the photoluminescence intensity. A detailed description of the procedure can be found in e.g. [150].

The method is based on the fact that iron point defects can occur in two different chemical states, with different electrical parameters. By storing the sample in the dark, interstitial iron (Fe_i) atoms will form FeB-pairs with dopant boron, and by re-exposing the sample to light the FeB-pairs will split back. The minority carrier lifetimes is measured in both states separately, at equally low injection conditions, and allows for calculation of the iron point defect concentration in boron-doped silicon wafers,

$$[Fe_i] = C(\Delta n)(\frac{1}{\tau_{Fe(i)}} - \frac{1}{\tau_{FeB}}) \qquad \text{(Equation 3.1)}$$

where $\tau_{Fe(i)}$ is the lifetime measured in the Fe_i-state, τ_{FeB} the lifetime in the FeB-state and $C(\Delta n)$ a factor depending on Shockley-Read-Hall pre-factors, Auger recombination and radiative recombination. Fe_i dominates at low injection levels while other defects dominate at 1 sun. The fraction of the total recombination caused by the existence of interstitial iron in the material ($FoR_{Fe(i)}$) can then be calculated by the following formula,

$$FoR_{Fe(i)} = \frac{\tau_{Fe(i)}}{\tau_{SRH,Fe(i)}} \qquad \text{(Equation 3.2)}$$

where $\tau_{SRH,Fe(i)}$ is the calculated lifetime associated with trap-assisted recombination, commonly known as Shockley-Read Hall recombination [46]. Note that the lower detection limit for Fei is approximately 10^{10}cm^{-3}, and values below this should be treated with care.

The actual procedure can be described as following:

1. Sample passivation.
   The measurements required surface passivated samples, e.g. by amorphous silicon.

2. Preparation of the FeB-state.
   This was done by annealing the sample at 353K in the dark for approximately 15min.

3. Photoluminescence image in the FeB-state (0.01/0.1 sun).
   The image was taken over a time span of 60 sec at a low injection level of 0.01/0.1 sun.

4. FeB splitting.
   In order to prepare the sample for the Fe_i-state, it was illuminated by a laser at max intensity (39.9A) for approximately 3 min. The laser was then set to be stabilized at a low injection level, by reducing the intensity of the laser to 0.01/0.1 sun for 120 sec.

5. Photoluminescence image in the Fe_i-state (0.01/0.1 sun).
   The image was taken over a time span of 60 sec at a low injection level of 0.01/0.1 sun.

6. Second photoluminescence image in the Fe_i-state (1 sun).
   The laser intensity was increased to 1 sun and after waiting 1-2 min for stabilization the image was taken over a time span of 0.2 sec.

7. Charge carrier lifetime measurements by QSSPL.
   In order to convert the photoluminescence intensity map into a lifetime map, a calibration factor was needed. The calibration factor was obtained by QSSPL at 1 sun and could be used for all injection levels.

8. Reflectivity and doping concentration measurements.
   In order to calculate the correct lifetime map both the reflectivity and doping concentration was needed.

9. Calculation of the Fe_i concentration map.
   The photoluminescence images were calibrated towards the QSSPL measurements and the Fei concentration map was calculated using Matlab.

4. CONCLUDING REMARKS AND FUTURE WORK

The final solar cell performance of multicrystalline silicon strongly depends on the microstructural properties achieved during solidification. As the foundations for the material microstructure are established already during the earliest stages of solidification, either during and/or shortly after nucleation, this work has targeted multiple approaches for controlling the initial growth conditions of directional solidification, and studied their effect on the final material properties.

The most common way to modify the initial microstructure of the ingot is by seeding. Both monocrystalline and multicrystalline materials can be used for seeding purposes, but they lead to very different microstructural characteristics of the final ingot. The microstructure will to a large extent reflect the default microstructure of the seed particles, meaning that monocrystalline seeds lead to a near-monocrystalline, or mono-like, microstructure, while fine-grained multicrystalline seeds lead to a more refined multicrystalline microstructure. Both methods have shown to improve the material characteristics, and to be applicable to industrial scales, but there are several new challenges and limitations that need to be addressed in order to utilize their full potential.

This work reveals two main challenges with the mono-like method, namely i) the parasitic grain structure developing from the periphery of the ingot, which reduces the fraction of monocrystalline material in the ingot, and ii) dislocation sources appearing, due to the necessary use of multiple seeds for larger crucibles.
Even though initial nucleation on the crucible bottom is avoided, random nucleation can still, and most definitively does, take place on the crucible wall during growth. These nuclei tend to grow inwards, into the interior of the ingot, at the expense of the monocrystal, and are therefore unwanted. On the other hand, we have also seen that a peripheral grain structure can limit dislocation propagation from the ingot periphery, suggesting that a well-designed peripheral grain structure, in fact, can be advantageous for the final device performance.

However, this work suggests that the most detrimental issues with the mono-like method are related to the formation of small-angle grain boundaries at the junctions between two or more seed crystals, and the large amount of accompanying dislocations. While dislocations generated at stress-points can be minimized by proper seed preparation, and by introducing small gaps between the seeds, the dislocation structures generated due to seed misorientation can become very detrimental for the material. On the contrary, further investigations suggest that the extent of these structures not only depends on the magnitude of the misorientation but also on its complexity. Different misorientations generate different dislocation types that again may interact differently with each other, the boundary plane and the silicon lattice, and, by gaining a better understanding of the mechanisms governing the dislocation behaviour at these junctions, one may be able to limit their advance. Mathematical models like Frank's formula and/or the more advanced O-Lattice theory may prove useful in such an assessment. The evolution of small-angle grain boundaries is not only interesting for mono-like silicon, but also for a more general understanding of dislocation behaviour in silicon. Such studies should, however, be supported by microscopic studies, e.g. by Transmissions Electron Microscopy (TEM).

While the mono-like method targets to eliminate both grain boundaries and dislocations, the high performance method sets out on utilizing certain properties of random angle grain boundaries to terminate the propagation of dislocation clusters. All in all, decorated grain boundaries are generally found to be less detrimental than decorated dislocation clusters, and one therefore typically observes a lower recombination activity in this type of material, compared to conventional multicrystalline silicon. High-performance multicrystalline silicon is usually seeded by very fine-grained seeds that also have a very high initial content of random angle grain boundaries, e.g. in the form of polysilicon (poly-Si) or fluidized bed reactor (FBR) material. There appears to be some potential for smaller grains by using larger poly-Si chips, as there is a considerable coarsening of the default as-grown microstructure of FBR seeds during directional solidification. However, this potential can only be fully utilized if one can prevent melt from penetrating below the main seed interface. On the contrary, the more uniformly shaped FBR seed-material appear to be more favourable in terms of dislocation generation, as it contains less morphological extremities for stress development. The mechanism behind the coarsening is currently unknown, but it is reasonable to believe that large and uniformly shaped seed particles may be beneficial, both for securing a fine-grained ingot microstructure and minimizing the dislocation generation.
The dependence upon small grains and a high grain boundary density does, however, challenge the future potential of the method. Reducing the recombination activity at grain boundaries will therefore be essential for realizing further lifetime improvements in this type of material, either through advances in the gettering process or through better impurity control during solidification.

Even though seeding with pre-defined silicon crystals has shown to be a relatively simple method to tune the microstructure of the final ingot, the importance of understanding the actual nucleation mechanisms should not be underestimated, which we believe can lead to even more attractive production methods in the future. The added costs related to production and design of seed material can also be avoided if similar microstructures can be achieved without seeding.

This work suggests that the free growth model, initially developed for grain refinement in aluminium melts, also may be appropriate for understanding nucleation phenomena that occurs during directional solidification of silicon. The model especially focuses on the size distribution of the underlying substrate particles, i.e. coating particles, and that initial nucleation occurs at very low undercoolings rather than several tens of degrees, as commonly reported in literature. The nucleation undercooling will be affected by the crystallographic mismatch between the solid silicon nucleus and the substrate particle. However, as long as parameters that differentiate nucleation conditions within a single coating material are only partially understood, the value of comparing different coating materials is relatively limited. Especially for highly potent substrate particles, such as Si_3N_4, where the energy required for adsorption from the melt is low, other parameters have to be responsible for the large variations observed for the nucleation undercooling in literature.

This work supports the idea that the nucleation conditions in a crucible coated with α-Si_3N_4 are largely independent of the coating properties, as experimental observations suggest that α-Si_3N_4 particles dissolve and reprecipitate as larger and thereby more favourable β-Si_3N_4 particles. It is important to note that we do not exclude nucleation on α-Si_3N_4 particles, as they, in fact, have similar crystallography and mismatch to silicon, and the preference towards β-Si_3N_4 is suggested to be mainly related to the larger particle size.

The clear signs of dendritic growth in all bottom cuts investigated indicate that dendrites play an important role also during directional solidification of multicrystalline silicon. Dendrites will lead to a coarsening of the grain structure, and should be avoided if a finer grain structure is desired, e.g. by utilizing a combination of slow cooling and a uniform distribution of large Si_3N_4 particles. Proper engineering of the Si_3N_4 particles together with certain cooling parameters may also prove useful for achieving other microstructures, and is something that should be studied further. Further work may therefore include studying the nucleation undercooling and microstructure as a function of particle size, where the particle size may be tailored, e.g. by utilizing different holding time of the melt before solidification, or by pre-defining the size of the β-Si_3N_4 particles, e.g. by sieving. If possible, one should try to detect any preference for the different crystallographic facets of the substrate particles. Finding a direct correlation between the crystallography of the facets and the silicon nucleus will be of interest, as this would imply that the initial grain structure may depend on the spatial orientation of the substrate particles. The support of TEM will be essential in such studies.

Structure control is a complex subject with several open questions and challenges. In this work we have clarified some of the issues, and pointed out the key role of understanding the earliest stages of solidification. One may argue that the ultimate goal for structure control is to achieve a complete monocrystalline microstructure with no defects. As introducing only a single nucleation event seems to be a bit farfetched, the only way to achieve this will be through improvements in the mono-like method. On the other hand, if a finer grain structure is to be viable also in the future, one should be able to attain this without being dependent on silicon seeding. For this, seeking knowledge that already exist within grain refinement of aluminium may prove useful also for silicon production. Precipitates are, however, generally unwanted in solar cell silicon and grain refinement in its traditional form is therefore uninteresting. Alternative grain refinement processes, with the coating material as a starting point, should therefore be studied, which further emphasises the importance of understanding the processes taking place on the coating material and proper knowledge of nucleation theory.

BIBLIOGRAPHY

[1] Secretariat PR. Renewables 2015 Global Status Report. Renewables 2015 Global Status Report, (2015).

[2] Agency IE. World Energy Outlook 2014 Factsheet. World Energy Outlook 2014 Factsheet, (2014).

[3] Fraunhofer Institute for Solar Energy Systems I. Presentation: Photovoltaics Report, August 2015. (2015).

[4] PVInsights.com [cited 2015 August].

[5] Sopori B, Li C, Narayanan S, Carlson D. Efficiency limitations of multicrystalline silicon solar cells due to defect clusters. Semiconductor Defect Engineering-Materials, Synthetic Structures and Devices **864**, 233 (2005).

[6] Ervik T. Dislocations in directionally solidified crystalline silicon [Doctoral Thesis]: Norwegian University of Science and Technology; 2013.

[7] Brynjulfsen I, Arnberg L. Nucleation of silicon on Si3N4 coated SiO2. J Cryst Growth **331**, 64 (2011).

[8] Safarian J, Tranell G, Tangstad M. Processes for upgrading metallurgical grade silicon to solar grade silicon. Technoport 2012 - Sharing Possibilities and 2nd Renewable Energy Research Conference (Rerc2012) **20**, 88 (2012).

[9] Hull D, Bacon DJ. Introduction to dislocations. 4th ed. Oxford Oxfordshire ; Boston: Butterworth-Heinemann; 2001. vii p.

[10] Moller HJ, Funke C, Rinio M, Scholz S. Multicrystalline silicon for solar cells. Thin Solid Films **487**, 179 (2005).

[11] Nordmark H. Microstructure studies of silicon for solar cells: Norwegian University of Science and Technology; 2009.

[12] Tan TY, Tice WK. Oxygen Precipitation and Generation of Dislocations in Silicon. Philos Mag **34**, 615 (1976).

[13] Schmid E, Wurzner S, Funke C, Galindo V, Patzold O, Stelter M. The effect of the growth rate on the microstructure of multi-crystalline silicon. J Cryst Growth **359**, 77 (2012).

[14] Odland I, Stokkan G. Mechanisms for Formation of Dislocations near the Bottom of a Multicrystalline Silicon Ingot. Proceedings of the 4th International Workshop on Science and Technology of Crystalline Silicon Solar Cells, (2010).

[15] Ervik T, Stokkan G, Buonassisi T, Mjos O, Lohne O. Dislocation foimation in seeds for quasi-monocrystalline silicon for solar cells. Acta Materialia **67**, 199 (2014).

[16] Stokkan G, Hu Y, Mjos O, Juel M. Study of evolution of dislocation clusters in high performance multicrystalline silicon. Sol Energ Mat Sol C **130**, 679 (2014).

[17] Ervik T, Kivambe M, Stokkan G, Ryningen B, Lohne O. Dislocation formation at Sigma=27a boundaries in multicrystalline silicon for solar cells. Proceedings of the 26th EUPVSEC, (2011).

[18] Di Sabatino M, Stokkan G. Defect generation, advanced crystallization, and characterization methods for high-quality solar-cell silicon. Phys Status Solidi A **210**, 641 (2013).

[19] Ryningen B, Stokkan G, Kivambe M, Ervik T, Lohne O. Growth of dislocation clusters during directional solidification of multicrystalline silicon ingots. Acta Materialia **59**, 7703 (2011).

[20] Kivambe M. Dislocations in multicrystalline silicon for solar cells [Doctoral Thesis]: Norwegian University of Science and Technology; 2012.

[21] Kivambe M, Stokkan G, Ervik T, Ryningen B, Lohne O. TEM Characterization of Near Sub-Grain Boundary Dislocations in Directionally Solidified Multicrystalline Silicon. Gettering and Defect Engineering in Semiconductor Technology Xiv **178-179**, 307 (2011).

[22] Takahashi I, Usami N, Kutsukake K, Stokkan G, Morishita K, Nakajima K. Generation mechanism of dislocations during directional solidification of multicrystalline silicon using artificially designed seed. J Cryst Growth **312**, 897 (2010).

[23] Kveder V, Kittler M, Schroter W. Recombination activity of contaminated dislocations in silicon: A electron-beam-induced current contrast behavior. Phys Rev B **63**, (2001).

[24] Hirth JP, Lothe J. Theory of dislocations. 2nd ed. Malabar, FL: Krieger Pub. Co.; 1992. xii p.

[25] Hornstra J. Dislocations in the Diamond Lattice. J Phys Chem Solids **5**, 129 (1958).

[26] Jacques A, Vallino F, Serbena F, George A. Dislocation multiplication in silicon at the onset of plasticity observed by in situ synchrotron x-ray topography. J Phys-Condens Mat **12**, 10045 (2000).

[27] Seitz F, Turnbull D, Ehrenreich H. Solid State Physics1969.

[28] Dhanaraj G. Springer handbook of crystal growth. Heidelberg ; New York: Springer; 2010. xxxviii p.

[29] Kivambe MM, Stokkan G, Ervik T, Ryningen B, Lohne O. The microstructure of dislocation clusters in industrial directionally solidified multicrystalline silicon. J Appl Phys **110**, (2011).

[30] Green D, Glaenzer RH, Jordan AG, Noreika AJ. Observation of Paralled Arrays of Pure Edge Dislocations in Silicon. J Appl Phys **39**, 2937 (1968).

[31] Vogel FL. On the Orientation Effect in the Polygonization of Bent Silicon Crystals. Acta Metall Mater **6**, 532 (1958).

[32] Ervik T, Kivambe M, Stokkan G, Ryningen B, Lohne O. High temperature annealing of bent multicrystalline silicon rods. Acta Materialia **60**, 6762 (2012).

[33] Booker GR, Stickler R. Dislocations in Mechanically Deformed Ge. Acta Metall Mater **10**, 993 (1962).

[34] Hill MJ, Rowcliff.Dj. Deformation of Silicon at Low-Temperatures. J Mater Sci **9**, 1569 (1974).

[35] Stickler R, Booker GR. Surface Damage on Abraded Silicon Specimens. Philos Mag **8**, 859 (1963).

[36] Dashevsky MY, Eidenson AM, Kazimtrov NI, Khatsernov MA. Low-angle Boundary Investigation in Silicon Single Crystals. Kristall Und Technik-Crystal Research and Technology **11**, 775 (1976).

[37] Rabier J, Pizzagalli L, Demenet JL. Dislocations in Silicon at High Stress. Dislocations in Solids **16**, 47 (2010).

[38] Stokkan G, Stoss A, Kivambe M, Ervik A, Ryningen B, Lohne O. Distribution of grain boundary types in multicrystalline silicon. 28th European Photovoltaic Solar Energy Conference and Exhibition, 1418 (2013).

[39] Stokkan G. Relationship between dislocation density and nucleation of multicrystalline silicon. Acta Materialia **58**, 3223 (2010).

[40] Autruffe A. Silicon directional solidification: Impurity segregation and defects [Doctoral Thesis]: Norwegian Univeristy of Science and Technology; 2014.

[41] Stokkan G. Twinning in multicrystalline silicon for solar cells. J Cryst Growth **384**, 107 (2013).

[42] Autruffe A, Hagen VS, Arnberg L, Di Sabatino M. Dislocation generation at near-coincidence site lattice grain boundaries during silicon directional solidification. J Cryst Growth **411**, 12 (2015).

[43] Trempa M, Reimann C, Friedrich J, Muller G, Krause A, Sylla L, et al. Influence of grain boundaries intentionally induced between seed plates on the defect generation in quasi-mono-crystalline silicon ingots. Cryst Res Technol **50**, 124 (2015).

[44] Kohyama M, Yamamoto R, Doyama M. Structures and Energies of Symmetrical [011] Tilt Grain-Boundaries in Silicon. Physica Status Solidi B-Basic Research **137**, 11 (1986).

[45] Kittler M, Seifert W, Knobloch K. Influence of contamination on the electrical activity of crystal defects in silicon. Microelectron Eng **66**, 281 (2003).

[46] Green MA. Solar cells : operating principles, technology, and system applications. Englewood Cliffs, NJ: Prentice-Hall; 1982. xiv p.

[47] Rohatgi A, Davis JR, Hopkins RH, Mcmullin PG. A Study of Grown-in Impurities in Silicon by Deep-Level Transient Spectroscopy. Solid State Electron **26**, 1039 (1983).

[48] Bentzen A, Holt A, Kopecek R, Stokkan G, Christensen JS, Svensson BG. Gettering of transition metal impurities during phosphorus emitter diffusion in multicrystalline silicon solar cell processing. J Appl Phys **99**, (2006).

[49] McHugo SA. Release of metal impurities from structural defects in polycrystalline silicon. Appl Phys Lett **71**, 1984 (1997).

[50] Chen J, Sekiguchi T, Yang D, Yin F, Kido K, Tsurekawa S. Electron-beam-induced current study of grain boundaries in multicrystalline silicon. J Appl Phys **96**, 5490 (2004).

[51] Chen J, Sekiguchi T, Xie R, Ahmet P, Chikyo T, Yang D, et al. Electron-beam-induced current study of small-angle grain boundaries in multicrystalline silicon. Scripta Mater **52**, 1211 (2005).

[52] Castellanos S, Kivambe M, Hofstetter J, Rinio M, Lai B, Buonassisi T. Variation of dislocation etch-pit geometry: An indicator of bulk microstructure and recombination activity in multicrystalline silicon. J Appl Phys **115**, (2014).

[53] Kurz W, Fisher DJ. Fundamentals of solidification. 4th rev. ed. Uetikon-Zuerich, Switzerland ; Enfield, N.H.: Trans Tech Publications; 1998. 305 p. p.

[54] Inatomi Y, Onishi F, Nagashio K, Kuribayashi K. Density and thermal conductivity measurements for silicon melt by electromagnetic levitation under a static magnetic field. Int J Thermophys **28**, 44 (2007).

[55] Turnbull D, Vonnegut B. Nucleation Catalysis. Ind Eng Chem **44**, 1292 (1952).

[56] Kelton K, Greer AL. Nucleation in Condensed Matter: Applications and Materials and Biology: Pergamon; 2010.

[57] Kim WT, Cantor B. An Adsorption Model of the Heterogeneous Nucleation of Solidification. Acta Metallurgica Et Materialia **42**, 3115 (1994).

[58] Cantor B. Heterogeneous nucleation and adsorption. Philos T Roy Soc A **361**, 409 (2003).

[59] Greer AL, Bunn AM, Tronche A, Evans PV, Bristow DJ. Modelling of inoculation of metallic melts: Application to grain refinement of aluminium by Al-Ti-B. Acta Materialia **48**, 2823 (2000).

[60] Maxwell I, Hellawell A. Simple Model for Grain Refinement during Solidification. Acta Metall Mater **23**, 229 (1975).

[61] Fujiwara K, Pan W, Sawada K, Tokairin M, Usami N, Nose Y, et al. Directional growth method to obtain high quality polycrystalline silicon from its melt. J Cryst Growth **292**, 282 (2006).

[62] Soiland AK, Ovrelid EJ, Engh TA, Lohne O, Tuset JK, Gjerstad O. SiC and Si3N4 inclusions in multicrystalline silicon ingots. Mat Sci Semicon Proc **7**, 39 (2004).

[63] Chen N, Liu BF, Qiu SY, Liu GH, Du GP. Study of SiC and Si3N4 inclusions in industrial multicrystalline silicon ingots grown by directional solidification method. Mat Sci Semicon Proc **13**, 231 (2010).

[64] Lotnyk A, Bauer J, Breitenstein O, Blumtritt H. A TEM study of SIC particles and filaments precipitated in multicrystalline Si for solar cells. Sol Energ Mat Sol C **92**, 1236 (2008).

[65] Heine V, Cheng C, Needs RJ. The Preference of Silicon-Carbide for Growth in the Metastable Cubic Form. J Am Ceram Soc **74**, 2630 (1991).

[66] Jennings HM, Danforth SC, Richman MH. Microstructural Analysis of Reaction-Bonded Silicon-Nitride. Metallography **9**, 427 (1976).

[67] Mjøs ØS, G.; Søiland, A. K.; Arnberg, L. . Mapping of Silicon Carbide and Silicon Nitride Precipitates on Chemical-Mechanically Polished mc-Silicon Wafers. European PV Solar Energy Conference and Exhibition 2014, (2004).

[68] Reimann C, Trempa M, Friedrich J, Muller G. About the formation and avoidance of C and N related precipitates during directional solidification of multi-crystalline silicon from contaminated feedstock. J Cryst Growth **312**, 1510 (2010).

[69] Hatayama T, Tarui Y, Fuyuki T, Matsunami H. Low-Temperature Heteroepitaxial Growth of Cubic Sic on Si Using Hydrocarbon Radicals by Gas-Source Molecular-Beam Epitaxy. J Cryst Growth **150**, 934 (1995).

[70] Freitas JA, Bishop SG, Edmond JA, Ryu J, Davis RF. Photoluminescence Spectroscopy of Ion-Implanted 3c-Sic Grown by Chemical Vapor-Deposition. J Appl Phys **61**, 2011 (1987).

[71] Kuwabara A, Matsunaga K, Tanaka I. Lattice dynamics and thermodynamical properties of silicon nitride polymorphs. Phys Rev B **78**, (2008).

[72] Brynjulfsen I. Nucleation and Early Growth of Multicrystalline Solar Cell Silicon [Doctoral Thesis]. Trondheim: Norwegian University of Science and Technology; 2012.

[73] Wang L, Wang XS, Tang JC, Cue N. Investigation of Si and Ge growth on Si3N4/Si. Mater Charact **48**, 189 (2002).

[74] Yamabe N, Yamamoto Y, Ohachi T. Epitaxial growth of beta-Si3N4 by the nitridation of Si with adsorbed N atoms for interface reaction epitaxy of double buffer AlN(0001)/beta-Si3N4/Si(111). Physica Status Solidi C: Current Topics in Solid State Physics, Vol 8, No 5 **8**, (2011).

[75] Pupazan V, Negrila R, Bunoiu O, Nicoara I, Vizman D. Effects of crucible coating on the quality of multicrystalline silicon grown by a Bridgman technique. J Cryst Growth **401**, 720 (2014).

[76] Croll A, Lantzsch R, Kitanov S, Salk N, Szofran FR, Tegetmeier A. Melt-crucible wetting behavior in semiconductor melt growth systems. Cryst Res Technol **38**, 669 (2003).

[77] Wald FW. Crystals: Growth, Properties and Applications. 5th edition ed. Berlin: Springer; 1981.

[78] Sangiorgi R, Muolo ML, Chatain D, Eustathopoulos N. Wettability and Work of Adhesion of Nonreactive Liquid-Metals on Silica. J Am Ceram Soc **71**, 742 (1988).

[79] O'Donnell T, Leipold M, Hagan M. Compatibility Studies of Various Refractory Materials in Contact with Molten Silicon. DOE/JPL-1012-77/6, (1978).

[80] Li JG, Hausner H. Influence of Oxygen Partial Pressure on the Wetting Behaviour of Silicon Nitride by Molten Silicon. J Eur Ceram Soc **9**, 101 (1992).

[81] Li JG, Hausner H. Wettability of Silicon-Carbide by Gold, Germanium and Silicon. J Mater Sci Lett **10**, 1275 (1991).

[82] Whalen TJ, Anderson AT. Wetting of Sic, Si3n4, and Carbon by Si and Binary Si Alloys. J Am Ceram Soc **58**, 396 (1975).

[83] Barsoum MW, Ownby PD. Surfaces and Interfaces in Ceramic and Ceramic-Metal Systems. New York: Plenum Press; 1981.

[84] Drevet B, Pajani O, Eustathopoulos N. Wetting, infiltration and sticking phenomena in Si3N4 releasing coatings in the growth of photovoltaic silicon. Sol Energ Mat Sol C **94**, 425 (2010).

[85] Brynjulfsen I, Bakken A, Tangstad M, Arnberg L. Influence of oxidation on the wetting behavior of liquid silicon on Si3N4-coated substrates. J Cryst Growth **312**, 2404 (2010).

[86] Martin C, Ndzogha C, Rancoule G, Grygowski J. Development of various crucible coating concepts for crystallization of multi crystalline silicon ingots. Proceedings of the 23rd European Photovoltaic Solar Energy Conference and Exhibition, EUPVSEC, (2008).

[87] Nikolopoulos P, Agathopoulos S, Angelopoulos GN, Naoumidis A, Grubmeier H. Wettability and Interfacial Energies in Sic-Liquid Metal Systems. J Mater Sci **27**, 139 (1992).

[88] Brynjulfsen I, Fujiwara K, Usami N, Amberg L. Growth velocity and grain size of multicrystalline solar cell silicon. J Cryst Growth **356**, 17 (2012).

[89] Li WJ, Shi EW, Zhong WZ, Yin ZW. Growth mechanism and growth habit of oxide crystals. J Cryst Growth **203**, 186 (1999).

[90] Appapillai AT, Sachs C, Sachs EM. Nucleation properties of undercooled silicon at various substrates. J Appl Phys **109**, (2011).

[91] Tsoutsouva MG, Duffar T, Garnier C, Fournier G. Undercooling measurement and nucleation study of silicon droplet solidification. Cryst Res Technol **50**, 55 (2015).

[92] Li D, Herlach DM. High undercooling of bulk molten silicon by containerless processing. Europhys Lett **34**, 423 (1996).

[93] Beaudhuin M, Zaidat K, Duffar T, Lemiti M. Nitrogen reaction with silicon: Investigation of Si undercooling and Si3N4 growth. J Cryst Growth **336**, 77 (2011).

[94] Beaudhuin M, Chichignoud G, Bertho P, Duffar T, Lemiti M, Zaidat K. Carbon reaction with levitated silicon - Experimental and thermodynamic approaches. Mater Chem Phys **133**, 284 (2012).

[95] Alphei L, Braun A, Becker V, Feldhoff A, Becker JA, Wulf E, et al. Crystallization of supercooled silicon droplets initiated through small silicon nitride particles. J Cryst Growth **311**, 1250 (2009).

[96] Bonzel HP. 3D equilibrium crystal shapes in the new light of STM and AFM. Phys Rep **385**, 1 (2003).

[97] Fujiwara K. Crystal Growth Behaviors of Silicon during Melt Growth Processes. Int J Photoenergy **2012**, 1 (2012).

[98] Eaglesham DJ, White AE, Feldman LC, Moriya N, Jacobson DC. Equilibrium Shape of Si. Phys Rev Lett **70**, 1643 (1993).

[99] Tokairin M, Fujiwara K, Kutsukake K, Usami N, Nakajima K. Formation mechanism of a faceted interface: In situ observation of the Si(100) crystal-melt interface during crystal growth. Phys Rev B **80**, (2009).

[100] Fujiwara K, Gotoh R, Yang XB, Koizumi H, Nozawa J, Uda S. Morphological transformation of a crystal-melt interface during unidirectional growth of silicon. Acta Materialia **59**, 4700 (2011).

[101] Duffar T, Nadri A. On the twinning occurrence in bulk semiconductor crystal growth. Scripta Mater **62**, 955 (2010).

[102] Di Sabatino M, Juel M, Arnberg L, Syvertsen M, Tranell G. Control of grain size and -orientation in multi-crystalline silicon ingots. T Indian I Metals **62**, 511 (2009).

[103] Willeke G, Weber ER. Semiconductors and Semimetals: Advances in Photovoltaics, Part 4: Elsevier Inc; 2015.

[104] Stokkan G, Riepe S, Lohne O, Warta W. Spatially resolved modeling of the combined effect of dislocations and grain boundaries on minority carrier lifetime in multicrystalline silicon. J Appl Phys **101**, (2007).

[105] Sopori B, Wei C, Yi Z, Madjdpour J. High-speed mapping of grown-in defects and their influence in large-area silicon photovoltaic devices. J Cryst Growth **210**, 346 (2000).

[106] Hartman K, Bertoni M, Serdy J, Buonassisi T. Dislocation density reduction in multicrystalline silicon solar cell material by high temperature annealing. Appl Phys Lett **93**, (2008).

[107] Choi HJ, Bertoni MI, Hofstetter J, Fenning DP, Powell DM, Castellanos S, et al. Dislocation Density Reduction During Impurity Gettering in Multicrystalline Silicon. Ieee J Photovolt **3**, 189 (2013).

[108] Reimann C, Friedrich J, Meissner E, Oriwol D, Sylla L. Response of as grown dislocation structure to temperature and stress treatment in multi-crystalline silicon. Acta Materialia **93**, 129 (2015).

[109] Yeh KM, Hseih CK, Hsu WC, Lan CW. High-quality multi-crystalline silicon growth for solar cells by grain-controlled directional solidification. Prog Photovoltaics **18**, 265 (2010).

[110] Usami N, Yokoyama R, Takahashi I, Kutsukake K, Fujiwara K, Nakajima K. Relationship between grain boundary structures in Si multicrystals and generation of dislocations during crystal growth. J Appl Phys **107**, (2010).

[111] Wang TY, Hsu SL, Fei CC, Yei KM, Hsu WC, Lan CW. Grain control using spot cooling in multi-crystalline silicon crystal growth. J Cryst Growth **311**, 263 (2009).

[112] Yang YM, Yu A, Hsu B, Hsu WC, Yang A, Lan CW. Development of high-performance multicrystalline silicon for photovoltaic industry. Prog Photovoltaics **23**, 340 (2015).

[113] Kutsukake K, Abe T, Usami N, Fujiwara K, Morishita K, Nakajima K. Formation mechanism of twin boundaries during crystal growth of silicon. Scripta Mater **65**, 556 (2011).

[114] Nakajima K, Murai R, Morishita K, Kutsukake K, Usami N. Growth of multicrystalline Si ingots using noncontact crucible method for reduction of stress. J Cryst Growth **344**, 6 (2012).

[115] Nakajima K, Murai R, Monshita K. Growth of square Si single bulk crystals with large side-face widths using noncontact crucible method. Jpn J Appl Phys **53**, (2014).

[116] Nakajima K, Murai R, Ono S, Morishita K, Kivambe MM, Powell DM, et al. Shape and quality of Si single bulk crystals grown inside Si melts using the noncontact crucible method. Jpn J Appl Phys **54**, (2015).

[117] Zulehner W. Czochralski Growth of Silicon. J Cryst Growth **65**, 189 (1983).

[118] Usami N, Takahashi I, Kutsukake K, Fujiwara K, Nakajima K. Implementation of faceted dendrite growth on floating cast method to realize high-quality multicrsytalline Si ingot for solar cells. J Appl Phys **109**, (2011).

[119] Joonwichien S, Takahashi I, Matsushima S, Usami N. Towards implementation of floating cast method for growing large-scale high-quality multicrystalline silicon ingot using designed double crucibles. Prog Photovoltaics **22**, 726 (2014).

[120] Nakajima K, Morishita K, Murai R, Usami N. Formation process of Si3N4 particles on surface of Si ingots grown using silica crucibles with Si3N4 coating by noncontact crucible method. J Cryst Growth **389**, 112 (2014).

[121] Nakajima K, Murai R, Morishita K, Kutsukake K. Growth of Si single bulk crystals with low oxygen concentrations by the noncontact crucible method using silica crucibles without Si3N4 coating. J Cryst Growth **372**, 121 (2013).

[122] Stoddard N, inventorMethods and Apparatuses for Manufacturing Geometric Multicrystalline Cast Silicon and Geometric Multicrystalline Cast Silicon Bodies for Photovoltaics patent WO/2007/084936. 2007.

[123] Gu X, Yu XG, Guo KX, Chen L, Wang D, Yang DR. Seed-assisted cast quasi-single crystalline silicon for photovoltaic application: Towards high efficiency and low cost silicon solar cells. Sol Energ Mat Sol C **101**, 95 (2012).

[124] Jouini A, Ponthenier D, Lignier H, Enjalbert N, Marie B, Drevet B, et al. Improved multicrystalline silicon ingot crystal quality through seed growth for high efficiency solar cells. Prog Photovoltaics **20**, 735 (2012).

[125] Trempa M, Reimann C, Friedrich J, Muller G, Oriwol D. Mono-crystalline growth in directional solidification of silicon with different orientation and splitting of seed crystals. J Cryst Growth **351**, 131 (2012).

[126] Jouini A, Jay F, Amaral V, Pihan E, Veschetti Y. Achievements and future potential on mono-like silicon wafers combined with advanced solar cells processes towards η>20%. Proceedings of the 7th International Workshop on Crystalline Silicon Solar Cells (CSSC7), 89 (2013).

[127] Jiptner K, Miyamura Y, Harada H, Kakimoto K, Sekiguchi T. Origin of dislocations in Si ingots grown by seeded directional solidification. The 7th International Workshop on Crystalline Silicon Solar Cells, 60 (2013).

[128] Jiptner K, Gao B, Harada H, Miyamura Y, Fukuzawa M, Kakimoto K, et al. Thermal stress induced dislocation distribution in directional solidification of Si for PV application. J Cryst Growth **408**, 19 (2014).

[129] Guerrero I, Parra V, Carballo T, Black A, Miranda M, Cancillo D, et al. About the origin of low wafer performance and crystal defect generation on seed-cast growth of industrial mono-like silicon ingots. Prog Photovoltaics **22**, 923 (2014).

[130] Trempa M, Reimann C, Friedrich J, Muller G, Krause A, Sylla L, et al. Defect formation induced by seed-joints during directional solidification of quasi-mono-crystalline silicon ingots. J Cryst Growth **405**, 131 (2014).

[131] Takahashi I, Taisho I, Joonwichien S, Usami N. Seed manipulation for artificially controlled defects technique (SMART) as a new growth method for high-quality mono-like silicon crystals. Proceedings of the 8th International Workshop on Crystalline Silicon Solar Cells (CSSC8), (2015).

[132] Kutsukake K, Usami N, Ohno Y, Tokumoto Y, Yonenaga I. Mono-Like Silicon Growth Using Functional Grain Boundaries to Limit Area of Multicrystalline Grains. Ieee J Photovolt **4**, 84 (2014).

[133] Miyamura Y, Harada H, Jiptner K, Chen J, Prakash RR, Nakano S, et al. Crystal growth of 50 cm square mono-like Si by directional solidification and its characterization. J Cryst Growth **401**, 133 (2014).

[134] Gao B, Nakano S, Harada H, Miyamura Y, Sekiguchi T, Kakimoto K. Reduction of polycrystalline grains region near the crucible wall during seeded growth of monocrystalline silicon in a unidirectional solidification furnace. J Cryst Growth **352**, 47 (2012).

[135] Zhu DD, Ming L, Huang ML, Zhang ZY, Huang XM. Seed-assisted growth of high-quality multi-crystalline silicon in directional solidification. J Cryst Growth **386**, 52 (2014).

[136] Wong YT, Hsu C, Lan CW. Development of grain structures of multi-crystalline silicon from randomly orientated seeds in directional solidification. J Cryst Growth **387**, 10 (2014).

[137] Prakash RR, Sekiguchi T, Jiptner K, Miyamura Y, Chen J, Harada H, et al. Grain growth of cast-multicrystalline silicon grown from small randomly oriented seed crystal. J Cryst Growth **401**, 717 (2014).

[138] Hsieh CC, Wu YC, Lan A, Hsu HP, Hsu C, Lan CW. Comparison of defect formations in solar silicon growth from small random and large oriented seeds. J Cryst Growth **419**, 1 (2015).

[139] Jenkins MW. New Preferential Etch for Defects in Silicon-Crystals. J Electrochem Soc **124**, 757 (1977).

[140] Secco d' Aragona F. Dislocation Etch for (100) Planes in Silicon. J Electrochem Soc **119**, 948 (1972).

[141] Sopori BL. A New Defect Etch for Polycrystalline Silicon. J Electrochem Soc **131**, 667 (1984).

[142] EDAX. OIM Data Collection 5.2 Manual.

[143] Goldstein J. Scanning electron microscopy and x-ray microanalysis. 3rd ed. New York: Kluwer Academic/Plenum Publishers; 2003. xix p.

[144] Nome AJ, Tangen SM, Hjelen J, Saetre TO. Detection of Dislocations and Subgrain Boundaries in Solar Cell Silicon - Studied by the EBSD Technique. 52nd annual meeting of the Scandinavian Society for Electron Microscopy, SCANDEM 2001, (2001).

[145] Usami N, Kutsukake K, Fujiwara K, Nakajima K. Modification of local structures in multicrystals revealed by spatially resolved x-ray rocking curve analysis. J Appl Phys **102**, (2007).

[146] Lehmann T, Trempa M, Meissner E, Zschorsch M, Reimann C, Friedrich J. Laue scanner: A new method for determination of grain orientations and grain boundary types of multicrystalline silicon on a full wafer scale. Acta Materialia **69**, 1 (2014).

[147] Søndenå R, Ekstrøm KE, Dalaker H, Lehmann T, Arnberg L, Di Sabatino M. Effect of Phosphorus Gettering on Quasi-Single-Crystalline Silicon Wafers. Proceedings of the 31st EUPVSEC, (2015).

[148] Trupke T, Bardos RA, Schubert MC, Warta W. Photoluminescence imaging of silicon wafers. Appl Phys Lett **89**, (2006).

[149] Sinton RA, Cuevas A, Stuckings M. Quasi-steady-state photoconductance, a new method for solar cell material and device characterization. Conference Record of the Twenty Fifth Ieee Photovoltaic Specialists Conference - 1996, 457 (1996).

[150] Schubert MC, Habenicht H, Warta W. Imaging of Metastable Defects in Silicon. Ieee J Photovolt **1**, 168 (2011).

[151] Engler O, Randle V. Introduction to texture analysis : macrotexture, microtexture, and orientation mapping. 2nd ed. Boca Raton: CRC Press; 2010. xv p.

[152] Quey R. Orientation Library: A collection of routines for orientation manipulation (Ver. 2.0), http://sourceforge.net/projects/orilib2008.

[153] Buonassisi T, Istratov AA, Heuer M, Marcus MA, Jonczyk R, Isenberg J, et al. Synchrotron-based investigations of the nature and impact of iron contamination in multicrystalline silicon solar cells. J Appl Phys **97**, (2005).

[154] Fenning DP, Hofstetter J, Bertoni MI, Coletti G, Lai B, del Canizo C, et al. Precipitated iron: A limit on gettering efficacy in multicrystalline silicon. J Appl Phys **113**, (2013).

APPENDICES

APPENDIX A: MISORIENTATION CALCULATIONS

Misorientation measurements and calculations were performed as a part of the work on dislocation development in mono-like silicon. During this work it became desirable to measure the crystallographic misorientation over the six small-angle grain boundaries that formed as a result of misoriented seeds. A typical mono-like wafer used for these measurements is illustrated in Figure A.1 (a).

Total misorientation:
The crystallographic orientation of each grain (X_c, Y_c, Z_c) was recorded as a set of Euler rotations relative to the coordinate system of the sample (X_s, Y_s, Z_s) by the X-ray Laue Scanner.

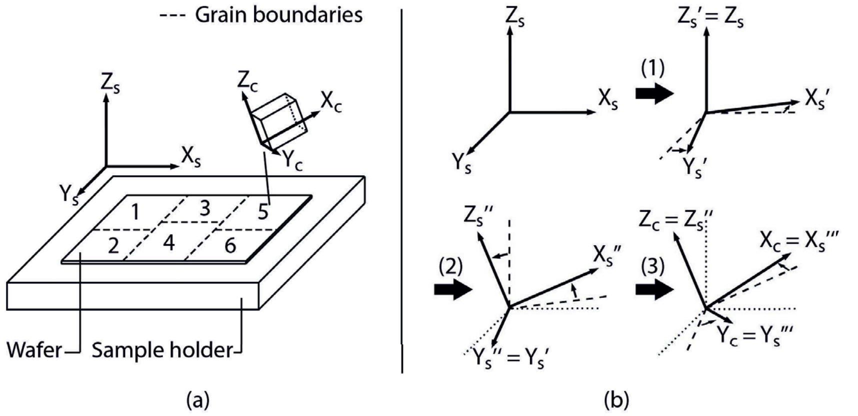

(a) (b)

Figure A.1. (a) The crystallographic orientation of each of the six grains (X_c, Y_c, Z_c) of the mono-like ingot was measured as a set of Euler rotations relative to the orientation of the wafers (X_s, Y_s, Z_s). (b) The Euler rotations consist of three rotations performed successively in order to rotate the sample coordinate system to the grain coordinate system.

The Euler method is illustrated in Figure A.1 (b) and consists of three successive rotations, relating the coordinate system of the sample to the coordinate system of the given grain. The method consists of the following three steps:

1. The sample (X_s, Y_s, Z_s) is rotated an angle φ_1 around its Z_s axis, transforming into a new set of coordinates, (X_s', Y_s', Z_s').

2. The sample (X_s', Y_s', Z_s') is now rotated an angle Φ around its Y_s' axis, transforming into a new set of coordinates, (X_s'', Y_s'', Z_s'').

3. The sample (X_s'', Y_s'', Z_s'') is finally rotated an angle φ_2 around its Z_s'', transforming into the final orientation of the specific grain, $(X_s''' = X_c, Y_s''' = Y_c, Z_s''' = Z_c)$.

The Euler angles are given for the six grain in Table A.1.

Table A.1. Set of Euler angles $(\varphi_1, \Phi, \varphi_2)$ measured for the six grains illustrated in Figure A.1 (a).

Grain	1	2	3	4	5	6
φ_1 [°]	89.294	88.692	89.395	89.211	89.196	89.053
Φ [°]	89.182	89.061	89.246	89.181	89.154	89.058
φ_2 [°]	42.942	42.940	43.090	43.111	43.098	43.272

However, the relationship between the coordinate system of a sample $(\boldsymbol{C_s})$ and the coordinate system of a grain $(\boldsymbol{C_c})$ is more commonly expressed as an orientation matrix $\boldsymbol{G}$,

$$\boldsymbol{C_c} = \boldsymbol{G} \cdot \boldsymbol{C_s} \qquad \text{(Equation A.1)}$$

where the orientation matrix $\boldsymbol{G}$ embodies the respective Euler rotations and is written as a square 3x3 matrix [151], as in Equation A.2.

$$\boldsymbol{G} = \begin{bmatrix} g_{11} & g_{12} & g_{13} \\ g_{21} & g_{22} & g_{23} \\ g_{31} & g_{32} & g_{33} \end{bmatrix} \qquad \text{(Equation A.2)}$$

The previously recorded Euler angles can now be converted into respective orientation matrices by the following set of formulas [151]:

$$\begin{aligned} g_{11} &= \cos\varphi_1 \cos\varphi_2 - \sin\varphi_1 \sin\varphi_2 \cos\Phi \\ g_{12} &= \sin\varphi_1 \cos\varphi_2 + \cos\varphi_1 \sin\varphi_2 \cos\Phi \\ g_{13} &= \sin\varphi_1 \sin\Phi \\ g_{21} &= -\cos\varphi_1 \sin\varphi_2 - \sin\varphi_1 \cos\varphi_2 \cos\Phi \\ g_{22} &= -\sin\varphi_1 \sin\varphi_2 + \cos\varphi_1 \cos\varphi_2 \cos\Phi \\ g_{23} &= \cos\varphi_2 \sin\Phi \\ g_{31} &= \sin\varphi_1 \sin\Phi \\ g_{32} &= -\cos\varphi_1 \sin\Phi \\ g_{33} &= \cos\Phi \end{aligned} \qquad \text{(Equation A.3)}$$

After calculating the orientation matrices for all six grains (i.e. $\boldsymbol{G_{1-6}}$) the misorientation between two and two grains can be found [151, 152]. Note that, due to crystal symmetry, there are several possible misorientation values. It is therefore common to use the term disorientation $(\boldsymbol{G_d})$ instead, and represents the smallest possible misorientation value. The disorientation matrix between two grains can either be expressed in the coordinate system of the sample $(\boldsymbol{G_{d,s}})$ or of grain 1 $(\boldsymbol{G_{d,c1}})$.

$$\begin{aligned} \boldsymbol{G_{d,s}} &= \boldsymbol{G_1}^{-1}\boldsymbol{G_2} \\ \boldsymbol{G_{d,c1}} &= \boldsymbol{G_2}\boldsymbol{G_1}^{-1} \end{aligned} \qquad \text{(Equation A.4)}$$

For easier visualization, the disorientation matrix can be transformed into an angle/axis pair (Ch. 2.2.2), i.e. $\theta_{\vec{r}}$ and $\vec{r} = \langle r_1, r_2, r_3 \rangle$, by the following set of formulas:

$$\begin{aligned} \cos\theta_{\vec{r}} &= \frac{\left(g_{d,11} + g_{d,22} + g_{d,23} - 1\right)}{2} \\ r_1 &= \frac{\left(g_{23} - g_{32}\right)}{2\sin\theta_{rot}} \\ r_2 &= \frac{\left(g_{31} - g_{13}\right)}{2\sin\theta_{rot}} \\ r_3 &= \frac{\left(g_{12} - g_{21}\right)}{2\sin\theta_{rot}} \end{aligned} \qquad \text{(Equation A.5)}$$

The calculated angle/axis pairs for the different junctions are presented in Table A.2.

Table A.2. The rotation axis, total misorientation angle and the decomposed misorientation angles calculated from the Euler rotations previously given in Table A.1.

		Rotation axis,		Decomposed, θ_d [°]		
Grain 1	Grain 2	$\vec{r} = \langle r_1, r_2, r_3 \rangle$	Total, $\theta_{\vec{r}}$ [°]	$\theta_{d,Xs}$	$\theta_{d,Ys}$	$\theta_{d,Zs}$
1	3	$\langle 0.65, 0.27, 0.71 \rangle$	0.23	0.15	0.06	0.17
1	4	$\langle 0.99, -0.02, -0.12 \rangle$	0.17	0.17	0.00	0.02
2	4	$\langle 0.31, 0.21, 0.93 \rangle$	0.56	0.18	0.10	0.53
3	5	$\langle 0.03, -0.42, 0.91 \rangle$	0.22	0.01	0.09	0.20
4	5	$\langle -0.40, -0.80, -0.45 \rangle$	0.03	0.01	0.03	0.01
4	6	$\langle 0.62, -0.49, -0.61 \rangle$	0.26	0.16	0.12	0.16
1	2	$\langle -0.01, -0.22, -0.98 \rangle$	0.55	0.01	0.10	0.55
3	4	$\langle 0.10, -0.33, -0.94 \rangle$	0.20	0.02	0.06	0.19
5	6	$\langle 0.71, -0.41, -0.58 \rangle$	0.25	0.17	0.09	0.14

Decomposed disorientations:

While the angle/axis pair gives the total disorientation between two individual grains, we also wanted to decompose the total disorientation into individual disorientations components around the three main axes of the sample/ingot (i.e. X_s, Y_s and Z_s). This is illustrated in Figure A.2 (a) – (c) and will be described thoroughly.

Two arbitrarily oriented grains can now be represented by their respective orientation matrices, $\boldsymbol{G_1}$ and $\boldsymbol{G_2}$.

$$\boldsymbol{G_1} = \begin{bmatrix} g_{1,11} & g_{1,12} & g_{1,13} \\ g_{1,21} & g_{1,22} & g_{1,23} \\ g_{1,31} & g_{1,32} & g_{1,33} \end{bmatrix} \quad \boldsymbol{G_2} = \begin{bmatrix} g_{2,11} & g_{2,12} & g_{2,13} \\ g_{2,21} & g_{2,22} & g_{2,23} \\ g_{2,31} & g_{2,32} & g_{2,33} \end{bmatrix} \qquad \text{(Equation A.6)}$$

The following relationship can be made between the grains and the sample coordinate system, as illustrated in Figure A.2 (a) [151, 152]:

$$\langle X_s \rangle \parallel \langle g_{1,x} \rangle \parallel \langle g_{2,x} \rangle$$
$$\langle Y_s \rangle \parallel \langle g_{1,y} \rangle \parallel \langle g_{2,y} \rangle$$
$$\langle Z_s \rangle \parallel \langle g_{1,z} \rangle \parallel \langle g_{2,z} \rangle$$

Where,

$$\begin{aligned}
\langle g_{1,x} \rangle &= \langle g_{1,11}, g_{1,21}, g_{1,31} \rangle \\
\langle g_{1,y} \rangle &= \langle g_{1,12}, g_{1,22}, g_{1,32} \rangle \\
\langle g_{1,z} \rangle &= \langle g_{1,13}, g_{1,23}, g_{1,33} \rangle \\[1em]
\langle g_{2,x} \rangle &= \langle g_{2,11}, g_{2,21}, g_{2,31} \rangle \\
\langle g_{2,y} \rangle &= \langle g_{2,12}, g_{2,22}, g_{2,32} \rangle \\
\langle g_{2,z} \rangle &= \langle g_{2,13}, g_{2,23}, g_{2,33} \rangle
\end{aligned} \qquad \text{(Equation A.7)}$$

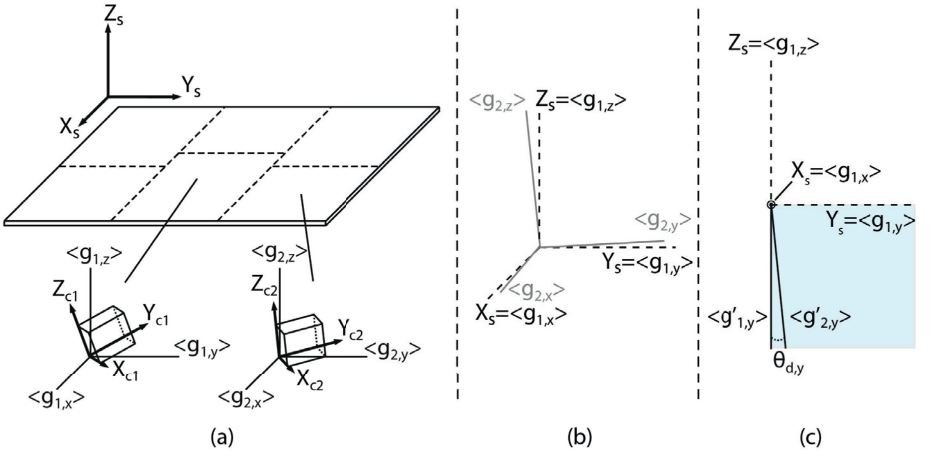

Figure A.2. (a) The relationship between two neighbouring grains can be given by the set of formulas in Equation A.7. (b) By inserting grain 2 into the coordinate system of grain 1 one may calculate the different tilt values. (c) This is done by projecting the respective vectors onto the planes that are perpendicular to the respective sample axes, according to the formulas sets given in Equations A.8 – A.10.

The different disorientations can be found by inserting the unit cell of grain 2 into the coordinate system of grain 1, as illustrated in Figure A.2 (b). The disorientation around e.g. the X_s-axis can be found by projecting $\langle g_{1,y} \rangle$ and $\langle g_{2,y} \rangle$ onto the X_s-plane, which is normal to the axis. Such a projection can be achieved by using the mathematical cross product, with the projected vectors ($\langle g'_{1,y} \rangle$ and $\langle g'_{2,y} \rangle$) and the disorientation angle $\theta_{d,y}$ (Figure A.2 (c)) being calculated as:

$$\begin{aligned}
\langle g'_{1,y} \rangle &= \langle g_{1,x} \rangle \times \langle g_{1,y} \rangle \\
\langle g'_{2,y} \rangle &= \langle g_{1,x} \rangle \times \langle g_{2,y} \rangle
\end{aligned}$$

$$\theta_{d,Xs} = \cos^{-1}\left(\frac{\langle g'_{1,y} \rangle \cdot \langle g'_{2,y} \rangle}{\left\| \langle g'_{1,y} \rangle \right\| \left\| \langle g'_{2,y} \rangle \right\|} \right) \qquad \text{(Equation A.8)}$$

The same procedure can be used to find the disorientations around the Y$_s$ ($\theta_{d,Ys}$) and Z$_s$ ($\theta_{d,Zs}$) axes.

Disorientation around the Y$_s$-axis:

$$\langle g'_{1,x}\rangle = \langle g_{1,y}\rangle \times \langle g_{1,x}\rangle$$
$$\langle g'_{2,x}\rangle = \langle g_{1,y}\rangle \times \langle g_{2,x}\rangle$$

$$\theta_{d,Ys} = \cos^{-1}\left(\frac{\langle g'_{1,x}\rangle \cdot \langle g'_{2,x}\rangle}{\left\|\langle g'_{1,x}\rangle\right\| \left\|\langle g'_{2,x}\rangle\right\|}\right) \qquad \text{(Equation A.9)}$$

Disorientation around the Z$_s$-axis:

$$\langle g'_{1,y}\rangle = \langle g_{1,z}\rangle \times \langle g_{1,y}\rangle$$
$$\langle g'_{2,y}\rangle = \langle g_{1,z}\rangle \times \langle g_{2,y}\rangle$$

$$\theta_{d,Zs} = \cos^{-1}\left(\frac{\langle g'_{1,y}\rangle \cdot \langle g'_{2,y}\rangle}{\left\|\langle g'_{1,y}\rangle\right\| \left\|\langle g'_{2,y}\rangle\right\|}\right) \qquad \text{(Equation A.10)}$$

The individual disorientation values calculated by these formulas are also reported in Table A.2 and are the basis for the discussion in paper P2.

APPENDIX B: IRON MEASUREMENTS IN HPMC SILICON

Iron is usually found in relatively high concentrations throughout mc-Si ingots, as iron silicide precipitates and other Fe-rich inclusions [153], and is known to be detrimental for the final device performance [154]. It was therefore desirable to evaluate the occurrence of iron in the high-performance multicrystalline silicon ingot, and to use the measurements as a baseline for studying the response to phosphorus gettering in this material. The concentration of interstitial iron (Fe_i) was measured, on samples previously used for minority carrier lifetime characterization (Paper P3), by a photoluminescence multitool developed “in house” at ISE Fraunhofer (Ch. 3.10). The technique is based on splitting and re-pairing of iron-boron complexes, and a short description of the technique and the necessary calculations are presented in the second part of Ch. 3.10.

Due to similar characteristics of the photoluminescence maps for all samples, Figure B.1 shows the results attained for the A120/A121 sample pair only. This figure shows both (a) the concentration of interstitial iron (Equation 3.1) and (b) fraction of the total recombination activity that can be related to interstitial iron (Equation 3.2) in both the as-cut (A120) and phosphorus gettered (A121) state. The mean iron concentrations are summarised for all positions in Figure B.2. Note that the lower detection limit for the tool is approximately 10^{10} cm^{-3}.

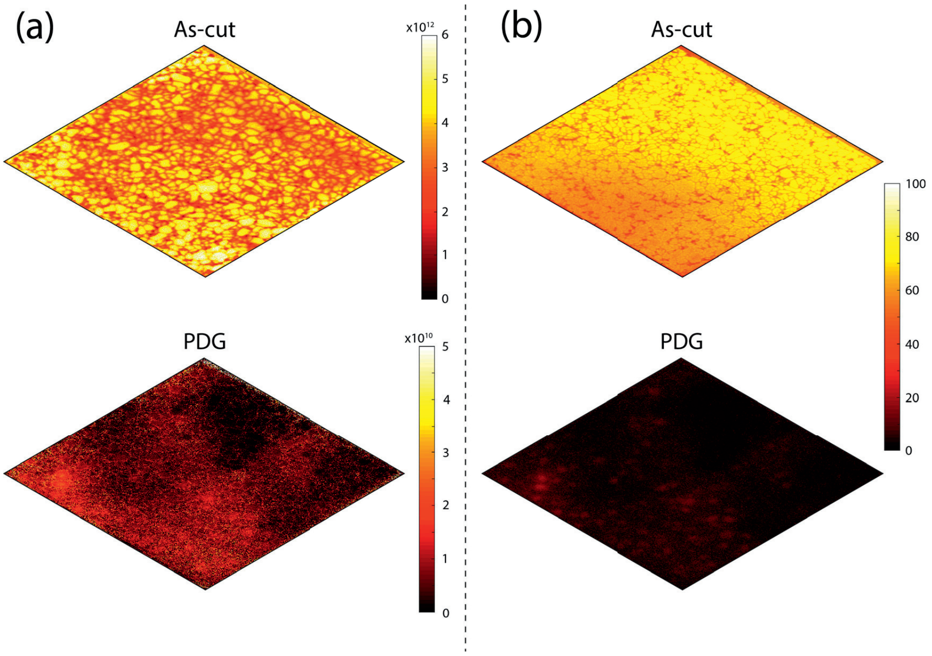

Figure B.1. (a) Fe_i concentration maps of the A120/A121 sample pair, as calculated from photoluminescence maps. (b) Recombination due to Fe_i, before and after phosphorus gettering.

As clearly seen from these figures, typical concentrations of interstitial iron are found to be approximately 10^{11} cm^{-3} - 10^{13} cm^{-3} before phosphorus gettering (i.e. the as-cut state). The typical intragranular Fe_i-concentration is found to be approximately 2-3 times larger than at grain boundaries, which we assume is related to interstitial iron being precipitated at the boundaries. The equipment will only detect interstitial iron, and not precipitated iron. As a result, recombination due to Fei contributes to approximately 60 – 80% of the total intragranular recombination activity, and below 40% at grain boundaries (Figure B.1 (b)). By correlating the large decrease in average Fe_i-concentration (Figure B.1(a)) with the previously reported increase in minority carrier lifetime we suggest that a large fraction of the Fe_i is readily removed by phosphorus gettering, leaving the samples with iron concentrations close to or below the detection limit of the tool (i.e. the PDG state).

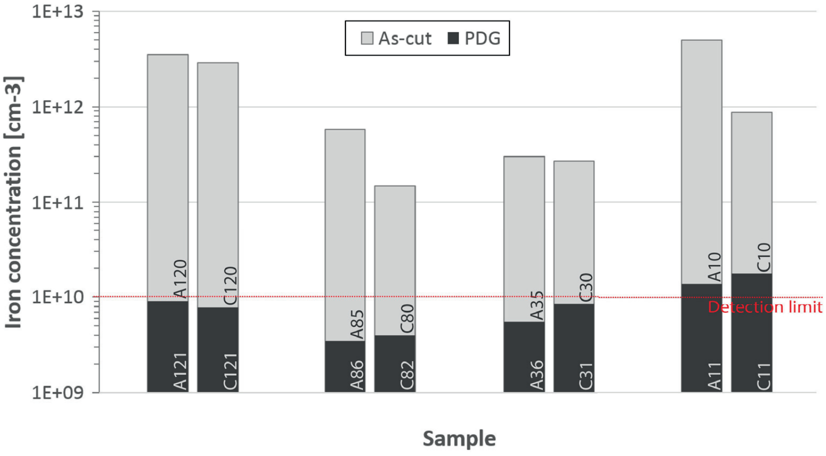

Figure B.2. The concentration of Fe_i in all sample pairs, before and after phosphorus gettering, for both compartments.

The reduced minority carrier lifetime observed at grain boundaries after phosphorus gettering can therefore not be related to Fe_i, and we posit that, due to the large initial Fe_i-concentration in the as-cut state, there is a high probability that the lifetime at the grain boundaries are limited by Fe-rich precipitates and/or inclusions instead.

APPENDIX C: SCIENTIFIC PAPERS

PAPER P1

K. E. Ekstrøm, H. Dalaker, A. Autruffe, R. Søndenå, G. Stokkan, L. Arnberg, M. Di Sabatino, «Characterization of mono-like silicon grown by a seed-assisted Bridgman method», Proceedings of The 7th International Workshop on Crystalline Silicon Solar Cells, 77-81 (2013).

PAPER P2

K. E. Ekstrøm, G. Stokkan, R. Søndenå, H. Dalaker, T. Lehmann, L. Arnberg, M. Di Sabatino, «Structure and dislocation development in mono-like silicon», Physica Status Solidi A: Applications and Materials Science, 212(10), 2278-2288 (2015).

PAPER P3

K. E. Ekstrøm, A. Autruffe, R. Søndenå, H. Dalaker, G. Stokkan, L. Arnberg, M. Di Sabatino, «The microstructure of multicrystalline silicon seeded by polysilicon chips and fluidized bed reactor granules", Journal of Crystal Growth, To be Submitted (2015).

PAPER P4

S. Castellanos, K. E. Ekstrøm, A. Autruffe, M. A. Jensen, A. E. Morishige, J. Hofstetter, P. Yen, B. Lai, G. Stokkan, C. del Cañizo, T. Buonassisi,
"Comparison of gettering responses and lifetime-limiting defects in high-performance and traditional multicrystalline silicon", IEEE Journal of Photovoltaics, Submitted (2015) .

PAPER P5

K. E. Ekstrøm, E. Undheim, G. Stokkan, L. Arnberg, M. Di Sabatino,"Beta-Si_3N_4 particles as nucleation sites in multicrystalline silicon", Acta Materialia, Submitted (2015).

D-6

Characterization of mono-like silicon grown by a seed-assisted Bridgman method

K. E. Ekstrøm[1]*, H. Dalaker[2], A. Autruffe[1], R. Søndenå[3], G. Stokkan[1], L. Arnberg[1], M. Di Sabatino[1]

[1]*Department of Materials Science and Engineering, NTNU, N-7491 Trondheim, Norway*

[2]*SINTEF Materials and Chemistry, N-7465 Trondheim, Norway*

[3]*Institute for Energy Technology, N-2007 Kjeller, Norway*

e-mail: kai.e.ekstrom@ntnu.no

Abstract

Preliminary studies have been carried out on small-scale ingots grown by seed-assisted directional solidification at speeds of 3µm/s and 30µm/s, where the crystallographic orientation on the seeds has been varied between <100>, <110>, <211> and <111>. Structural characterization shows a monocrystalline core limited by {111}-facets surrounded by a multicrystalline area which consists of twinned- and parasitic grains. Low pulling speeds seem to favor a twinned growth while a higher pulling-speed seems to favor parasitic growth from the crucible walls. The second part of the project focuses of growing a 12kg pilot-scale ingot from a seed-structure consisting of six {110}-seeds placed together. A clear dislocation-structure resembling the junction-structure has been observed, and will be subject for further investigation.

Introduction

There is still a large efficiency-gap between multicrystalline (mc-Si) and monocrystalline (mono-Si) silicon, and a large part of the current research on silicon is devoted to reducing this gap. Multicrystalline silicon is traditionally grown in a directional solidification furnace and results in an ingot consisting of a relatively large amount of randomly oriented grains, dislocations and impurities all of which have a profound effect on the material quality and final efficiency. This may be related to grain-orientation and grain-boundaries [1]; thus the importance of structure-control becomes clear, both at nucleation- and growth-level.

In recent years directional solidification together with monocrystalline seeding has gained increased attention, and the first part of this work consisted on growing small (Ø=32mm) silicon ingots based on <100>-, <110>-, <211>- and <111>-seeds in a small Bridgman furnace. While such small-sized experiments inevitably cause edge-effects to dominate the material-properties, they also represent unique possibilities in enabling large and inexpensive series of studies on e.g. specific grain-boundaries, nucleation and other aspects of solidification [2, 3, 4, 5]. Ingots have previously been grown from single <111> and <100> seeds with diameters up to 154mm [6]. However, it may prove difficult to cover larger crucibles with single seeds, especially for industrial crucibles, and a solution may be to create a seeding-structure consisting of several seeds placed together [7], also introducing seed-junctions and accompanying structure alternations [8]. Therefore, in the second part of this work a 12kg {110}-seeded ingot was grown (Ø=250mm) in a pilot-scale directional solidification furnace by using multiple {110}-seeds which had been prepared by grinding and etching. In order to study the effect of stress-development and dislocation development in the seed junctions two of the junctions were placed with a gap of 0.4mm and 1.6mm while the rest was close-packed.

Experimental

Seven small-scale silicon ingots (Ø=32mm) were grown in a small-scale Bridgman-type furnace [2] by placing seeds of different crystallographic orientations in the bottom of the crucible as shown in Fig. 1 (a). Seeds were drilled from a <100> monocrystalline Czochralski ingot with different crystallographic orientation, namely <100>, <110>, <111>, <211> and placed together with silicon feedstock in Si_3N_4-coated Al_2O_3-crucibles. The melting time was tuned to prevent complete melting of the seed, and the growth was done at speeds of 3μm/s (which is typical for an industrial process) and 30μm/s. The crystallographic orientation of the seeds was confirmed by X-ray diffraction (XRD).Vertical and horizontal slices were cut from respectively the middle and the top of the ingots and prepared by polishing for mainly Electron Backscatter Diffraction (EBSD) analysis.

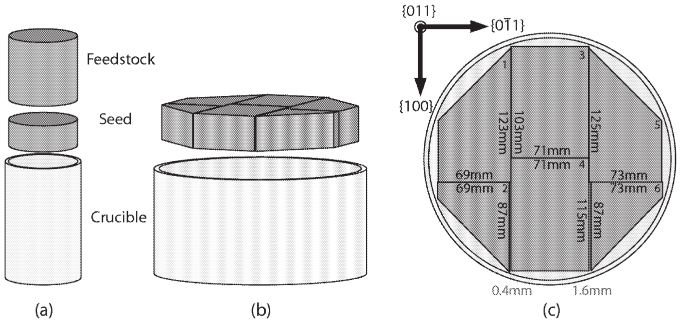

Fig. 1. Seeding method for (a) the small scale castings and (b) the pilot-scale casting where the latter consisted of six equally oriented {110} seeds placed close together (c) except junctions 2-4 and 4-6 which were placed with gaps of 0.4mm and 1.6mm respectively.

The pilot-scale ingot (Ø=250mm) was grown in a Crystalox DS 250 directional solidification furnace by placing a specially designed seeding-structure (Fig. 1 (c)) in the bottom of a Si_3N_4-coated SiO_2 crucible and filling the rest of the crucible with high-purity polysilicon as feedstock. The six seeds were cut with the same crystallographic orientation by a bandsaw specially designed for silicon and ground by automatic grinding equipment to attain parallel sides. In order to remove surface defects an additional 200μm were removed by coarse grinding (D107; FEPA standard) and 30μm by fine grinding (D28; FEPA standard) followed by 4 min of CP4 etching (HF, HNO_3 and $C_2H_4O_2$). The final seed dimensions are shown in Fig. 1 (c) with a uniform height of 39mm. Most of the seeds where close-packed, except the junctions between seeds 2 and 4 and between seeds 4 and 6 which were placed with a 0.4mm and 1.6mm gap respectively. The growth speed is assumed to be approximately 0.25 mm/min [9]. For characterization purposes the core of the ingot was wafered (156mm x 156mm x 200μm) while the rest was cut into a variety of vertical and horizontal slices. Preliminary characterization has been performed by light microscopy and photoluminescence but will be expanded to include EBSD and etching.

Results and discussion

I. Small-scale castings

Fig. 2 shows the vertical cross-sections of the seven ingots, revealing the dependence on the crystallographic orientation of the seeds [8]. The structure may be divided into a monocrystalline core and multicrystalline surroundings where the first attains an orientation equal to the seed. The core is separated from the multicrystalline area by low-energy {111}-planes and the shape of the core will therefore be defined by the angles between the {111}-planes and crystallographic orientation of the seed. The surrounding structure consist of a varying amount of both grains twinned from the seed and successive twinning, and randomly oriented parasitic grains nucleated on the crucible wall.

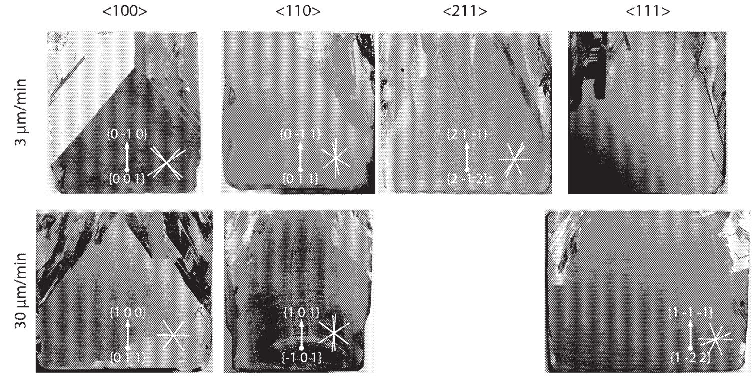

Fig. 2. Vertical cross sections from the middle of the ingots with corresponding {111} plane-traces and crystallographic orientations.

EBSD-analysis indicates that samples grown at 3μm/s are dominated by successive twinning while samples grown at 30μm/s are dominated by parasitic growth; a result of the growth-front becoming more concave at increased pulling-speeds because of an increased heat-transfer through the crucible wall [1] and thereby favoring nucleation and growth on the wall. Note that the monocrystalline core is preserved also at increased pulling speeds and the multicrystalline area is the only area affected.

Bulk properties are difficult to study in small ingots because of the dominance of edge-effects and a pilot-scale ingot was therefore grown, based on multiple {110}-seeds which also gave an opportunity to study dislocation development from seed-junctions. {110}-seeds were chosen because of the possibility of attaining {111}-facets with higher angles than obtainable by using {100}-seeds (Fig. 2) and the <110>-direction previously being reported as a rapid growth direction [10].

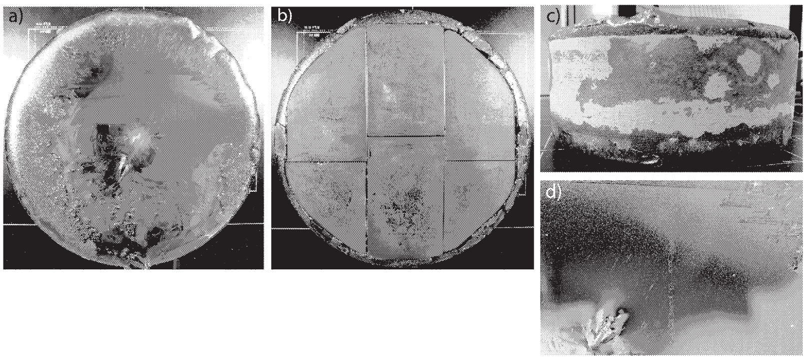

Fig. 3. Images of the pilot-scale ingot showing (a) the top, (b) the bottom and (c) the side. The dislocation structure resulting from the seed-junctions is clearly visible at the top of the ingot (d).

II. Pilot-scale casting

The pilot-scale ingot is shown in Fig. 3 (a) – (c) with the seed structure (Fig. 1 (c)) clearly visible in the bottom (b). The top is very clean and mirror-like with a large dendrite in the middle, the latter being a result of rapid solidification because of the argon-inlet at this location. Fig. 3(b) and (c) reveals incomplete melting of the feedstock at seed-level and the remaining feedstock has acted as nucleation points for large amount of grains (Fig. 4 (a)). The top of the ingot contains a large amount of twins perpendicular to the <100>-direction and dislocations visible to the naked eye as shown Fig. 4 (d); where the latter resembles the junctions in the bottom seeding-structure, confirming that the dislocations formed at the seed-junctions grow through the whole height of the ingot. Vertical slices cut around the central 156x156mm block reveals the structure of the ingot (Fig. 4 (a) – (b)), resembling that of the smaller <110>-ingots previously presented (Fig. 2); a central monocrystalline core limited by {111}-facets and surrounded by a multicrystalline structure. In this case a large part of the surrounding multicrystalline structure seems to nucleate from the remaining non-melted polysilicon chunks at seed-level, however twinning becomes dominating higher in the ingot. The height of the remaining seed-area was revealed by cutting 2mm horizontal slices (Fig. 4 (c) – (d)) and was found to be approximately 24.6mm which confirms a partial melting of the seeds. The orientation of the seed-junctions as well as the seed-spacing seems to affect the low-lifetime area and the dislocation generation; where the first may be related to the orientation of the glide-planes.

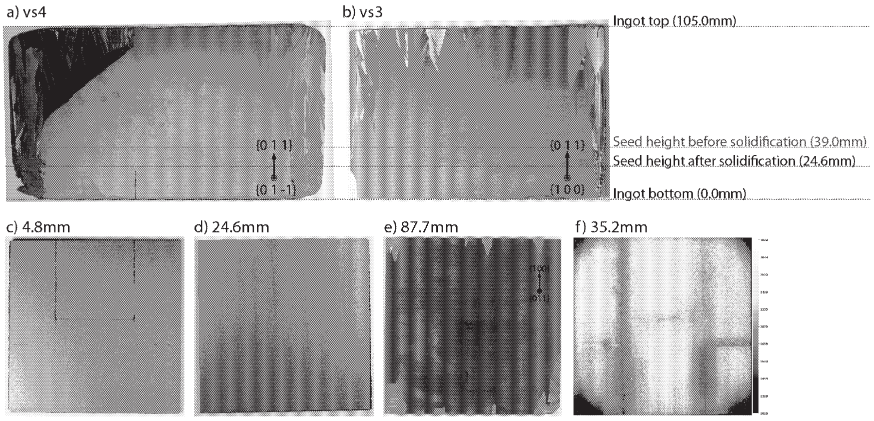

Fig. 4. Vertical slices perpendicular to (a) the <110>- and (b) <100>-direction. Slicing the bottom part of the central 156x156mm block reveals a (c) remaining seed-height of ~24.6mm. (e) Several grains enter the central block higher in the ingot and (f) PL-imaging shows low-lifetime areas related to dislocations from seed-junctions develop throughout the ingot.

Junctions perpendicular to the <110>-direction have a tendency for having a wider low-lifetime area than junctions perpendicular to the <100>-direction and a larger seed-spacing seems to also result in a wider low-lifetime area, presumably because of melt-expansion inside the junction. EBSD-analysis on selected wafers did not show any grain-boundaries representing the seed structure, it is however assumed that the low-lifetime areas are accompanied by low-angle grain-boundaries, but this is to be confirmed. The seed-junctions may also be subject to segregation phenomena previously observed at grain-boundaries [11, 2].

Closer characterization of this junction- and dislocation-structure by photoluminescence, etching and microscopy is currently ongoing and will be addressed in future work. Future work will also include a more complete lifetime map by Microwave Photoconductance Decay (μ-PCD) and Quasi Steady State Photoconductance Photoluminescence (QSSPC-PL) together with production and characterization of solar cells.

Conclusion

Preliminary studies on small scale ingots indicated that i) the shape and extent of the monocrystalline core depends on the crystallographic orientation of the seed and ii) the pulling-speed affects the probability of twinning, with increased twinning at low pulling speeds. A larger ingot has been grown, based on six {110}-oriented seeds placed together and an overview has been given on preliminary results regarding the structure and dislocation development.

Acknowledgements

This work is partly supported by The Centre for Environment-Friendly Energy Research (FME) under The Research Council of Norway (RCN) in cooperation with SINTEF Materials and Chemistry.

REFERENCES

[1] C. W. Lan, W. C. Lan, T. F. Lee, A. Yu, Y.M. Yang, W. C. Hsu, B. Hsu, A. Yang, Journal of Crystal Growth 360 (2012) 68 -75.

[2] A. Autruffe, L. Vines, L. Arnberg, M. Di Sabatino, Journal of Crystal Growth 372 (2013) 180 – 188.

[3] I. Takahashi, N. Usami, K. Kutsukake, G. Stokkan, K. Morishita, K. Nakajima, Journal of Crystal Growth 312 (2010) 897 – 901.

[4] K. Fujiwara, M. Ishii, K. Maeda, H. Koizumi, J. Nozawa, S. Uda, Scripta Materialia 69 (2013) 266 – 269.

[5] I. Brynjulfsen, L. Arnberg, A. Autruffe, Journal of Crystal Growth 361 (2012) 2006-2011.

[6] A. Jouini, D. Ponthenier, H. Lignier, N. Enjalbert, B. Marie, B. Drevet, E. Pihan, C. Cayron, T. Lafford, D. Camel, Progress in Photovoltaics: Research and Applications 20 (2012) 735 – 746.

[7] X. Gu, X. Yu, K. Guo, L. Chen, D. Wang, D. Yang. Solar Energy Materials & Solar Cells 101 (2012) 95 – 101.

[8] M. Trempa, C. Reimann, J. Friedrich, G. Müller, D. Oriwol, Journal of Crystal Growth 351 (2012) 131 – 140.

[9] R. Kvande, Ø. Mjøs, B. Ryningen, Materials Science and Engineering A 413-414 (2005) 545 – 549.

[10] K. Fujiwara, W. Pan, N. Usami, K. Sawada, M. Tokairin, Y. Nose, A. Nomura, T. Shishido, K. Nakajima, Acta Materialia 54 (2006) 3191 – 3197.

[11] S. Martinuzzi, I. Périchaud, O. Palais, Solar Energy Materials & Solar Cells 91 (2007) 1172 – 1175.

Phys. Status Solidi A **212**, No. 10, 2278–2288 (2015) / **DOI** 10.1002/pssa.201532105

physica status solidi a
www.pss-a.com
applications and materials science

Structure and dislocation development in mono-like silicon

K. E. Ekstrøm[*,1], **G. Stokkan**[2], **R. Søndenå**[3], **H. Dalaker**[2], **T. Lehmann**[4], **L. Arnberg**[1], **and M. Di Sabatino**[1]

[1] Department of Materials Science and Engineering, NTNU, 7491 Trondheim, Norway
[2] SINTEF Materials and Chemistry, 7465 Trondheim, Norway
[3] Institute for Energy Technology, 2007 Kjeller, Norway
[4] Fraunhofer Technology Centre for Semiconductor Materials THM, 09599 Freiberg, Germany

Received 17 February 2015, revised 11 June 2015, accepted 11 June 2015

Keywords crystal orientation, dislocations, grain boundaries, silicon, structure

---

[*] Corresponding author: e-mail kai.e.ekstrom@ntnu.no, Phone: +47 73 59 48 83, Fax: +47 73 55 02 03

The current paper investigates the structure of low-lifetime areas observed in a <110>-oriented mono-like silicon ingot grown from monocrystalline seeds. These areas are related to dislocation clusters forming at seed junctions and several generation mechanisms are discussed. Dislocations generated due to physical contact between seeds could only be completely avoided by introducing gaps between the seeds. Large gaps were, however, found to suffer from alternative generation processes not found in small gaps. Dislocations generated in the seeds and in peripheral grains does not necessarily move in to the main crystal and low-lifetime areas are mainly related to dislocations generated above the seeding structure. Dislocations are found to form clusters aligning along <111>-directions and are proposed to happen by glide on {111}-planes from the boundary plane between two seed crystals. The extent of low-lifetime areas and corresponding dislocation clusters, for junctions containing no or small gaps, appear to mainly depend on the misorientation between seeds and by attaining sufficiently low misorientation the high bulk lifetime can be retained also at the junctions. Analysis of the misorientations along principal axes indicates that larger misorientations can be tolerated if the misorientation is limited to a single tilt axis.

1 Introduction

In the recent years, seed-assisted growth of mono-like silicon has been proposed as a way of producing high quality near monocrystalline ingots by the inexpensive directional solidification method. The typical ingot structure consists of a monocrystalline core surrounded by a multicrystalline structure in the ingot periphery [1, 2]; however, methods are currently being developed in order to suppress this parasitic growth [3]. The main problem is currently the lack of control of dislocation generation during solidification and cooling of the ingot and further research is needed in order to grow dislocation-free mono-like ingots. Generation of dislocations in mono-like silicon has previously been related to thermal and mechanical stresses taking place both in bulk seeds and the main ingot [4, 5] and processes taking place in seed junctions for larger ingots which require multiple seeds [4, 6]. Dislocation movement in traditional multicrystalline silicon is limited because of large amounts of grain boundaries [7], but as mono-like crystals contain no or few grain boundaries, the dislocations may move relatively freely around the crystal interior.

The use of <110>-oriented seeds in the present experiment is based on previous results [1], which showed that the loss of the monocrystalline core to parasitic growth could be reduced by choosing <110>-seeds over the more frequently used <100>-seeds. This was attributed to more favorable orientation of the {111}-facets and rapid growth in the <110>-direction.

The importance of seed preparation has previously been addressed by Ervik et al. [9] and Trempa et al. [6] have investigated the effect of different grain boundary planes and introduction of gaps between the seeds in order to reduce the amount of contact-related dislocations.

In the present work, we address several processes leading to dislocation generation in a pilot-scale ingot grown from multiple single-crystalline seeds. It is suggested that the main reason for dislocation development in the main crystal is related to the misorientation between the seeds if the gap size is kept sufficiently small.

2 Experimental

A seed-assisted [Fig. 1(a)] 12 kg pilot-scale silicon ingot, with a diameter of 250 mm and height of 107 mm [Fig. 1(b)], has been grown in a Crystalox DS 250 directional solidification furnace. The seeds consisted of six equally oriented monocrystalline slabs, with a total weight of approximately 3.5 kg, cut from a Czochralski ingot and placed in the bottom of a Si_3N_4-coated SiO_2-crucible. A total of 8.5 kg of poly-Si feedstock was added on top of the seeds. The seeds form a total of nine junctions; six with {110}/{110} boundary planes and three with {100}/{100} boundary planes, which are denoted by 1.X and 2.Y, respectively, as shown in Fig. 1(c). This denomination will be used throughout the paper. In order to study the effect of gaps between the seeds on the ingot structure, gaps of 0.4 and 1.6 mm were added to junctions 1.3 and 1.6, respectively. The remaining seeds were placed in close contact.

The preparation of the seeds was performed by a combination of cutting, grinding, and etching. Cutting was done by a fine bandsaw designed for cutting silicon and grinding by automatic grinding equipment. Both coarse- (D107; FEPA standard) and fine-gritted (D28; FEPA standard) grinding wheels were used to make sure that all seed faces were planar and to reduce the amount of surface defects on the seeds. The preparation was finalized with a 4 min CP4 etch for smoothing extremities.

For characterization purposes, the final ingot was sectioned into a central 156 × 156 mm^2 block [Fig. 2(a)] and four 2 mm thick surrounding vertical sections, vs1–vs4, [Fig. 2(b)]. Due to inclusions, a top- and bottom seed section had to be removed before wafering of the central block.

Vertical sections and horizontal wafers were polished to mirror-like surfaces and etched in Sopori [10] to reveal dislocation structures for subsequent characterization by light microscopy (LM), scanning electron microscopy (SEM), and PVScan. An alternative Laue scanner method [11] had to be used in order to detect the crystallographic misorientation between the seeds as it was found to be below the lower detection limit [12] of traditional electron backscatter diffraction (EBSD). Photoluminescence (PL) imaging has been performed on as-cut and phosphorus-gettered samples in order to study the effect of junctions on the minority carrier lifetime and eventually final solar cell performance.

3 Results Removal of a 2 mm top slice of the ingot revealed the large central monocrystal previously shown in Fig. 2(a) surrounded by a multicrystalline structure, consisting of both randomly oriented and twinned grains. Although the former show a randomized structure and appear to be mainly confined to the outer periphery of the ingot, the twinned grains are clearly defined by {111}-planes and grow more actively toward the center of the ingot, parallel to the <100>-direction. Crystallographic {111}-facets has been added to Fig. 2(a) to aid this visualization. However, twinning is fairly limited and the 156 × 156 mm^2 core consists almost exclusively of a single <110>-oriented monocrystal. The interface between the remaining seeds and the solidified crystal, the seed interface, has been found at a height of approximately 25 mm, confirming a seed melt-back of approximately 10 mm before solidification.

Quantitative lifetime images of phosphorus-gettered samples taken at different positions in the ingot clearly show the destructive nature of the junctions [Fig. 3(a) and (b)]. Although bulk material far away from the junctions has an average minority carrier lifetime of approximately 400–500 μs after gettering, the areas surrounding most of the junctions show minority carrier lifetimes down to approximately 100 μs. Etch pit imaging on corresponding Sopori-etched samples show that the low-lifetime areas are mainly related to dislocation clusters appearing at the

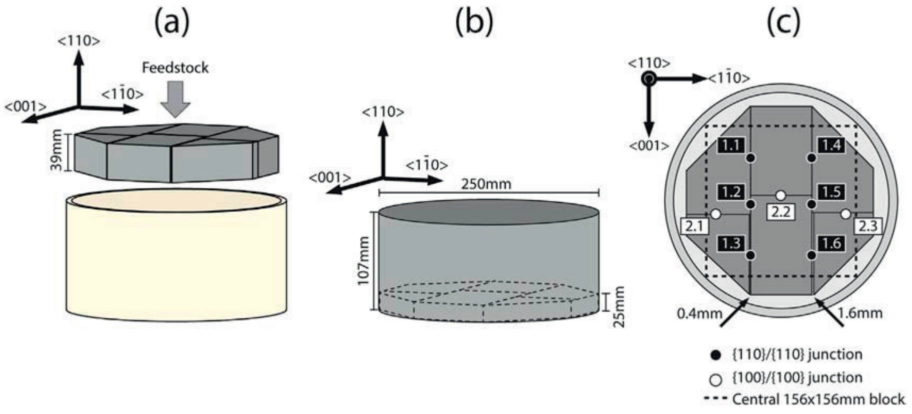

Figure 1 (a) Six equally oriented seeds were placed in the bottom of a crucible and covered with poly-Si feedstock. (b) Final ingot dimensions with a remaining seed height of 25 mm. (c) Seed junctions are numbered with respect to their boundary plane and gaps of 0.4 and 1.6 mm were introduced at junction 1.3 and 1.6. The central 156 × 156 mm^2 block cut for characterization purposes is marked with a dotted line.

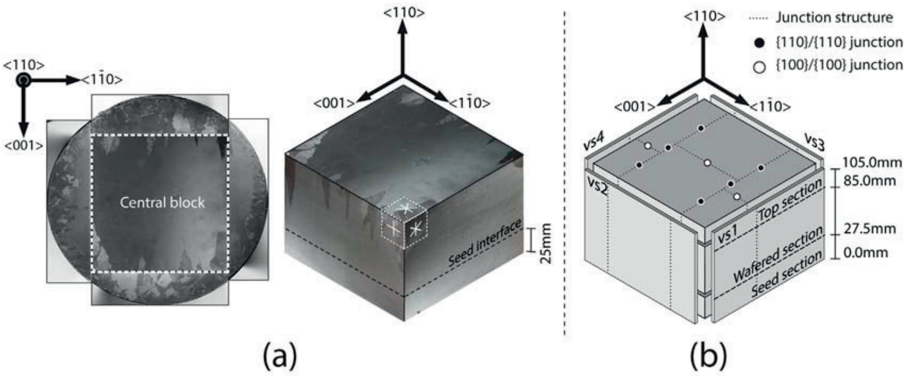

Figure 2 (a) Top- and block-view of the final ingot, after removal of a 2 mm top-cut, showing the central monocrystal surrounded by a parasitic multicrystalline structure. Twins, defined by {111}-facets, penetrate deeper into the central block than the remaining parasitic structure. (b) Four vertical sections (vs1–vs4) surrounding the central block were cut for characterization purposes. A top- and bottom-section was removed from the central block before wafering due to inclusions.

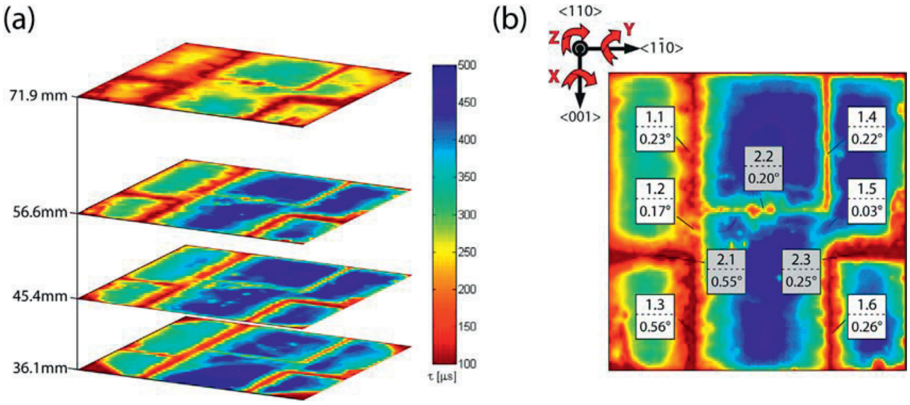

Figure 3 (a) Quantitative PL-mapping showing low-lifetime areas at seed junctions which increase in width with ingot height. (b) Calculated total misorientation values from Laue measurements. The values have also been decomposed to simple tilts around the three principal axes of the ingot (*X*, *Y*, and *Z*), shown in Table 1.

junctions and the average width of the low-lifetime areas corresponds well to the average width of the observed dislocation clusters (Table 1).

In addition to the high dislocation concentrations located at seed junctions, etch pit density (EPD) counting show different dislocation concentrations in different areas of the ingot [Fig. 4(a)]; with average values given in Table 2. The results and discussion has therefore been divided into three separate sections; representing the multicrystalline periphery, the seed-volume below the

Table 1 The average width of the dislocation clusters appearing at respective junctions measured perpendicular to the grain boundary plane. Misorientation data calculated from Laue measurements.

junction	1.1	1.2	1.3	1.4	1.5	1.6	2.1	2.2	2.3
average width [mm]	3.7	3.7	6.8	1.0	0.0	3.8	7.2	0.5	9.1
misorientation measurements:									
total [°]	0.23	0.17	0.56	0.22	0.03	0.26	0.55	0.20	0.25
X-tilt [°]	0.15	0.17	0.18	0.01	0.01	0.16	0.01	0.02	0.17
Y-tilt [°]	0.06	0.00	0.10	0.09	0.03	0.12	0.10	0.06	0.09
Z-tilt [°]	0.17	0.02	0.53	0.20	0.01	0.16	0.55	0.19	0.14

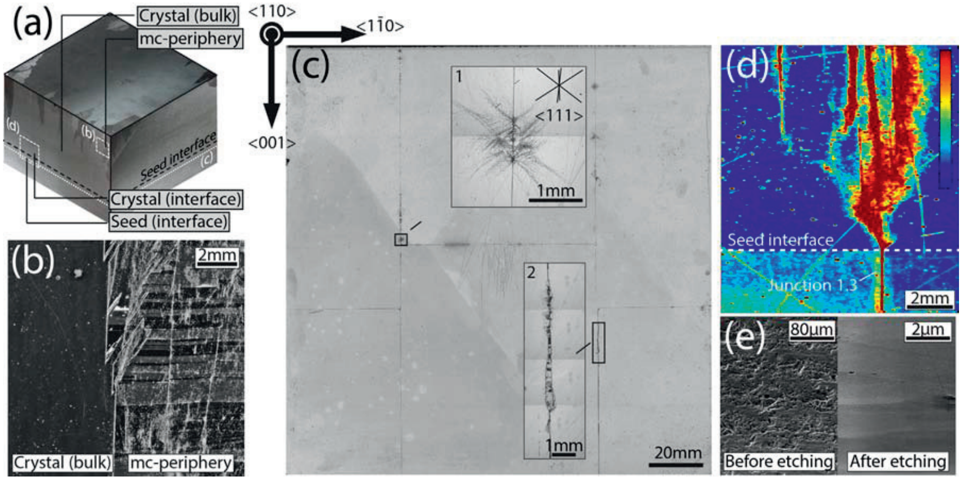

Figure 4 (a) Etch pit densities (EPD) have been measured in bulk monocrystal, peripheral grains, and just above and below the seed interface. (b) Comparison of EPD between the monocrystal and a peripheral grain. (c) A Sopori-etched sample showing the dislocation structures observed just below the seed interface. Dislocation rosettes (1) are frequently found at close-packed junctions and a large cluster (2) has been found in junction 1.6. (d) An EPD-map taken close to junction 1.3 showing a higher average density (light blue) below the seed interface than above (dark blue). (e) SEM images showing the surface roughness of the seeds before and after etching.

seed interface, and the bulk crystal above the seed interface, respectively.

3.1 Dislocations in the multicrystalline periphery

Figure 4(b) shows a magnified area of a transition between the central monocrystal and peripheral grains, revealing a considerable difference in the EPD between the two areas. Because of overlap of etch pits exact concentrations could not be determined, but images clearly show that peripheral grains have considerable higher etch pit concentrations than the main monocrystal.

3.2 Dislocations below the seed interface All seeds are found to grow together, either by sintering or by solidification of melt penetrating between the seeds. Figure 4(c), a Sopori-etched horizontal slab cut from just below the seed interface, shows a continuous structure with grain boundaries forming at the seed junctions. The Laue scanner method measured sub-degree misorientations over all junctions [Fig. 3(b)].

The average EPD count is, just below the seed interface, almost three times higher than the EPD count above the interface, as seen in Table 2. This can also be seen as a bright blue color below the seed interface in the EPD-map shown in Fig. 4(d) which has been taken from the vertical vs2 sample [Fig. 2(b)]. The small-angle grain boundary (SAGB) at junction 1.3 can also be seen as a red line in the same image.

Table 2 The average EPD found just below and above the seed interface, bulk main crystal, and in peripheral grains.

	seed (interface)	crystal (interface)	crystal (bulk)	Mc-periphery
conc. [cm^{-2}]	2×10^4	7×10^3	1×10^3	$\gg 10^3$

Based on previous observations by Ervik et al. [4], the seeds were prepared by grinding and etching in order to reduce the surface roughness and the amount of surface defects on the seed faces. Images taken before and after etching [Fig. 4(e)] show a considerable surface roughness remaining after grinding due to the surface damage inflicted by the grinding particles. Most of the remaining roughness was however successfully removed by the consecutive CP4 etch leaving the seed faces with a wavy morphology with a roughness of approximately 1 μm. Despite careful preparation of the seeds, contact-related dislocation rosettes still frequently appear at close-packed junctions [Fig. 4(c)]. Rosettes are known to form at stress points, such as contact points between seeds and consist of dislocations aligning in <111>-directions, thereby achieving the distinctive rosette-arms seen in (1).

The second feature (2) shown in Fig. 4(c) is a fairly broad dislocation cluster only observed at junction 1.6, which holds the largest 1.6 mm gap. This is suggested to be related to processes happening inside the gap.

SAGBs are composed of dislocations aligning in arrays. Indeed, the SAGBs for all close-packed junctions are found to consist of thin linear arrays of dislocation, both on horizontal and vertical cuts. However, it is remarkable that junction 1.3 also retains a straight alignment of dislocations

[Fig. 5(a)] despite the 0.4 mm gap introduced at this junction.

Junction 1.6, on the other hand, shows a more chaotic dislocation structure, as shown in Fig. 5(b). The majority of the junctions leave a void of height *h* at the crucible bottom [Fig. 5(c)] due to the limited space for melt penetration between the seeds. Such a void is not found for junction 1.6, which holds the biggest gap (1.6 mm). Here, the melt was found to penetrate all the way down to the crucible bottom and resulted in heterogeneous nucleation of secondary grains in the gap, as confirmed by EBSD in Fig. 5(d).

3.3 Dislocations above the seed interface

Low-lifetime areas are, as previously shown in Fig. 3, mainly located directly above seed junctions in the main crystal and can be related to high dislocation concentrations existing at the junctions. It becomes evident that large concentrations of dislocations are generated at the junctions separating the different seeds. In all cases, these can be found to lead back to initial points of generation, located at the intersection between the SAGB and the seed-interface.

Dislocations often move into energetically favorable arrays which can be visualized by using the so-called Thompsons tetrahedron [Fig. 5(e)]. The Thompsons tetrahedron is constructed from the four {111}-planes in the diamond type crystal-structure; such as for silicon. For simplicity, the tetrahedron has been rotated to correspond to the projection of the neighboring SEM images shown in Fig. 6(a) and (d).

Above the seed interface, the dislocations are found to arrange themselves in V-shaped cascades, which in most cases can be related to certain crystallographic directions. The height of the V-shape is found to vary considerably between the different junctions; from a couple of hundred micrometers to several millimeters.

2.Y junctions consisting of {001}/{001} boundary planes, as shown for junction 2.3 in Fig. 6(b), contain initial V-shaped cascades with an angle of approximately 35° to the growth direction. This corresponds well to the theoretic angles of the two opposite <111>-directions in the projected Thompsons tetrahedron. After the initial V-shape, the dislocations align in alternative directions, as shown in Fig. 6(c), which is a continuation of Fig. 6(b). The dislocations now align, with angles of 0° and 56° to the growth direction, perpendicular to the <111>-directions, or parallel to the {110}-facets, instead.

Similar trends are observed for 1.X junctions, consisting of {110}/{110} boundary planes, and are presented by junction 1.1 and 1.4 in Fig. 6(e) and (f), respectively. In this case, the initial dislocations tend to align in V-shaped cascades with angles of approximately 48° to the growth direction, or parallel to the {110}-facets in the Thompsons tetrahedron. As previously seen for junction 2.3 in Fig. 6(c), the dislocations tend to align in alternative directions above the V-shape. In most of the 1.X junctions, dislocations are found to align both parallel (0°) and perpendicular (90°) to the growth direction [Fig. 6(e)]. By comparing these alignments with the Thompsons tetrahedron, it can be found that 0°-alignments may correspond to both <110>- and <111>-direction while 90°-alignments corresponds only to the horizontal <111>-direction. In the case of junction 1.4 [Fig. 6(f)], so little dislocations are generated that no clear

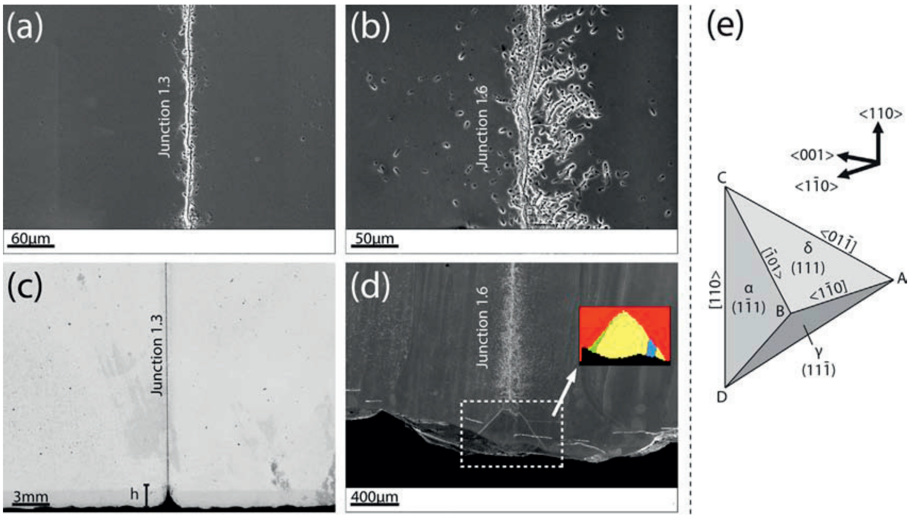

Figure 5 SEM images showing the dislocation structures in junction 1.3 (a) and junction 1.6 (b). (c) Unfinished melt penetration in junction 1.3. (d) Complete melt penetration in junction 1.6 followed by nucleation of parasitic grains. (e) The Thompson's tetrahedron defined by {111}-planes and oriented according to the ingot.

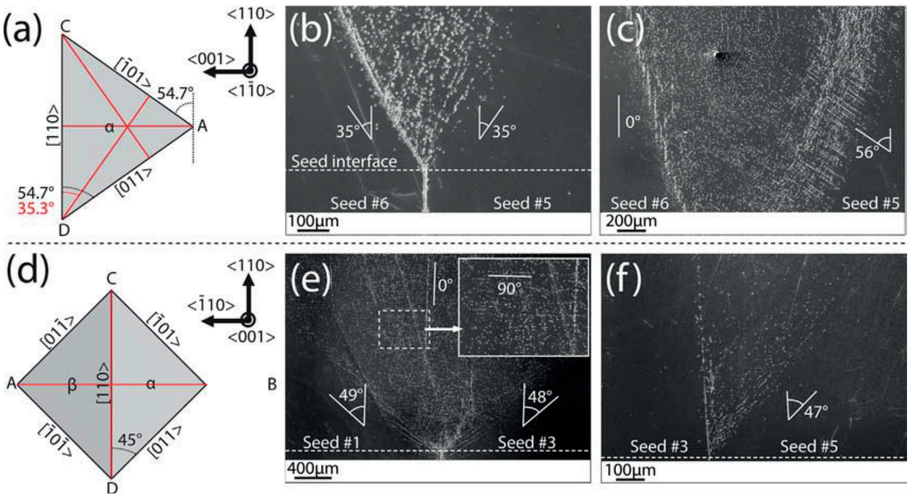

Figure 6 (a) Projected Thompson tetrahedron for junctions (b) and (c). Red lines indicate <111>-directions. (b) V-shaped cascades appearing at the seed interface for junction 2.3. (c) Continuation of the image in (b). (d) Projected Thompson tetrahedron for junctions (e) and (f). V-shaped cascades at junction 1.1 (e) and 1.4 (f).

alignments, apart from what appears to be a continuation of the SAGB from below the seed interface, can be observed.

Figure 7(a)–(g) shows a selection of junctions, imaged from above by conventional light microscopy on horizontally cut wafers, together with the projected Thompson's tetrahedron and EBSD data. The shape of the clusters are clearly defined by dislocations arranging in <111>-directions and in most cases, the clusters are also found to be elongated along a single <111>-direction, as shown for junction 1.1 and 2.3 in Fig. 7(b) and (e), respectively.

All 1.X junctions containing large dislocation concentrations develop elongated clusters, as shown for junction

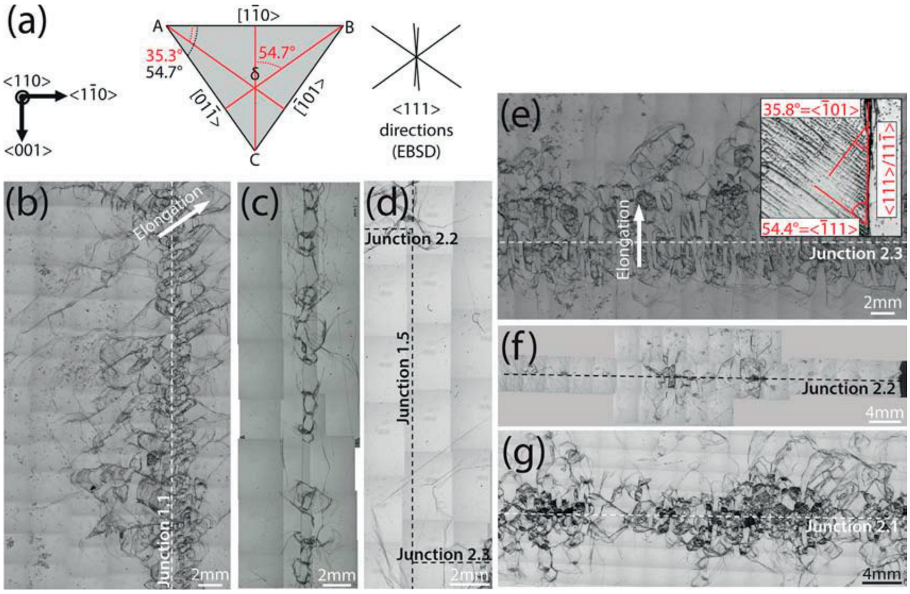

Figure 7 (a) Projected Thompson tetrahedron according to viewing the ingot from above. Dislocation structures observed for junction (b) 1.1, (c) 1.4, (d) 1.5, (e) 2.3, (f) 2.2, and (g) 2.1 at a height of 81 mm.

1.1 in Fig. 7(b). The clusters are elongated with an angle of 54.7° to the boundary plane, which corresponds to the $<\bar{1}11>$-direction from the Thompson's tetrahedron and is common for all the junctions. Junction 1.4 and 1.5 are the only junctions not showing any elongation, assumedly because of the limited generation at both junctions. Junction 1.4 consists of a linear SAGB surrounded by small clusters [Fig. 7(c)] whereas junction 1.5 show no dislocations at all [Fig. 7(d)].

In the case of 2.X junctions, only junction 2.3 [Fig. 7(e)] shows clear elongation, which in this case happens perpendicular to the boundary plane, parallel to both the $<111>$ and $<11\bar{1}>$-directions. A closer inspection of the clusters found in junction 2.3 reveals that the inner parts of the clusters often contains dislocations which are aligned in both $<110>$-and $<111>$-directions, where $<110>$-aligned arrays hold larger etch pit spacing than $<111>$-aligned arrays. Junction 2.2 show no elongated dislocation clusters at all and the dislocation generation is limited to few localized clusters only, as shown in Fig. 7(f). Junction 2.1, on the other hand, shows considerable dislocation generation [Fig. 7(g)] but lacks any clear elongation of the clusters appearing more random than in the other cases.

4 Discussion Parasitic growth in the ingot periphery consists of both randomly oriented grains nucleated on the crucible wall and twinned grains, which arise due to twinning mechanisms happening on the {111}-facet planes of the main crystal. Twinning has shown to be detrimental for the central monocrystalline volume as these grains tend to grow inwards forming a roof above the main crystal [2]. Twinning in mono-like silicon mainly happens on the edges of the ingot, at the triple-point between the growing ingot, the melt and the crucible wall. Mono-like ingots are frequently based on $<100>$-seeds, but because of the orientation of the {111}-planes, they will result in a considerable roof-structure. A corresponding roof structure has also been found in the current $<110>$-oriented ingot, but not as pronounced as previously presented by Trempa et al. [2].

Figure 8(a) and (b) compares the Thompson's tetrahedron for a $<001>$- and $<110>$-ingot, showing a considerable difference in the orientation of the {111}-planes between the two tetrahedra. In a $<001>$-oriented crystal [Fig. 8(a)], all four {111}-planes are inclined toward the growth direction and may therefore initiate roof-formation. A $<110>$-oriented crystal on the other hand [Fig. 8(b)] only have two {111}-planes inclined with the growth direction (δ and γ). The two other planes (α and β) are parallel to the growth direction and can therefore do not form a roof-structure. Any twin growth on these planes will not be as detrimental for the monocrystalline core as on the planes inclined to the growth direction. In the previous work by Trempa [2], one assumed that twinning happens as soon as growth initiated at the seed interface; however, by using the available {111}-facets [Fig. 8(b)] in a simple geometric analysis [Fig. 8(c)], we can estimate at what height two central twins intersect with the edge of the seeds and thereby their initial twinning height. The distance from the imaged vertical section to the seed edge was found to be 29 mm and by employing the inclined {111}-facet (γ), the intersection is found at a height of 53 mm, or approximately 28 mm above the seed interface. This means that twinning does not necessarily happen at the seed interface and we note that if the central monocrystal can be kept from twinning a roof-structure may possibly be avoided.

Peripheral grains contain large amounts of dislocations [5], as observed in Fig. 4(b), and can mainly be attributed to temperature gradients imposed by radial heat fluxes inside

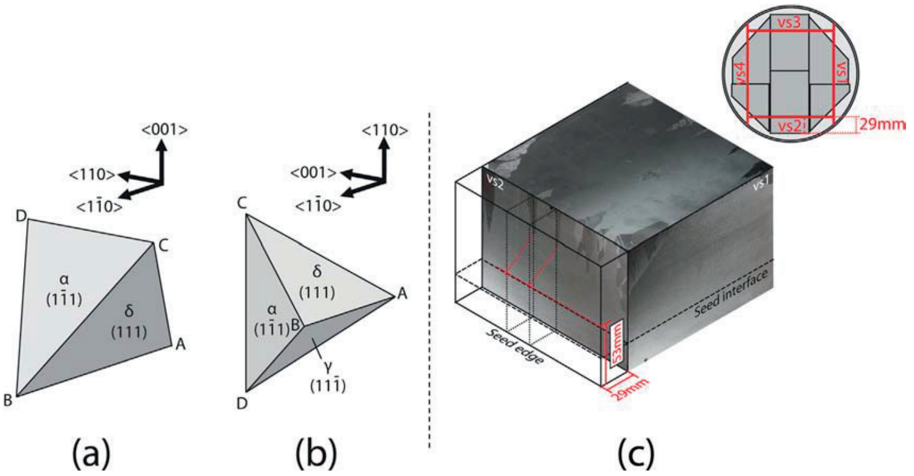

Figure 8 The Thompson's tetrahedron oriented according to an arbitrary (a) $<001>$ and (b) $<110>$ crystal. (c) Two twins extrapolated to the seed edge by following the $<111>$-facets earlier given in Fig. 2(a).

the furnace [13, 14]. However, grain boundaries are known to be strong barriers to dislocation motion and unless strict requirements are met, such as for CSL boundaries, dislocations are not able to move past grain boundaries [16]. A peripheral multicrystalline structure can therefore be beneficial for limiting dislocation movement from the outer periphery into the central monocrystal and can be an explanation for the sudden drop in EPD observed in Ch. 3.1.

4.1 Dislocations below the seed interface

Earlier investigation by Ervik et al. [4] addressed several dislocation sources in industrially grown mono-like silicon and found that the majority of sources could be related to the quality of the seed surfaces and surface preparation. As a result of this investigation, all the seeds in the present study were ground and etched in order to reduce the amount of surface sources. An evenly distributed amount of dislocations of approximately $2 \times 10^4\,\mathrm{cm}^{-2}$ was found in the seeds after solidification. Although we do not have quantitative reference data, the absence of the cell structure observed by Ervik, suggests reduced dislocation generation from surface defects.

The average bulk concentration in the seeds is assumed to be generated mainly from stresses induced by the several kilograms of feedstock placed on top of the seeds. Some of these dislocations will disappear during partial melting of the seeds, but as the seeds are also pushed toward the rough crucible bottom, dislocations can also be generated at this interface throughout the whole solidification process and move into the seeds at elevated temperatures.

As shown in Fig. 5, increased dislocation concentrations are mainly localized at contact-interfaces between seeds, either as small-angle grain boundaries or local dislocation structures resulting from localized stresses. Small-angle grain boundaries develop in order to compensate for misorientation between two crystals [15] and stress concentrators typically develop as a result of indentation [4] or impingement [17]. Indentation leads to formation of star-shaped dislocation rosettes, which in the current ingot are only found at a few locations at close-packed junctions. There is no doubt that a surface with a fine homogeneous surface roughness will lead to less morphological extremes for stress concentration; however, a complete removal of all indentation points is not practically possible. However, dislocation rosettes are highly localized structures and are not found to trespass the seed interface into the main crystal even if they are located close to the interface.

The only way to remove contact stresses was to introduce gaps between the seeds. Neither of the two gaps displayed any dislocation rosettes, but instead suffered from other effects. There is a considerable difference in dislocation generation at the two junctions [Fig. 5(a) and (b)], where junction 1.6 shows a considerably more chaotic structure than junction 1.3. This cannot be related to misorientation as junction 1.3 has a larger misorientation [Fig. 3(b)] than junction 1.6. Instead, three other mechanisms may influence the generation of dislocations in these junctions [Fig. 9(a)]; namely thermal expansion, precipitation, and melt impingement.

Liquid silicon expands during solidification and can potentially lead to stress generation within the gap. Freezing of silicon on the seed walls [Fig. 9(b)] is assumed to take place as soon as the melt starts penetrating the gap, resulting in a horizontal growth component which ultimately may block growth from below. As a result, melt will become trapped or impinged and lead to stresses upon solidification [Fig. 9(c)].

Metallic and other impurities such as oxygen, carbon, and nitrogen are readily available in the furnace and a horizontal growth component could lead to increased segregation and probability of precipitation within the gaps [18, 19]. As precipitates usually have different thermal expansion coefficients than the surrounding silicon matrix, they can therefore lead to additional stress development during cooling of the ingot. However, we do not consider precipitation within the gap to be particularly extensive, mainly due to the limited melt volume within the gap and the purity of the seeds. We would also expect precipitates to result in localized dislocation sources, such as dislocations rosettes [Fig. 4(c)] or other point sources [Fig. 7(f)], which do not correlate well to the long dislocation structure observed for junction 1.6 in Fig. 4(c).

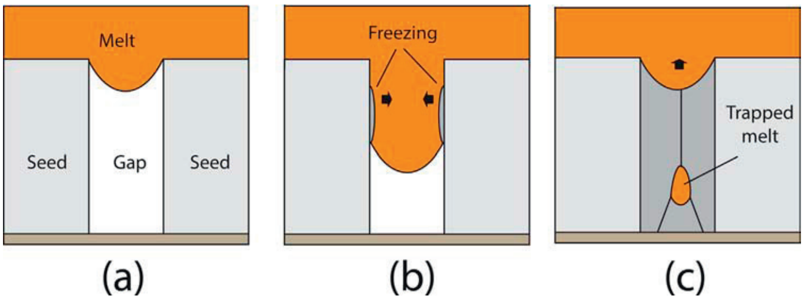

Figure 9 (a) The melt starts penetrating an arbitrary gap between two seeds. (b) Freezing of melt on the seed walls leading to horizontal growth. (c) Melt solidified from below can be trapped leading to stress and dislocation generation.

A fourth contribution to dislocation generation may come from parasitic growth within the junction gap, as shown in Fig. 5(d). As indicated earlier, junction 1.6 is the only junction where melt has reached the crucible bottom resulting in heterogeneous nucleation and growth of randomly oriented grains. In this case, the grains are quickly overgrown by the surrounding seeds, but this can potentially lead considerable polycrystalline growth if the gaps become too large [6].

As a summary of this section, we have seen that seeds placed close together suffers from contact-related stresses generating localized dislocation clusters as rosettes. In order to prevent such stresses junction-gaps had to be introduced and we have seen that by choosing a sufficiently small gap junctions with very little dislocations can be achieved. The absence of dislocations clusters in junction 1.3 (0.4 mm) together with the linearity of the SAGB makes us believe that dislocation generation in this case is mainly related to the misorientation between the two seeds. For the larger junction 1.6 (1.6 mm), a considerable dislocation generation is observed and several processes can be involved, where in this case parasitic growth within the gap is the most obvious one. Because of the limited melt volume within the gap and the purity of the seeds segregation and precipitation within the gap is considered to be limited. On the other hand, as more melt is able to reach the lower parts of the junction, the possibility of melt impingement increases. The observed dislocation generation in this case is therefore assumed to be mainly related to parasitic growth within the gap and melt impingement.

4.2 Dislocations above the seed interface The average dislocation concentration found just above the interface was approximately half of that below the interface (Table 2), implying that dislocations generated in the seed does not necessarily move into the solidified crystal, including dislocations generated at stress points. This is similar to what happens during the stabilization part of the necking process of the Czochralski method [8], i.e., the period where the seed is held in steady state, neither melting nor growing, before the actual necking starts. Chikawa observed by *in-situ* x-ray topography [8] that dislocations in contact with a faceted solid–liquid interface combined and retracted from the interface. This is consistent with reduction in Gibbs free energy at the interface since the spiral step introduced by the dislocation on the interface is removed and because of reduction of the total dislocation length. The slow and gradual change from melting to solidification on the seeds will allow plenty of time for such dislocation reactions to occur.

Dislocations in the main crystal are, as previously presented, mainly located directly above the seed junctions, thereby resulting in areas of low lifetimes [Fig. 3(a) and (b)] throughout the ingot. The initial clusters formed at the seed interface will in most cases continue to grow and multiply throughout the whole ingot height. There are clear trends that the dislocation development at each junction depends on the misorientation between the two corresponding seeds, but a detailed study of the clusters dependence on misorientation will be the basis for a coming paper and the present paper will therefore only give an overview of the current results.

Dislocations show different trends close to the seed interface than higher in the ingot. As shown in Fig. 6(b), the V-shaped dislocation cascades clearly align in <111>-directions for {001}/{001} boundaries, which is a typical recovery structure observed for <211> ½[110] edge-dislocations [9] attained by glide on parallel {111} slip-planes.

The following mechanism is suggested to explain the V-shape of the cascades. Dislocations are released from the small-angle grain boundary as growth proceeds and glide out- and down-wards along the {111}-planes, as shown by an illustration in Fig. 10. At a certain position, they will meet the strain field from previously aligned dislocations and become locked there [15], not able to glide past the plane perpendicular to the {111}-planes. The dislocations contained inside the V-shape may be of other slip-systems and therefore have no reason for aligning in the <111>-directions defining the V-shape; however, they seem not to be able to move past the arrays of <111>-aligned dislocations and their movement are therefore constricted by the V-shape.

As mentioned before, dislocations tend to attain mixed alignments above the V-shape. Observations on vertical sections show that arrays tend to align parallel to the <111>-directions in 1.X junctions [Fig. 6(e)] and parallel to <110>-directions in 2.X junctions [Fig. 6(c)]. Complementary images taken from above on horizontal wafers [Fig. 7(a)–(g)] give a better macroscopic overview of the different junctions. These images show that the shape of the individual clusters in all cases are mainly defined by the projected <111>-directions, independent of junction type. The clusters are in most cases, except junction 2.1, also

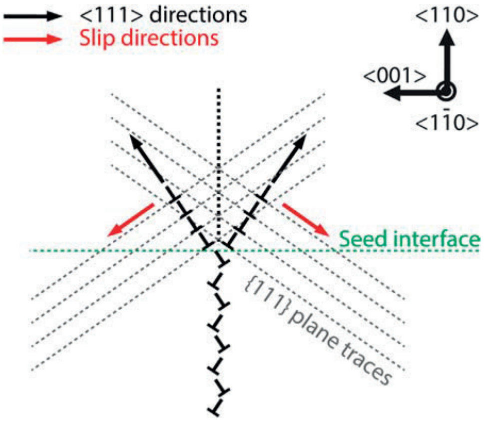

Figure 10 Dislocations initially generated as a linear small-angle grain boundary may slip on {111}-planes into more energetically favorable arrangements close to the seed interface.

elongated in one of the <111>-directions, as shown for junction 1.1 and 2.3 in Fig. 7(b) and (e), respectively. A closer look at the clusters in junction 2.3 [Fig. 7(e)] reveals that dislocations contained within the clusters also align in <111>-directions in addition to the <110>-directions previously observed on the vertical sections. <111>-aligned dislocation clusters can however not be observed in the corresponding vertical cut [Fig. 6(c)] which may be explained by the following two reasons: (1) The vertical section may not cover any of these dislocations and (2) the dislocation lines may be parallel to the cutting plane. The latter of these hypotheses can be confirmed by using the Thompson's tetrahedron.

A possible reason for the more randomized structure in junction 2.1 [Fig. 7(g)] may be related to the initial dislocation generation close to the seed interface. Figure 11 compares the initial generation approximately 3 mm above the seed interface for junctions (a) 2.1 and (b) 2.3, where the latter is the general case observed for most junctions. Junction 2.1 is the only junction showing localized generation at several positions on the junction and may be a result of localized stresses, e.g., from precipitates or contact points. Such stresses may generate additional dislocations, which may interfere with the delocalized dislocation structure preventing the alignment in periodic elongated arrays as seen in all other cases.

By comparing the dislocation structures with the corresponding Laue measurements [Fig. 3(b)], one can see correlations between the extent of the dislocation structures and the misorientation values at the respective junctions (Table 1); large misorientations lead to large extent of dislocation clusters and *vice versa*. For instance, junction 1.5 does not generate any significant amount of dislocations [Fig. 7(d)] and therefore holds no low-lifetime area, which can be related to the particularly low misorientation of 0.03° over the junction. This general trend is valid, except for junctions 1.4 and 2.2, which both show very limited generation despite having relatively high misorientation values. Compare, e.g., the dislocation pattern of junctions 1.4 to 1.1 and 2.2 to 2.3; similar misorientation results in very different dislocation generation. This may be a result of the boundaries having different tilt character. The tilt character of a grain boundary was found by decomposing the total tilt into separate tilts around three principal axes defining the junctions ($X = <001>$, $Y = <1\bar{1}0>$, and $Z = <110>$), as shown in Fig. 3(b). The decomposed tilt values are presented in Table 1 and from these values one can see a considerable difference in tilt character between the mentioned junctions. Although junction 1.4 is tilted mainly around a single axis (Z-axis), junction 1.1 shows comparable tilts around two axes (X- and Z-axis). Simple tilt boundaries can usually be described by arrays of a single edge-dislocation [15], but as the complexity of the tilt character increases multiple dislocation types will be needed in order to successfully describe the boundary. The straightness of the SAGB in junction 1.4 [Fig. 7(c)] may be an indication of the low complexity of the junction, enabling edge-dislocations to align in low-energy configurations along the boundary plane.

Junction 1.2, on the other hand, holds an even lower tilt value (0.17°), mainly around a single axis, but shows considerable wider clusters than junction 1.4. This may be related to the main tilt taking place around the X-axis instead of the Z-axis, possibly leading to generation of dislocation types not able to align along the boundary plane. However, confirmation beyond these observations and assumptions require a deeper understanding of the dislocations dependence on misorientation and further optical characterization by, e.g., Transmission Electron Microscopy and therefore has to be the subject of a later paper. A similar evaluation can be done for junction 2.2, which is also tilted mainly around a single axis (Z-axis), while junction 2.3 shows comparable tilts around multiple axes. The two radial low-lifetime sources found at junction 2.2 [Fig. 7(f)] can be followed down to the seed interface and is assumed to be related to stress concentrators appearing close to the interface.

By comparing junction 1.3 with 1.6, one can observe that junction 1.6 develops smaller dislocation clusters and a thinner low-lifetime area despite its larger gap. The dislocation structures are more likely related to the misorientations measured over the junction than the gap width, indicating that gaps can potentially be employed without considerable dislocation generation. We therefore assume that the reason for junctions containing gaps being prone to considerable dislocation development in literature is mainly related to the increased difficulty in placing the seeds without misorientation.

5 Conclusions The current work reports on several mechanisms resulting in dislocation generation both below and above the seed interface in seed-assisted mono-like silicon. Seed preparation by grinding and etching appear to

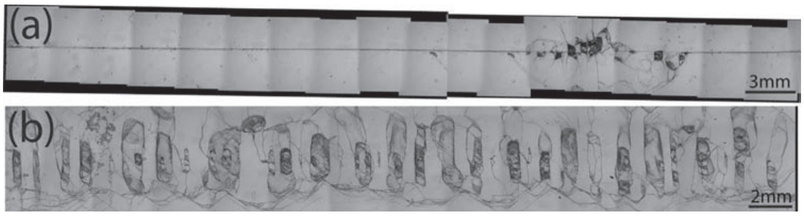

Figure 11 Dislocation structures observed in junction 2.1 (a) and 2.3 (b) approximately 3 mm above the seed interface.

have a positive impact on dislocation generation below the seed interface, but the only way to completely remove contact-related dislocations was to introduce gaps between the seeds. Dislocations generated below the seed-interface however do not necessarily move into the main crystal because of a proposed mechanism similar to the stabilization part during necking in Czochralski growth.

Dislocations in the main crystal are mainly located in clusters aligning above the seed junctions, clearly defined by $<111>$-directions, and the alignment is proposed to take place by glide down- and out-wards on $\{111\}$-planes from the boundary plane between the two corresponding crystals. Introduction of large gaps resulted in considerable dislocation generation both above and below the seed interface because of processes taking place within the gaps, but as long as the gap is kept small, it can be introduced without any noticeable alteration of the dislocation generation at the junctions and in the main crystal. Seed misorientation resulting from imperfect placement of seeds therefore appears to be the decisive parameter both for junctions with small gaps and for junctions without gaps and by attaining sufficiently low misorientations, the bulk lifetime can be retained also over the junctions. Misorientations that produce tilt around several primary axes appear to generate more dislocation clusters than misorientations producing tilt around a single axis only. We propose that this is related to the dislocation structure and hence stability of the SAGB.

Acknowledgements This work was partly supported by The Centre for Environment-Friendly Energy Research (FME) under The Research Council of Norway (RCN) in co-operation with SINTEF Materials and Chemistry.

References

[1] K. E. Ekstrøm, H. Dalaker, A. Autruffe, R. Søndenå, G. Stokkan, L. Arnberg, and M. Di Sabatino, 7th International Workshop on Crystalline Silicon Solar Cells, 77 (2013).
[2] M. Trempa, C. Reimann, J. Friedrich, G. Muller, and D. Oriwol, J. Cryst. Growth **351**, 131 (2012).
[3] A. Jouini, F. Jay, V. Amaral, E. Pihan, and Y. Veschetti, 7th International Workshop on Crystalline Silicon Solar Cells, 89 (2013).
[4] T. Ervik, G. Stokkan, T. Buonassisi, O. Mjos, and O. Lohne, Acta Mater. **67**, 199–206 (2013).
[5] K. Jiptner, Y. Miyamura, H. Harada, K. Kakimoto, and T. Sekiguchi, The 7th International Workshop on Crystalline Silicon Solar Cells, 60 (2013).
[6] M. Trempa, C. Reimann, J. Friedrich, G. Muller, A. Krause, L. Sylla, and T. Richter, J. Cryst. Growth **405**, 131 (2014).
[7] G. Stokkan, Y. Hu, O. Mjos, and M. Juel, Sol. Energy Mater. Sol. Cells **130**, 679 (2014).
[8] J. Chikawa and F. Sato, Inst. Phys. Conf. Ser. **59**, 95–109 (1980).
[9] T. Ervik, M. Kivambe, G. Stokkan, B. Ryningen, and O. Lohne, Acta Mater. **60**, 6762 (2012).
[10] B. L. Sopori, J. Electrochem. Soc. **131**, 667 (1984).
[11] T. Lehmann, M. Trempa, E. Meissner, M. Zschorsch, C. Reimann, and J. Friedrich, Acta Mater. **69**, 1 (2014).
[12] A. J. Nome, S. M. Tangen, J. Hjelen, and T. O. Saetre, 52nd Annual Meeting of the Scandinavian Society for Electron Microscopy, SCANDEM 2001 (2001).
[13] B. Gao, S. Nakano, H. Harada, Y. Miyamura, and K. Kakimoto, The 7th International Workshop on Crystalline Silicon Solar Cells, 23 (2013).
[14] B. Gao, S. Nakano, H. Harada, Y. Miyamura, and K. Kakimoto, Cryst. Growth Des. **13**, 2661 (2013).
[15] D. Hull and D. J. Bacon, Introduction to Dislocations, 4th edn. (Butterworth-Heinemann, Oxford, Boston, 2001).
[16] M. Kivambe, Dislocations in multicrystalline silicon for solar cells, Ph.D. thesis, Norwegian University of Science and Technology (2012).
[17] K. Kutsukake, T. Abe, N. Usami, K. Fujiwara, I. Yonenaga, K. Morishita, and K. Nakajima, J. Appl. Phys. **110**, 083530 (2011).
[18] V. Ganapati, S. Schoenfelder, S. Castellanos, S. Oener, R. Koepge, A. Sampson, M. A. Marcus, B. Lai, H. Morhenn, G. Hahn, J. Bagdahn, and T. Buonassisi, J. Appl. Phys. **108**, 063528 (2010).
[19] M. G. Tsoutsouva, V. A. Oliveira, D. Camel, T. N. Tran Thi, J. Baruchel, B. Marie, and T. A. Lafford, J. Cryst. Growth **401**, 397 (2014).

Microstructure of multicrystalline silicon seeded by polysilicon chips and fluidized bed reactor granules

K. E. Ekstrøm[1*], G. Stokkan[2], A. Autruffe[1], R. Søndenå[3], H. Dalaker[2], L. Arnberg[1], M. Di Sabatino[1]

[1]*Department of Materials Science and Engineering, NTNU, N-7491 Trondheim, Norway*

[2]*SINTEF Materials and Chemistry, N-7465 Trondheim, Norway*

[3]*Institute for Energy Technology, N-2007 Kjeller, Norway*

Abstract

This paper focuses on the microstructures achieved by seeding of multicrystalline silicon by polycrystalline silicon chips and fluidized bed reactor silicon granules. The microstructures are also compared to a conventional multicrystalline silicon ingot grown at similar conditions. Both compartments display a considerable reduction in both grain size and dislocation generation. By a simple texture analysis, we observe that the initially random grain structure develops a weak preference for near-<111> and near-<112> oriented grains upwards in the ingot. Closer investigations of the respective seeds reveal a considerable coarsening of the as-grown microstructure of the seeds during directional solidification, especially for fluidized bed reactor granules. Due to the irregular shapes of polysilicon chips, melt can penetrate into the seeding structure and nucleate below the main seed interface. Ingots seeded with chips may also be more prone to dislocation generation, due to indentation of individual chips. However, the difference in dislocation generation may also be related to a higher ratio of ∑27 grain boundaries in the polysilicon case. Nevertheless, the high density of grain boundaries limits the gettering response of the material, especially for smaller grains, and further performance improvements depends upon improvements to impurity control and/or post-treatment techniques.

Introduction

Multicrystalline silicon (mc-Si) has traditionally been characterized by considerable dislocation generation [1], where dislocations tend to multiply and follow the columnar grains from the point of generation into the ingot, and produce large dislocation clusters. These clusters can readily interact with impurities and form areas with increased recombination activity and reduced minority carrier lifetimes. Post-processing, such as phosphorus gettering, is not effective in removing impurities trapped by dislocations [2], and it is therefore desirable to develop alternative techniques to reduce the amount of dislocations in the final material. One of the most successful techniques is the so-called High-Performance Multicrystalline silicon technique (HPMCSi). HPMCSi is a generalized term that describes certain characteristics of the final material that are superior to those of conventional mc-Si, with an increased ability to reduce the amount of dislocations in the material below what is typically found in mc-Si. In addition to a lower density of dislocation clusters, typical characteristics include smaller grains and increased fractions of random angle grain boundaries [3]. A smaller grain size is not necessarily directly beneficial for the minority carrier lifetime, as this implies an increased amount of grain boundaries. However, as previously shown by Stokkan et al [4], dislocation clusters tend to terminate at random angle grain boundaries and, due to the small grain size, the clusters are not allowed to dominate the structure to the same extent as in conventional mc-Si. A recent study by Yang et al [5] stated that the small grain size was not the sole reason for the lowered dislocation concentration. They argued for the small grains and the large fraction of non-coherent grain boundaries also being beneficial for stress relaxation, thereby also leading to reduced dislocation generation.

There is no strictly defined method for producing ingots with these characteristics, but the most commonly reported method is seeding, where multicrystalline seeds are placed in the bottom of the crucible and partially melted together with the feedstock. This eliminates the initial nucleation step and solidification will initiate by growth on the seed particles instead.

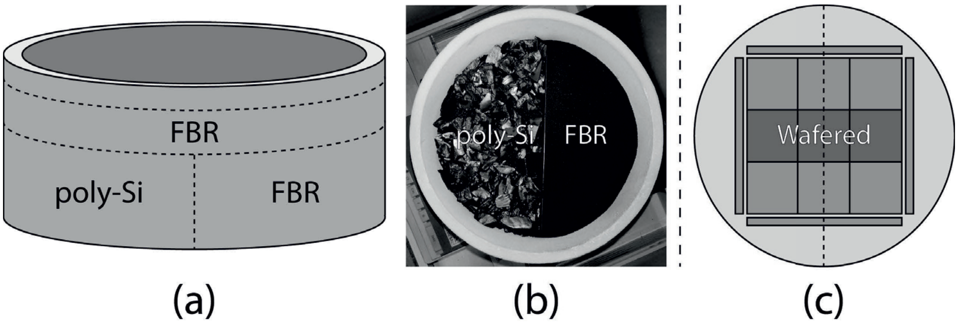

Figure 1. (a) / (b) The crucible was divided into two separate compartments, i.e. poly-Si and FBR. (c) The final ingot was cut into nine 50mm x 50mm blocks surrounded by four 2mm thick vertical blocks for characterization purposes.

Different types of multicrystalline silicon have previously been used for seeding of HPMCSi ingots [6-9], however, the effect of seeding material on the ingot microstructure has, to our knowledge, not previously been published. This work presents a comparison of using fluidized bed reactor (FBR) granules and polysilicon (poly-Si) chips as seeding material. Microstructural characterization has mainly been done by Electron Backscatter Diffraction (EBSD) and etch pit imaging. The material quality has also been assessed by Quasi Steady State Photoconductivity (QSSPC) calibrated photoluminescence (PL) imaging.

Experimental

A. Material solidification and preparation

A 12kg pilot-scale ingot, with a diameter of 250mm and a height of 105mm, has been grown in a Crystalox DS 250 directional solidification furnace. The solidification was performed in a SiO_2-crucible coated with α-Si_3N_4, where half of the seed volume was filled with poly-Si chips and the other half with FBR granules, as illustrated in Figure 1 (a) and (b). The size of the poly-Si chips and FBR granules was approximately 6 – 15mm and 0.4 – 0.9mm, respectively. The seed volume held a total weight of 8.4kg, and a 3.6kg top layer of FBR material was added in order to achieve the desired ingot size. The final ingot was cut into nine 50x50mm blocks surrounded by four 2mm thick vertical sections, as illustrated Figure 1 (c). The central row of blocks was wafered for characterization purposes.

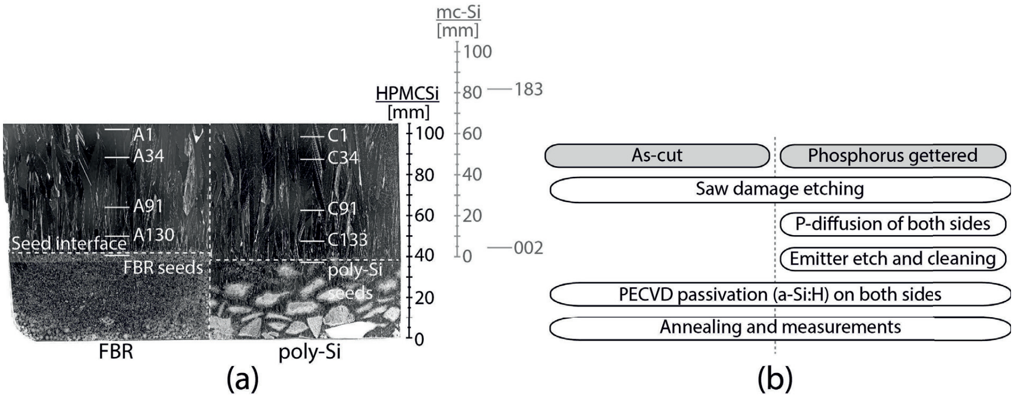

Figure 2. (a) Wafers from the FBR and poly-Si compartments are numbered AX and CY, respectively. Wafers from the conventional mc-Si ingot are marked in a second, light grey, axis. (b) The preparation procedure for photoluminescence-based minority carrier lifetime analysis, both in as-cut and phosphorus gettered state.

B. Microstructural characterization

The microstructure has mainly been characterized by Electron Backscatter Diffraction (EBSD) on near mirror-like polished 50x50mm samples. The samples have been cut from four positions on each side of the ingot, as marked on the vertical section imaged in Figure 2

(a) and are numbered A1 – A130 and C1 – C133 for the FBR- and poly-Si seeded compartments, respectively. Corresponding measurements have also been done on samples cut from just below the respective seed interfaces (i.e. poly-Si and FBR in Figure 2 (a)), and from a conventional mc-Si ingot which has been grown in the same furnace, with similar growth parameters, crucible and polysilicon feedstock. Both ingots were grown with a susceptor temperature of 1808K and a main cooling rate of 0.1 K/min. The z-axis of the mc-Si ingot is also shown in Figure 2 (a). Note that the z-axis of the mc-Si ingot has been adapted so that the point of nucleation (0mm) corresponds to the point of initial growth for the HPMC ingot (~40mm). The data analysis has been performed with the EDAX Orientation Microscopy (OIM) Data Analysis software. Additional characterization of the grain- and defect-structures has been done by conventional microscopy on Sopori [10] etched samples.

C. Minority carrier lifetime measurements

Four pairs of neighbouring sister-wafers (as-cut and phosphorus gettered) were taken from both sides of the ingot, at positions corresponding to those used for microstructural characterization (Figure 2 (a)). The wafers went through the processing procedure illustrated in Figure 2 (b), whereas one of the sister-wafers went through a phosphorus gettering process. The minority carrier lifetimes were then measured on both as-cut and phosphorus gettered samples by PL, and calibrated by QSSPC at 1 sun.

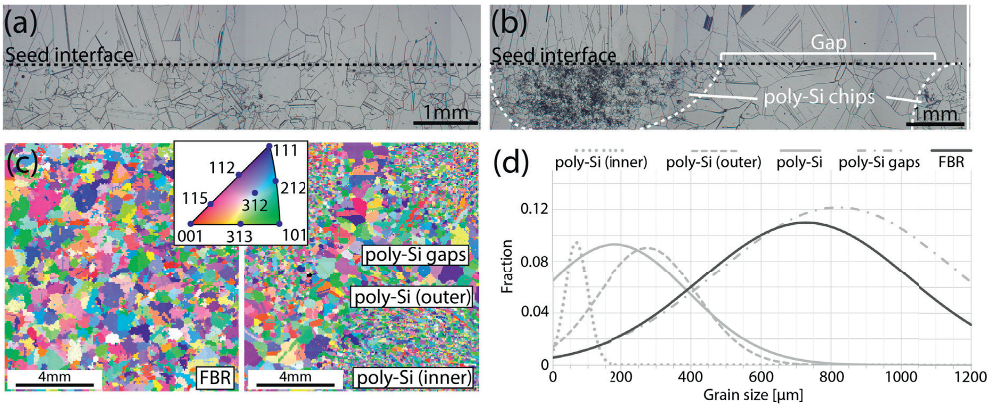

Figure 3. Vertical cuts of the seed interface of the (a) FBR and (b) poly-Si compartments. (c) EBSD images taken just below the respective seed interfaces. (d) The grain size of poly-Si and FBR seeds in the ingot after directional solidification.

Results

A. Microstructural characterization

The microstructure has been characterized in terms of grain size, grain orientation and grain boundary characteristics. Figure 2 (a) shows a Sopori-etched vertical cut of both seed compartments that clearly shows that growth initiates on the top of the seed particles. However, while FBR granules pack closely together (Figure 3 (a)), and result in a uniform structure, there are large gaps between the irregularly shaped poly-Si chips (Figure 3 (b)). Note that the black areas within the poly-Si chips do not represent the grain structure, but an unknown defect structure that appears after the etching step. The gap can also clearly be seen from the EBSD map in Figure 3 (c), as it contains grains with sizes much larger than the default poly-Si grain size. The average grain size for isolated poly-Si chips was found to be approximately 180µm (Figure 3 (d)). However, while the central region of the chips, i.e. poly-Si (inner), had an average grain size of approximately 67µm, the outer rim of the chips, i.e. poly-Si (outer), was found to have an average grain size of approximately 274µm. The grains located within the gaps between the chips were much larger, with an average grain size of approximately 820µm. EBSD scans from the FBR seeds showed a relatively uniform distribution of grains, with an average grain size of approximately 727µm.

An overview of the four EBSD scans taken from above the poly-Si seed interface is shown in Figure 4 (a). The scans from the FBR compartment are similar, and therefore not included.

Grain orientation: As seen from Figure 4 (a) and Figure 4 (b), most of the inverse pole figure is represented throughout the ingot. It can be very difficult to ascertain clustering of grain orientations, and a potential grain orientation preference, from discrete inverse pole figures (IPF) of fine grained materials, due to overlap of discrete measuring points. In order to get an impression of any grain orientation preference a simple texture analysis was done [11]. The texture analysis gives a qualitative overview of the occurrence of different grain orientations in the growth direction of the ingot, relative to a completely random grain structure. The occurrence is represented as a multiple of a completely random structure, indicated by a color scale from blue to red, with a higher number indicating a grain orientation preference. Such maps should be assessed carefully, as, even though the color distribution may indicate a texture, the magnitude of the value may still be too low to describe a texture. In this work we define a minimum value of 2 required for a map to successfully display a texture, which in metallurgical terms is more commonly known as a weak texture.

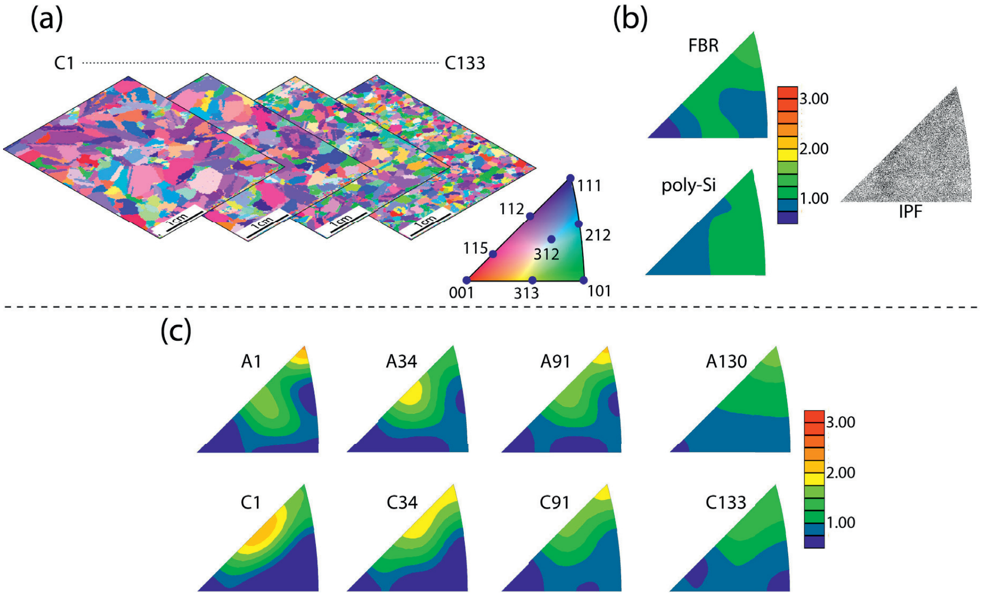

Figure 4. (a) EBSD scans of the four positions of the poly-Si seeded compartment. (b) Texture and inverse pole figure (IPF) of the respective seed particles in the growth direction of the ingot. (c) The texture recorded for the four positions of both compartments.

Texture analysis of the respective seed areas (Figure 4 (b)) gives a maximum value of approximately 1.2, which is a very low value and therefore indicates a random structure with no notable grain preference. This can also be seen from the IPF in the same figure, showing an almost completely even distribution of grain orientations. In the solidified part of the ingot (Figure 4 (c)), there is no clear texture for the lowest A130/C133 wafer pair. However, a weak texture appears as we continue towards the top of the ingot, showing a weak preference for near-<111> and near-<112> oriented grains for both compartments.

Average grain size: As previously seen in Figure 3 (d), the average grain size of the FBR seeds (727μm) after ingot solidification is approximately four times that of poly-Si chips (180μm). However, due to the gaps appearing in-between the poly-Si chips, the average grain size just below the poly-Si interface, as a whole, increases to approximately 706μm, and thereby relatively similar to that of the FBR compartment. In the bottom wafer-pair (A130/C133) the average grain size for the poly-Si compartment is approximately 24% larger than the FBR compartment. This does, however, shift towards the top of the ingot (A1/C1), where the FBR compartment show an average grain size that is approximately 16% larger than the poly-Si compartment. There are, however, some uncertainty related to the average grain size in the top wafers, due to few grains within the scanned areas. The average grain sizes for the HPMC ingot are, on the other hand, considerably smaller than that of the mc-Si ingot. At e.g. wafer 002, which has a position comparable to that of the A130/C133 wafer pair, the average grain size of the mc-Si ingot is approximately a factor 10 larger.

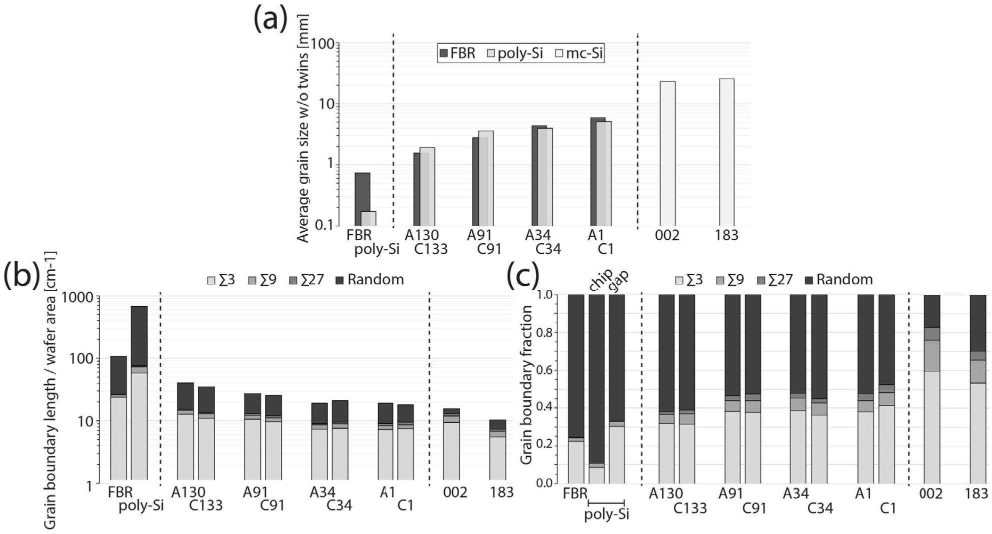

Figure 5. Data extracted from EBSD scans at the positions previously marked in Figure 2 (a), including (a) average grain size, (b) total grain boundary density and (c) fraction of different grain boundary types commonly observed in mc-Si. The data for the poly-Si seeds only covers grains within poly-Si chips, and not gaps. Grains located within the gaps are included as a separate graph in (c).

<u>Grain boundary density and fraction:</u> The grain boundary density is calculated by dividing the length of the different grain boundary types by the respective scan area, and is summarized in Figure 5 (b). Due to the small grain size within the seed particles, the grain boundary density becomes high. The seed material is clearly dominated by random grain boundaries, which contribute to approximately 80% - 90% of the total grain boundary length (Figure 5 (c)). Note that the data for the poly-Si seeds has been isolated from the gaps, where the gaps show a fraction of ∑3-boundaries that is three times larger than within the chips. As the grain size increases towards the top of the ingot, the total grain boundary density reduces. Even though the grain boundary density reduces considerably, the fractions of the most commonly observed grain boundary types change only slightly. The fraction of random angle grain boundaries reduces by approximately 10% towards the top of the ingot, and can be

attributed to a corresponding increase in the fraction of ∑3 boundaries. The conventional mc-Si ingot is to a larger degree dominated by ∑3 grain boundaries, with a fraction above 50%.

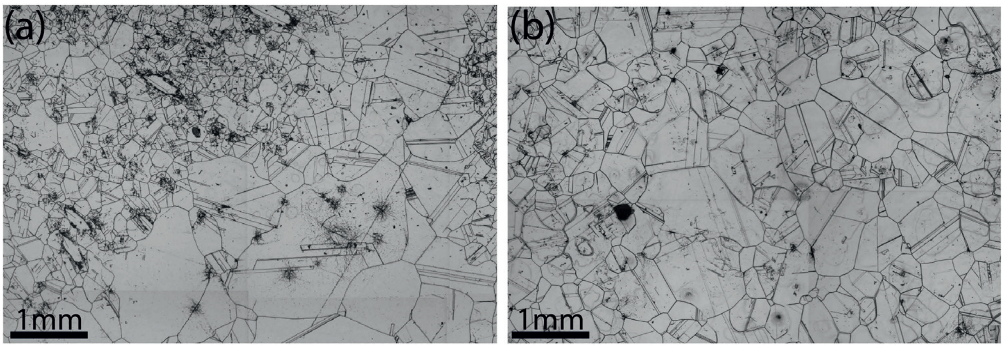

Figure 6. Micrographs of the (a) poly-Si and (b) FBR seed interfaces, where the poly-Si shows large numbers of dislocation rosettes appearing.

<u>*Dislocation density:*</u> The dislocation density has been measured by visual inspection on Sopori etched wafers. Poly-Si chips are found to generate larger amounts of dislocation rosettes, below the main seed interface (Figure 6 (a)), than FBR granules (Figure 6 (b)). Above the seed interface (Figure 7 (a)) the difference between the two compartments is relatively small, with the poly-Si wafer (C133) having approximately 10% more area covered in dislocation clusters than the FBR wafer (A130). This difference does, however, increase towards the top of the ingot, where the top poly-Si wafer (i.e. C1; Figure 7 (b)) has approximately 35% more area covered in dislocation clusters than the top FBR wafer (i.e. A1; Figure 7 (c)). Compared to the mc-Si ingot, where almost 33% of the top measured wafer is covered in dislocation clusters, there is considerably less dislocation generation in both seeded compartments. Position 002 shows a fraction comparable to that of the top-most wafer from the poly-Si seeded compartment.

B. Minority carrier lifetime analysis

The measured minority carrier lifetime maps are shown for the FBR material, in both the as-cut and phosphorus gettered state, in Figure 8 (a) and (b) respectively.

As clearly seen, the wafers have been cut partly into the red-zone of the ingot. The average minority carrier lifetimes are summarized in Figure 8 (c). While the lifetimes are generally below 30µs for the as-cut samples, there is a significant lifetime increase with phosphorus gettering. The difference between the two compartments is small, except at the top-most positions, where there is a 25µs difference in favour of the FBR compartment. In order to study the effect of grain size on the ability to perform efficient phosphorus gettering we define a response to phosphorus gettering parameter, or RPG, as the lifetime after phosphorus gettering τ_{PDG} divided by the lifetime before phosphorus gettering τ_{as-cut} (i.e. in the as-cut state):

$$RPG = \frac{\tau_{PDG,norm}}{\tau_{as-cut,norm}} \qquad \text{(Eq. 3.1)}$$

This parameter has been plotted in Figure 8 (d), and shows that the RPG maximise around 300 - 400 for grains larger than 20mm^2, and decreases to 50 for very small grains.

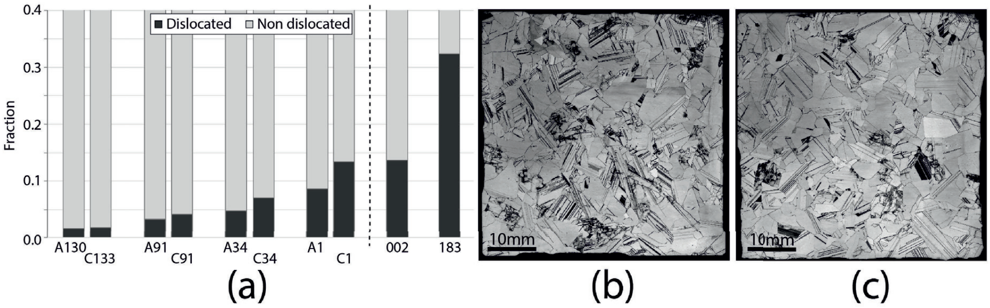

Figure 7. (a) The fraction of the total wafer area covered in visible dislocation clusters for the two ingots investigated. Micrographs of Sopori-etched (b) C1 and (c) A1 wafers.

Discussion

A. Microstructural characterization

Contrary to conventional growth of mc-Si, which initiates by random nucleation on the crucible bottom (Figure 9 (a)), seeded growth initiates directly on top of the seed particles instead. Grains that are in contact with the solidifying melt will act as the foundation for the final structure of the ingot (Figure 9 (b)), and the microstructural characteristics of the final ingot will, to a certain extent, reflect the microstructure of the seed particles. Both seed materials consists of a highly randomized grain structure, as suggested by the wide distribution of grain orientations in Figure 4 (b), and the high fraction of random angle grain boundaries in Figure 5 (c). The grain size of the FBR seed particles are, however, approximately four times larger than that of the poly-Si chips (Figure 3 (d)). Freshly grown poly-Si rods and FBR granules usually show a much smaller size than found in this work. Poly-Si chips usually display feather-like grains, having typical diameters and lengths of 1µm and 10µm, respectively. However, after annealing at 1400°C for 7hrs, the feathers changed into more equiaxial structures with average grain sizes of 4µm [12]. The grain size of FBR granules is even smaller, with an average equiaxial grain size on nanometre scale [13]. This suggests that there is a coarsening of the grain structure when the material is used for seeding purposes. Even though the actual mechanism governing this coarsening is still unknown, the measurements in Figure 3 (d) reveal that the edge of the poly-Si chips have a larger average grain size than the in the middle of the chips, suggesting that the coarsening starts on the surface of the seed particles. As the FBR granules are smaller than the poly-Si chips, they may be more prone to coarsening, thereby explaining the larger grain size.

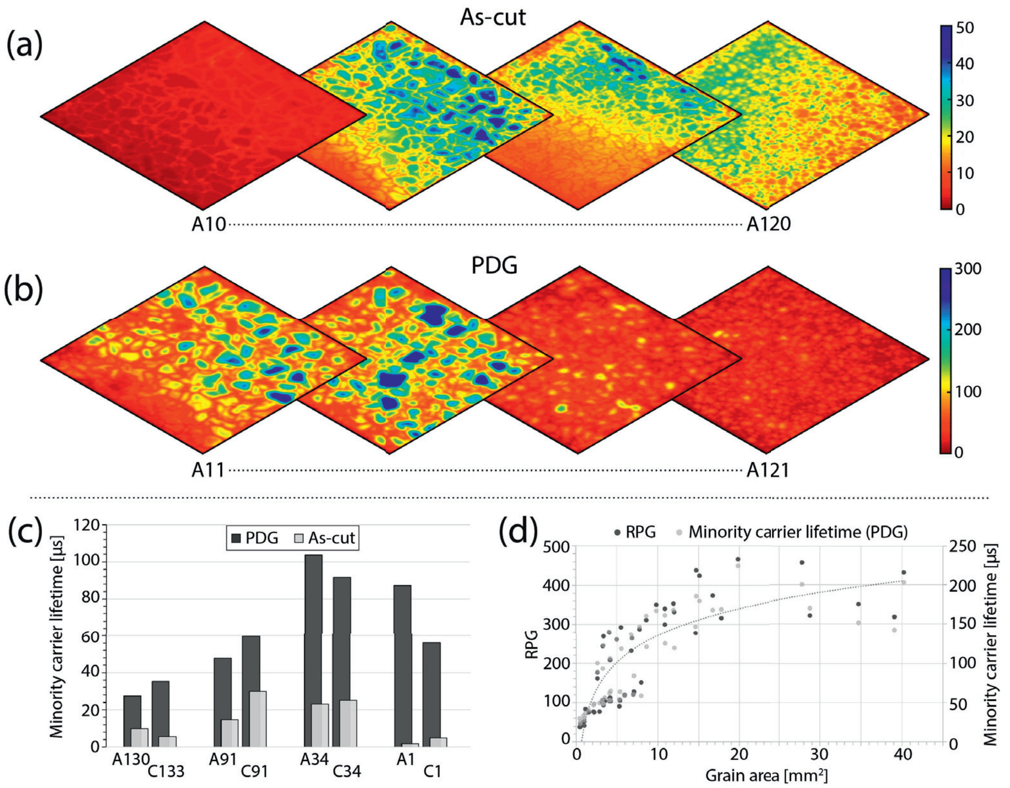

Figure 8. Minority carrier lifetime maps of the (a) as-cut and (b) phosphorus gettered state of the FBR material. (c) The average lifetimes for all positions of the HPMCSi ingot. (d) The response to phosphorus gettering (RPB), as given by Eq. 3.1, and the corresponding increase in lifetime by phosphorus gettering, plotted as a function of grain size.

As previously mentioned, gaps appear between poly-Si seeding chips that allows melt to penetrate into the seed structure and solidify below the main seed interface. The grains forming below the seed interface will grow towards the main seed interface and lead to an increase of the average grain size and grain size distribution found at the main interface. The average grain size (Figure 3 (d)), including the grains within the gaps, was measured to approximately 706µm, which is only marginally lower than the average grain size measured for FBR seeds (727µm). The two compartments have similar starting points in terms of grain size, and display a similar grain size development throughout the whole ingot height. Compared to the conventional mc-Si ingot the average grain size is smaller for both HPMCSi compartments. The grain size and grain structure of conventional mc-Si are mainly governed by grain nucleation and selection taking place during the early stages of solidification [14], and the most common growth conditions for mc-Si therefore typically lead to a grain structure that is dominated by fewer and larger grains already from the point of nucleation.

The initial random grain structure of the seed particles is reflected upwards in the ingot. However, there appears to be some preference for near-<111> and near-<112> oriented grains at higher positions ((Figure 4 (c)). Grain selection is a complex subject, and is still far from completely understood, but the dominance of <112>-oriented grains have been reported in several publications before [7, 15]. There is, however, currently no clear explanation to this phenomenon. One of the groups observed that <112>-oriented grains tend to form by transformation of an initially <110>-oriented grain [15], which may be explained by twinning on {111}-facets existing at the growing liquid-solid interface [16, 17].

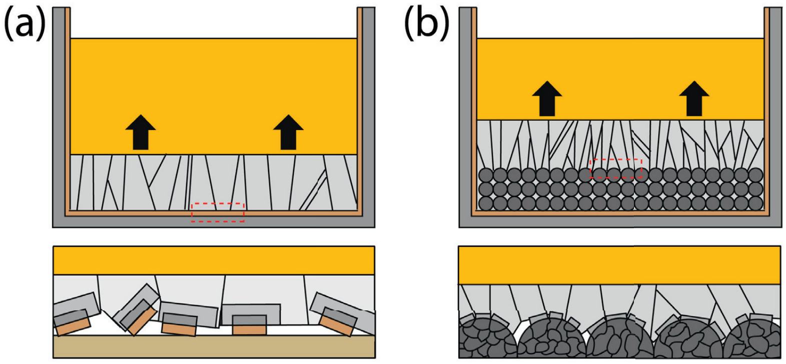

Figure 9. While the microstructure of conventional mc-Si is largely determined by grain selection taking place during nucleation and early growth, the microstructure of (b) seed-assisted solidification is largely determined by the microstructure of the seed particles.

As previously seen in Figure 5 (b) and (c), the seed particles also contain very high grain boundary densities, where 80% - 90% of the total grain boundary length is random grain boundaries. These characteristics are also reflected throughout the ingot, with relatively high

fractions of random angle grain boundaries compared to the conventional mc-Si ingot. The grain boundary density reduces rapidly towards the top of the ingot due to increasing grain size, but the fraction of random grain reduces only from ~60% to ~50% over the same height. The reduction in random angle grain boundaries is accompanied by a corresponding increase in ∑3 boundaries, and is therefore probably related to twinning taking place during the growth process [18]. Conventionally grown mc-Si ingots usually display higher fractions of ∑3 [19], as twins form already at the point of nucleation [20]. The apparent increase in the fraction of random angle grain boundaries towards the top of the mc-Si ingot is probably related to statistical uncertainties, as the top EBSD scan contains very few grains.
The poly-Si chips appear to have approximately half the fraction of ∑3 boundaries of FBR granules (Figure 5 (c)). However, as seen from the neighbouring column in the figure, representing the grains within the gaps, the fraction of ∑3 boundaries has already reached a value of 0.3, suggesting that a considerable amount of twinning happens relatively early in the solidification process.

The concentration of dislocations is significantly lower in the HPMCSi ingot than in the conventional mc-Si ingot, and almost completely absent close to the seed-interface (Figure 7 (a)). While the total area covered by dislocation clusters reaches almost 32% in the top of the mc-Si ingot, it is only 10% - 15% in the top of the HPMCSi ingot. This has previously been related to the combined effect of small grain size and high density of random grain boundaries, which are known to terminate dislocation clusters [4]. The clusters are therefore not allowed to dominate to the same extent, as in conventional mc-Si. There is an increasing fractional difference in the area covered with dislocation clusters towards the top of the two HPMCSi compartments, where the poly-Si compartment have approximately 35% more area covered in dislocation clusters than the FBR compartment. By studying Sopori etched samples cut just below the main seed interface one can observe that poly-Si chips appear to generate more dislocations, in the form of so-called dislocation rosettes, than FBR granules (Figure 6 (a) and (b)). While FBR granules are spherical and pack densely together, poly-Si chips, on the other hand, have a much more irregular shape with sharp edges that can readily indent and scratch neighboring chips. Such indentation points are well-known to lead to formation of dislocation rosettes [21]. Due to the complexity of such rosettes, the dislocations are considered to be relatively immobile and may be why we do not observe the rosettes in the A130/C133 wafer pair. However, such concentration points may still trigger other dislocation sources. Scratches and other surface damages are well-known to introduce dislocations at temperatures above 900°C that may propagate to relieve elastic strain. Another possible source of dislocations at the seed level may be the expansion of melt in-between the seed-particles. Liquid silicon expands on solidification, which may lead to generation of stresses if the expanding liquid meets any form of resistance. Due to the irregular shape of poly-Si chips the stress may distributed inhomogeneously throughout the seed volume, and can therefore potentially lead to areas where the stress exceeds the critical stress limit for plastic deformation [22], resulting in dislocation generation and/or multiplication. The difference in the dislocation concentration in the lowest A130/C133 wafer pair is low, but this may just be related to the clusters still being very small, and thereby having minimal influence on the area fraction containing dislocations at this level. Another explanation may be the influence of ∑27 boundaries, which can act as sites for nucleation of dislocations [18]. The influence can be estimated by calculating the ratio between the density of ∑27 grain boundaries (i.e. generating boundaries) and the density of random angle grain boundaries (i.e. terminating boundaries). This ratio is found to be approximately 67% higher in the C133 wafer than in the A130 wafer, and averaged to approximately 20% higher for the other wafers of the poly-Si compartment, suggesting that the increased density of ∑27 also may explain the increased dislocation generation observed in the poly-Si compartment.

B. Minority carrier lifetime analysis

As-grown multicrystalline silicon ingots are generally known to contain metallic impurities which in the end can be very detrimental to the minority carrier lifetime and final device efficiency [23]. These impurities can, in their dissolved state, be removed from the material by phosphorus gettering [2], which explains the increase in intragranular minority carrier lifetime after phosphorus gettering (Figure 8 (c)). However, defects, such as dislocations and grain boundaries, tend to internally getter impurities and trigger precipitation [24]. Precipitates respond poorly to phosphorus gettering [25], and will therefore reduce the local minority carrier lifetime by increased recombination activity [26, 27]. The recombination activity of grain boundaries has previously been found to depend on the degree of lattice coincidence of the boundary, where higher Coincident Site Lattice (CSL) and non-CSL boundaries are found to have higher activities than lower, and more symmetrical, CSL boundaries [28, 29]. When not containing any dislocation clusters, larger grains tend to have relatively high intergranular lifetimes after phosphorus gettering, as e.g. seen on the top wafers in Figure 8 (b). The lifetime gain (i.e. the lifetime increase from as-cut to PDG state) has been plotted as a function of grain area in Figure 8 (d), and shows a considerable reduction in intragranular lifetime for smaller grains. This suggests that grain boundaries still play a major role in limiting the lifetime of smaller non-dislocated grains, as a higher fraction of the minority carriers will be generated their vicinity, and further improvement to this material depends upon improvements to the gettering and/or other post-treatment techniques.

Conclusions

High-performance characteristics, i.e. small grain, low dislocation density and high density of random angle grain boundaries, were found for both compartments. By a simple texture analysis we observe that the initially random grain structure develops a weak preference for near-<111> and near-<112> oriented grains upwards in the ingot. Closer investigations of the seed structures reveal a considerable coarsening of the default as-grown microstructure of the two seed materials, but appears to be more extensive in the FBR material. Polysilicon chips therefore have the potential of providing ingots with finer grain structure than FBR seeded ingots, but in order to achieve this, one should prevent the gaps that appear due to the irregularities of the chips. Ingots seeded by poly-Si chips may, however, be more prone to dislocation generation than ingots seeded by FBR granules, due to morphological irregularities, and a more uniform granular seed morphology may therefore be better fitted for seeding applications. The small grained structure required for this type of material leads to a high grain boundary density and, combined with the lack of dislocation clusters, grain boundaries become an even more prominent defect.

Acknowledgements

This work was partly supported by The Centre for Environment-Friendly Energy Research (FME), with additional support through the “Impurity Control in High Performance Multicrystalline Silicon” project, both financed by The Research Council of Norway (RCN), and research and industry partners in Norway.

[1] Moller HJ, Funke C, Rinio M, Scholz S. Multicrystalline silicon for solar cells. Thin Solid Films **487**, 179 (2005).

[2] Bentzen A, Holt A, Kopecek R, Stokkan G, Christensen JS, Svensson BG. Gettering of transition metal impurities during phosphorus emitter diffusion in multicrystalline silicon solar cell processing. J Appl Phys **99**, (2006).

[3] Lan CW, Lan WC, Lee TF, Yu A, Yang YM, Hsu WC, et al. Grain control in directional solidification of photovoltaic silicon. J Cryst Growth **360**, 68 (2012).

[4] Stokkan G, Hu Y, Mjos O, Juel M. Study of evolution of dislocation clusters in high performance multicrystalline silicon. Sol Energ Mat Sol C **130**, 679 (2014).

[5] Yang YM, Yu A, Hsu B, Hsu WC, Yang A, Lan CW. Development of high-performance multicrystalline silicon for photovoltaic industry. Prog Photovoltaics **23**, 340 (2015).

[6] Zhu DD, Ming L, Huang ML, Zhang ZY, Huang XM. Seed-assisted growth of high-quality multi-crystalline silicon in directional solidification. J Cryst Growth **386**, 52 (2014).

[7] Wong YT, Hsu C, Lan CW. Development of grain structures of multi-crystalline silicon from randomly orientated seeds in directional solidification. J Cryst Growth **387**, 10 (2014).

[8] Prakash RR, Sekiguchi T, Jiptner K, Miyamura Y, Chen J, Harada H, et al. Grain growth of cast-multicrystalline silicon grown from small randomly oriented seed crystal. J Cryst Growth **401**, 717 (2014).

[9] Hsieh CC, Wu YC, Lan A, Hsu HP, Hsu C, Lan CW. Comparison of defect formations in solar silicon growth from small random and large oriented seeds. J Cryst Growth **419**, 1 (2015).

[10] Sopori BL. A New Defect Etch for Polycrystalline Silicon. J Electrochem Soc **131**, 667 (1984).

[11] EDAX. OIM Data Collection 5.2 Manual.

[12] Fancher RW, Watkins CM, Norton MG, Bahr DF, Osborne EW. Grain growth and mechanical properties in bulk polycrystalline silicon. J Mater Sci **36**, 5441 (2001).

[13] Dahl MM, Bellou A, Bahr DF, Norton MG, Osborne EW. Microstructure and grain growth of polycrystalline silicon grown in fluidized bed reactors. J Cryst Growth **311**, 1496 (2009).

[14] Ekstrom KE, Undheim E, Stokkan G, Arnberg L, Di Sabatino M. Beta-Si3N4 particles as nucleation sites in multicrystalline silicon. (To be published), (2015).

[15] Li TF, Yeh KM, Hsu WC, Lan CW. High-quality multi-crystalline silicon (mc-Si) grown by directional solidification using notched crucibles. J Cryst Growth **318**, 219 (2011).

[16] Tokairin M, Fujiwara K, Kutsukake K, Kodama H, Usami N, Nakajima K. Pattern formation mechanism of a periodically faceted interface during crystallization of Si. J Cryst Growth **312**, 3670 (2010).

[17] Duffar T, Nadri A. On the twinning occurrence in bulk semiconductor crystal growth. Scripta Mater **62**, 955 (2010).

[18] Stokkan G. Twinning in multicrystalline silicon for solar cells. J Cryst Growth **384**, 107 (2013).

[19] Stokkan G, Stoss A, Kivambe M, Ervik A, Ryningen B, Lohne O. Distribution of grain boundary types in multicrystalline silicon. 28th European Photovoltaic Solar Energy Conference and Exhibition, 1418 (2013).

[20] Ekstrom KE, Undheim E, Stokkan G, Arnberg L, Di Sabatino M. Beta-Si3N4 particles as possible nucleation sites for multicrystalline silicon. (Review pending), (2015).

[21] Ervik T, Stokkan G, Buonassisi T, Mjos O, Lohne O. Dislocation foimation in seeds for quasi-monocrystalline silicon for solar cells. Acta Materialia **67**, 199 (2014).

[22] Hull D, Bacon DJ. Introduction to dislocations. 4th ed. Oxford Oxfordshire ; Boston: Butterworth-Heinemann; 2001. vii p.

[23] Green MA. Solar cells : operating principles, technology, and system applications. Englewood Cliffs, NJ: Prentice-Hall; 1982. xiv p.

[24] Autruffe A, M'hamdi M, Ekstrom KE, Schindler F, Schubert MC, Di Sabatino M, et al. Grain structure and iron precipitation in multicrystalline silicon. (To be published), (2015).

[25] Buonassisi T, Istratov AA, Peters S, Ballif C, Isenberg J, Riepe S, et al. Impact of metal silicide precipitate dissolution during rapid thermal processing of multicrystalline silicon solar cells. Appl Phys Lett **87**, (2005).

[26] Kittler M, Seifert W, Knobloch K. Influence of contamination on the electrical activity of crystal defects in silicon. Microelectron Eng **66**, 281 (2003).

[27] Fell TS, Wilshaw PR, Decoteau MD. Ebic Investigations of Dislocations and Their Interactions with Impurities in Silicon. Physica Status Solidi a-Applied Research **138**, 695 (1993).

[28] Buonassisi T, Istratov AA, Pickett MD, Marcus MA, Ciszek TF, Weber ER. Metal precipitation at grain boundaries in silicon: Dependence on grain boundary character and dislocation decoration. Appl Phys Lett **89**, (2006).

[29] Chen J, Sekiguchi T, Yang D, Yin F, Kido K, Tsurekawa S. Electron-beam-induced current study of grain boundaries in multicrystalline silicon. J Appl Phys **96**, 5490 (2004).

High-Performance and Traditional Multicrystalline Silicon: Comparing Gettering Responses and Lifetime-Limiting Defects

Sergio Castellanos, Kai E. Ekstrøm, Antoine Autruffe, Mallory A. Jensen, Ashley E. Morishige,
Jasmin Hofstetter, Patricia Yen, Barry Lai, Gaute Stokkan, Carlos del Cañizo, Tonio Buonassisi

***Abstract*—In recent years, high-performance multicrystalline silicon (HPMC-Si) has emerged as an attractive alternative to traditional ingot-based multicrystalline silicon (mc-Si), with a similar cost structure but improved cell performance. Herein, we evaluate the gettering response of traditional and high-performance multicrystalline silicon. Microanalytical techniques demonstrate that HPMC-Si and mc-Si share similar lifetime-limiting defect types, but have different relative concentrations and distributions. HPMC-Si shows a substantial lifetime improvement after P-gettering compared to mc-Si, chiefly because of lower area fraction of dislocation-rich clusters. In both materials, the dislocation clusters and grain boundaries were associated with relatively higher interstitial iron point defect concentrations after diffusion, suggestive of dissolving metal-impurity precipitates. The relatively fewer dislocation clusters in HPMC-Si are shown to exhibit similar characteristics to those found in mc-Si. Given similar governing principles, a proxy to determine relative recombination activity of dislocation clusters developed for mc-Si is successfully transferred to HPMC-Si. The lifetime in the remainder of HPMC-Si material is found to be limited by grain-boundary recombination. To reduce the recombination activity of grain boundaries in HPMC-Si, coordinated impurity control during growth, gettering, and passivation must be developed.**

***Index Terms*—defects, dislocations, dislocation recombination activity, eccentricity variation, high-performance multicrystalline silicon, minority-carrier lifetime, photovoltaics, recombination, synchrotron.**

I. INTRODUCTION

Given the recent downward price trend for photovoltaic (PV) modules, industry is pressed to reduce costs to improve profitability. Increasing module efficiency is an effective approach to system cost reduction [1, 2]. Because module efficiency is governed in part by wafer quality, industry efforts are focused on reducing wafer defect density while retaining low cost-per-area [3]. In particular, much attention is focused on reducing the density of dislocations, i.e., one-dimensional extended defects, which are among the most detrimental defects in ingot-based multicrystalline silicon (mc-Si) [4-6].

The properties of dislocations have been studied in model structures, such as organized Si/SiGe misfit dislocation arrays [7-9], as well as in industrial multicrystalline silicon [10, 11]. The recombination activity of dislocations has been associated with the decoration of transition metal impurities [12]. A lower dislocation density reduces the number of energetically favorable heterogeneous nucleation sites for metal impurities [13]. During subsequent process steps including phosphorus diffusion gettering and hydrogenation, larger bulk minority-carrier lifetime improvements are observed in silicon with lower dislocation densities [14-19], substantiating the strong empirical link [19-21] between the presence of dislocations and final device performance.

Recent works have detailed the growth methods and structural characteristics of an emerging material referred to as high-performance multicrystalline silicon (HPMC-Si), which has higher quality than mc-Si [22-24]. In contrast to mc-Si, HPMC-Si is known for a lower average grain size and a lower dislocation cluster density due to controlled grain-growth kinetics that render grain boundary (GB) types favorable to a low density of dislocation clusters [25]. However, some dislocation clusters are still present in HPMC-Si.

Because defects, in particular dislocations, can result in an inhomogeneous electrical response after phosphorous diffusion gettering (P-gettering) [13, 18, 19] it is unclear how HPMC-Si responds to P-gettering and how this response compares to P-gettered mc-Si grown under similar conditions. Understanding this response is essential to maximizing the wafer and cell performance, and to guiding future crystal growth developments.

Herein, we study both mc-Si and HPMC-Si materials grown under identical growth conditions (e.g., furnace, crucible, crucible lining materials, and feedstock). Samples are selected for processing and analysis at equal ingot heights to elucidate the differences between their dislocation densities and electrical performances upon P-gettering. We compare and quantify the lifetime improvements of both materials after processing. We correlate local differences in regions of low performance with structural and elemental origins (e.g., dislocations and impurities) to assess the root cause(s) of performance differences between mc-Si and HPMC-Si. We also test and validate a methodology in HPMC-Si, previously proposed in mc-Si material [26], which can help determine the relative electrical recombination activity of dislocation clusters in a rapid manner.

II. MATERIALS AND METHODS

A. Material Growth

To enable comparison on the basis of material properties, HPMC-Si and mc-Si ingots are prepared using the same polysilicon feedstock, growth furnace, crucible, and crucible lining material. Two *p*-type 12 kg pilot-scale ingots, a seed-assisted HPMC-Si ingot and a conventional mc-Si reference ingot, are grown in a Crystalox DS 250 directional solidification furnace. The crucible used for both materials is a Fused Silica Solar Crucible from Vesuvius coated with Si_3N_4 from UBE America, containing approximately 29 ppmw and 10 ppmw of Fe, respectively.

The mc-Si ingot is grown from polysilicon chips with 6N purity with a final ingot diameter of 250 mm and height of 105 mm. Melting is performed over a time span of 420 min at a plateau temperature on the susceptor of 1535 °C (actual temperature in the crucible is lower). The cooling process is split into two parts; the first part has a cooling rate of 0.75 °C/min for 70 min, while the second part has a cooling rate of 0.1 °C/min for 400 min, until complete solidification is achieved.

The section of HPMC-Si ingot studied herein is grown also from polysilicon chips, and in the same crucible as the mc-Si ingot. The time-temperature profile differs from that of the mc-Si ingot in that the melting step is shortened in order to prevent complete melting of the polysilicon feedstock (i.e., leaving a residual seed-layer of polysilicon chips on the bottom of the crucible). Melting is performed at the same susceptor temperature of 1535 °C but over a total time span of 170 min, with a split cooling rate of 0.75 °C/min the first 80 min and a cooling rate of 0.1 °C/min for the remaining 360 min. The final ingot is cut into nine $50 \times 50 \times 105$ mm^3 bricks, and the three bricks in the central row are wafered by a slurry-based wire-saw.

Sample wafers are extracted and laser cut (50 mm × 50 mm × 200 µm) from the same solidified fraction height (f = 0.75) from both mc-Si and HPMC-Si grown bricks, with measured resistivity values of 0.97 Ω-cm and 0.92 Ω-cm, respectively.

B. Minority-Carrier Lifetime Analysis

To conduct minority-carrier lifetime analysis, samples are first saw-damage etched in a HNO_3:CH_3COOH:HF volumetric ratio mixture of 36:12:5 for five minutes, which removes approximately 20 µm from the wafer. Samples are then cleaned in an RCA solution to eliminate organic and metal contaminants prior to surface passivation. Surface passivation is performed by first depositing 20 nm of Al_2O_3 via atomic layer deposition in a Cambridge NanoTech Savannah 200 tool at a temperature of 200 °C, then subsequently annealing the samples at 350 °C for ten minutes in a N_2 environment.

Lifetime is mapped with a Semilab WT-2000 microwave-photoconductance decay (µ-PCD) tool with a pixel resolution of 250 µm, both for the as-grown state and after phosphorus diffusion. Normalized "lifetime ratio" maps are produced by matching spatial coordinates between the as-grown and P-gettered lifetime maps, and dividing their pixel (lifetime) values. The µ-PCD lifetime values are obtained by fitting a single time constant to a decay curve. Given the low generation rate from the μ-PCD technique and the correlation with lifetime values measured by calibrated photoluminescence at low injection, we note that μ-PCD lifetime maps are low-injection lifetime values dominated by Shockley-Read-Hall recombination.

Photoluminescence imaging (PLI) is performed with a pixel resolution of approximately 50 μm. PLI is acquired by illuminating passivated samples with a 25 W, 808 nm, fiber-coupled diode laser, and captured with a PIXIS 1024BR Si CCD camera with an InP wafer and a Schott RG1000 long-pass filter to improve sensitivity.

Interstitial iron concentration (Fe_i) is calculated by measuring lifetime after dissociating iron-boron (Fe_i-B_s) pairs, and then allowing for re-association for 150 min in the dark, then measuring lifetime again by quasi steady-state photoconductance (QSSPC) (Sinton WCT-120) [27, 28]. The calculation and experimental parameters used herein are detailed in [29]. Noise analysis for the Fe_i-B_s measurement technique is based on the analysis for the Cr_i-B_s measurement technique described in [30].

Qualitative, spatially-resolved interstitial iron concentration (i.e., [Fe_i]) maps are acquired with the PLI experimental setup (laser and camera). The maps are acquired after dissociating Fe_i-B_s pairs with the diode laser and allowing for pair re-association.

The impact of grain boundaries and grain size upon P-gettering and its combined effect with intragranular dislocation clusters is assessed on the HPMC-Si P-gettered sample by performing line scans between GBs on a PL image. PLI values are normalized from 0 to 1, with a pixel resolution of approximately 50 μm.

C. *Phosphorous Diffusion Gettering*

Wafers are cleaned prior to gettering using an RCA clean. Phosphorous gettering is performed in a Tystar Tytan 2800 $POCl_3$ furnace, using a time-temperature profile that consists of loading the sample at 700 °C, ramping up to 845 °C, and holding for 30 min before cooling down at a rate of 4.5 °C/min and unloading at 750 °C.

After phosphorous gettering, the samples are etched again in a HNO_3:CH_3COOH:HF solution (volumetric ratio mixture of 36:12:5) for two minutes removing 8 μm in total and the entire formed emitter, cleaned in RCA, and surface-passivated with Al_2O_3 for characterization of the materials' lifetime-performance response to the P-gettering process, with the same lifetime analysis procedure detailed before.

D. *Defect Elucidation and Eccentricity Characterization*

Samples are etched with a Sopori solution (HNO_3:CH_3COOH:HF with a volumetric ratio of 36:15:1) [31] for 45 s followed by a room-temperature dilute KOH quench described in [32] to reveal dislocations intersecting the sample surface as etch pits, averaging 6 μm in diameter. Dislocation etch pits are imaged with a Nikon LV 100 optical microscope at a pixel resolution of 1.46 μm.

A previous study associated dislocation recombination activity with the variance of dislocation etch-pit ellipticity [26]. To quantify the variance of dislocation etch-pit ellipticity, two regions on the HPMC-Si samples are analyzed at a higher pixel resolution of 0.15 μm. From the existing dislocation etch pits in these regions, eccentricity values of the etch pits are computed by fitting the pit major and minor axes, as detailed in [26].

E. *Metal-Decoration Analysis*

To identify the presence of metals decorating dislocation clusters, synchrotron-based micro X-Ray Fluorescence (μ-XRF) measurements are performed at Beamline 2-ID-D at the Advanced Photon Source at Argonne National Laboratory with 10 keV X-ray energy and a 200 nm full-width at half-maximum beam spot size. The selected dislocation etch pits from two different dislocation clusters are scanned via a flyscan method, with a 220 nm step size and a 900 ms dwell time per spot.

III. RESULTS

Fig. 1a shows the change in mc-Si minority-carrier lifetime after P-gettering. The first two µ-PCD maps show the as-grown and P-gettered lifetimes, using the same scale corresponding to lifetime values up to 100 µs. The third frame shows the ratio of P-gettered to as-grown lifetime maps. Lifetime values (i.e., pixels) that did not change after P-gettering have a numerical value of 1. Areas that perform worse after gettering are shown in red, and lighter shades of gray color indicate greater lifetime improvement after P-gettering.

To quantify the differences observed in the lifetime ratio map, the values from both as-grown and P-gettered mc-Si lifetime maps are plotted on the *x*-axis and *y*-axis, respectively, of **Fig. 1c**. The lifetime performance evolution of the mc-Si sample from as-grown and after P-gettering is represented in orange circles. The median lifetime values are binned in 5 µs intervals and shown as yellow triangles. Lifetime performance evolution of HPMC-Si is also shown in gray circles in the background, with their median lifetime values acquired in 5 µs intervals and shown as white squares.

Shown in the same scatter plot are three lines with different slopes denoting: no difference in lifetime between the as-grown and P-gettered state ("1:1"), 50% lifetime improvement by P-gettering ("1.5:1"), and 100% improvement after P-gettering ("2:1"). Two arrows show the tendency of lifetime performance after gettering, with directions towards "Better" (above 1:1 slope line), or "Worse" (below 1:1 slope line) regions. The majority of median values for mc-Si lie below the 1:1 dashed line, indicating a decrease in lifetime after P-gettering. Only median values between ~50 µs and ~60 µs in the as-grown state improved.

Fig. 1b shows two µ-PCD lifetime maps of the as-grown and P-gettered HPMC-Si sample, with the third image corresponding to a ratio between P-gettered and as-grown maps. Color-code and values represent the same performance changes as in **Fig. 1a**. Lifetime values are normalized to the same color bar, corresponding to lifetime values up to 250 µs.

In **Fig. 1d**, the lifetime values from both HPMC-Si as-grown and P-gettered lifetime maps are plotted on the *x*-axis and *y*-axis, respectively. The lifetime performance evolution of the HPMC-SI sample, as-grown and after P-gettering, is represented in green circles, with median lifetime values binned in 5 µs intervals shown as blue squares. Lifetime performance evolution of mc-Si (shown in orange color in **Fig. 1c**) is also plotted in gray circles in the background, with respective median lifetime values shown as white triangles.

Lines with different improvement intensity slopes are also shown. The majority of median values for HPMC-Si lie above the 1:1 dashed line, and in some instances, close to 2:1. An increased performance is observed in low as-grown lifetime regions (~0 to 50 µs), and in higher as-grown lifetime regions (~60 to100 µs).

Lifetime ratio maps for both mc-Si (**Fig. 2a**) and HPMC-Si (**Fig. 2c**) are shown with corresponding [Fe$_i$] maps in **Fig. 2b** and **2d**, respectively. Both ratio maps and [Fe$_i$] maps (acquired after P-gettering) have a yellow-dashed line enclosing a representative region of interest.

Dislocation etch pit maps from the yellow regions in the mc-Si and HPMC-Si samples are shown in **Figs. 2e** and **2f,** respectively. A higher area fraction of densely clustered dislocation etch pits are observed in the mc-Si sample than the HPMC-Si sample. The red (underperforming) areas correspond to regions with dense dislocation clusters in both samples.

Likewise, the underperforming (red) areas also coincide with higher [Fe$_i$] values. Quantitative iron-boron (Fe-B) pair dissociation measurements indicate an average as-grown [Fe$_i$] concentration of 1.3×10^{11} cm^{-3} in an adjacent mc-Si sample. After a standard P-gettering process, the [Fe$_i$] is reduced to 1.1×10^{10} cm^{-3}. The as-grown [Fe$_i$] in the HPMC-Si sample is reduced by 95% from 1.1×10^{11} cm^{-3} to 5.4×10^{9} cm^{-3} upon P-gettering.

A photoluminescence (PL) image of a HPMC-Si region is shown in **Fig. 3a**. Dark regions represent low counts and low lifetime, while bright regions indicate higher counts and relatively higher lifetime. The PL image corresponds to a region of the

HPMC-Si sample that contains dislocation etch pits, as observed in **Fig. 3b**. Dislocation populations 5.6 mm apart are selected from regions with high PL counts (white square on the left) and low PL counts (white square on the right).

The areas enclosed in the white squares are surveyed for etch-pit eccentricity analysis. Optical micrographs of the two surveyed areas are shown in **Fig. 3c**, where the high PL counts region corresponds to the dislocation etch pits shown on the left, and the low PL counts region corresponds to the dislocation etch pits shown on the right.

Frequency histograms of etch-pit eccentricity for each of the dislocation populations are shown in **Fig. 3d**. These histograms demonstrate the total fraction of dislocation etch pits measured with a given eccentricity value, ranging from 0 (perfect circle) to 1 (elongated ellipse). The ellipticity distribution for the population labeled "Low Recombination" (high PLI counts) is narrower than the distribution for the population labeled "High Recombination" (low PLI counts) in **Fig. 3d**.

Regions around the enclosed area in white in **Fig. 3b** are further surveyed with μ-XRF analysis to determine the presence of metal decoration. A total surface area of 912 μm^2 and a total surface area of 606 μm^2 are scanned from the high- and low-recombination activity regions, respectively. The μ-XRF map from the high-recombination activity region is shown in **Fig. 4**. Different elements are measured; however, given the relatively high detection of Fe fluorescence compared to other elements and its known detrimental impact on solar cell performance, only Si and Fe maps are shown. Dark regions in the Si channel are dislocation etch pits, and dark regions in the Fe channel correspond to a higher count rate of Fe-Kα radiation, indicating the presence of Fe-rich particles. A magnified map within the recombination-active region reveals the presence of Fe-rich particles with an area density of up to 0.037 $\mu g/cm^2$. There is no signal above the noise floor of 0.010 $\mu g/cm^2$ detected in the Fe channel for the five recombination-inactive dislocation etch pits surveyed (not shown).

To determine the combined effect of intragranular dense dislocation clusters with GBs — the latter being present in relatively higher density in HPMC-Si — a minority carrier lifetime analysis is performed in the P-gettered HPMC-Si sample across different grains, with and without dense dislocation clusters.

A PL image of the HPMC-Si P-gettered sample is shown in **Fig. 5a**. Dark regions represent low PL counts and relate to low minority-carrier lifetimes, while bright regions indicate high counts and relatively higher lifetimes. The influence of grain boundaries in minority-carrier lifetime is analyzed by performing a linescan analysis between two grains and across a grain boundary, shown by a red line in **Fig. 5b**, where the normalized minority-carrier lifetime variation is shown as a function of distance from the grain boundary. The maximum normalized PLI count is acquired at the center of 65 different grains, indicating their relative intragranular carrier lifetime, and plotted on the *y*-axis of **Fig. 5c**. On the *x*-axis, the distance measured between GBs through their minor axes (conservative proxy for grain size) is plotted. The open circles correspond to grains without dense intragranular dislocation clusters, and red rhomboids correspond to grains with high densities of intragranular dislocations.

IV. DISCUSSION

A striking electronic-quality difference between HPMC-Si and mc-Si is their response to P-gettering. A much larger lifetime improvement is observed after gettering of HPMC-Si than mc-Si, as quantified in **Fig. 1**. For HPMC-Si, 75% of the analyzed wafer area in **Fig. 1** improve after gettering, i.e., have a "lifetime ratio" (final divided by initial lifetimes) greater than one. In contrast, for mc-Si, only 49% of the lifetime values improve upon gettering (i.e., found above the 1:1 ratio line in **Fig. 1c**.)

To assess the root cause(s) of the difference in performance improvement with gettering, microanalytical techniques are employed. Our results show that HPMC-Si and mc-Si share similar lifetime-limiting defect types, yet the relative concentrations and distributions are different. Compared to traditional mc-Si, HPMC-Si contains a smaller area-fraction affected by high dislocation density; those remaining dislocations in HPMC-Si nevertheless exhibit similar characteristics to those in mc-Si. Furthermore, the grain boundaries of HPMC-Si are recombination active, and the recombination activity thereof must be reduced (e.g., through impurity control during growth, gettering, and passivation) to enable high-performance devices.

A. Dislocated Area Fraction Governs Gettering Response

Regions of high dislocation density in **Figs. 2e** and **2f** correspond to red-colored regions (i.e., degraded lifetime after gettering) in **Figs. 2a** and **2c**. We note that the selection of mc-Si and HPMC-Si samples at the same solidification height (*f*=0.75) and crystallization environment ensures consistency in height-dependent variables, such as dopant/impurity segregation and in-diffusion. Therefore, we conclude that differences in gettering response of our HPMC-Si and mc-Si grown under similar conditions can be attributed chiefly to differences in crystal structure and area fraction of high dislocation density. This can be understood in the context of studies of other crystalline-silicon-based materials [13-16, 18, 19], that areas of high dislocation density resist lifetime improvement during gettering.

Although HPMC-Si contained far fewer dislocation-rich regions (and hence, fewer red regions in **Fig. 2c**), our results indicate room for further improvement by reducing the area affected by dislocations. In HPMC-Si, as in mc-Si, the recombination activity of dislocations can be inhomogeneous, warranting a detailed assessment on the impact of such dislocation clusters for further crystal growth and cell processing improvements. For the etch-pit geometry analysis, the two dislocation etch pit populations from HPMC-Si selected are less than 6 mm apart and show a significantly different PL contrast, indicating a difference in electrical recombination activity. We verify a characterization method developed for mc-Si [26] in which the eccentricity variation of the dislocation etch pits can also be used to determine relative recombination activity of a dislocation cluster in HPMC-Si. Literature suggests that when the distribution of the etch pits' eccentricity varies highly, as shown in **Fig. 3c**, metal precipitation at such dislocations is shown to be favorable [26]. The data obtained on HPMC-Si, although limited, is consistent with this trend.

It should be noted that the eccentricity proxy is more effective to study populations of dislocations that are not densely (>10^6 cm^{-2}) clustered, because dense dislocation clusters tend to have a significant amount of overlapping etch pits, inhibiting accurate eccentricity assessment. Dense dislocation clusters, as observed from the plain dark regions in **Figs. 2e** and **2f**, tend to have an ineffective gettering response. These results suggest that further engineering of thermal profiles during growth [4-6, 33, 34] or seeding optimization [35] should be pursued to reduce the concentration of dense dislocation clusters in HPMC-Si.

B. Role of Impurities in Differences of Gettering Response

From studies on other crystalline-silicon-based materials, it is known that the recombination activity of dislocations is enhanced by impurity point defects [8, 11, 36, 37] and precipitates [12]. During gettering, precipitates at structural defects such as dislocations are known to dissolve (partially or fully), releasing metal point-defects into the surrounding material and locally enhancing recombination activity [13, 38]. In contrast, dislocation-free single-crystalline regions with medium- (e.g., Fe) and fast-diffusing (e.g., Cu, Ni) impurities are known to respond well to gettering, resulting in lower impurity point defects after gettering and correspondingly higher bulk lifetimes [13, 15].

Some authors have suggested dividing any crystalline silicon wafer into these two types of region — dislocated defect clusters and defect-free single-crystalline regions — and modeling wafer performance using an equivalent circuit model comprised of these two types of region [20, 21, 39, 40]. One could take this one step farther, and consider the gettering response of the as-grown material in the context of dislocation-rich and dislocation-free regions. Thus the area fraction of dislocation-rich material in the as-grown wafer could be expected to dictate the post-gettering area affected by high concentrations of impurity point defects, and consequently, the as-gettered bulk lifetime.

These observations in other materials appear consistent with our measurements of impurity and minority-carrier lifetime distributions in HPMC-Si and standard mc-Si. μ-XRF indicates some precipitated metals at a recombination-active structural defect cluster in HPMC-Si. Though no metals were detected at the five etch pits analyzed in the recombination-inactive cluster, there are insufficient statistics to render judgment on the absolute absence of metals at other recombination-inactive etch pit clusters. Our results, however, are consistent with previous observations where recombination-inactive dislocations do not tend to coincide with metal-rich precipitates [20]. We therefore posit that the mechanism for preferential metal decoration at energetically favorable heterogeneous nucleation sites (disordered dislocation etch pits) in HPMC-Si is likely similar to that reported in conventionally grown mc-Si.

Distilling the insights of the previous two paragraphs, HPMC-Si contains a smaller area fraction affected by recombination-active dislocations than mc-Si, hence it is unsurprising that an overall lower $[\mathrm{Fe_i}]$ is measured by PLI and QSSPC after P-gettering in HPMC-Si than mc-Si (**Fig. 2**). The lower $[\mathrm{Fe_i}]$ present after P-gettering matches an increased effective lifetime in comparison to mc-Si, as evidenced in **Fig. 1**.

After P-gettering of HPMC-Si, QSSPC measurements indicate a wafer-average $[\mathrm{Fe_i}]$ of 5.4×10^{9} $\mathrm{cm^{-3}}$, which yields a bulk lifetime entitlement of 2.8 ms at $\Delta n=1\times10^{14}$ $\mathrm{cm^{-3}}$. However, the highest measured lifetime in **Fig. 1** is only ~250 μs. We examine several possible root causes for this discrepancy. By repeating the analysis reported in [41], we exclude the BO complex in our material, as we only observe a 6% variation in lifetime influenced by this defect. Remaining possibilities not excluded by experimental data are (i) the presence of other metal point defects, especially non-getterable slow diffusers, and (ii) the presence of sparse isolated dislocations. However, a simpler explanation exists, which also appears supported by the data: If bulk lifetime is large and grain size is small, carriers can diffuse to and recombine at the nearest grain boundary. In the next sub-section, we show this hypothesis to be consistent with our data.

C. Role of Grain Boundaries in Differences of Gettering Response and Residual Recombination Activity

Although some regions degrade during P-gettering of HPMC-Si (i.e., red areas in lifetime ratio map) because of the presence of dislocation clusters, elsewhere, there is a lower-than-expected and inhomogeneous lifetime improvement upon P-gettering. In this section, we posit that GBs limit the intragranular lifetime in HPMC-Si. Two pieces of evidence support this hypothesis: (1) The grain boundaries in HPMC-Si are highly recombination active. The large PL contrast seen at GBs in **Fig. 5a**, and measured through a linescan in **Fig. 5b**, indicate that GBs play a significant role in limiting the as-gettered minority carrier lifetime. GBs in HPMC-Si are predominantly random-angle in character [22], and random-angle GBs are known to be among the most recombination active in silicon, both intrinsically and also when contaminated with iron [42, 43]. Our HPMC-Si samples exhibit measureable concentrations of iron point defects near GBs, as shown in the $[\mathrm{Fe_i}]$ image in **Fig. 2d**. Literature suggests that during P-gettering, iron-silicide precipitates found at GBs [44] can (partially) dissolve [45], releasing point defects into the surrounding material [46, 47]. (2) The lifetime in intragranular regions appears to be strongly affected by carriers diffusing to and recombining at the nearest GB. The impact of grain size is plotted in **Fig. 5c**, where larger grain sizes correspond to higher maximum minority-carrier lifetimes. The open circles in **Fig. 5c** show a consistent trend between the measured maximum PL counts after P-gettering, and distance between GBs. This appears consistent with previous modeling studies in which intragranular bulk lifetime is high and the effective lifetime is governed by point-defect recombination at or near grain boundaries [47, 48]; in such materials, the effective lifetime seldom plateaus at the true bulk lifetime, because carrier diffusion to the nearest recombination-active grain boundary limits the effective lifetime. In contrast, when selecting grains that contain dense dislocation clusters (lower bulk lifetimes), the maximum PL counts computed is significantly depressed, as shown by the red rhomboids in **Fig. 5c**. Grains with dense dislocation clusters tend to have the lowest measured PL counts for a given grain size, when compared to dislocation-free grains. Interestingly, the dense dislocation clusters were mostly found at small grain sizes, and in few quantities, as shown in **Fig. 2f** and illustrated in **Fig. 5c**.

D. Outlook: Integrated Defect Engineering to Improve Bulk Lifetime of HPMC-Si

To mitigate the above effects and further improve bulk lifetime of HPMC-Si, we suggest a three-step approach to reducing GB recombination activity: (i) reduce the concentration of metals entering the as-grown crystal, through judicious selection of crucible and lining materials [49-53], (ii) develop and apply an optimized gettering process to reduce the density of recombination-active metal defects at grain boundaries and other structural defects [38, 45, 54, 55], and (iii) apply an optimized hydrogen passivation process to reduce recombination activity of residual recombination centers at structural defects [16, 56-58].

V. CONCLUSION

To elucidate root causes of different responses to P-gettering between HPMC-Si and mc-Si, we performed a systematic comparative study of the impact of iron point defects and structural defects, namely dislocations and grain boundaries. Identical growth environments and feedstock quality minimize uncontrolled variables. We observe that HPMC-Si achieves a better gettering response than mc-Si because of a significant lower concentration (area fraction) of dense dislocation clusters. After gettering, a higher Fe_i concentration is observed at these dense dislocation clusters and at GBs in both materials, likely the result of dissolving metal precipitates.

Although the concentrations of defects in mc-Si and HPMC-Si are different, the physics governing their recombination activity appears to be similar, offering a path for further improvements in HPMC-Si. As in mc-Si, the recombination activity of dislocation clusters in HPMC-Si was found to be inhomogeneous. We tested and validated a proxy to measure the relative recombination activity of non-dense dislocation clusters in this new industrial material and found that the degree of disorder of the dislocation etch pits can be correlated to the electrical performance of a dislocation cluster. This suggests that some similar approaches might be effective to minimize dislocation density in both HPMC-Si in mc-Si.

The non-dislocated regions of P-gettered HPMC-Si appear to be limited by GB recombination, as evidenced by the tight correlation between grain size and maximum intragranular lifetime. Stated differently, the GB-limited lifetime does not appear to reach the plateau entitled by the bulk point-defect concentration. Reducing GB recombination in HPMC-Si is essential to realize further lifetime improvements. Advanced gettering and passivation, coupled to as-grown impurity control during crystallization, may offer a pathway to achieve this objective

ACKNOWLEDGMENT

The MIT portion of this work was supported by the National Science Foundation (NSF) and the U.S. Department of Energy (DOE) under NSF CA No. EEC-1041895. The NTNU portion of this work was supported by The Centre for Environment-Friendly Energy Research (FME) under The Research Council of Norway (RCN), and was performed in co-operation with SINTEF Materials and Chemistry. C. del Cañizo acknowledges the support of the Department of Mechanical Engineering at the Massachusetts Institute of Technology through the Peabody Visiting Professorship, and the Spanish Ministerio de Economía y Competitividad through the TABACO project ENE2014-56069-C4-2-R. M.A. Jensen and P. Yen acknowledge support from the National Science Foundation Graduate Research Fellowship under Grant No. 1122374. A.E. Morishige acknowledges the support of the Department of Defense through the National Defense Science and Engineering Graduate Fellowship Program. μ-XRF was performed at the Advanced Photon Source, a U.S. Department of Energy (DOE) Office of Science User Facility operated for the DOE Office of Science by Argonne National Laboratory under Contract No. DE-AC02-06CH11357. ALD was performed at the Center for Nanoscale Systems (CNS), a member of the National Nanotechnology Infrastructure Network (NNIN), which is supported by the National Science Foundation under NSF Award No. ECS-0335765.

REFERENCES

[1] T. Surek, "Progress in U.S. photovoltaics: Looking back 30 years and looking ahead 20," presented at the 3rd World Conference on Photovoltaic Energy Conversion, Osaka, Japan, 2003.

[2] A. Goodrich, P. Hacke, Q. Wang, B. Sopori, R. Margolis, T. L. James*, et al.*, "A wafer-based monocrystalline silicon photovoltaics road map: Utilizing known technology improvement opportunities for further reductions in manufacturing costs," *Solar Energy Materials and Solar Cells,* vol. 114, pp. 110-135, 2013.

[3] D. M. Powell, M. T. Winkler, H. J. Choi, C. B. Simmons, D. Berney Needleman, and T. Buonassisi, "Crystalline silicon photovoltaics: A cost analysis framework for determining technology pathways to reach baseload electricity costs," *Energy and Environmental Science,* vol. 5, pp. 5874-5883, 2012.

[4] C. Häßler, G. Stollwerck, W. Koch, W. Krumbe, A. Müller, D. Franke*, et al.*, "Multicrystalline Silicon for Solar Cells: Process Development by Numerical Simulation," *Advanced Materials,* vol. 13, pp. 1815-1819, 2001.

[5] M. M'Hamdi, E. A. Meese, H. Laux, and E. J. Øvrelid, "Thermo-Mechanical Analysis of Directional Crystallisation of Multi-Crystalline Silicon Ingots," *Materials Science Forum,* vol. 508, pp. 597-602, 2006.

[6] D. Franke, T. Rettelbach, C. Häßler, W. Koch, and A. Müller, "Silicon ingot casting: process development by numerical simulations," *Solar Energy Materials and Solar Cells,* vol. 72, pp. 83-92, 2002.

[7] M. Kittler, C. Ulhaq-Bouillet, and V. Higgs, "Influence of copper contamination on recombination activity of misfit dislocations in SiGe/Si epilayers: Temperature dependence of activity as a marker characterizing the contamination level," *Journal of Applied Physics,* vol. 78, pp. 4573-4583, 1 October 1995.

[8] M. Kittler, Seifert, W., Knobloch, K. , "Influence of contamination on the electrical activity of crystal defects in silicon," *Microelectronic engineering,* vol. 66, pp. 281-288, 2003.

[9] D. M. Lee and G. A. Rozgonyi, "Low-temperature gettering of trace iron and copper by misfit dislocations in Si/Si(Ge) epitaxy," *Applied Physics Letters,* vol. 65, pp. 350-352, 1994.

[10] M. Rinio, Peters S., Werner M., Lawerenz A., Moller H.J., "Measurement of the Normalized Recombination Strength of Dislocations in Multicrystalline Silicon Solar Cells," *Solid State Phenomena,* vol. 82-84, pp. 701-706, 2002.

[11] M. Kittler and W. Seifert, "Estimation of the upper limit of the minority-carrier diffusion length in multicrystalline silicon: limitation of the action of gettering and passivation on dislocations," *Solid State Phenomena,* vol. 95-96, pp. 197-204, 2004.

[12] M. I. Bertoni, D. P. Fenning, M. Rinio, V. Rose, M. Holt, J. Maser*, et al.*, "Nanoprobe X-ray fluorescence characterization of defects in large-area solar cells," *Energy & Environmental Science,* vol. 4, pp. 4252-4257, 2011.

[13] A. Bentzen, A. Holt, R. Kopecek, G. Stokkan, J. S. Christensen, and B. G. Svensson, "Gettering of transition metal impurities during phosphorus emitter diffusion in multicrystalline silicon solar cell processing," *Journal of Applied Physics,* vol. 99, p. 093509, 2006.

[14] S. Pizzini, L. Bigoni, M. Beghi, and C. Chemelli, "On the effect of impurities on the photovoltaic behavior of solar grade silicon. II. Influence of titanium, vanadium, chromium, iron, and zirconium on photovoltaic behavior of polycrystalline solar cells," *Journal of the Electrochemical Society,* vol. 133, pp. 2363-73, 1986.

[15] S. A. McHugo, H. Hieslmair, and E. R. Weber, "Gettering of metallic impurities in photovoltaic silicon," *Applied Physics A: Material Science & Processing,* vol. 64, pp. 127-137, 1997.

[16] S. Pizzini, "Chemistry and Physics of Segregation of Impurities at Extended Defects in Silicon," *Physica Status Solidi A,* vol. 171, pp. 123-132, 1999.

[17] A. Bentzen, A. Holt, R. Kopecek, G. Stokkan, J. S. Christensen, and B. G. Svensson, "Gettering of transition metal impurities during phosphorus emitter diffusion in multicrystalline silicon solar cell processing," *Journal of Applied Physics,* vol. 99, p. 093509, 2006.

[18] O. Schultz, S. W. Glunz, S. Riepe, and G. P. Willeke, "High-efficiency solar cells on phosphorus gettered multicrystalline silicon substrates," *Progress in Photovoltaics Research and Applications,* vol. 14, pp. 711-719, 2006.

[19] K. Nakayashiki, V. Meemongkolkiat, and A. Rohatgi, "Effect of material inhomogeneity on the open-circuit voltage of string ribbon Si solar cells," *Electron Devices, IEEE Transactions on,* vol. 52, pp. 2243-2249, 2005.

[20] T. Trupke, J. Nyhus, and H. J., "Luminescence imaging for inline characterisation in silicon photovoltaics," *physica status solidi (RRL) - Rapid Research Letters,* vol. 5, pp. 131-137, 2011.

[21] B. Sopori and W. Chen, "Influence of distributed defects on the photoelectric characteristics of large-area device," *Journal of Crystal Growth,* vol. 210, pp. 375-378, 2000.

[22] Y. M. Yang, A. Yu, B. Hsu, W. C. Hsu, A. Yang, and C. W. Lan, "Development of high-performance multicrystalline silicon for photovoltaic industry," *Progress in Photovoltaics: Research and Applications*, 2013.

[23] C. W. Lan, A. Yu, Y. M. Yang, W. C. Hsu, B. Hsu, and A. Yang, "Development of high-quality multi-crystalline silicon for photovoltaic industry in Taiwan," presented at the 6th International Workshop on Crystalline Silicon Solar Cells, Aix les Baines, France, 2012.

[24] X. Tang, L. A. Francis, L. Gong, F. Wang, J.-P. Raskin, D. Flandre*, et al.*, "Characterization of high-efficiency multi-crystalline silicon in industrial production," *Sol. Energ. Mat. Sol. Cells,* vol. 117, pp. 225-230, 2013.

[25] G. Stokkan, Hu, Y., Mjøs, Ø., Juel, M. , "Study of evolution of dislocation clusters in high performance multicrystalline silicon," *Sol. Energ. Mat. Sol. Cells,* vol. 130, pp. 679-685, 2014.

[26] S. Castellanos, M. Kivambe, J. Hofstetter, M. Rinio, B. Lai, and T. Buonassisi, "Variation of dislocation etch-pit geometry: An indicator of bulk microstructure and recombination activity in multicrystalline silicon," *J. Appl. Phys.* vol. 115, p. 183511, 2014.

[27] D. Macdonald, T. Roth, P. N. K. Deenapanray, T. Trupke, and R. A. Bardos, "Doping dependence of the carrier lifetime crossover point upon dissociation of iron-boron pairs in crystalline silicon," *Applied Physics Letters,* vol. 89, pp. 142107-3, 2006.

[28] D. Macdonald, T. Roth, P. N. K. Deenapanray, K. Bothe, P. Pohl, and J. Schmidt, "Formation rates of iron-acceptor pairs in crystalline silicon," *Journal of Applied Physics,* vol. 98, pp. 083509-5, 2005.

[29] D. M. Powell, J. Hofstetter, D. P. Fenning, R. Hao, T. S. Ravi, and T. Buonassisi, "Effective lifetimes exceeding 300 ls in gettered p-type epitaxial kerfless silicon for photovoltaics," *Appl. Phys. Lett.,* vol. 103, 2013.

[30] M. A. Jensen, J. Hofstetter, A. E. Morishige, G. Coletti, B. Lai, D. P. Fenning*, et al.*, "Synchrotron-based analysis of chromium distributions in multicrystalline silicon for solar cells," *Appl. Phys. Lett.,* vol. 106, p. 202104, 2015.

[31] B. L. Sopori, "A New Defect Etch for Polycrystalline Silicon," *Journal of The Electrochemical Society,* vol. 131, pp. 667-672, March 1, 1984.

[32] D. Berney Needleman, H. J. Choi, D. M. Powell, and T. Buonassisi, "Rapid dislocation-density mapping of as-cut crystalline silicon wafers," *physica status solidi (RRL) - Rapid Research Letters,* vol. 7, pp. 1041-1044, 2013.

[33] B. Ryningen, Stokkan, G., Kivambe, M., Ervik T., Lohne O. , "Growth of dislocation clusters during directional solidification of multicrystalline silicon ingots," *Acta Materialia,* vol. 59, pp. 7703-7710, 2011.

[34] Z. Wu, G. Zhong, Z. Zhang, X. Zhou, Z. Wang, and X. Huang, "Optimization of the high-performance multi-crystalline silicon solidification process by insulation partition design using transient global simulations," *Journal of Crystal Growth,* vol. 426, pp. 110-116, 2015.

[35] K. Kutsukake, M. Deura, Y. Ohno, and I. Yonenaga, "Characterization of silicon ingots: Mono-like versus high-performance multicrystalline," *Japanese Journal of Applied Physics,* vol. 54, 2015.

[36] T. S. Fell and P. R. Wilshaw, "The effect of different transition metals on the recombination efficiency of dislocations," *Journal de Physique IV,* vol. 1, pp. C6-211-216, 1991.

[37] V. Kveder, M. Kittler, and W. Schröter, "Recombination activity of contaminated dislocations in silicon: A model describing electron-beam induced current contrast behavior," *Physical Review B,* vol. 63, p. 115208, 2001.

[38] D. P. Fenning, A. S. Zuschlag, M. I. Bertoni, B. Lai, G. Hahn, and T. Buonassisi, "Improved iron gettering of contaminated multicrystalline silicon by high-temperature phosphorus diffusion," *Journal of Applied Physics,* vol. 113, p. 214504, 2013.

[39] J. Isenberg, J. Dicker, and W. Warta, "Analysis of the effect of diffusion length distributions on global solar cell parameters by simplified 2D modelling," in *EC-PVSEC*, München, p. 1571, 2001.

[40] J. Isenberg, J. Dicker, and W. Warta, "Averaging of laterally inhomogeneous lifetimes for one-dimensional modeling of solar cells," *Journal of Applied Physics,* vol. 94, pp. 4122-4130, 2003.

[41] M. C. Schubert, H. Habenicht, and W. Warta, "Imaging of Metastable Defects in Silicon," *IEEE Journal of Photovoltaics,* vol. 1, pp. 168-173, 2011.

[42] J. Chen, T. Sekiguchi, D. Yang, F. Yin, K. Kido, and S. Tsurekawa, "Electron-beam-induced current study of grain boundaries in multicrystalline silicon," *Journal of Applied Physics,* vol. 96, pp. 5490-5495, 2004.

[43] T. Buonassisi, A. A. Istratov, M. D. Pickett, M. A. Marcus, T. F. Ciszek, and E. R. Weber, "Metal precipitation at grain boundaries in silicon: dependence on grain boundary character and dislocation decoration," *Applied Physics Letters,* vol. 89, p. 042102, 2006.

[44] T. Buonassisi, A. A. Istratov, M. Heuer, M. Marcus, R. Jonczyk, J. Isenberg*, et al.*, "Synchrotron-based investigations of the nature and impact of iron contamination in multicrystalline silicon solar cell materials," *Journal of Applied Physics,* vol. 97, p. 074901, 2005.

[45] D. P. Fenning, J. Hofstetter, M. I. Bertoni, G. Coletti, B. Lai, C. del Canizo*, et al.*, "Precipitated iron: A limit on gettering efficacy in multicrystalline silicon," *Journal of Applied Physics,* vol. 113, pp. 044521-12, 2013.

[46] T. Buonassisi, A. A. Istratov, S. Peters, C. Ballif, Z. Cai, B. Lai*, et al.*, "Impact of metal silicide nanoprecipitate dissolution during rapid thermal processing of multicrystalline silicon solar cells," *Applied Physics Letters,* vol. 87, p. 121918, 2005.

[47] S. Riepe, O. Schultz, and W. Warta, "Redistribution of recombination active defects and trapping effects in multicrystalline silicon after wet thermal oxidation," in *IEEE 4th World Conference on Photovoltaic Energy Conversion*, pp. 956-959, 2006.

[48] G. Micard, Hahn, G., Zuschlag, A., Seren, S., Terheiden, B., "Quantitative evaluation of grain boundary activity in multicrystalline semiconductors by light beam induced current: An advanced model," *J. Appl. Phys.,* vol. 108, p. 034516, 2010.

[49] T. Buonassisi, A. A. Istratov, M. D. Pickett, J. P. Rakotoniaina, O. Breitenstein, M. A. Marcus*, et al.*, "Transition metals in photovoltaic-grade ingot-cast multicrystalline silicon: Assessing the role of impurities in silicon nitride crucible lining material," *Journal of Crystal Growth,* vol. 287, pp. 402-407, 2006.

[50] M. C. Schubert, Schon, J., Schindler, F., Kwapil, W., Abdollahinia, A., Michl, B., Warta, W., "Impact of impurities from crucible and coating on mc-silicon quality—The example of iron and cobalt," *IEEE Journal of Photovoltaics,* vol. 3, pp. 1250-1258, 2013.

[51] R. Kvande, L. Arnberg, and C. Martin, "Influence of crucible and coating quality on the properties of multicrystalline silicon for solar cells," *Journal of Crystal Growth,* vol. 311, pp. 765-768, 2009.

[52] S. Meyer, S. Wahl, A. Molchanov, K. Neckermann, C. Möller, K. Lauer*, et al.*, "Influence of the feedstock purity on the solar cell efficiency," *Solar Energy Materials & Solar Cells,* vol. 130, pp. 668-672, 2014.

[53] E. Olsen and J. Øvrelid, "Silicon Nitride Coating and Crucible—Effects of Using Upgraded Materials in the Casting of Multicrystalline Silicon Ingots," *Progress in Photovoltaics: Research and Applications,* vol. 16, pp. 93-100, 2008.

[54] J. Schon, H. Habenicht, M. C. Schubert, and W. Warta, "Understanding the distribution of iron in multicrystalline silicon after emitter formation: Theoretical model and experiments," *Journal of Applied Physics,* vol. 109, p. 063717, 2011.

[55] A. Haarahiltunen, H. Savin, M. Yli-Koski, H. Talvitie, M. I. Asghar, and J. Sinkkonen, "As-grown iron precipitates and gettering in multicrystalline silicon," *Materials Science and Engineering B,* vol. 159-160, pp. 248-252, 2009.

[56] L. J. Geerligs, Y. Komatsu, I. Röver, K. Wambach, I. Yamaga, and T. Saitoh, "Precipitates and hydrogen passivation at crystal defects in n- and p-type multicrystalline silicon," *Journal of Applied Physics,* vol. 102, p. 093702, 2007.

[57] G. Hahn, P. Geiger, D. Sontag, P. Fath, and E. Bucher, "Influence of hydrogen passivation on majority and minority charge carrier mobilities in ribbon silicon," *Solar Energy Materials & Solar Cells,* vol. 74, pp. 57-63, 2002.

[58] G. Hahn, M. Käs, and B. Herzog, "Hydrogenation in crystalline silicon materials for photovoltaic applications," *Solid State Phenomena,* vol. 156-158, pp. 343-349, 2010.

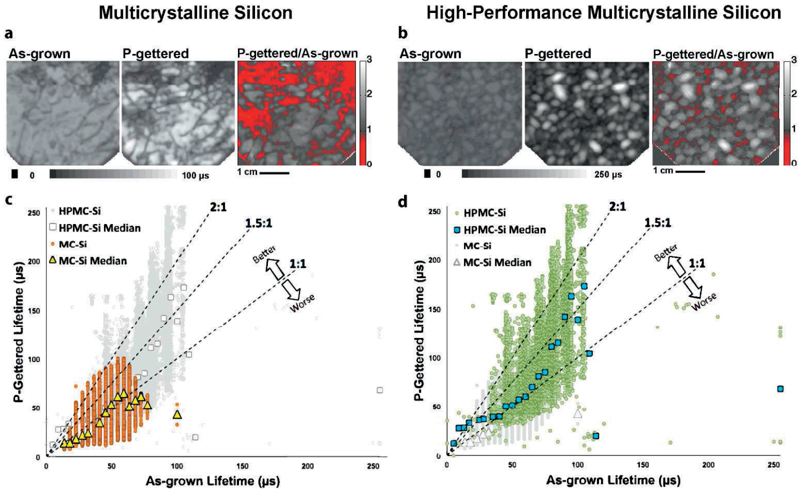

Fig. 1. µ-PCD lifetime images: before P-gettering, after P-gettering, and the ratio of P-gettered/as-grown are shown for (a) mc-Si and (b) HPMC-Si. Red colors in the ratio images (values below 1) denote a decrease in minority-carrier lifetime, and gray scale (values above 1) denotes a lifetime improvement. A scatter plot of P-gettered lifetime vs. as-grown lifetime is shown for (c) mc-Si and (d) HPMC-Si, where the data plotted is the same in both graphs, but the colors emphasize the material being analyzed. In these plots, slopes with different lifetime ratio improvements are shown as 1:1, 1.5:1, and 2:1. Median values for every 5 µs intervals in the as-grown lifetime are shown as yellow triangles for mc-Si, and blue squares for HPMC-Si.

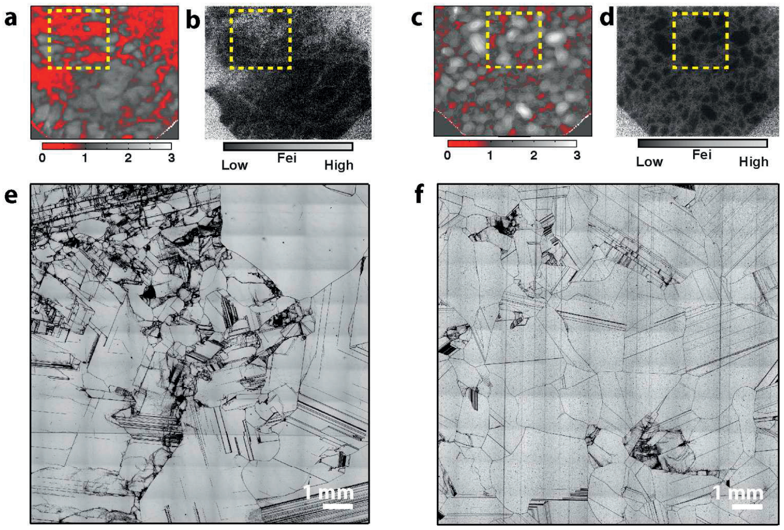

Fig. 2. Lifetime ratio map of (a) mc-Si and (c) HPMC-Si. Qualitative Fei maps for the same samples are shown in (b), and (d), respectively. Microscope images after chemical etching of the yellow-dashed regions are shown for (e) mc-Si and (f) HPMC-Si, where dislocation etch pits are shown as dark spots. These dislocation etch-pit maps are acquired from representative (average-performance) regions within each sample.

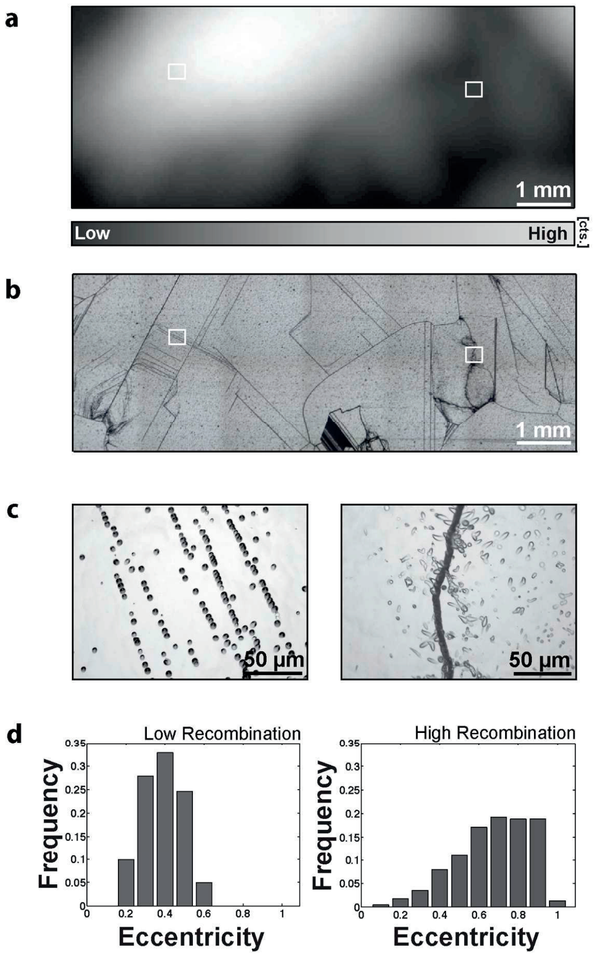

Fig. 3. (a) PLI of a HPMC-Si region with low PL counts regions (low lifetime) shown in dark color, and high PL counts regions (high lifetime) shown in bright color. (b) Light micrograph of the Sopori-etched region corresponding to the PLI from (a), where two dislocations populations (c), one from a low recombination-activity region (left) and one from a high recombination-activity region (right) are selected. The etch-pit eccentricity analysis, for (c) is shown in (d).

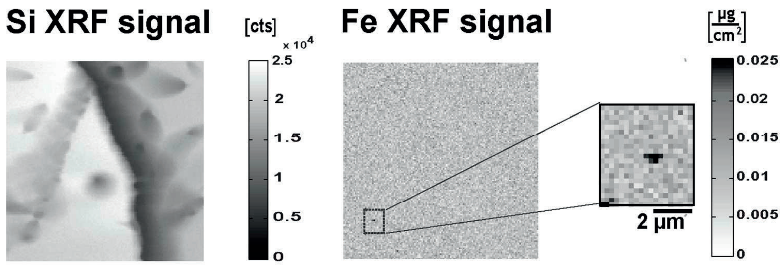

Fig. 4. µ-XRF map from the high recombination activity region selected in Fig. 3(b). X-ray metal point defect analysis shows the presence of Fe precipitates in the vicinity of dislocations from the recombination active cluster. No metal impurity precipitates are found in the surveyed recombination-inactive dislocation etch pits.

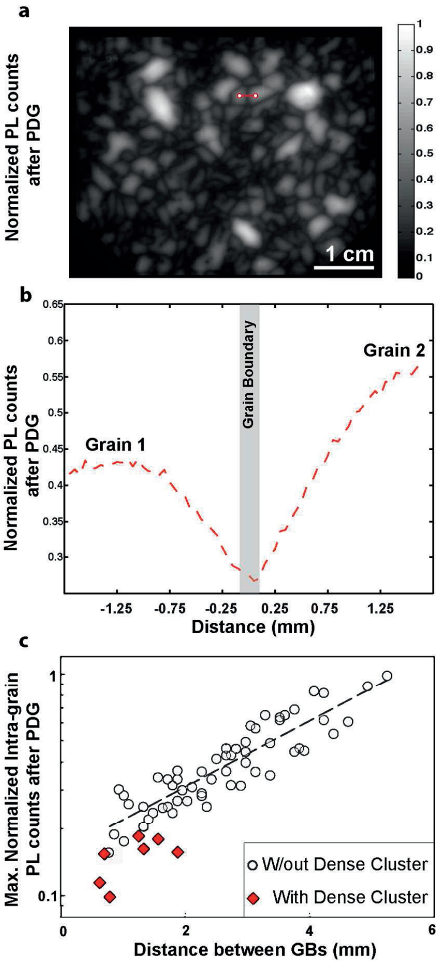

Fig. 5. (a) A PL image of P-gettered HPMC-Si, where dark and bright color represents low and high normalized PL counts, respectively. Red line connecting two grains represents the path for a linescan analysis. (b) Linescan on normalized PL counts between two grains crossing through a grain boundary. (c) Maximum normalized PL counts computed for 65 grains without dense intragranular dislocation clusters (open circles), and with dense intragranular dislocation clusters (red rhomboids)

Beta-Si_3N_4 particles as nucleation sites in multicrystalline silicon

K. E. Ekstrøm[1*], E. Undheim[1], G. Stokkan[2], L. Arnberg[1], M. Di Sabatino[1]

[1]Department of Materials Science and Engineering, NTNU, 7491 Trondheim, Norway

[2]SINTEF Materials and Chemistry, 7465 Trondheim, Norway

* Corresponding author. Tel.: +47 73 55 12 19. E-mail address: kai.e.ekstrom@ntnu.no (K. E. Ekstrøm).

Abstract

This work presents β-Si_3N_4 as being the main nucleation site for multicrystalline silicon grown by directional solidification in crucibles coated with Si_3N_4-based coatings. We argue for initial nucleation occurring on the largest β-Si_3N_4 particles at very small undercoolings, in accordance with the free-growth model, with an increasing nucleation potency for smaller particles as the nucleation undercooling increases. A nearly continuous layer of large β-Si_3N_4 particles is found between the α-Si_3N_4 coating and the solidified silicon, confirming a transformation from α- to β-Si_3N_4 in the presence of liquid silicon. The layer appears to be in contact with the solidified ingot only at localized positions, and the apparent accumulation of parallel twins and other grain boundaries suggest that nucleation has occurred at these positions. We therefore suggest that dendrites have a pronounced effect on the grain structure also for conventionally grown multicrystalline silicon. The unpredictable occurrence of rapidly growing dendrites limits the grain refinement potential for the most common growth conditions. However, this work suggests that a certain degree of refinement can be achieved by utilizing a uniform distribution of large Si_3N_4 particles together with a slow cooling procedure. By engineering the size of the Si_3N_4 particles one should therefore be able to control the initial grain structure and to a certain degree tailor the final grain structure of the ingot.

Keywords: Silicon, Nucleation, Solidification, Grain refinement, Microstructure

1. Introduction

The combined demand for high performance solar-cells and reduced production costs stresses the importance of improving the crystal quality of silicon grown by the inexpensive directional solidification method. Considerable work has therefore been done to understand the mechanisms which determine the grain structure of the ingots, potentially leading to improved quality of the crystals grown by this method. This research has so far lead to two main approaches; the first consisting of imposing large undercoolings to the initial growth step in order to promote dendritic growth [1, 2] and the second utilizing different seeding techniques in order to avoid the nucleation step altogether [3, 4]. However, such methods bring additional costs and other challenges to the production process, and we suggest that new and even more potent methods can be developed by focusing on the understanding of the actual nucleation mechanism instead.

It is widely accepted that nucleation takes place on inoculant particles in contact with the molten silicon feedstock [5] by heterogeneous nucleation, and grains in multicrystalline silicon are generally found to nucleate on the crucible bottom and grow as elongated grains parallel to the temperature gradient towards the top of the ingot.

The crucibles used in the solidification process are usually coated with a thin layer of α-Si_3N_4 particles to prevent sticking of the ingot to the crucible, and as these coating particles are in direct contact with the melt they are clearly involved in the initial nucleation process. However, for particles to act as potent inoculants, certain criteria need to be fulfilled. Classical nucleation theory states that, in order for a nucleus to become stable and grow into a macroscopic crystal it needs to reach a certain critical size [5]. Potent inoculants therefore have to provide crystallographic facets with sizes allowing particles with this critical size [6, 7] to form. The critical size of a nucleus (r_{het}^{*}) can be expressed as in Eq. 1.1, where y_{SL} is the interfacial energy between the newly formed solid nucleus and the surrounding liquid, T_m is the melting temperature, ΔH_v is the enthalpy of change for solidification and ΔT is the nucleation undercooling.

$$r_{het}^{*} = \frac{-2\gamma_{SL}T_m}{\Delta H_v \Delta T} \tag{1.1}$$

Due to the dependence on nucleation undercooling, numerous studies have been performed on measuring the nucleation undercooling for silicon on different substrates in silicon melts [8-12]. The measured temperatures do however span over several magnitudes (2 – 150K), as clearly seen in Fig. 1, also within the same sample sets, making it difficult to find any clear trends in terms of the nucleation potency. The variations found within sample sets can be assumed to be related to nucleation on impurities instead, and not necessary on the substrate under investigation. Therefore one typically assumes that the actual undercooling for nucleation on the substrate is the maximum undercooling measured within each sample set. Most of the measurements have been reported by Appapillai et al [10], but smaller sample sets from Brynjulfsen et al [8] and Tsoutsouva et al [12] have also been included. The grouping is based on the inner-most layer which is in direct contact with the silicon melt, and includes dry- and wet-oxidized silicon (Si), fused quartz (SiO_2), deposited amorphous Si_3N_4 (a-Si_3N_4), α-Si_3N_4 coating and Al_2O_3 crucible material. While SiO_2 substrates reach maximum undercoolings above 100K, Si_3N_4 substrates appear to favour undercoolings below 40K, suggesting that Si_3N_4 substrates are more potent inoculants. The reason for the comparable values of amorphous Si_3N_4 (a-Si_3N_4) and the crystalline α-Si_3N_4 coating may be related to a transformation of a-Si_3N_4 into a crystalline β-Si_3N_4 phase, as previously observed by Alphei et al [13]. The increase in nucleation undercooling for the Si/SiO_2/Si_3N_4 40nm sample was explained by Appapillai in terms of thermal stresses between the two layers, but may also just be a result of an increased influence from the underlying SiO_2 layer due to the $S_{i3}N_4$ layer being very thin. Tsoutsouva et al performed measurements on two fused silica products and found only a small difference in the measured nucleation undercooling. However, the reported sample size is small and the values are within the variance of the measurements done by Appapillai and Brynjulfsen, and clear conclusions cannot be made.

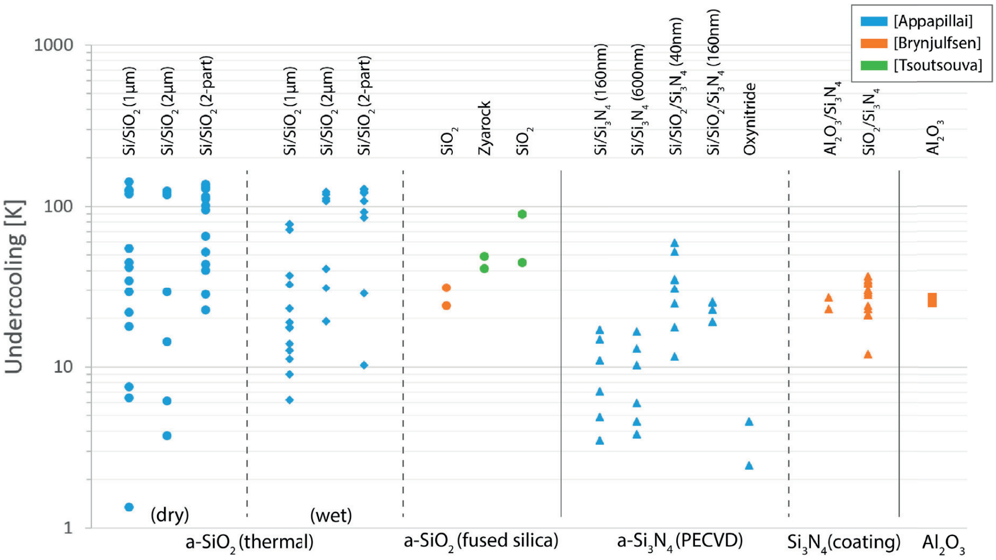

Fig. 1. Overview of nucleation undercoolings as measured by Appapillai et al [10], Brynjulfsen et al [8] and Tsoutsouva et al [12] for different substrates. Grouping is based on the innermost layer which is in direct contact with the melt; including dry and wet oxidized silicon (Si), fused quartz (SiO_2), deposited amorphous Si_3N_4 (a-Si_3N_4), α-Si_3N_4 coating and Al_2O_3 crucible material.

In all these studies the authors employ techniques to detect crystallization through changes in some macroscopic property, techniques which we believe do not correctly capture the initial stages of nucleation and real melt conditions present during directional solidification. Calorimetric techniques, as employed in the first study by Brynjulfsen et al [8] and in the studies by Appapillai et al [9, 10], are unfit for detecting initial nucleation as the change in the heat flow is too small to be detected. The reported values do instead indicate when the collective size of all nuclei, i.e. the solid phase, is large enough to produce a detectable change in the heat flow. The later work by Brynjulfsen et al [11] and a more recent work by Tsoutsouva et al [12] employed equipment for detecting recalescence. The undercooling was reported as the temperature difference between the melting point of silicon and the onset of recalescence. However, nucleation theory states that nucleation proceeds only until the total latent heat release is sufficient enough to cause recalescence [5, 14, 15], as illustrated in Fig. 2 (a). This implies that the nucleation undercooling ΔT in these works is overestimated and that initial nucleation takes place much sooner and at lower undercoolings. At the point of recalescence the latent heat release is large enough to counter the heat flow induced by cooling, leading to a temperature increase, loss of undercooling and final cease of nucleation.

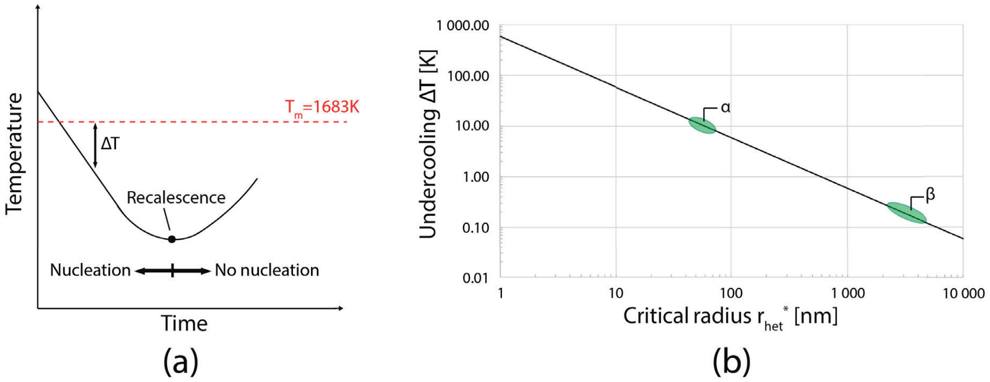

Fig. 2. (a) A typical cooling curve for silicon solidification is illustrated. The undercooling ΔT increases continuously until the onset of recalescence and loss of undercooling. Nucleation stops at the point of recalescence [7]. (b) The critical radius (r^*_{het}) calculated, from eq. 1.1, as a function of nucleation undercooling; $\gamma_{SL} = 0.68\frac{J}{m^2}$ [16], $\Delta H_v = 46.6\frac{kJ}{mol}$ [17], $T_m = 1683K$ [17]. The measured size distribution for α- and β-Si_3N_4 are also marked in this figure.

The so-called free-growth model [7], a well-established model for grain-refinement in aluminium solidification, states that nucleation initially occurs on favourable inoculant particles at very low undercoolings, and on the largest and most favourably orientated facets.

Progressively smaller inoculant particles will become active as the undercooling increases. The dependence of the critical radius on nucleation undercooling has been plotted in Fig. 2 (b), showing a considerable increase in nucleation undercooling for sub-micrometre radii.

The radius of the nuclei will be limited by the smallest dimension of the crystallographic facet of the inoculant, and the small size generally found for α-Si_3N_4 coating particles (< 1μm [6]) is therefore not consistent with nucleation at small undercoolings. However, a much larger β-polymorph of Si_3N_4 (β-Si_3N_4) is frequently found in solidified silicon [18, 19]. Both polymorphs are known to have hexagonal crystal structures which are closely related to each other [20]. Beta-Si_3N_4 particles are believed to form by dissolution of α-Si_3N_4 followed by re-precipitation [19, 21], and are frequently found as needles with sizes of several of tens to above several hundreds of micrometres, with correspondingly large hexagonal facets [18, 19]. Precipitated β-Si_3N_4 have already been suggested as potent inoculants by several authors [6, 13, 22], with measured undercoolings down to 1-2K. These particles have also shown to lead to structure loss in monocrystalline silicon ingots grown by the non-contact crucible method developed by Nakajima et al [23]. The particles show very low lattice mismatch (~1%) to silicon [24, 25], which ensures a low interfacial energy between the particle and the silicon nucleus and thereby promotes a high catalytic potency [7] towards silicon nucleation. Large β-SiC particles are also present in silicon ingots [19] which also have shown to act as potential inoculants for silicon [26, 27], but with a much larger crystallographic mismatch (~20%) to silicon [28]. We therefore argue for preferable nucleation of silicon on β-Si_3N_4 inoculants with low nucleation undercoolings (i.e. the undercooling required to reach the critical radius of the nucleus), and possibly below 1K.

Inoculant particles active during the initial stages of directional solidification must be situated in the bottom parts of the melt, and the current study therefore focuses on locating particles on bottom cuts from grown ingots. Features and particles of interest are mainly studied by

Scanning Electron Microscopy (SEM) assisted by Energy Dispersive Spectroscopy (EDS) for qualitative composition analysis. Possible nucleation points are also revealed by Sopori etching and discussed in terms of existing literature.

2. Experimental

The current work is divided into two parts. The initial part consisting of an initial investigation of the size distribution and morphology of α-Si_3N_4 before solidification, and the main part of locating possible inoculants on bottom slices cut from solidified ingots.

2.1. Investigation of as-coated sample

A small silicon slab was spray-coated with α-Si_3N_4 coating. The size distribution and morphology of the coating particles were then investigated by Scanning Electron Microscopy (SEM). Firing of the coating was not performed in this part of the investigation to prevent formation of oxide-particles.

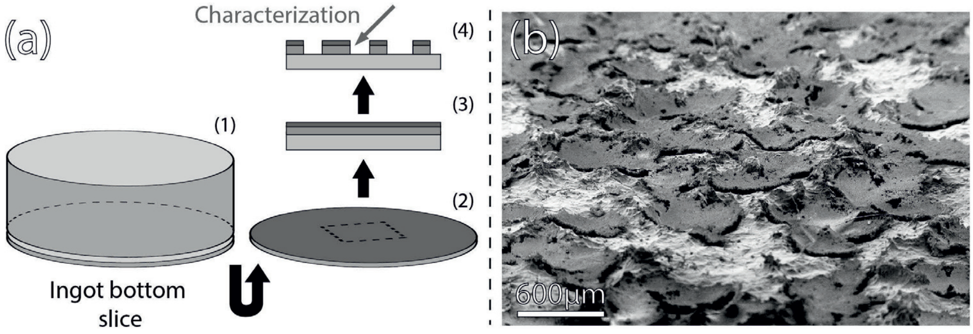

Fig. 3. (a) Characterization has been performed on the bottom face of slices cut from ingot bottoms (1-2). Most of the bottom slices were completely covered in residual coating (3), and the samples had to be etched in order to access underlying particles (4), resulting in the final morphology shown in (b).

2.2. Investigation of solidified ingots

Bottom slices were cut from a 12kg pilot-scale conventional multicrystalline ingot and an industrially grown high-performance multicrystalline (HPMC) ingot, grown without seeding. The bottom faces of the samples were investigated by Scanning Electron Microscopy SEM equipped with EDS for qualitative composition analysis, as shown in Fig. 3 (a). Residual coating covered most of the bottom slices, and in order access underlying particles the samples had to be etched for approximately 2min in Sopori etch (which should remove approximately 10µm of a bare silicon surface [29]). This resulted in samples only partly covered in residual coating, as seen in Fig. 3 (b), and underlying particles could now be studied in SEM by tilting the samples 60-70°. An additional etching step was added to some of the samples, up to a total of 4min, in order to remove enough coating to study any possible underlying nucleation sites.

3. Results

3.1. Investigation of as-coated sample

SEM investigation of the as-coated sample show that the α-Si_3N_4 coating mainly consists of sub-micrometre particles. The hexagonal faces are clearly visible in the magnified micrographs shown in Fig. 4 (a) even though the resolution is low due to electrical charging of the particles in the microscope. The morphology of a hexagonal particle is commonly noted by its top $\{0001\}$ basal-plane and $\{01\bar{1}0\}$ side-plane. A nucleus on the top basal-plane will be limited by the edges of the hexagon, having an approximate diameter a, while a nucleus on a side-plane in most cases will be limited by the width b of the plane. Both have been measured and are presented in Fig. 4 (b). The size distribution is approximated by Gauss curves, giving mean values of approximately $a = 145nm$ and $b = 90nm$.

3.2. Investigation of solidified ingots

Magnified SEM micrographs of coating islands remaining after the first etch procedure, seen in Fig. 3 (b), reveal large amounts of particles below the top coating layer, as seen in Fig. 5 (a). By investigating the coating islands at tilted angles, as in Fig. 5 (b), one can observe what appears to be a nearly continuous layer of large hexagonal particles below the coating layer, whose silicon- and nitrogen-content can be confirmed by EDS, as in Fig. 5 (c).

The layer does, however, not appear to be in continuous contact with the underlying silicon, with an observed gap between the silicon and the particle layer of up to 100 - 200µm, i.e. much more than the estimated thickness of silicon removed by the etch.

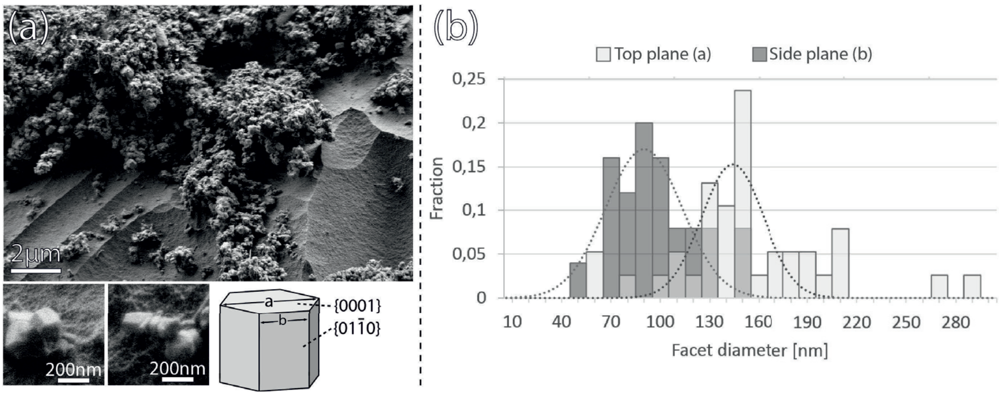

Fig. 4. (a) The α-Si_3N_4 coating are found to mainly consist of sub-micrometre particles with clear hexagonal facets. (b) The size distribution of the two main planes defining the hexagons are measured, showing an average diameter of approximately 90 – 145nm. For the $\{01\bar{1}0\}$-facet the smallest side of the facet is measured.

There is a large variation in observed particle size (Fig. 5 (d)), and the size distribution spans over several tens of micrometres, as shown in in Fig. 6 (a). The size distribution is also here approximated by Gauss curves, giving mean values of approximately $a = 9500nm$ and $b = 4000nm$, which are considerably larger than what was previously measured for α-Si_3N_4 coating particles. However, it becomes evident that the particles do not display any visible $\{0001\}$ planes, and the top and bottom faces appears to be limited by higher index planes arranged in pyramidal structures instead, as shown in Fig. 5 (d) and Fig. 6 (b).

By increasing the etching time to 4 minutes most of the residual coating was removed, and only small islands remained. These remaining particle-clusters are clearly embedded into the silicon, as seen in Fig. 7 (a) and (b), whereas several of them appear to accumulate grain boundaries and parallel twins.

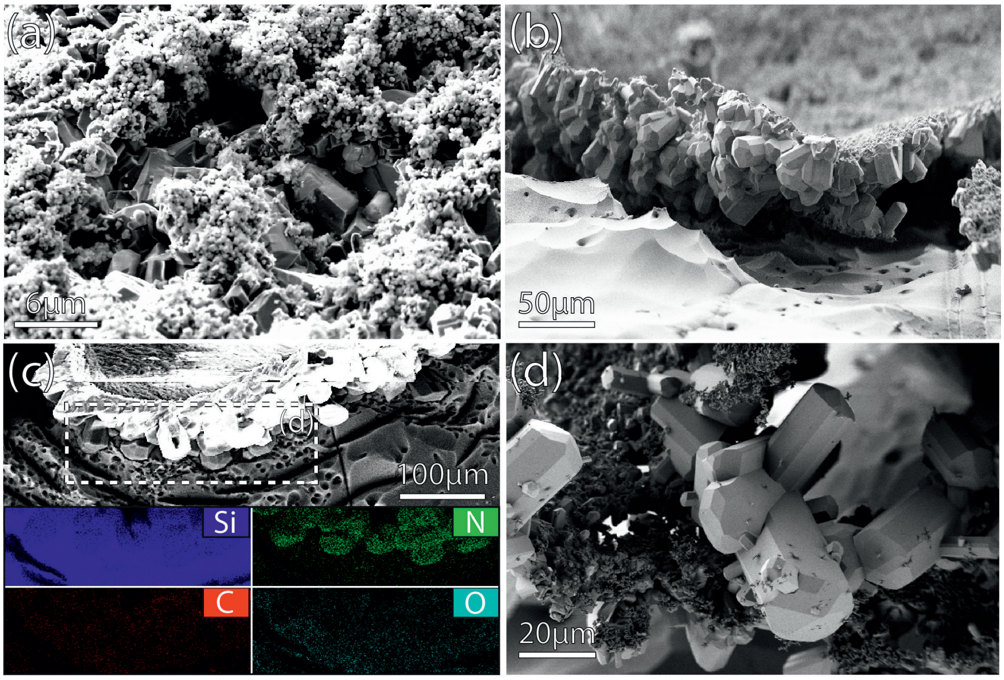

Fig. 5. (a) Underlying particles can readily be observed below residual coating on solidified ingots. (b) Tilting the sample reveals what appears to be near-continuous layer of large β-Si_3N_4 particles. (c) The nitrogen content of the particles is confirmed by EDS. (d) The particles show large and clear crystallographic facets. Residual α-Si_3N_4 coating can be found surrounding the large β-particles.

4. Discussion

4.1. Beta-Si_3N_4 as inoculant particles

The free-growth model, as proposed by Greer et al [14], states that the size of the silicon nucleus is limited by the facet size of the inoculant particle. A particle with a facet diameter *d* can therefore only successfully facilitate critical nuclei with a maximum size given by eq. 4.1.

$$r_{het}^{*} = \frac{d}{2} \tag{4.1}$$

The critical radius of a silicon nucleus has previously been plotted as a function of the nucleation undercooling in Fig. 2 (b) by inserting $\gamma_{SL} = 0.68\frac{J}{m^2}$ [16], $T_m = 1683K$ [17] and $\Delta H_v = 46.6\frac{kJ}{mol}$ [17] into eq. 1.1. Nucleation starts as soon as the required undercooling for nucleation on an arbitrary inoculant particle is met. As soon as the cooling process is started and the temperature is lowered below the melting point there will be an onset of an initially small undercooling in the bottom of the crucible. The critical radius for heterogeneous nucleation of a stable nucleus will in this case be very large (> 20μm), requiring inoculant particles with diameters above 40μm. The previously measured facet sizes of both α- and β-Si_3N_4, in Fig. 4 (a) and Fig. 6 (a), have been included in Fig. 2 (b). Due to the significantly larger size, the β-particles can promote nucleation sooner and at much lower undercoolings (~ 0.1 – 0.3K) than α-particles (~ 6 - 11K), as indicated by the arbitrary cooling curve in Fig. 2 (a). A previous study by Beaudhuin et al [22] found a strong influence of nitrogen on the undercooling in electromagnetic levitated silicon droplets. Even though such experiments do not correctly reflect conditions present during direction solidification they observed an undercooling down to approximately 1K at high nitrogen concentrations, which may to some extent reflect the conditions close to the coated crucible wall. An additional study by Alphei et al [13] found that amorphous silicon nitride particles added to the melt transformed into crystalline silicon nitride rods with diameters of 100 – 300nm and lead to nucleation of silicon at undercoolings as low as 2K < ΔT < 6K, which corresponds well to the graph in Fig. 2 (b).

In order to secure a high catalytic potency the interfacial free energy between the inoculant and the silicon nucleus should be kept to a minimum, which is only possible with a low crystallographic mismatch between them [7]. In the case of grain refinement of aluminium, which has been extensively studied in terms of nucleation properties, nucleation undercoolings as low as below 0.5K can be attained by adding inoculants with a crystallographic mismatch of ~3.7% to the melt [14, 30]. In the case of silicon, the atomic mismatch between e.g. $\{111\}_{Si}$ and $\{0001\}_{\beta-Si_3N_4}$ is found to be approximately 1% [24], while calculations from lattice parameters [20] show that the atomic mismatch between $\{111\}_{Si}$ and $\{0001\}_{\alpha-Si_3N_4}$ is approximately 2.1%. We therefore find no reason not to believe that initial nucleation in silicon also can progress at undercoolings even less than 1K. The lack of {0001}-facets in Fig. 5 (d) and Fig. 6 (b) is probably related to both the Sopori etch and the growth habits of hexagonal crystals. While the {0001}-planes may be exposed to the melt during initial nucleation, the high growth rate of this facet [31] will make it progressively disappear during growth and replaced by more slowly growing facets [32].

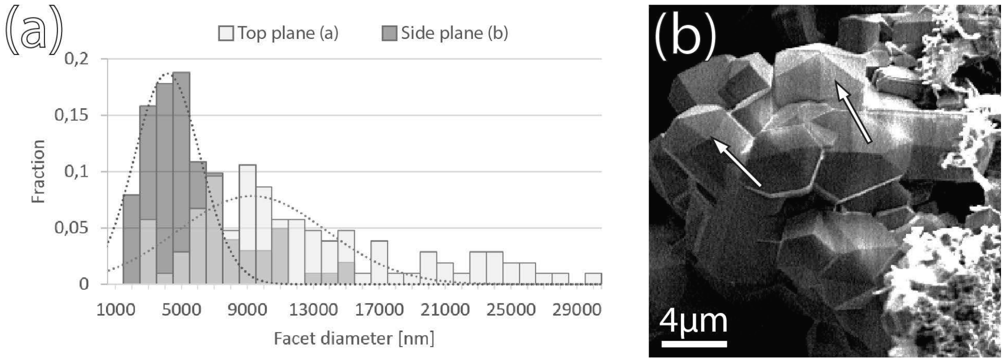

Fig. 6. (a) The size distribution of same facets as previously measured for α-Si_3N_4 particles are also measured here for β-Si_3N_4 particles. (b) The long hexagonal particles rarely show flat ends, and are instead limited by high-index planes, forming a pyramidal structure.

It is important to note that we do not rule out α-Si_3N_4 particles as possible inoculants for silicon nucleation, as the crystallographic mismatch is comparable to that of β-Si_3N_4. However, due to their smaller size, which requires substantial undercooling for forming a stable nucleus, we assume that there is a high probability that these particles already have been overgrown by grains nucleated at lower undercoolings, i.e. on the larger β-Si_3N_4 particles.

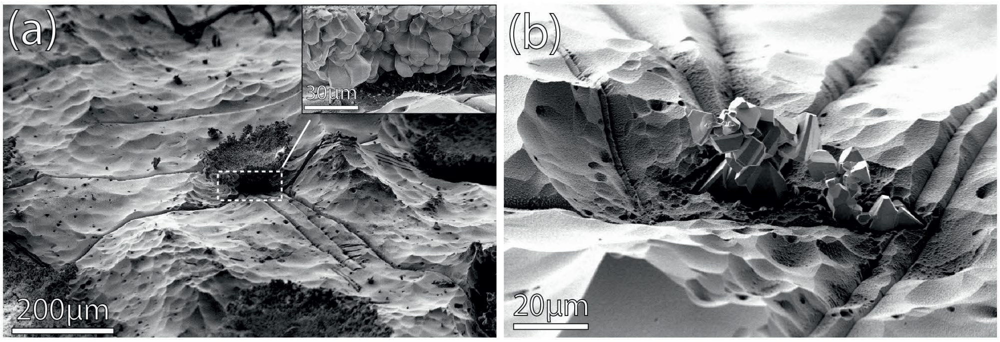

Fig. 7. (a) Increased etching time removed most of the residual coating, revealing points of physical contact between the particle-layer and the solidified silicon. (b) The particles are clearly embedded into the silicon and can often be found to accumulate parallel twins and other grain boundaries.

4.2. Observations of nucleation sites

As clearly seen from Fig. 5 (b), there appears to be a considerable gap between large parts of the coating layer and the solidified silicon. Direct contact between the two is only found at localized positions, as shown for two separate positions in Fig. 7 (a) and (b), where the particles are clearly embedded into the solidified silicon. The 100 – 200μm gap is much larger than the 10μm expected to be removed by 2min of Sopori etch, and one may also expect a much smoother silicon surface with few sharp extremities. We therefore suggest that the silicon melt is in fact not in continuous contact with the coating layer during growth, which we further relate to the non-wetting properties of the coating towards the liquid silicon and the surface tension of the liquid. We also propose that the actual contact between the coating and the melt will be limited to certain contact points and affected by the roughness of the bottom face of the crucible and coating, as illustrated in Fig. 8 (a). Particles not in contact with the melt, as illustrated in Fig. 8 (b), will therefore not be able to facilitate nucleation.

The contact area between the melt and the particle layer will fluctuate during the solidification process due to natural convection, and therefore the particles which are in contact with the melt will change over time. However, the illustration in Fig. 8 (b) can still be viewed as a snapshot in time at the start of nucleation, thereby still limit the amount of particles able to facilitate nucleation. However, as clearly seen in Fig. 5 (b), β-Si_3N_4 particles appear to form also without contact with liquid silicon, suggesting that the transformation of α to β also can proceed without direct contact with liquid silicon. The transformation may in this case go through gas-phase reactions, as previously discussed by Moulson [33] and Jennings [34]. This is based on the assumption that the voids are supplied with a vapour pressure of silicon from the melt and with nitrogen from dissolution of α-Si_3N_4 particles, leading to the following nitridation reaction [33]:

$$\begin{gathered} 3Si(g) + 2N_2(g) \leftrightarrow Si_3N_4(s) \\ \Delta G^0 \approx -2080 + 0.757 \cdot T \frac{kJ}{mol} \end{gathered} \tag{4.2}$$

Note that this is just a theoretical assessment and has yet to be confirmed experimentally. Parallel twin boundaries are features commonly observed for facetted dendrites, which grow rapidly by atomic adsorption on re-entrant corners in undercooled melts [1]. In a previous work by Kutsukake et al [35] it was observed how the majority of such twin boundaries led back to the crucible wall, and combined with the high occurrence of parallel twin boundaries observed on the bottom cuts in the current work we suggest that dendrites in fact have an important role also during initial growth of conventional multicrystalline silicon. It has in several cases been suggested that a nucleus will retain its spherical shape up to a certain size, after which the sphere breaks down and transforms into a cellular or dendritic morphology [14, 32, 36] due to increasing instabilities. This theory has, however, not been confirmed for pure silicon melts. In the current work parallel twins are frequently found to accumulate together with other grain boundaries at contact points, as e.g. shown in the micrographs in Fig. 7 (a) and (b), suggesting that these points in fact act as nucleation sites.

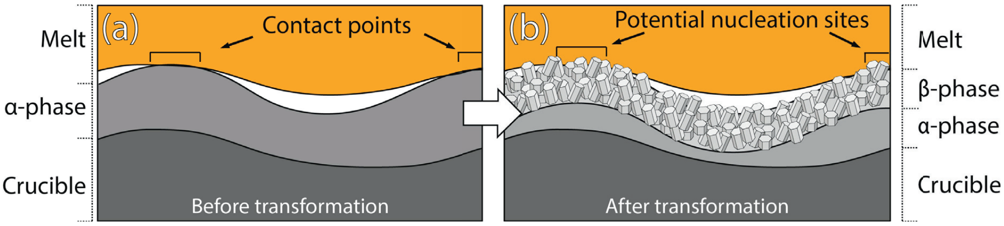

Fig. 8. (a) The coating holds a certain roughness towards the silicon melt, and the contact area between the coating and melt is minimized as a result of the non-wetting properties of the coating and the surface tension of the melt. The contact is therefore limited only to the top extremities of the α-phase coating. (b) The β-phase appears to form as what appears to be a near-continuous layer closest to the melt, also without direct contact with liquid silicon. However, nucleation of solid silicon can only form on particles which are in direct contact with liquid silicon.

Dendrites have previously been shown to grow rapidly in undercooled melts [37] and, as previously suggested for solidification of multicrystalline silicon by Stokkan [38], they may grow with their main stem in any spatial direction from their point of formation. While a dendrite can grow relatively freely parallel to the crucible bottom it will be more or less confined by the melting isotherm if it grows at an angle inclined away from the crucible bottom. It may even reach a point where it is favourable to change grow direction. If a higher undercooling is not deliberately maintained by the furnace, as it is in the case of the dendritic growth method proposed by Fujiwara et al [37], most of the undercooling will be lost at the end of the nucleation step (i.e. the point of recalescence) and the dendritic growth will cease. At this point the initial structure will consist of a certain fraction of dendritic and non-dendritic grains, which will continue to grow collectively by epitaxial growth. We therefore suggest that the composition of the initial structure not only depends on the cooling parameters, but also the size of the Si_3N_4 particles in contact with the melt, and we will try to illustrate this by considering three hypothetical cases. It is, however, important to realise that there are both theoretical and practical limitations to the cooling parameters, as the cooling rate and the temperature gradient is closely related.

Uniform distribution of large Si_3N_4 particles: Large particles require only small undercoolings in order to facilitate nucleation, and the probability of nucleating dendrites should be small. The most interesting scenario will arise from combining this particular case with a slow cooling rate. This scenario is ideal for generating a high density of small, surviving nuclei, which are allowed to grow forth before overgrowth of neighbouring grains, and will thereby lead to a more refined structure. Substantial growth of dendrites is not compatible with this method as they will rapidly overgrow neighbouring Si_3N_4 particles and thereby lead to a coarsening of the grain structure. However, the slow cooling rate will ensure further suppression of the dendritic growth in addition to allowing a homogeneous distribution of surviving nuclei.

Uniform distribution of small Si_3N_4 particles: Smaller particles require larger undercooling in order to facilitate nucleation, and there is therefore a higher probability of forming dendrites. Due to the rapid growth of dendrites we expect them to have a pronounced effect on the final grain structure. The exact magnitude of the effect will also depend on the cooling process, but due to the unpredictability of dendrites it may be more difficult to control. Depending on the spatial orientation of the dendrites the initial structure will mainly be dominated by dendrites having the most pronounced horizontal growth kinetics, and due to a high degree of overgrowth we expect to see a considerable coarsening of the grain structure. The vertical growth will, however, depend on the vertical temperature gradient in the melt. A large temperature gradient will confine the vertical growth of the dendrites to the melting isotherm and only the most favourable dendrites will grow forth, corresponding to the dendritic casting method [37]. A small temperature gradient, on the other hand, will not be as confining as a high temperature gradient, and dendrites may grow much more freely. This will allow more dendrites to grow forth and thereby lead to a finer structure, with a wider span of crystal orientations, than in the previous case.

A mixture of small and large Si_3N_4 particles: In the most general case, which is also the most realistic, the size distribution spans over a large interval of different particle sizes inhomogeneously distributed over the crucible bottom. The first nucleation events will take place on the largest Si_3N_4-particles available, as soon as the undercooling reaches the necessary value. However, as these nuclei grow forth, there will be a simultaneous increase in the undercooling, as illustrated in Fig. 2 (a), allowing continuously smaller particles to facilitate nucleation. The probability of nucleating dendrites will therefore increase along with the increased undercooling, and the initial structure will consist of a fraction of both dendritic and non-dendritic grains. The amount of nuclei allowed to grow forth, and the smallest particle allowed to nucleate silicon, will depend on how rapidly the initial nuclei overgrow neighbouring Si_3N_4-particles. If allowed to grow forth, dendrites will in most cases dominate, leading to a coarsening of the early grain structure, as typically seen in conventional multicrystalline silicon. Nevertheless, the vertical progression of the dendritic grains will also here be partly controllable by the cooling parameters, e.g. the vertical temperature gradient, as described previously.

This leads us to our final remarks. The current work has shown how the size of Si_3N_4 particle may affect the grain structure of silicon ingots solidified by directional solidification. The unpredictable occurrence of rapidly growing dendrites appears to limit the grain refinement potential for the most common growth conditions. However, this work also suggests that a certain degree of grain refinement may be achieved by utilizing a uniform distribution of large Si_3N_4 particles together with a slow cooling procedure. By engineering the size of the Si_3N_4 particles one should therefore be able to control the initial grain structure and to a certain degree tailor the final grain structure of the ingot. The transformation from small α-Si_3N_4 particles to the larger β-Si_3N_4 particles appear to be inevitable and a possible way of achieving a more even distribution of larger particles may be by extending the holding time before solidification, allowing for a more complete α-to-β transformation and additional growth time for the β-particles. The opposite effect may be achieved by minimizing the contact time between the coating and the silicon melt (such as in the conventional casting method, by pouring liquid melt into a crucible). One may also consider coating the crucible with a pre-defined size distribution of β-Si_3N_4 particles.

Conclusion

In this work we have shown the existence of a nearly continuous layer of large and clearly faceted β-Si_3N_4 particles between the α-Si_3N_4 coating and the solidified silicon. By using established nucleation theory we have argued for initial nucleation of silicon on the large facets of β-Si_3N_4 particles at low undercoolings. We do not rule out nucleation on α-Si_3N_4 particles, but due to the higher undercooling required for nucleation on such small particles we believe that there is a probability that these nucleation sites will be overgrown by grains nucleating earlier at lower undercoolings. The limited contact area between the solidified silicon and the particle layer suggests that nucleation only take place at localized contact points, which is further supported by accumulation of grains and parallel twins at these positions. Due to the sheer amount of parallel twins we suggest that dendrites have a pronounced effect on the grain structure also for conventionally grown multicrystalline silicon, therefore limiting the potential for grain refinement for the most common growth conditions. However, we suggest that, by engineering the size of the Si_3N_4-particles and carefully controlling the temperature profile of the solidification process one should be able to control the initial grain structure, and to a certain degree tailor the final grain structure of the ingot.

Acknowledgements

This work was partly supported by The Centre for Environment-Friendly Energy Research (FME) under The Research Council of Norway (RCN) in cooperation with SINTEF Materials and Chemistry. The authors also want to acknowledge A. Autruffe of the Norwegian University of Science and Technology for useful discussions.

References

[1] Fujiwara K. Crystal Growth Behaviors of Silicon during Melt Growth Processes. Int J Photoenergy **2012**, 1 (2012).

[2] Di Sabatino M, Juel M, Arnberg L, Syvertsen M, Tranell G. Control of grain size and -orientation in multi-crystalline silicon ingots. T Indian I Metals **62**, 511 (2009).

[3] Wong YT, Hsieh CT, Lan A, Hsu C, Lan CW. The effect of silica nucleation layers on grain control of multi-crystalline silicon in directional solidification. J Cryst Growth **404**, 59 (2014).

[4] Trempa M, Reimann C, Friedrich J, Muller G, Oriwol D. Mono-crystalline growth in directional solidification of silicon with different orientation and splitting of seed crystals. J Cryst Growth **351**, 131 (2012).

[5] Kurz W, Fisher DJ. Fundamentals of solidification. 4th rev. ed. Uetikon-Zuerich, Switzerland ; Enfield, N.H.: Trans Tech Publications; 1998. 305 p. p.

[6] Brynjulfsen I. Nucleation and Early Growth of Multicrystalline Solar Cell Silicon [Doctoral Thesis]. Trondheim: Norwegian University of Science and Technology; 2012.

[7] Kelton K, Greer AL. Nucleation in Condensed Matter: Applications and Materials and Biology: Pergamon; 2010.

[8] Brynjulfsen I, Arnberg L. Nucleation of silicon on Si3N4 coated SiO2. J Cryst Growth **331**, 64 (2011).

[9] Appapillai A, Sachs E. The effect of substrate material on nucleation behavior of molten silicon for photovoltaics. J Cryst Growth **312**, 1297 (2010).

[10] Appapillai AT, Sachs C, Sachs EM. Nucleation properties of undercooled silicon at various substrates. J Appl Phys **109**, (2011).

[11] Brynjulfsen I, Arnberg L, Autruffe A. Nucleation in small scale multicrystalline silicon ingots. J Cryst Growth **361**, 206 (2012).

[12] Tsoutsouva MG, Duffar T, Garnier C, Fournier G. Undercooling measurement and nucleation study of silicon droplet solidification. Cryst Res Technol **50**, 55 (2015).

[13] Alphei L, Braun A, Becker V, Feldhoff A, Becker JA, Wulf E, et al. Crystallization of supercooled silicon droplets initiated through small silicon nitride particles. J Cryst Growth **311**, 1250 (2009).

[14] Greer AL, Bunn AM, Tronche A, Evans PV, Bristow DJ. Modelling of inoculation of metallic melts: Application to grain refinement of aluminium by Al-Ti-B. Acta Materialia **48**, 2823 (2000).

[15] Maxwell I, Hellawell A. Simple Model for Grain Refinement during Solidification. Acta Metall Mater **23**, 229 (1975).

[16] Jian ZY, Kuribayashi K, Jie WQ, Chang FG. Solid-liquid interface energy of silicon. Acta Materialia **54**, 3227 (2006).

[17] Haynes WM. CRC Handbook of Chemistry and Physics, 95th Edition 2014.

[18] Mjøs ØS, G.; Søiland, A. K.; Arnberg, L. . Mapping of Silicon Carbide and Silicon Nitride Precipitates on Chemical-Mechanically Polished mc-Silicon Wafers. European PV Solar Energy Conference and Exhibition 2014, (2004).

[19] Soiland AK, Ovrelid EJ, Engh TA, Lohne O, Tuset JK, Gjerstad O. SiC and Si3N4 inclusions in multicrystalline silicon ingots. Mat Sci Semicon Proc **7**, 39 (2004).

[20] Kuwabara A, Matsunaga K, Tanaka I. Lattice dynamics and thermodynamical properties of silicon nitride polymorphs. Phys Rev B **78**, (2008).

[21] Messier DR, Riley FL, Brook RJ. Alpha-Beta-Silicon Nitride Phase-Transformation. J Mater Sci **13**, 1199 (1978).

[22] Beaudhuin M, Zaidat K, Duffar T, Lemiti M. Nitrogen reaction with silicon: Investigation of Si undercooling and Si3N4 growth. J Cryst Growth **336**, 77 (2011).

[23] Nakajima K, Morishita K, Murai R, Usami N. Formation process of Si3N4 particles on surface of Si ingots grown using silica crucibles with Si3N4 coating by noncontact crucible method. J Cryst Growth **389**, 112 (2014).

[24] Wang L, Wang XS, Tang JC, Cue N. Investigation of Si and Ge growth on Si3N4/Si. Mater Charact **48**, 189 (2002).

[25] Yamabe N, Yamamoto Y, Ohachi T. Epitaxial growth of beta-Si3N4 by the nitridation of Si with adsorbed N atoms for interface reaction epitaxy of double buffer AlN(0001)/beta-Si3N4/Si(111). Physica Status Solidi C: Current Topics in Solid State Physics, Vol 8, No 5 **8**, (2011).

[26] Beaudhuin M, Chichignoud G, Bertho P, Duffar T, Lemiti M, Zaidat K. Carbon reaction with levitated silicon - Experimental and thermodynamic approaches. Mater Chem Phys **133**, 284 (2012).

[27] Pupazan V, Negrila R, Bunoiu O, Nicoara I, Vizman D. Effects of crucible coating on the quality of multicrystalline silicon grown by a Bridgman technique. J Cryst Growth **401**, 720 (2014).

[28] Hatayama T, Tarui Y, Fuyuki T, Matsunami H. Low-Temperature Heteroepitaxial Growth of Cubic Sic on Si Using Hydrocarbon Radicals by Gas-Source Molecular-Beam Epitaxy. J Cryst Growth **150**, 934 (1995).

[29] Sopori BL. A New Defect Etch for Polycrystalline Silicon. J Electrochem Soc **131**, 667 (1984).

[30] Schumacher P, Greer AL, Worth J, Evans PV, Kearns MA, Fisher P, et al. New studies of nucleation mechanisms in aluminium alloys: implications for grain refinement practice. Mater Sci Tech-Lond **14**, 394 (1998).

[31] Li WJ, Shi EW, Zhong WZ, Yin ZW. Growth mechanism and growth habit of oxide crystals. J Cryst Growth **203**, 186 (1999).

[32] Wang RY, Lu WH, Hogan LM. Twin Related Silicon-Crystals in Al-Si Alloys and Their Growth-Mechanism. Mater Sci Tech-Lond **11**, 441 (1995).

[33] Moulson AJ. Reaction-Bonded Silicon-Nitride - Its Formation and Properties. J Mater Sci **14**, 1017 (1979).

[34] Jennings HM. On Reactions between Silicon and Nitrogen .1. Mechanisms. J Mater Sci **18**, 951 (1983).

[35] Kutsukake K, Abe T, Usami N, Fujiwara K, Morishita K, Nakajima K. Formation mechanism of twin boundaries during crystal growth of silicon. Scripta Mater **65**, 556 (2011).

[36] Mullins WW, Sekerka RF. Morphological Stability of a Particle Growing by Diffusion or Heat Flow. J Appl Phys **34**, 323 (1963).

[37] Fujiwara K, Pan W, Sawada K, Tokairin M, Usami N, Nose Y, et al. Directional growth method to obtain high quality polycrystalline silicon from its melt. J Cryst Growth **292**, 282 (2006).

[38] Stokkan G. Relationship between dislocation density and nucleation of multicrystalline silicon. Acta Materialia **58**, 3223 (2010).